Title
THERMODYNAMICS AND KINETICS OF SINTERING

Author
Hoge, Carl Edward.

Publication Date
1975

LBL-3116

THERMODYNAMICS AND KINETICS OF SINTERING

Carl Edward Hoge
(Ph. D. thesis)

January 1975

Prepared for the U. S. Atomic Energy Commission
under Contract W-7405-ENG-48

LBL-3116

DISCLAIMER

THERMODYNAMICS AND KINETICS OF SINTERING

Table of Contents

PART B: THERMODYNAMICS AND KINETICS OF LIQUID PHASE SINTERING

THERMODYNAMICS AND KINETICS OF SINTERING

Carl Edward Hoge

Inorganic Materials Research Division, Lawrence Berkeley Laboratory
and Department of Materials Science and Engineering,
College of Engineering; University of California,
Berkeley, California 94720

ABSTRACT

Thermodynamic approaches to sintering have as yet received little theoretical or experimental investigation although a thorough understanding of thermodynamic factors is required to accurately predict sintering phenomena. Since the basic driving force for sintering is the reduction in interfacial energy associated with changes in interfacial areas of powder compacts, the differential of the free energy, δG, must remain negative for sintering to proceed. If δG becomes equal to zero, sintering ceases and possible endpoint densities less than theoretical will result.

In Part A of this report, a thermodynamic analysis of solid phase sintering for several geometric assemblages is performed. In this analysis, the solid-vapor dihedral angle is related to critical ratios of γ_{ss}/γ_{sv} that determine endpoint densities for each packing array. The experimental dihedral in a sintering compact is also shown to influence the vacancy concentrations near internal and external interfaces, and to determine the thermodynamic driving force for densification.

Thermodynamic analyses of grain boundary motion indicate that pores pin planar grain boundaries and that a critical grain boundary curvature is necessary for grain boundaries to sweep past pores leaving

them isolated and that this curvature is relatively independent of the dihedral angle for most solid phase sintering systems.

In order to compare theory with experiment, the sintering of MgO compacts is investigated. Results indicate that sintering rates are dependent upon the thermodynamic driving force for densification and that possible endpoint densities less than theoretical may be an inherent characteristic of MgO for certain packing arrays.

In Part B, a thermodynamic analysis is performed for liquid phase sintering systems forming zero and nonzero solid-liquid dihedral angles. Results indicate that critical ratios of $\gamma_{s\ell}/\gamma_{\ell v}$ exist which are dependent on the magnitude of the dihedral for the system and on the volume fraction of liquid phase.

Additionally, kinetic analyses are performed using numerical integration techniques which enable a more accurate description of liquid phase sintering rates than have previously been discussed. These models are described in terms of particle size differences, in terms of magnitudes of dihedral angles; and in terms of volume of liquid phase in sintering compacts. From these analyses, densification parameters are related to time and to the initial particle sizes. The models are then discussed in terms of existing experimental data.

PART A: THERMODYNAMICS OF SOLID PHASE SINTERING

I. INTRODUCTION

If an array of particles of equilibrium single phase composition is subjected to sufficient temperature such that mass transfer mechanisms become operative, the areas of solid/vapor interfaces begin to decrease as solid/solid interfaces form. This process is defined as sintering, and the basic driving force for sintering is the resulting reduction in free energy of the system.

In order to fully characterize sintering, knowledge of thermodynamic and kinetic factors is necessary. From thermodynamic analyses, interfacial energy relationships can be obtained which correspond to minimum free energy configurations for specific geometric assemblages of particulates. However, since these relationships yield only free energy states independent of time, they do not reveal the path of densification of a compact. From kinetic considerations, which encompass mechanistic approaches, the sintering path may be traced as a function of time.

Generally, idealized models are formulated to simulate the kinetics of a sintering compact. Since no one model can accurately describe the entire sintering process, several are needed. When one model becomes inoperative, a "stage" of sintering is said to be completed, and a different model must then be applied to describe further sintering.

The initial stage of sintering of a solid-vapor system has been associated with the formation of a "neck" at particle contact points and was described by Kuczynski[1] in terms of a two-sphere model for several mechanisms of mass transport. The vaporization-condensation mechanism is based on the fact that the equilibrium vapor pressure of the solid is

higher above a convex or spherical surface than above a planar surface, and higher above a planar surface than above a concave surface. When two spheres are in contact, as in the model, a concave surface forms between them. Then a vapor pressure gradient exists between the convex and concave surfaces, and material transport occurs through the vapor phase forming a circular "neck" region and a grain boundary between the spheres. A similar model based on a surface diffusion mechanism leads to the same geometric configuration.[1,2] Neither model leads to densification of a compact.

A model which does lead to densification is based on Nabarro's[3] analysis that, for a crystalline solid, there exists a greater concentration of vacancies under a concave surface than under a stress-free planar surface or a convex surface. Such a concentration difference gives rise to a vacancy concentration gradient between the "neck" region of a two-sphere model and the planar grain boundary or the convex surface. Since material flows counter to vacancy flow, mass transfer occurs. This mechanism is the basis for numerous kinetic solutions for densification during various stages of solid phase sintering.

Kingery,[4] Johnson,[5] Coble,[6] and others[7-12,1] have derived kinetic equations for volume and grain boundary diffusion models for densification of solid-vapor systems of the form

$$\frac{\Delta L}{L_o} = \left\{ \frac{K\gamma_{sv}\, a^3 D}{kTR^m} \right\}^y t^y \qquad (1)$$

where y, m, and K are numerical constants, D is the volume or grain

boundary diffusion coefficient, a^3 is the atomic volume, γ_{sv} is the solid-vapor interfacial tension, T is the absolute temperature, k is Boltzmann's constant, and R is the particle radius.

For volume diffusion mechanisms, the exponent of time, y, ranges from 0.40 to 0.50, depending on the geometry of the sintering model employed; and for grain boundary diffusion, y ranges from 0.31 to 0.33. The exponent, m, of particle size is 3 for volume diffusion mechanisms and 4 for grain boundary diffusion mechanisms.

If an ideal one component crystalline compact is subjected to sufficient temperature such that the various mass transfer mechanisms mentioned above become operative, solid-solid contacts begin to form or increase between particles. After a sufficient time, the compact is characterized by a solid network and an interconnecting pore phase. Upon further sintering, the pore phase becomes discontinuous, and eventually is eliminated. At this point, all of the solid-vapor interfacial area has also been eliminated and the compact has attained theoretical density. This point, however, in most cases does not constitute a minimum free energy configuration since internal surfaces (grain boundaries) can generally continue to migrate and decrease in area until a minimum free energy configuration, corresponding to planar grain boundaries,[13-15] is attained. Ideally, grain boundary motion would continue until all internal surfaces were eliminated and a single crystal would form.

In practice, densities less than theoretical are often obtained during sintering when pores become disassociated from grain boundaries and isolated in the grains due to grain boundary motion. Removal of isolated pores depends on long vacancy diffusion paths between the pore

surface and the grain boundary. Although the free energy of such a system is not at its minimum value, the change in free energy with time becomes so small that for all practical purposes sintering ceases, i.e., the slope of the free energy versus time curve approaches zero, Fig. 1.

The effect of thermodynamic factors on endpoint densities and densification rates in real compacts has as yet received little attention. Therefore, several idealized geometric models will be investigated in order to determine thermodynamic constraints on densification and on grain boundary motion away from pores.

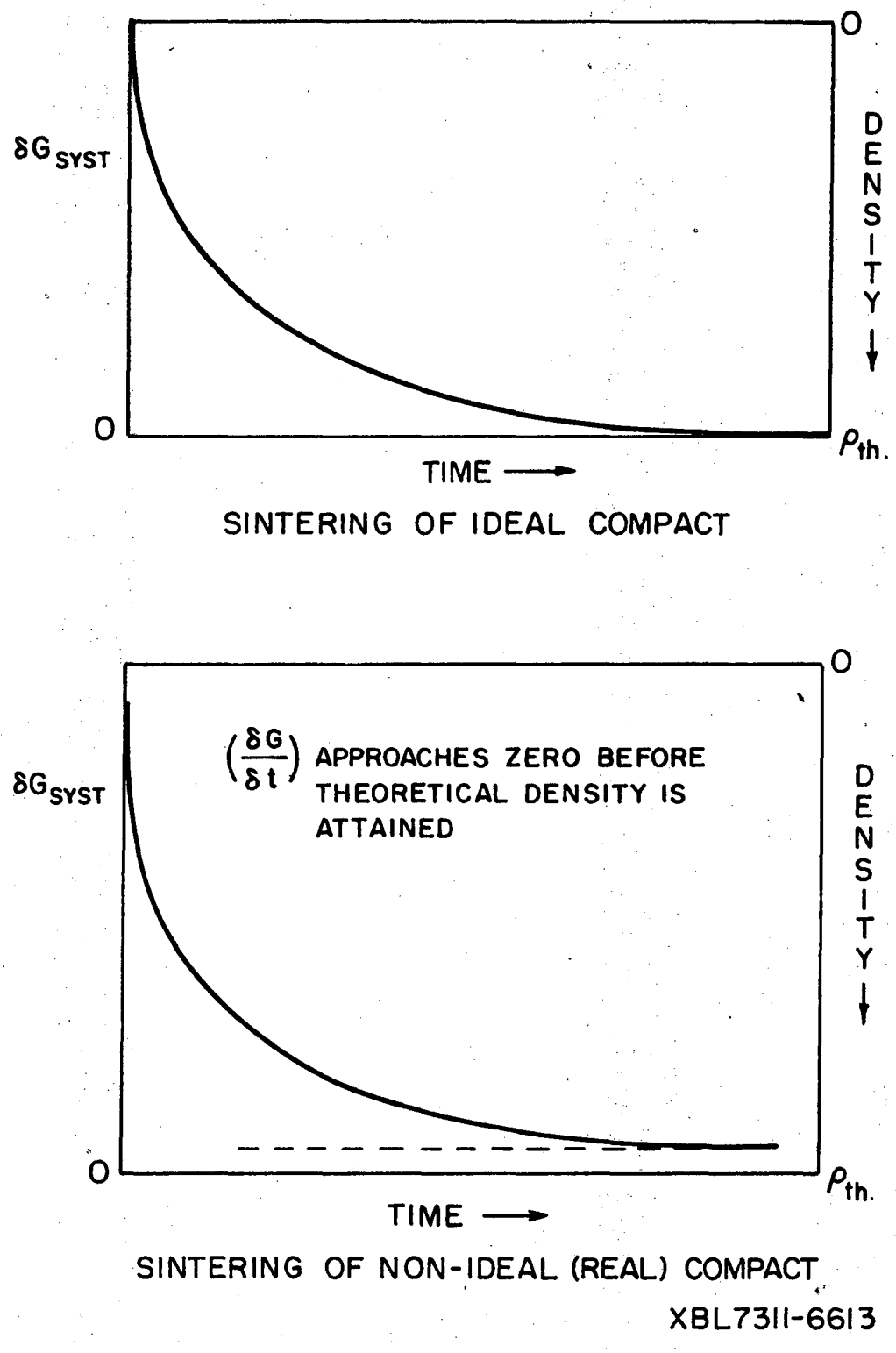

Figure 1. Incremental free energy change with time for sintering of an ideal compact (top) and a real compact (bottom).

II. THERMODYNAMIC CONSIDERATIONS

A. Thermodynamics of Endpoint Densities

In a sintering powder compact as the solid/vapor interfacial area decreases, the solid/solid interfacial area increases. The change in free energy of the system at constant temperature, pressure and mole fraction can then be expressed as

$$\delta(G_{syst}) = \gamma_{sv} dA_{sv} + \gamma_{ss} dA_{ss} \qquad (2)$$

where

γ_{sv} = solid/vapor interfacial energy

γ_{ss} = solid/solid interfacial energy

dA_{sv} = differential solid/vapor interfacial area

dA_{ss} = differential solid/solid interfacial area

As long as $\delta(G)$ remains less than zero, sintering will continue. The first term on the right of the equation is always negative and the second, positive. Therefore, $\delta(G)$ will be a function of the relative interfacial areas (geometry of the system) and interfacial energies.

Four sintering geometries were analyzed for uniform sized spherical particles: diamond cubic, simple cubic, body-centered cubic, and face-centered cubic (corresponding to particle coordination numbers of 4, 6, 8 and 12). The particles are assumed to be single phase, crystalline, and their interfacial energies isotropic. The interfacial energies are related as:

$$\gamma_{ss} = 2\gamma_{sv} \cos \frac{\phi}{2} \qquad (3)$$

where ϕ is the dihedral angle.

The densification model used is based on the concept that the cap material removed at a contact, or grain boundary, between two spheres is uniformly distributed on the free surfaces; the particle centers then move toward each other and the radii of the spheres increase, keeping the total solid volume constant.[16] This model differs from the bridging neck at model contacts normally employed for predicting kinetics of solid phase sintering. Although neck formation is often experimentally observed during sintering, such a geometry is not correct for predicting equilibrium conditions for thermodynamic analysis since it does not correspond to the minimum free energy configuration for the system.

If two spheres are just in contact, Fig. 2A, the free energy of the system is a maximum. Now, if the spheres interpenetrate until a certain cap height, h_0, is removed and deposited in the neck region, Fig. 2B, the radius of each sphere is unchanged. At this point, if no further densification as determined by h_0 or by keeping the centers of the spheres fixed occurs, but the solid/solid, and the solid/vapor interfaces equilibrate, as shown in Fig. 2C, material from the neck region is then deposited uniformly on the surfaces of the spheres and R_0 increases to R and h_0 to h_1 so that $R_0-h_0 = R-h_1$. This geometry corresponds to the minimum free energy configuration for that particular degree of densification and becomes the model used in this analysis. It is the equilibrium geometry when δG in Eq. (2) becomes equal to zero. The γ_{ss}/γ_{sv} can then be determined for this equilibrium configuration.

Proceeding with the thermodynamic analysis, let us consider the densification mechanism represented by the two-sphere model shown in

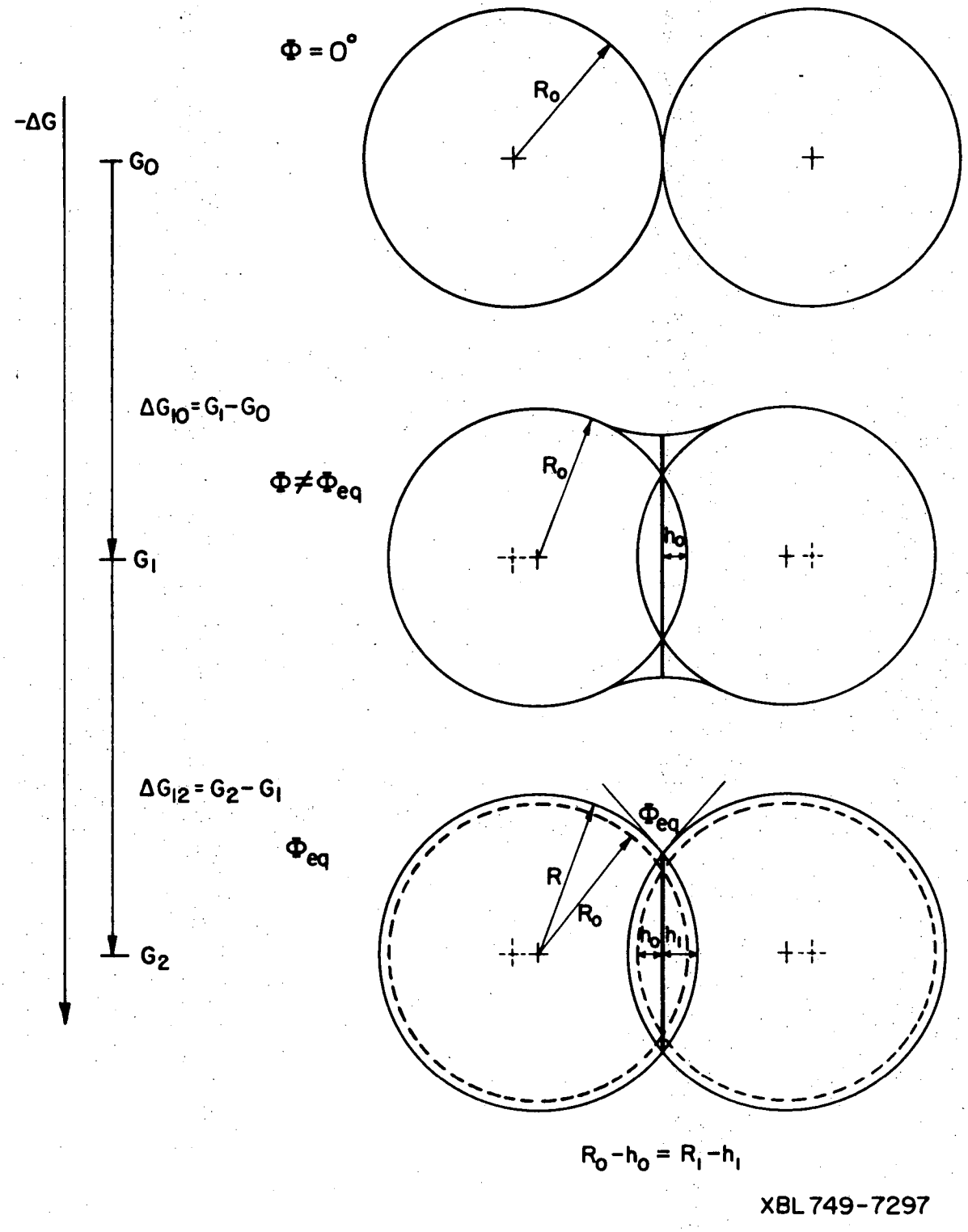

Figure 2. Change in free energy of a two sphere model during interpenetration at particle-particle contact. Spheres just touch (top); neck forms (middle); and equilibrium dihedral angle forms (bottom).

Fig. 2C. The solid-vapor interfacial area is given by

$$A_{sv} = 4\pi R^2 - 2n_1 \pi R h_1 \tag{4}$$

where R is the radius of the sphere and h_1 is the height of the spherical segment at any degree of densification, and n_1 is the coordination of nearest neighbors around each sphere. Setting P_1 as a variable equal to h_1/R, (similar to Stevenson and White[16]),

$$\frac{A_{sv}}{\pi} = 4R^2 - 2n_1 P_1 R^2 \tag{5}$$

Equating the original volume of the sphere, radius R_0, with the volume of the sphere minus caps, radius R, yields the relationship between R_0 and R for any value of P_1.

$$R^3 = \frac{4R_0^3}{4-3n_1P_1^2 + n_1P_1^3} \tag{6}$$

Substituting (6) into (5),

$$\frac{A_{sv}}{(4)^{2/3}\pi R_0^2} = \frac{4 - 2n_1P_1}{(4-3n_1P_1^2 + n_1P_1^3)^{2/3}} \tag{7}$$

and on differentiating,

$$\frac{d\,A_{sv}}{(4)^{2/3}\pi R_0^2} = \left\{ (4 - 3n_1P_1^2 + n_1P_1^3)^{2/3} (-2n_1) - \frac{2}{3} (4 - 3n_1P_1^2 + n_1P_1^3)^{-1/3} \right.$$

$$\left. (-6n_1P_1 + 3n_1P_1^2)(4 - 2n_1P_1) \right\} dP_1 \Big/ (4 - 3n_1P_1^2 + n_1P_1^3)^{4/3} \qquad (8)$$

Since each solid-solid contact is shared by two spheres, the solid-solid area per sphere is expressed as

$$A_{ss} = \pi n_1 h_1 (2R - h_1)/2 \qquad (9)$$

where

$$\frac{(2Rh_1 - h_1^2)\pi}{2}$$

is half the boundary area per contact for a single sphere.

By substituting (6) into (9), and P_1R for h_1,

$$\frac{A_{ss}}{(4)^{2/3}\pi R_0^2} = n_1P_1(2-P_1) \Big/ 2(4-3n_1P_1^2 + n_1P_1^3)^{2/3} \qquad (10)$$

and on differentiating,

$$\frac{dA_{ss}}{(4)^{2/3}\,\pi R_0^2} = \Big\{(4-3n_1P_1^2+n_1P_1^3)^{2/3}\,(2-2P_1)n_1 - \tfrac{2}{3}\,(4-3n_1P_1^2+n_1P_1^3)^{-1/3}$$

$$X[-6n_1P_1 + 3n_1P_1^2](2P_1-P_1^2)n_1\Big\}\,dP_1 \Big/ 2(4-3n_1P_1^2+n_1P_1^3)^{4/3} \qquad (11)$$

Substituting (11) and (8) into (2),

$$\frac{\delta(G_{syst})}{(4)^{2/3}\,\pi R_0^2} = \left\{\frac{(\ )}{(\ )}\,\gamma_{ss} + \frac{(\ )}{(\ )}\,\gamma_{sv}\right\} dP_1 \qquad (12)$$

and setting $\delta(G_{syst}) = 0$,

$$\frac{\gamma_{ss}}{\gamma_{sv}} = \frac{-2((4-3n_1P_1^2+n_1P_1^3)^{2/3}\,(-2n_1) - \frac{2}{3}\,(4-3n_1P_1^2+n_1P_1^3)^{-1/3}}{(4-3n_1P_1^2+n_1P_1^3)^{2/3}\,(n_1(2-2P_1)) - \frac{2}{3}\,(4-3n_1P_1^2+n_1P_1^3)^{-1/3}}\,X$$

$$X\,\frac{(-6n_1P_1+3n_1P_1^2)(4-2n_1P_1))}{(-6n_1P_1+3n_1P_1^2)(2P_1-P_1^2)n_1} \qquad (13)$$

As the interpenetration of nearest neighbor spheres and densification occur for each packing array, second nearest neighbors approach each other and planar faces in the sintering unit cell (such as (110) in BCC packing of spheres) densify. For a given sized particle the rate at which any planar face densifies remains essentially constant but the total amount of shrinkage at this rate depends on the coordination number of spheres in the plane or the degree of packing. At the point when second

nearest neighbors touch, or when one planar face in the unit cell has completely densified, however, Eq. (13) no longer applies. Each of the packing arrays sinters differently after Eq. (13) becomes invalid and, therefore, must be discussed separately.

For BCC packing of spheres (fractional void volume of 0.32), densification proceeds according to the model until contacts form with second nearest neighbors along <100> directions and the coordination increases from 8 to 14, as seen in Fig. 3. At this point h_1 continues to increase, but new contacts formed with second nearest neighbors result in removal of additional cap material of height h_2 and the creation of new solid-solid interfaces. It is evident that Eq. (13) no longer describes the sintering of BCC packing correctly since the effect of second nearest neighbor contacts is not included in the analysis.

Proceeding in a manner similar to the analysis for nearest neighbor contacts,

$$A_{sv} = 4\pi R^2 - 2\pi n_1 R h_1 - 2n_2 \pi R h_2 \qquad (14)$$

where n_2 is the coordination of second nearest neighbors, and h_2 is the height of the cap material removed from second nearest neighbor contacts. Substituting $h_1 = P_1 R$ and $h_2 = P_2 R$ into Eq. (14),

$$A_{sv} = \pi R^2 (4 - 2n_1 P_1 - 2n_2 P_2) \qquad (15)$$

By equating the original volume of the spherical particle with the volume of the sphere, at some value of P, minus both sets of caps, (similar to

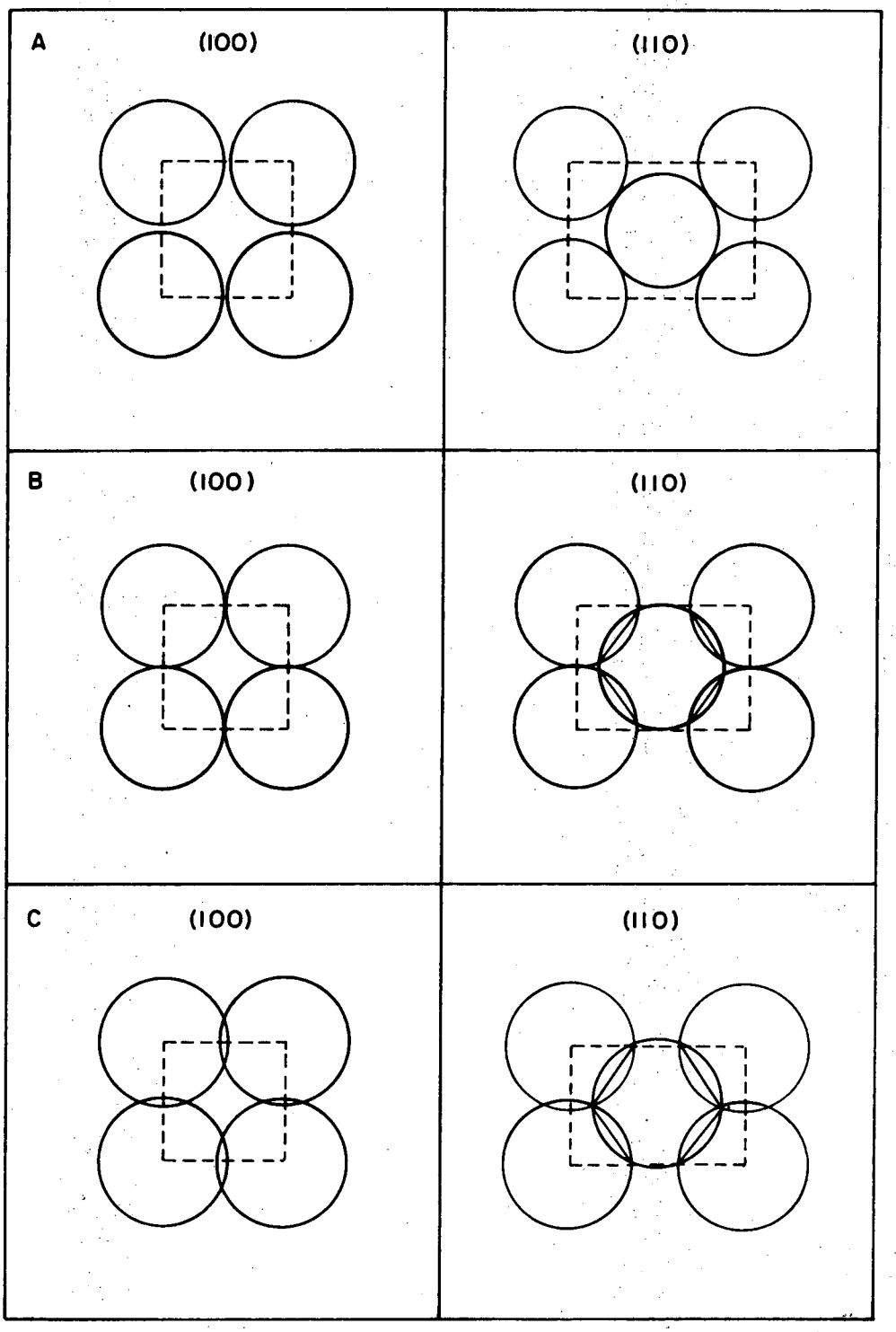

Figure 3. Interpenetration of spheres in a body-centered cubic array.

Eq. (6)), R may be determined in terms of R_0, P_1, and P_2.

$$R^3 = \frac{R_0^3}{\left\{ 1 - \frac{n_1 P_1^2(3-P_1) - n_2 P_2^2(3-P_2)}{4} \right\}} \tag{16}$$

Substituting Eq. (16) into (15)

$$A_{sv} = \frac{\pi R_0^2 \, (4-2n_1P_1 - 2n_2P_2)}{\left\{ 1 - \frac{n_1 P_1^2(3-P_1) - n_2 P_2^2(3-P_2)}{4} \right\}^{2/3}} \tag{17}$$

The solid-solid area is given by

$$A_{ss} = \frac{\pi n_1 h_1 (2R-h_1)}{2} + \frac{\pi n_2 h_2 (2R-h_2)}{2} \tag{18}$$

By substituting P_1R for h_1, and P_2R for h_2, and Eq. (16) into (18),

$$A_{ss} = \frac{\pi R_0^2 \left\{ n_1 P_1(2-P_1) + n_2 P_2(2-P_2) \right\}}{2 \left\{ 1 - \frac{n_1 P_1^2(3-P_1) - n_2 P_2^2(3-P_2)}{4} \right\}^{2/3}} \tag{19}$$

The free energy change from the original configuration of spheres just touching to the configuration at any value of P is

$$\Delta G = \Delta A_{ss} \, \gamma_{ss} + \Delta A_{sv} \, \gamma_{sv} \tag{20}$$

Since initially A_{ss} is equal to zero, and $A_{sv} = 4\pi R_0^2$

$$\Delta G(P) = A_{ss}\,\gamma_{ss} + \gamma_{sv}\,(A_{sv} - 4\pi R_0^2) \tag{21}$$

For two particular values of P, P_A and P_B, the free energy change is

$$\Delta G(P_A) = \gamma_{ss}\,(A_{ss}(P_A)) + \gamma_{sv}\,(A_{sv}(P_A) - 4\pi R_0^2) \tag{22}$$

and

$$\Delta G(P_B) = \gamma_{ss}\,(A_{ss}(P_B)) + \gamma_{sv}\,(A_{sv}(P_B) - 4\pi R_0^2) \tag{23}$$

And the change in free energy from state A to state B is

$$\Delta G = \Delta G(P_B) - \Delta G(P_A) \tag{24}$$

or

$$\Delta G = \gamma_{ss}(A_{ss}(P_B) - A_{ss}(P_A)) + \gamma_{sv}\,(A_{sv}(P_B) - A_{sv}(P_A)) \tag{25}$$

Setting $\Delta G = 0$, gives the critical ratio of γ_{ss}/γ_{sv} for the incremental densification from A to B. That is,

$$\frac{\gamma_{ss}}{\gamma_{sv}} = -\frac{\left(A_{sv}(P_B) - A_{sv}(P_A)\right)}{\left(A_{ss}(P_B) - A_{ss}(P_A)\right)} \tag{26}$$

This ratio is identical to that determined in Eq. (13) for the increment A to B.

Since Eqs. (17) and (19) are somewhat lengthy, it is more convenient to use Eq. (26) than to differentiate Eqs. (17) and (19) and substitute them in Eq. (2) to determine the critical ratios of γ_{ss}/γ_{sv} for a given degree of densification. Therefore, by using the proper values of n_1, n_2, and P_2 for Eq. (26), the critical ratios of γ_{ss}/γ_{sv} for the entire system of sintering spheres can be determined for BCC packings where $n_1 = 8$, $n_2 = 6$, and $P_2 = (\sqrt{3} - 2)/\sqrt{3} + 2P/\sqrt{3}$.

When an array of spheres sinter, densification will generally be described by two dihedral angles; the nearest neighbor dihedral angle, Φ_1, and the second nearest neighbor dihedral angle, Φ_2. As second neighbors interpenetrate, Φ_1 continues to decrease while Φ_2 begins at 0°. Therefore, Φ_1 will be larger than Φ_2 at any value of P.

Since the largest dihedral angle for a particular system determines the critical ratio of γ_{ss}/γ_{sv}, it is necessary to determine values of Φ_1 after second nearest neighbor interpenetration has begun. The critical ratio for the entire system is determined by subsitution of Eqs. (17) and (19) into Eq. (26). But when Eqs. (16), (5), and (9) are substituted into Eq. (26), the critical ratio of γ_{ss}/γ_{sv} for nearest neighbor contacts can be determined at values of P corresponding to second neighbor interpenetration.

Thus, it is necessary to calculate the critical ratios of γ_{ss}/γ_{sv} for nearest neighbor contacts as well as for the sum of the contacts of the entire system in order to determine the specific thermodynamic barriers to densification for a particular array of spheres.

Referring to Fig. 3 for BCC packing of spheres, the densification proceeds from configuration 3A, (nearest neighbors just touching), to

configuration 3B, (second nearest neighbors just touching), and is described by Eq. (13). Beyond this point, Eq. (13) is no longer valid. Configuration 3c corresponds to the point at which second nearest neighbors have interpenetrated sufficiently to cause complete densification of the unit cell. The densification path from 3B to 3C is described by Eqs. (17), (19), and (26).

Since densification is measured as $\Delta L/L_0$ (equivalent to h_0/R_0) where ΔL is the linear shrinkage and L_0 is the original linear dimension, it is not strictly valid to use P_1, i.e., h_1/R as a measure of densification since R according to the model increases from R_0 as the spheres interpenetrate, as seen in Fig. 2.

For two interpenetrating spheres,

$$R - h_1 = R_0 - h_0 \tag{27}$$

or

$$R(1-P_1) = R_0(1-P_0) \tag{28}$$

where $P_0 = h_0/R_0$, thus

$$P_0 = \frac{1 - R(1-P_1)}{R_0} \tag{29}$$

Using Eqs. (6) or (16), the ratio of R/R_0 may be substituted into (29) to give the true linear shrinkage, P_0. Therefore, when Eqs. (13) and (26) are plotted as a function of P_0, curves are obtained for critical ratios of γ_{ss}/γ_{sv} at any degree of densification for which the

model holds.

Figure 4 shows the results for BCC packing. Equation (13) describes the sintering of the 8 nearest neighbors until second nearest neighbors touch represented by segment a-b of curve a-c. At this point, $P_0 = 0.102$ and $\gamma_{ss}/\gamma_{sv} = 1.734$, corresponding to a dihedral angle $\Phi_1 = 59.6°$. Beyond point b, the curve, which splits into two segments, is described by Eq. (26). The nearest neighbor dihedral angle continues to increase along the segment b-c of the curve (described by substitution of Eqs. (5), (9), and (16) into (26)), while the second nearest neighbor dihedral angle begins to increase from 0°. At point c on the curve, just prior to complete densification of the unit cell, the nearest neighbor dihedral angle, determined by graphical methods, is $\Phi_1 = 71.5°$, or $\gamma_{ss}/\gamma_{sv} = 1.625$; while the second nearest neighbor dihedral angle is $\Phi_2 = 42°$ or $\gamma_{ss}/\gamma_{sv} = 1.814$. The value of $\gamma_{ss}/\gamma_{sv} = 1.625$ corresponds to $P_0 = 0.112$ on the curve at point c. However, at this value of P_0 (linear shrinkage) calculation of the fractional void volume in the unit cell according to the mathematical model yields a value of 0.031 even though the degree of linear shrinkage is sufficient to completely densify the cubic cell. The reason for the discrepancy is that although h_1 and R both increase during densification, in the early stages of sintering h_1 increases faster than R and therefore $(R-h_1)$ decreases while at large values of P_1, R begins to increase faster than h_1. Thus $(R-h_1)$ actually goes through a minimum and then begins to increase. For all the packing arrays treated here, the model breaks down before the minimum of $(R-h_1)$ is reached and therefore, the values of γ_{ss}/γ_{sv} critical obtained from

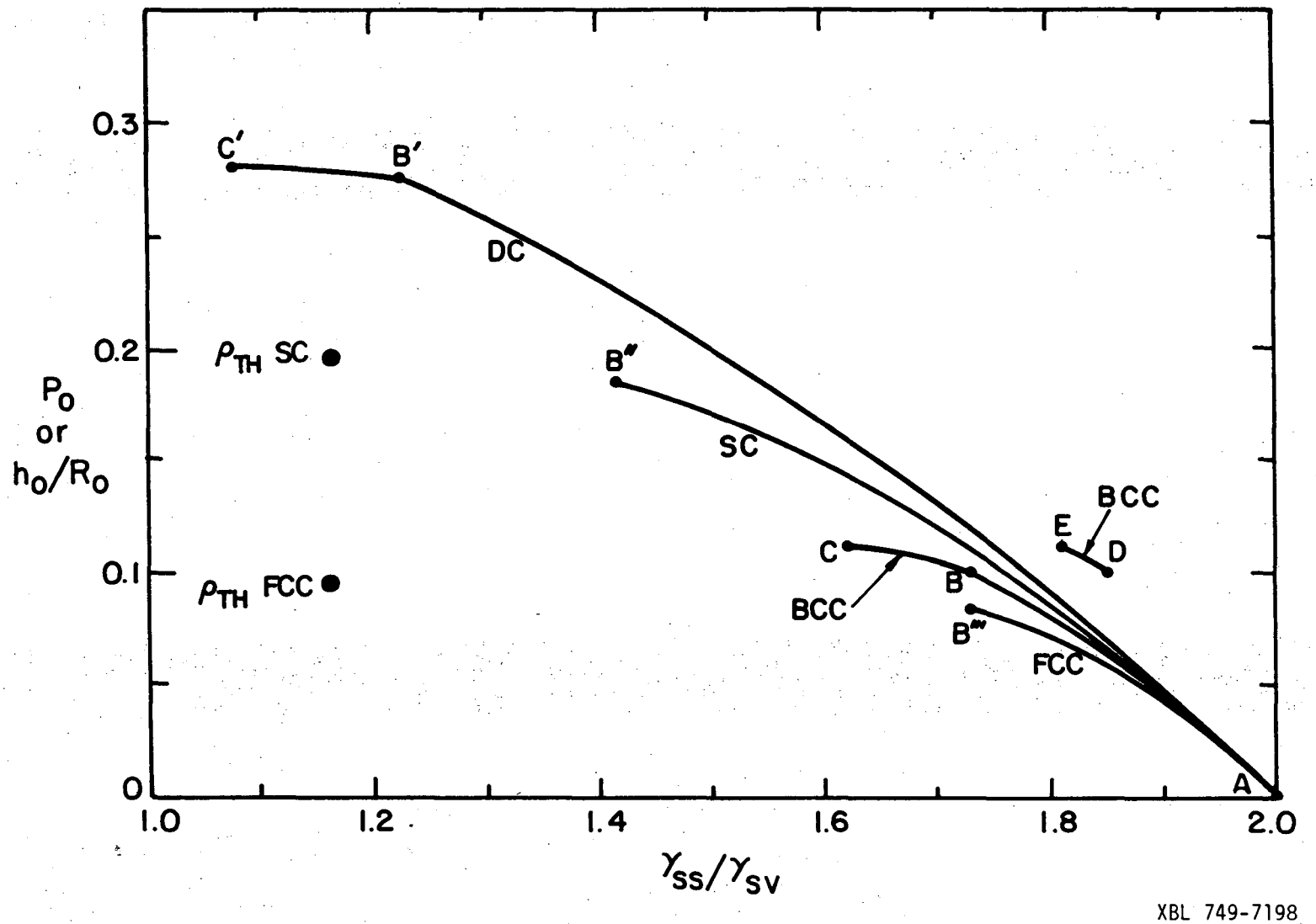

Figure 4. Densification versus critical ratio of γ_{ss}/γ_{sv} for four sintering geometries.

Eq. (26) are still valid. However, calculation of the fractional void volume in the unit cell from P_0 leads to erroneous results at large values of P_1, Eq. (29).

By assuming that the initial edge length of the unit cell is 1, and that at theoretical density the edge length is the cube root of the fractional final volume (for BCC, $\sqrt[3]{0.68}$), one can obtain the true value of $\Delta L/L_0$, called P_0' in Table I, at theoretical density for the model. The value for BCC packing is $P_0' = 0.121$.

The solid-vapor dihedral angle then becomes a solid-solid triple point with grain boundaries forming angles of 109°, 125.5°, and 125.5°. The combined free energy contribution of first and second neighbors (Eqs. (17) and (19) substituted into Eq. (26)), results in the curve shown along path d-e. At second neighbor contacts, the curve breaks discontinuously from a-b to d-e because the dihedral angle for second neighbor interpenetration begins at 0°. Therefore, the sum of the contribution of the nearest, and second nearest neighbor free energies yields the total for the system, and results in the curve d-e.

The critical dihedral angle for sintering of the BCC array is 71.5° which is the value of the nearest neighbor dihedral angle, Φ_1, just prior to complete densification of the unit cell. At any value of P_0, one can determine the critical ratio of γ_{ss}/γ_{sv} for that particular degree of densification, by finding the ratio of γ_{ss}/γ_{sv} on the abscissa of Fig. 4 corresponding to the point at which P_0 intersects the curve. If the ratio of γ_{ss}/γ_{sv} is larger, or if the dihedral angle, Φ_1, is smaller than the value obtained from the curve, that particular value of P_0, and therefore, that degree of densification cannot be obtained for the

Table I. Parameters for solid phase sintering models

	DC	SC	BCC	FCC
Fractional initial void volume:	0.68	0.48	0.32	0.26
At point of second neighbor contacts:				
P_0 (Linear shrinkage based on Eq. (28))	0.277	0.184	0.102	-
Φ	104.4	89.6	59.6	-
γ_{ss}/γ_{sv}	1.226	1.416	1.734	-
Fractional void volume	0.101	0.036	0.062	-
At endpoint of the mathematical model:				
P_0 (Linear shrinkage from Eq. (28))	0.280	0.184	0.112	0.084
Φ	115	89.6	71.5	59.6
γ_{ss}/γ_{sv}	1.074	1.416	1.625	1.734
Fractional void volume	0.088	0.036	0.031	0.035
At theoretical density:				
P_0' (Linear shrinkage of cube with original edge length of 1)	0.316	0.196	0.121	0.095
Φ		109	71.5	109
γ_{ss}/γ_{sv}	-	1.161	1.625	1.161
Fractional void volume	0.0	0.0	0.0	0.0

real system. Therefore, to densify a BCC array of spheres, the equilibrium dihedral angle must be greater than 71.5° and the ratio of γ_{ss}/γ_{sv} must be less than 1.625. If these values are fulfilled in a real system which approaches the configuration of the model, then no thermodynamic barrier to densification exists.

For diamond cubic packing, (fractional void volume of 0.68), Figs. 5 and 6A, four nearest neighbors interpenetrate until contacts form with second nearest neighbors, Fig. 6B. The ratio of γ_{ss}/γ_{sv} as a function of P_0 is described by Eq. (13), and segment a-b' of Fig. 4. At b', P_0 = 0.277, γ_{ss}/γ_{sv} = 1.226, and Φ_1 = 104.4°. Beyond b', Eq. (13) becomes invalid since interpenetration of second nearest neighbor contacts begins. Equations (17) and (19) may not be applied to the analysis since interpenetration of nearest neighbor spheres creates a line of intersection between second neighbor spheres instead of a second nearest neighbor solid-solid planar boundary. However, Eqs. (16), (5) and (9) may be substituted into Eq. (26) to yield dihedral angles for sintering of nearest neighbors since Φ_1 continues to increase after second neighbors have contacted, and the shape of the nearest neighbor solid-solid interface remains circular.

When interpenetration of second nearest neighbors is such that a 120° solid-solid triple point forms, Fig. 6C, the model is assumed to have reached its endpoint since the spherical character of the particles is lost. However, the unit cell has not densified completely at this point, and a residual fractional porosity of 0.088 remains, (based on a cube of unit edge length and a fractional porosity of 0.68). The value

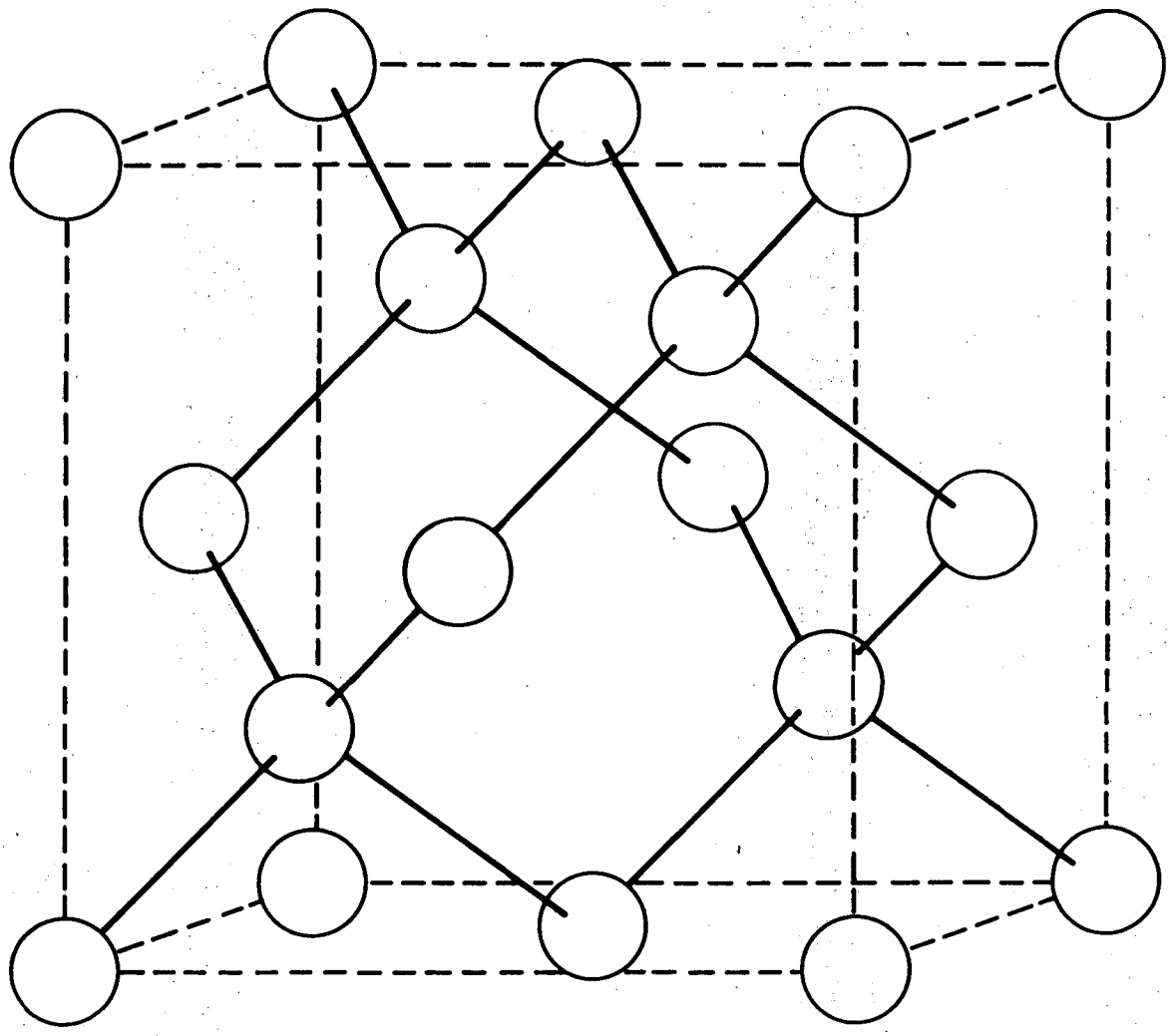

Figure 5. Diamond cubic array of spheres.

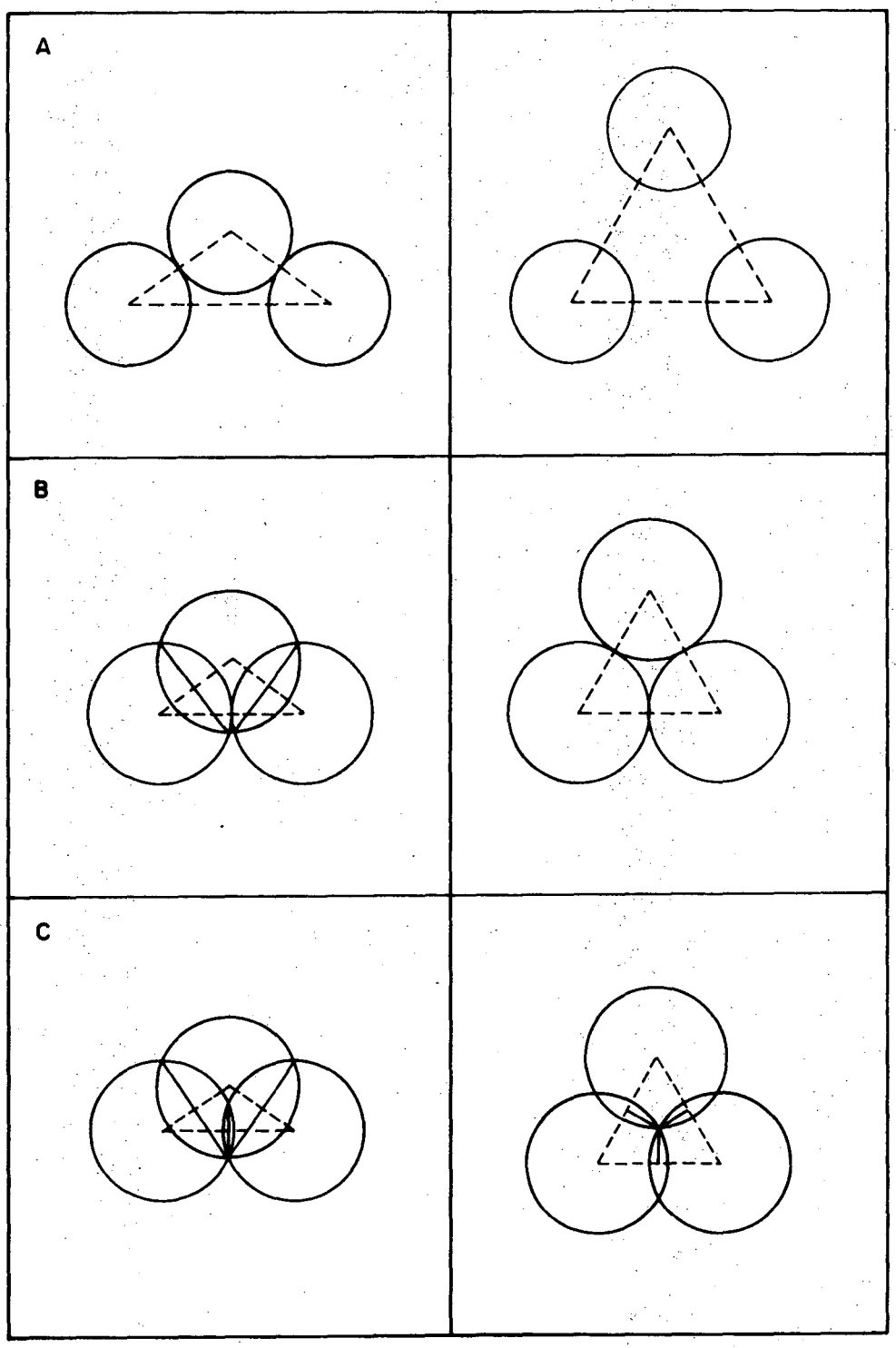

Figure 6. Interpenetration of a diamond cubic array of spheres.

of P_0 is 0.280, γ_{ss}/γ_{sv} = 1.074, and Φ_1 = 115°. The curve for this step in densification corresponds to segment b'-c' of Fig. 4. For the model, theoretical density occurs at P_0' = 0.316; however, in order to reach a densification corresponding to P_0 = 0.280, Φ_1 must be greater than 115° or γ_{ss}/γ_{sv} must be less than 1.074.

For simple cubic packing of spheres, (fractional void volume of 0.48), Fig. 7A, six nearest neighbors interpenetrate according to Eq. (13), the densification is described by segment a-b'' of Fig. 4 until contacts form with second nearest neighbors along <110> directions. At this point, P_0 = 0.184, the solid-vapor dihedral angle is 89.6°, and γ_{ss}/γ_{sv} = 1.416. As the coordination increases from 6 to 18, Fig. 7B, the (100) faces become completely densified, and four solid-solid interfaces (grain boundaries) intersect at 90°. However, residual porosity remains on the (110) faces, Fig. 7B, and the nearest neighbor dihedral angle increases past 90°. In order for further densification to occur, the area of the (100) faces must be reduced in order that the volume of the unit cell can continue to decrease. As densification proceeds, by some other mechanism than that described in the model, material is removed from first and second nearest neighbor contacts. However, the coordination of solid-solid interfaces does not increase as for BCC packing, but rather remains at 6. Instead, a line is formed from the intersection of the two (1/2 00) grain boundary planes as second neighbor interpenetration occurs, Fig. 7C. Equation (13) is no longer valid for describing the densification of the system since solid-vapor area is being removed from second neighbors, as well as from nearest neighbors. Also, the description of the solid-solid interfaces is no longer that of

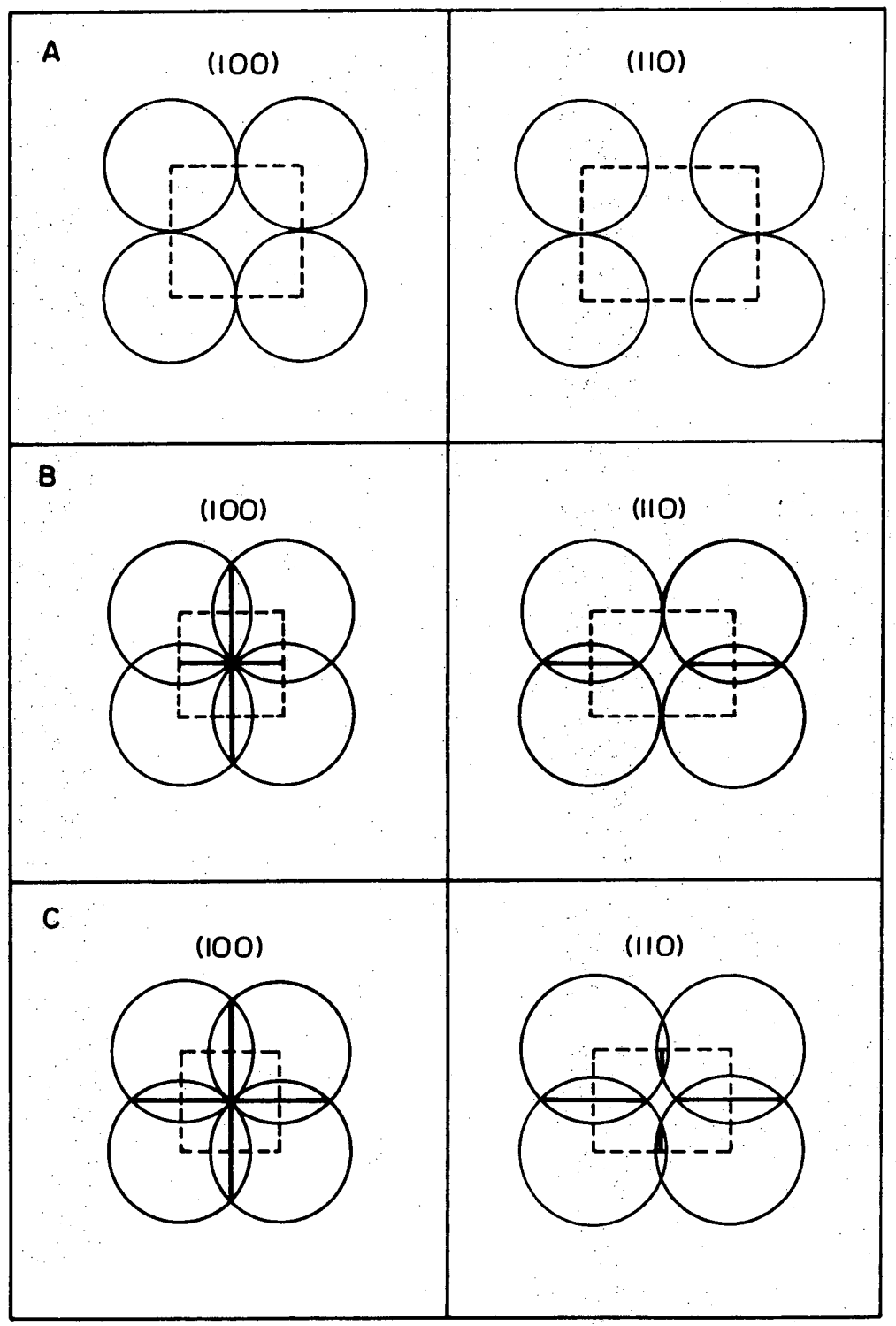

Figure 7. Interpenetration of a simple cubic array of spheres.

a circular section for nearest neighbors. Therefore, neither Eqs. (17) and (19) nor (16), (5), and (9) may be applied to the model.

On (110) planes, as second neighbor interpenetration begins, the dihedral angle increases from $\Phi_2 = 0°$, Fig. 7B and 7C. However, the nearest neighbor dihedral angle on these planes continues to increase past 90°. Just prior to complete densification of the (110) face, the nearest neighbor dihedral angle (determined by graphical techniques), is $\Phi_1 = 109°$, and $\gamma_{ss}/\gamma_{sv} = 1.161$.

At this point, the second nearest neighbor dihedral angle is $\Phi_2 = 89.6°$. Assuming that the unit cell shrinks to a volume equal to that of the original sphere, the value of P_0' at theoretical density is 0.196. Thus, in order to densify a simple cubic array of spheres, Φ_1 must be greater than 109° or γ_{ss}/γ_{sv} must be less than 1.161. If these conditions are met, there is no thermodynamic barrier to densification although kinetic barriers may arise since the system must shrink by some other mechanism, after second neighbors contact, than that described in the present model.

For FCC packing of spheres, (fractional void volume of 0.26), 12 nearest neighbor spheres interpenetrate as shown in Fig. 8A, until the (111) face of the unit cell has densified completely. Equation (13) described the sintering along segment a-b''' of Fig. 4. At b''', $P_0 = 0.084$, the solid vapor dihedral angle, $\Phi_1 = 59.6°$, and $\gamma_{ss}/\gamma_{sv} = 1.734$. When the (111) plane has densified, a solid-solid triple point forms with grains intersecting at 120° angles. Second nearest neighbors have not yet touched. However, as for the simple cubic case, in order for the volume of the FCC unit cell to continue to decrease, the area of the (111)

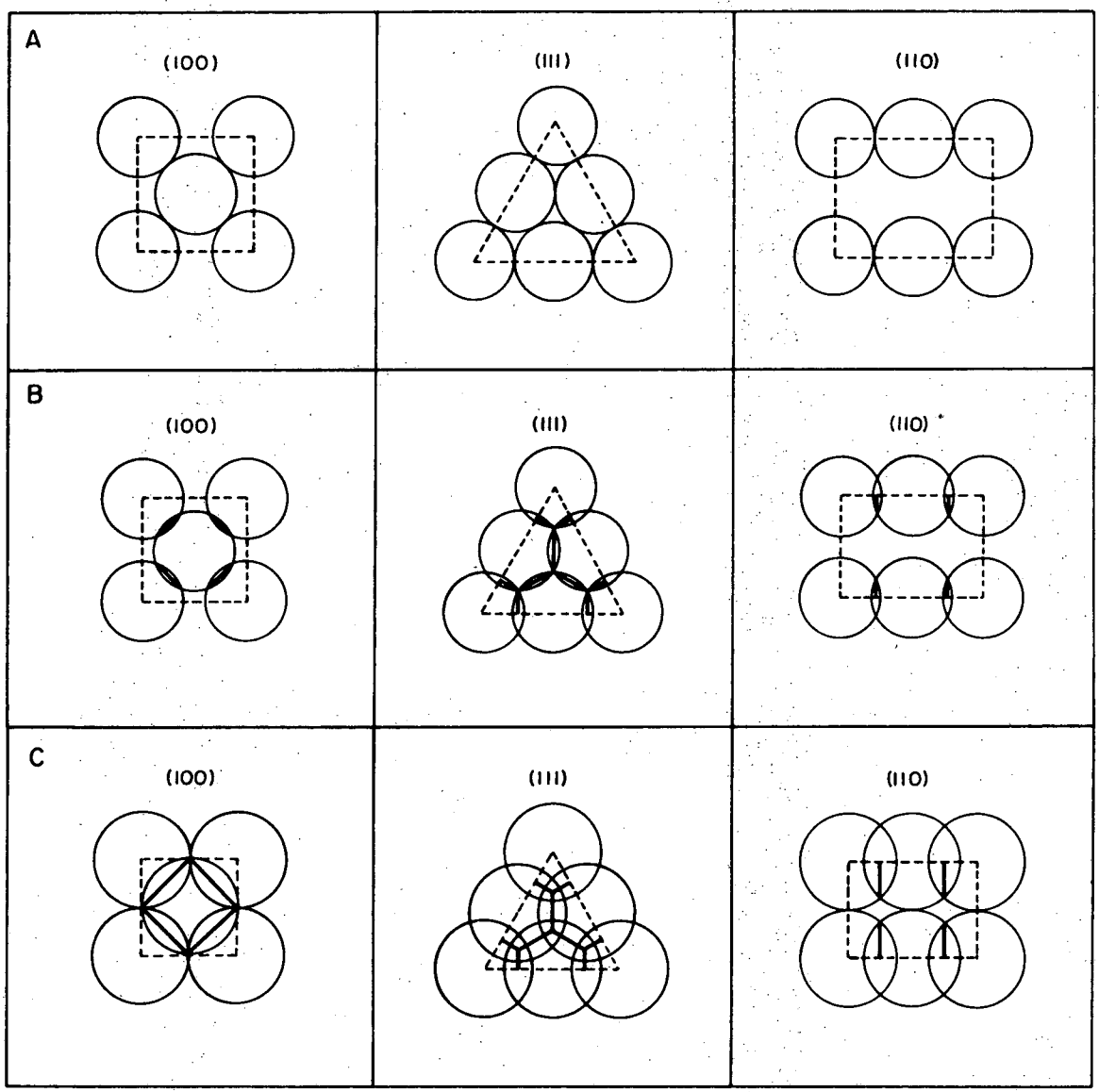

Figure 8. Interpenetration of a face-centered cubic array of spheres.

planes must be reduced. Again, it is evident that Eq. (13) is not valid beyond this point.

If densification is to proceed further, sintering must occur by some other mechanism which allows for the redistribution of some of the material from the (111) planes. Shrinkage may then continue until contacts form with second nearest neighbors of (100) faces, Fig. 8C. Just prior to contact, the nearest neighbor dihedral angle on the (100) face is $\Phi_1 = 89.6°$. After contact, the (100) plane is densified and four solid-solid interfaces intersect forming 90° angles, Fig. 8C. (100) and (111) faces have now densified but residual closed porosity remains on the (110) faces.

As further shrinkage occurs, again by some other mechanism than that described in the present model, the second nearest neighbor dihedral angle, Φ_2, on the (110) face increases from 0°, while the nearest neighbor dihedral angle, Φ_1, increases past 90°.

When the porosity on the (110) face is eliminated, the unit cell is completely densified. Just prior to the elimination of the last traces of porosity, graphical methods indicate that the nearest neighbor dihedral angle, on the (110) face, is $\Phi_1 = 109°$, the second nearest neighbor dihedral angle, $\Phi_2 = 68°$, and $P_0' = 0.095$.

Therefore, if Φ_1 is greater than 109°, or γ_{ss}/γ_{sv} is less than 1.161, there is no thermodynamic barrier to complete densification of an FCC array of spheres, (δG_{syst}) is always less than zero. However, as for simple cubic packing, kinetic barriers may exist. Results for all coordinations of spheres are given in Table I.

Analysis of the four sintering geometries presented here reveals that in the early stages of densification, when only nearest neighbors are in contact, the larger the coordination of spheres, the larger is γ_{ss}/γ_{sv} critical. Thus, the thermodynamic barriers to densification are least for FCC packing (coordination = 12) and greatest for diamond cubic packing (coordination = 4). For DC and SC arrays when second nearest neighbors come in contact, the mathematical model described by Eqs. (13) and (26) breaks down. Some of the material from circular solid-solid contact areas which formed during the interpenetration of nearest neighbor spheres must redistribute itself laterally in order that further densification may occur since the contact area loses its circularity. For FCC packing, the (111) face of the unit cell densifies prior to the formation of second nearest neighbor contacts. At this point, the model also breaks down and redistribution of material must occur by some other mechanism to cause complete densification. On the other hand, the model for BCC packing continues to describe sintering past the point where second nearest neighbor contacts form and is valid until theoretical density is attained. For this packing array, the model sinters uniformly throughout the densification process, forming a 14 sided polygonal solid (tetrakaidecahedron) which fills space.

Referring to Table I, at theoretical density for each packing array, γ_{ss}/γ_{sv} critical is the largest for BCC (1.625), and much smaller for all other coordinations of spheres, i.e., 1.074 for DC and 1.161 for SC and FCC. Each of the latter three packing arrays forms closed porosity prior to complete densification while BCC is characterized by open porosity throughout the entire densification process. Additionally,

the fractional void volume is proportionately greater for BCC than for other packings when second nearest neighbors form contacts, Table I.

At second nearest neighbor contact points for BCC, $P_0 = 0.102$ and the fractional void volume is 0.062, while for simple cubic packing at $P_0 = 0.184$ (second nearest neighbors form contacts) the fractional void volume is 0.036. The larger fraction of porosity for BCC allows continuation of uniform sintering while for other packing arrays some of the crystallographic faces in the unit cells must lose some material in order to achieve complete densification for the compact.

This nonuniformity in sintering results in large values of the nearest neighbor dihedral angle, Φ_1, relative to the second nearest neighbor dihedral angle, Φ_2. Since a large dihedral angle causes γ_{ss}/γ_{sv} critical to be small, the thermodynamic barriers to complete densification are increased by nonuniform sintering. This effect is evident by comparison of SC and FCC packings, Table I. The initial fractional void volume for SC is 0.48 while that for FCC is 0.26. At second nearest neighbor contact points for SC, $P_0 = 0.184$ and $\gamma_{ss}/\gamma_{sv} = 1.416$, while for FCC when the (111) face has densified $P_0 = 0.084$ and $\gamma_{ss}/\gamma_{sv} = 1.734$. In both cases uniform sintering has occurred up to these points and γ_{ss}/γ_{sv} is larger for FCC than for SC. However, any further densification must proceed by nonuniform sintering of the spheres. This nonuniformity causes both ratios of γ_{ss}/γ_{sv} critical to attain the same value, 1.161, when the unit cells have densified even though the original fractional void volume for SC is almost twice as large as that for FCC.

In real powder compacts, nonuniformity can arise in several ways and can lead to kinetic as well as thermodynamic barriers to sintering.

Inhomogeneous packing due to poor mixing or agglomeration can cause nonuniform porosity distributions throughout a powder compact. During the sintering anneal, regions of higher density of packing densify prior to regions of lower density. Further shrinkage of the compact will cause tensile stresses to arise in the less dense regions which in turn will decrease the sintering rate or produce endpoint densities. Such a phenomenon is analogous to the nonuniform densification which occurs in the models for DC, SC, and FCC packing arrays.

Even if a compact has a homogeneous density distribution, a wide particle size distribution can cause nonuniform sintering. Coble[17] has shown that stresses, which retard the densification kinetics, arise during sintering of nonuniform sized spherical particles. Therefore, if a powder compact is to be densified completely, the equilibrium dihedral angle should be large as determined by control of interfacial energies, the particle size distribution should be as narrow as possible, in order that uniform sintering (interpenetration of particles) will occur at all particle-particle contacts, and the packing should be homogeneous and such that open porosity is present for as much of the sintering anneal as possible. If these conditions are met, uniform sintering at all contact points will occur throughout the sintering process and the thermodynamic and kinetic barriers to complete densification will be a minimum.

B. Thermodynamics of Dihedral Angles

1. Vacancy Concentrations and Gradients

Thus far the interpenetration of the spherical particles presented in the model has been discussed from a purely thermodynamic approach. Since such an analysis considers only the initial and final states of the

system, the path of densification or the mechanism by which actual mass transfer leading to densification occurs has not been considered. Therefore, it is of interest to examine, on an atomistic scale, the process by which mass transfer occurs and an equilibrium configuration is attained for a two sphere model forming no bridging neck. The analysis is based on differences in vacancy concentrations at the solid-solid and solid-vapor interfaces which are caused by stresses arising from interfacial tensions and surface curvatures. Before discussing the model directly, it is necessary to establish some general relationships concerning the formation of vacancies in a crystalline material.

The equilibrium concentration of lattice vacancies in the bulk of a pure one component crystalline material is given by

$$N_o = N \exp(-\frac{Q_f}{RT}) \tag{30}$$

where N_o is the vacancy concentration, N is the concentration of occupied lattice sites, Q_f is the work associated with the creation of a lattice vacancy. In a homogeneous single crystal material at thermal equilibrium, N_o is constant throughout the bulk phase. However, in regions adjacent to planar solid-vapor interfaces, the equilibrium vacancy concentration, N_{sv}, is not equal to N_o.

Consider the two dimensional simple square array of atoms shown in Fig. 9a. Three different locations, labeled 1, 2, and 3, where vacancies can be created are indicated. Figure 9b shows the same lattice array with atoms 1, 2, and 3 removed revealing the three possible types of vacancies. In order to determine the most favorable site for vacancy

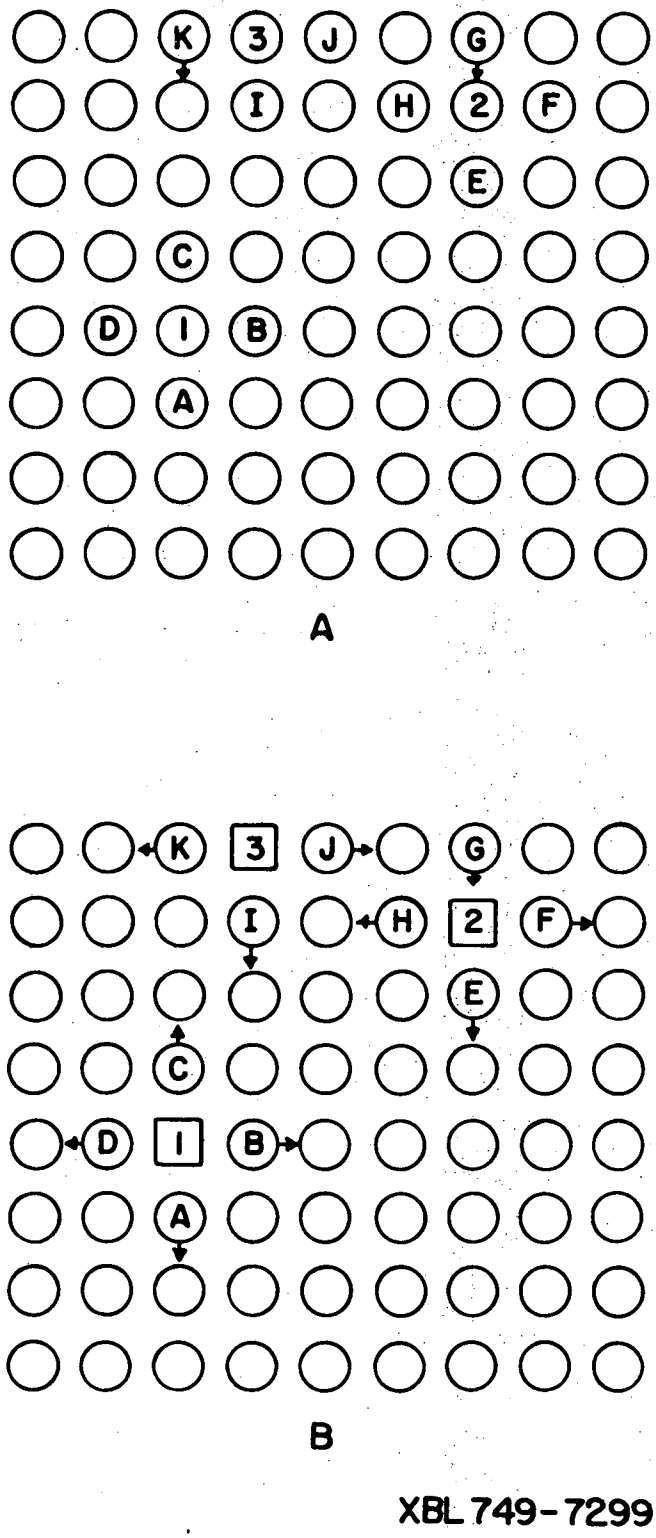

Figure 9. (A) A simple square array of atoms showing atomic lattice sites located in the bulk (1), just below the surface (2), and at the surface (3).
(B) Vacancies formed at sites (1), (2) and (3).

formation, it is necessary to calculate the internal energy associated with the creation of each type of lattice vacancy.

Examining first the atom labeled 1 in Fig. 9a, one sees that there is no net stress on this atom or on the surrounding atoms labeled A, B, C, and D. When a vacant lattice site is created at position 1, as in Fig. 9b, the four nearest neighbor atoms, (A, B, C and D), are placed in a state of tension associated with the breaking of four bonds with atom 1.

The next case to examine is atom 2, Fig. 9a, which is in an identical location as atom 1 with respect to nearest neighbors except that atom G, a surface atom located directly above atom 2, is in a state of tension. When a vacant lattice site is created in position 2, Fig. 9b, four bonds are broken, and atoms E, F, and H are placed in a state of tension. On the other hand, the tension on atom G is reduced since this tension is now created by atom E instead of atom 2. Thus in creating a vacancy at position 2, the internal energy of the system is increased by the breaking of four bonds, but it is also decreased due to the reduction in the tension on atom G. Therefore, less energy is necessary to create a vacancy at position 2 than at position 1.

Finally, consider atom 3 which is at the surface of the simple square array in Fig. 9a. This atom is in a state of tension due to the inward pull of atom I. When a vacancy is created at position 3, Fig. 9b, three bonds are broken and atoms I, J, and K are placed in a state of tension. The tension which was associated with atom 3, however, is reduced. It is evident that the internal energy associated with the creation of a vacancy at position 3 is less than that associated with positions 2 or 1. Neglecting any entropy effects and using Eq. (30), it

can be shown that

$$N_{(3)} >> N_{(2)} > N_{(1)} = N_o \tag{31}$$

where $N_{(i)}$ indicates the location of the vacancy.

At a specific temperature, there are equilibrium concentrations of vacancies associated with the bulk and surface regions of a material. These concentrations are given by Eq. (30) and although they are not equal, there is no net flow of vacancies since no chemical potential gradient exists. The excess concentration of vacancies in the surface region may then be considered as analagous to positive adsorption of solute atoms under equilibrium conditions. In effect the stresses introduced by the surface tension cause the establishment of a vacancy concentration gradient which leads to vacancy flow until equilibrium vacancy compositions and a constant chemical potential are reached.

In polycrystalline materials internal surfaces (grain boundaries) are present as well as external surfaces. The nature of the structure of grain boundaries is not well understood, but when two crystallographic orientations intersect forming a grain boundary, there will be a somewhat smaller coordination of atoms in this region than in the bulk. Therefore, fewer bonds will be broken in creating a vacancy at a grain boundary than in the bulk and a somewhat higher concentration of vacancies is expected. It should be noted, however, that since the coordination of atoms in the grain boundary is probably very close to that in the bulk, the excess vacancy concentration N_{gb} over that in the bulk, N_o, is small and is less than the concentration at the solid-vapor interface, N_{sv}.

Furthermore, a tensile stress field acting on the grain boundary would be expected to increase the vacancy concentration at the grain boundary.

Now consider a configuration similar to Fig. 10, which shows the intersection of two solid-vapor interfaces with a solid-solid interface forming a dihedral angle, Φ, between the two. The horizontal component of the solid-vapor surface tension causes atoms in the grain boundary to be in a state of tension. The well known analysis of Nabarro[3] indicates that vacancies form preferentially in a region of tension. Thus, it is expected that the presence of a solid-solid/solid-vapor dihedral angle will cause an enhanced vacancy concentration at the grain boundary over a stress free grain boundary with a maximum at the root of the dihedral angle which increases as the dihedral angle increases. When the dihedral angle reaches equilibrium, the vacancy chemical potential gradient between the solid-vapor and solid-solid interfaces becomes zero.

Now, consider the application of these arguments to the sintering of a two sphere model which does not form a neck of concave curvature but rather is described by the intersection of two spheres as discussed in Section II-A, forming a dihedral angle, Φ_1, which is less than the equilibrium value, Φ_{eq}, as in Fig. 11a. The vacancy concentration at the solid-vapor interface will also be a function of the convex curvature and therefore will be less than that for a planar interface, but still greater than that for the bulk. Thus

$$N_{sv}(\infty) > N_{sv}(R_1,\Phi_1) > N_o \qquad (32)$$

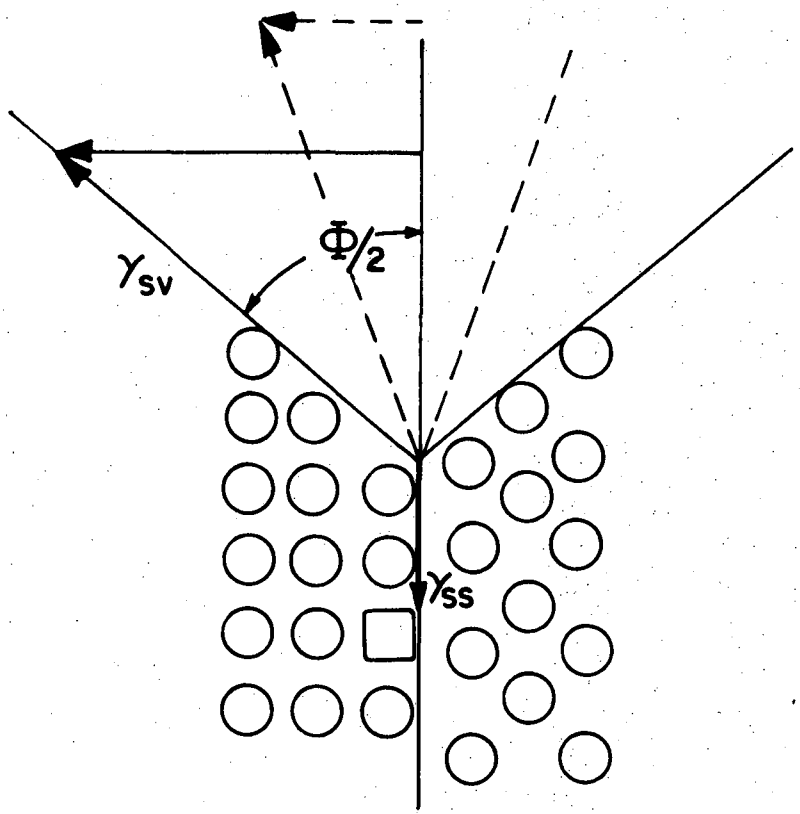

AS Φ INCREASES, THE TENSILE STRESSES AT THE GRAIN BOUNDARY ALSO INCREASE

XBL 749-7298

Figure 10. A solid/solid-solid/vapor triple point indicating how the horizontal component of the solid/vapor interfacial tension increases as the dihedral angle increases, creating tensile stresses at the grain boundary.

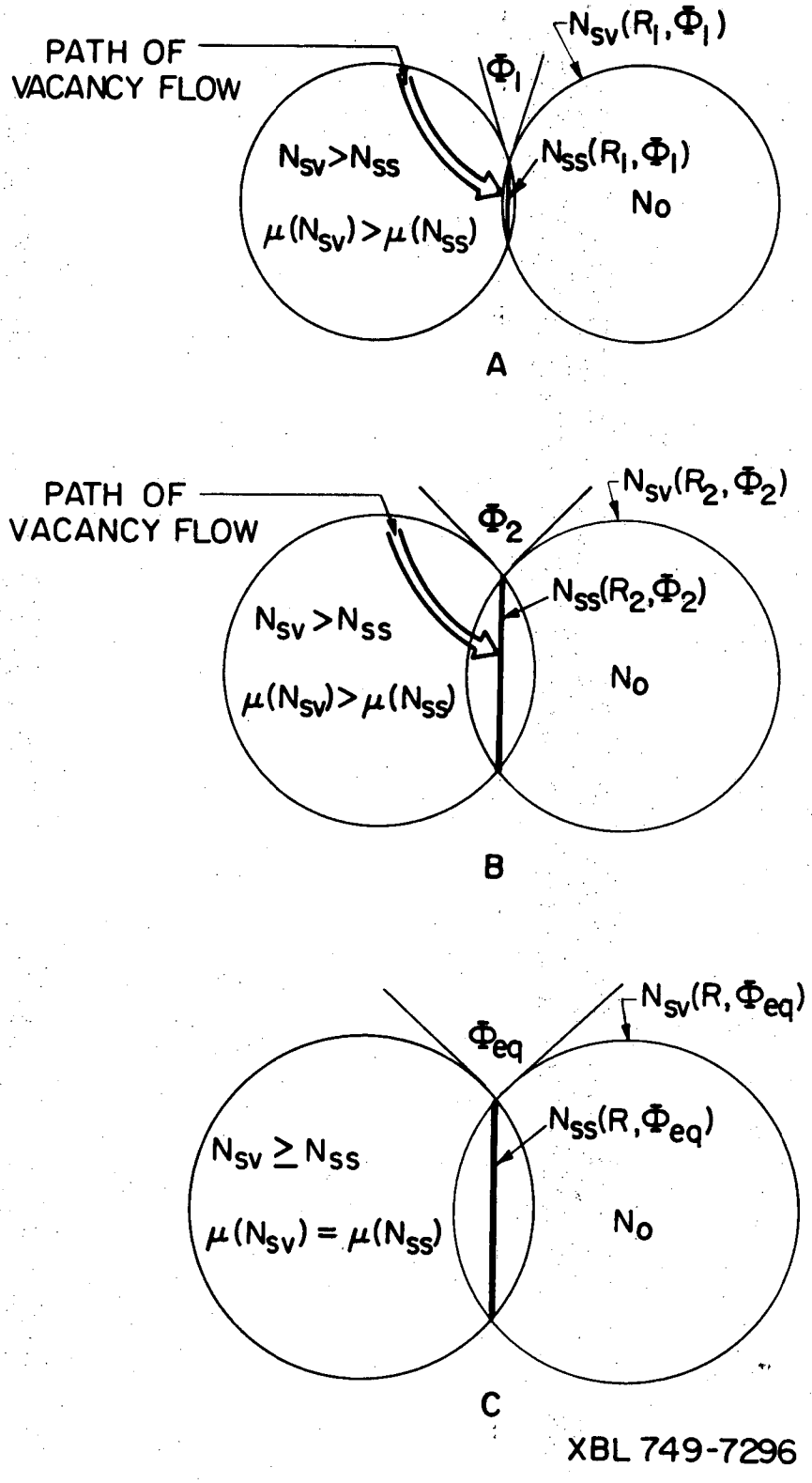

Figure 11. Path of vacancy flow for systems not forming bridging necks. Flow proceeds from the solid/vapor interface to the solid/solid interface as interpenetration of the spheres occurs (A) to (B). When the equilibrium dihedral angle forms, vacancy flow ceases (C).

Also, the concentration of vacancies at the solid-vapor interface is greater than that at the grain boundary,

$$N_{sv}(R_1,\Phi_1) > N_{ss}(R_1\Phi_1) \tag{33}$$

This concentration gradient of vacancies is a function of the chemical potential gradient which creates a flow of vacancies from the solid-vapor surface to the solid-solid interface and a counter flow of materials. As interpenetration of the particles proceeds, material is deposited on the outer surface of the spheres; the radius of the spheres, R_1, increases to R_2, and the dihedral angle increases to Φ_2, Fig. 11b. Since the radius of the spheres increases from R_1 to R_2, the vacancy concentration at the solid-vapor interface, $N_{sv}(R_2,\Phi_2)$ will increase as interpenetration of the spheres proceeds. Simultaneously, the dihedral angle increases from Φ_1 to Φ_2 and the tensile stresses on the grain boundary increase; therefore, the vacancy concentration at the solid-solid interface, $N_{ss}(R_2,\Phi_2)$ increases. When $\Phi = \Phi_{eq}$, Fig. 11c,

$$\mu(N_{ss}) = \mu(N_{sv}) \tag{34}$$

The vacancy chemical potential gradient between the solid-vapor and solid-solid interfaces then vanishes and sintering ceases. A schematic representation of the manner in which the vacancy concentration gradient changes with dihedral angles is shown in Figs. 12, 13, and 14 for 1, 10, and 100 micron size spherical particles forming an equilibrium dihedral angles of 68.4°, assuming that the activity of the vacancies is equal to

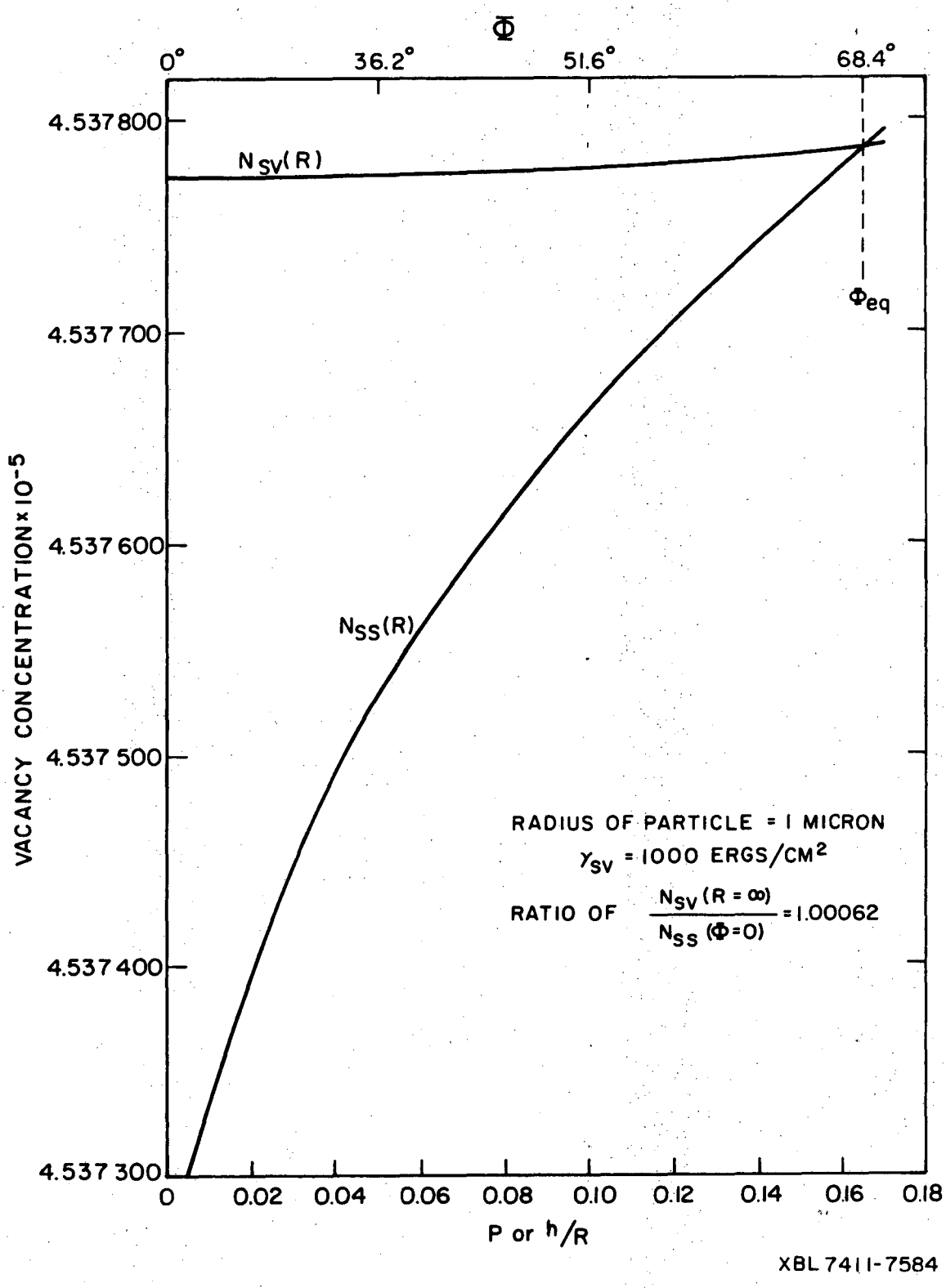

Figure 12. Vacancy concentrations at the solid/solid and solid/vapor interfaces versus P or h/R for interpenetration of 1 micron spheres forming no bridging neck. (See Appendix 1.)

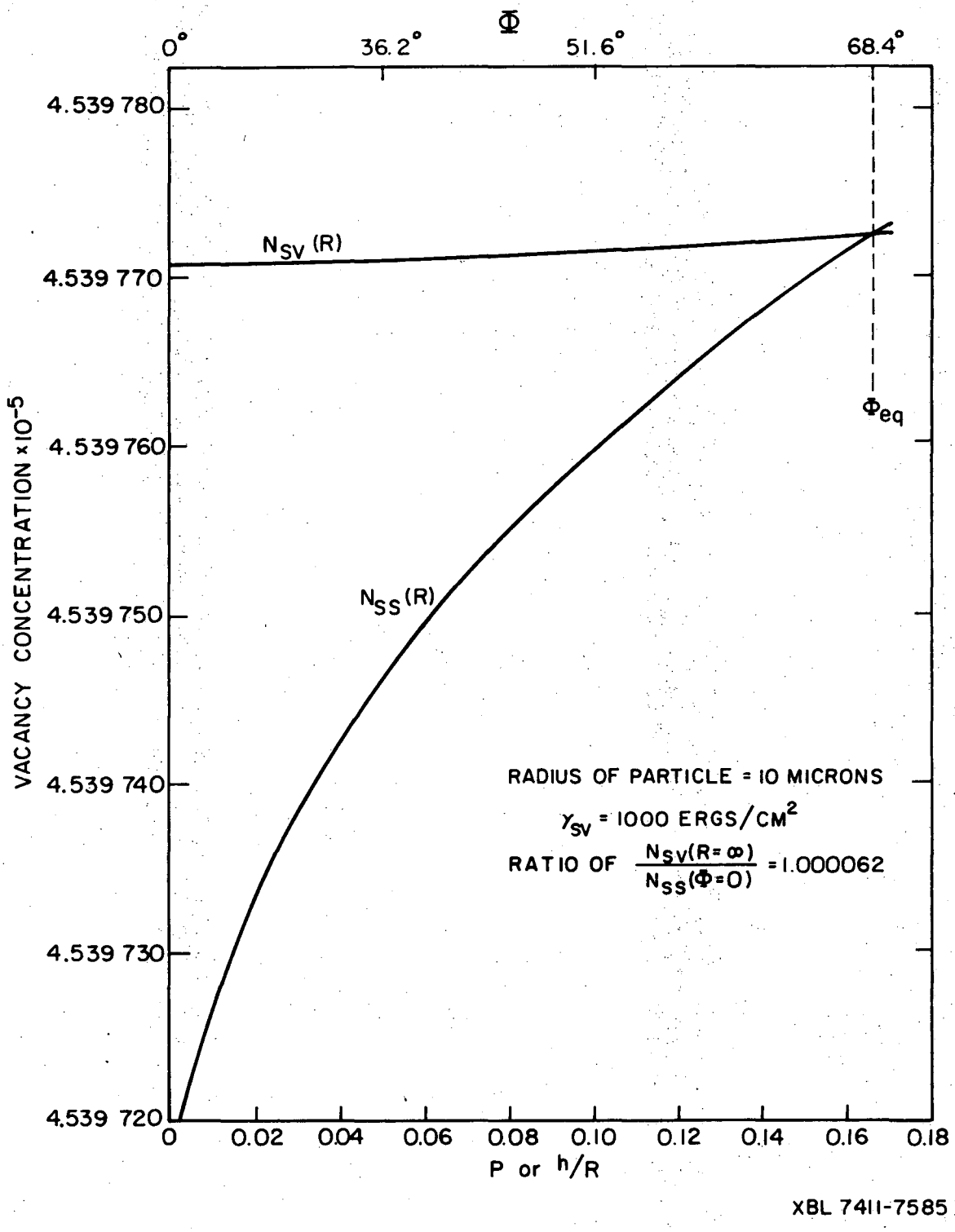

Figure 13. Vacancy concentrations at the solid/solid and solid/vapor interfaces versus P or h/R, for interpenetration of 10 micron spheres forming no bridging neck. (See Appendix 1.)

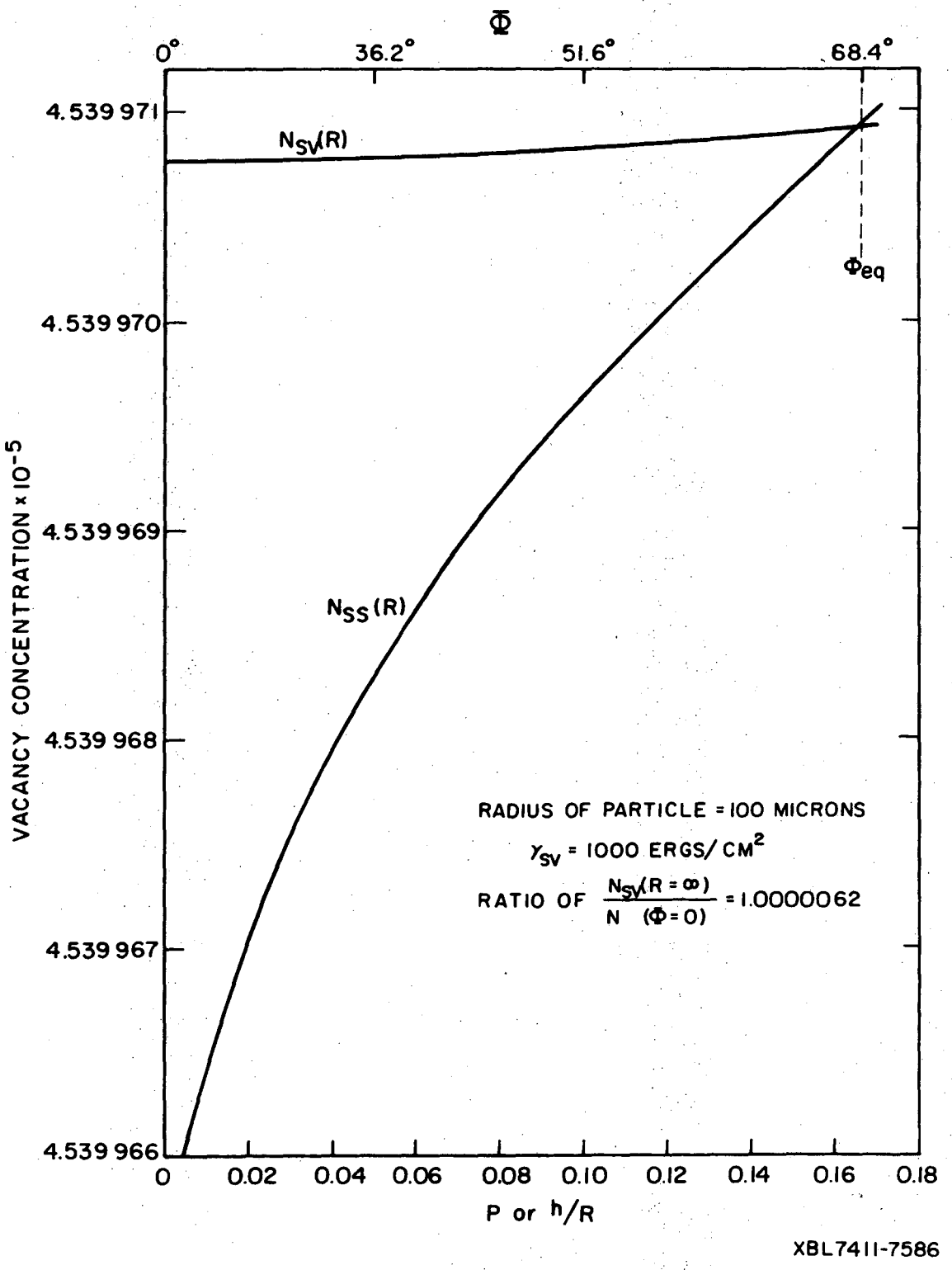

Figure 14. Vacancy concentrations at the solid/solid and solid/vapor interfaces versus P or h/R, for interpenetration of 100 micron spheres forming no bridging neck. (See Appendix 1.)

their mole fraction, (ideal solution approximation). As can be seen from the figures, the vacancy concentrations at the solid-vapor and solid-solid interfaces both increase as interpenetration of the spheres proceeds, but the concentration of vacancies at the solid-solid interfaces increases at a faster rate and becomes equal to the concentration at the solid-vapor interface when the equilibrium dihedral angle forms (see Appendix 1 for details of the calculations used in obtaining Figs. 12, 13 and 14). Figure 15 shows a schematic diagram of how the chemical potentials of vacancies change at each interface as Φ increases from 0° to Φ_{eq}.

2. Thermodynamic Driving Force

At any instance during sintering, if the experimental or dynamic dihedral angle is less than the equilibrium value, there is a thermodynamic driving force for continued mass transport and sintering. As was shown in the thermodynamic analysis of endpoint densities, (Section II-A), the further the experimental dihedral angle is from the equilibrium value, the more negative is the differential free energy in going from the nonequilibrium to the equilibrium configuration, and the greater is the thermodynamic driving force for further densification.

This overall driving force for sintering may be expressed as

$$\Delta\Phi = \Phi_{eq} - \Phi_{dyn} \tag{35}$$

where Φ_{eq} is the value based on γ_{ss} for a planar grain boundary and on γ_{sv} for surfaces in equilibrium with their own vapor; and Φ_{dyn} is the instantaneous value in a sintering compact which is dependent on

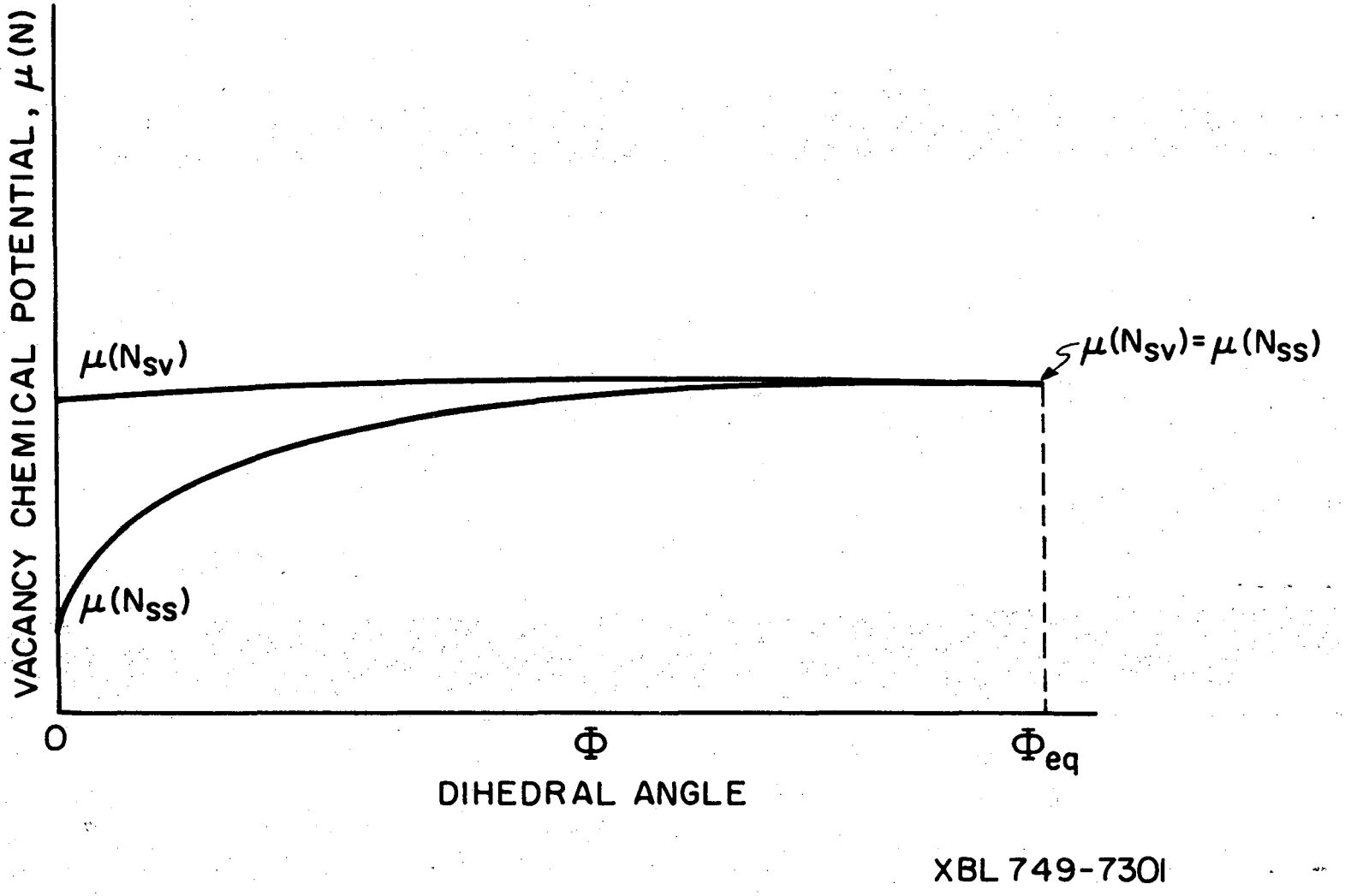

Figure 15. Schematic diagram of vacancy chemical potentials at solid/solid and solid/vapor interfaces versus dihedral angle.

atmospheric conditions, chemical effects, and geometry. Mathematically, when Φ_{dyn} becomes equal to Φ_{eq} sintering ceases since the thermodynamic driving force for sintering is eliminated.

Under static conditions where the vapor phase is in equilibrium with the solid, an equilibrium dihedral angle is attained. However, under dynamic conditions, the vapor species above a specimen can be swept away, and in an attempt to restore the equilibrium vapor pressure for the system, material will vaporize more from the higher energy curved surface at the groove root. If vaporization is rapid compared to other mass transport mechanisms which attempt to restore the equilibrium shape of the dihedral angle, a nonequilibrium or experimental dihedral angle which is smaller than the equilibrium angle will result. This decrease in dihedral angle can be referred to as a "corrosion" effect.

Φ_{dyn} is also dependent on chemical effects since adsorption or desorption of material from solid-vapor surfaces will vary depending on the curvature of the surface. For instance, a solute atom which positively adsorbs but is somewhat larger in atomic size than the solvent atom will generate compressive stresses in the atomic lattice. Such an atom will therefore preferentially adsrob in the concave surface of the neck region of a two sphere model which is in radial tension as opposed to the convex surfaces of the spheres which are in radial compression. Correspondingly, changes in γ_{sv} occur during sintering and Φ_{dyn} is affected.

The third parameter, geometry represents the effect of purely geometric conditions changing during sintering. Interpenetration of spheres in the absence of neck formation has already been discussed. A

more common condition that should be discussed further is associated with the formation of bridging necks between particles. Nichols[2] has shown mathematically that for a two sphere model having a briding neck between the spheres, (actually infinite cylinders), surface diffusion alone will lead to an "undercut" region adjacent to the neck, Fig. 16. Similar undercutting has been predicted when volume diffusion mechanisms are operative.[11] These derivations assumed no contribution from the grain boundary energy to the shape of the surfaces, i.e., a 180° dihedral angle. However, for any dihedral angle less than 180° it can be shown by inspection that the degree of undercutting must decrease as the equilibrium dihedral angle decreases and that as equilibrium conditions are approached all surface inflections (undercuts) must disappear. Therefore, when bulk and surface diffusion fluxes are similar, material diffusing from the bulk and depositing at the surface of the neck region will continue to diffuse by surface diffusion mechanisms from the concave surface (neck region) to the undercut region thus reducing or flattening out the degree of undercutting and in turn reducing the dihedral angle. In an attempt to attain a minimum free energy configuration, further material transport will occur via bulk or grain boundary diffusion mechanisms from the grain boundary towards the neck region. The deposition of material from this source will tend to restore the equilibrium dihedral angle. The two processes will continue on an atomistic scale until surface inflection points disappear and the equilibrium configuration is reached. During this interval, if geometric effects provide the principal contribution to $\Delta\Phi$, there will be a small incremental value of $\Delta\Phi$ during sintering which will decrease with increasing neck radius and

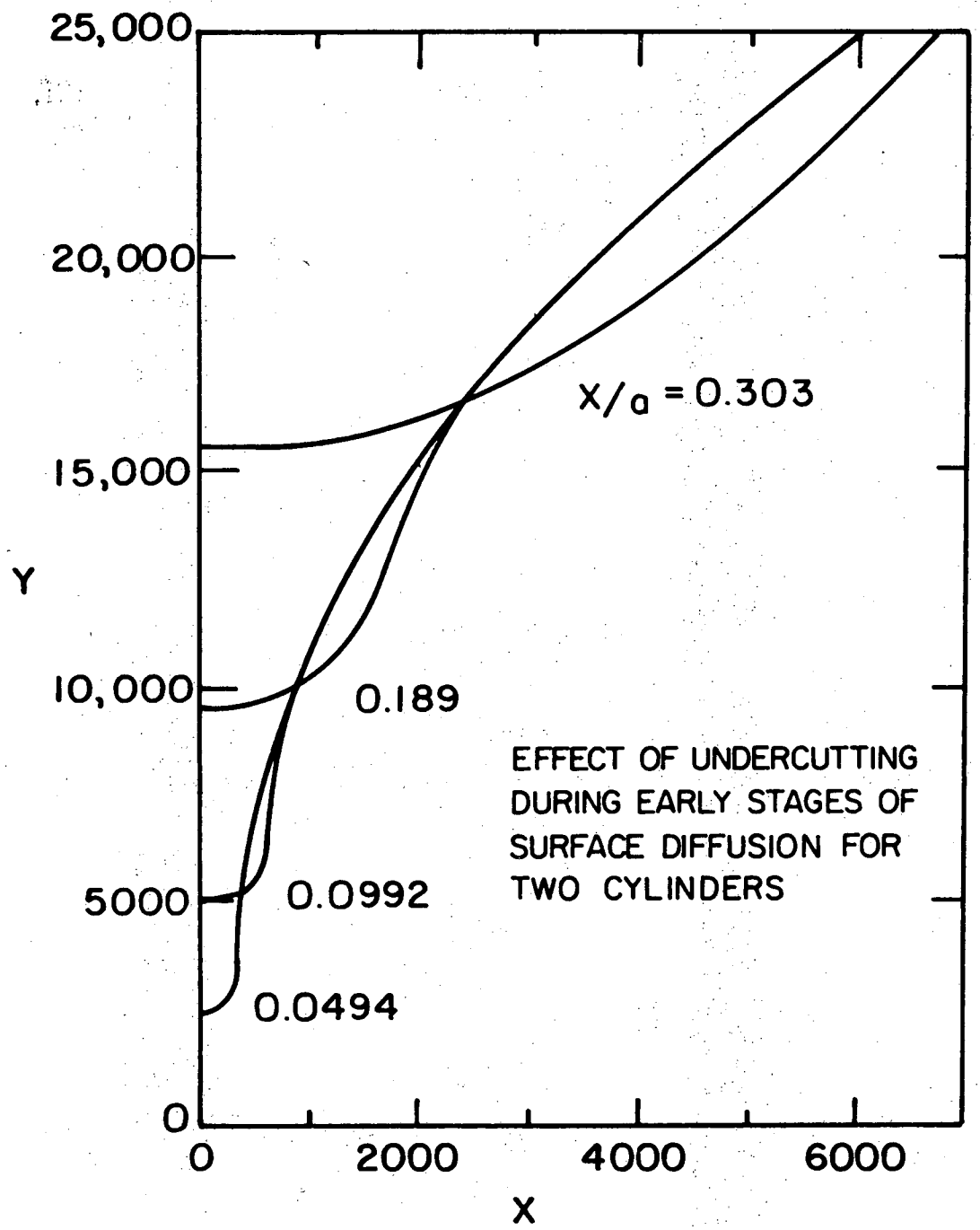

(From F. A. Nichols, Acta. Met., Vol. 16, 1968, pp 109)

XBL 748-6875

Figure 16

become zero at equilibrium.

In the absence of corrosion or chemical effects, this $\Delta\Phi$ will be the only thermodynamic driving force for densification. If the surface diffusion flux is rapid compared to the bulk or grain boundary diffusion flux, the surface topography created by the ratio of γ_{ss}/γ_{sv} will tend to eliminate the undercut region as the neck radius increases. Equilibrium conditions will then be approached without any measurable densification.

Therefore, when geometry is the dominant parameter contributing to the driving force for densification, surface diffusion fluxes and bulk diffusion fluxes must be similar in order that a situation will exist whereby the contribution of surface diffusion will be to reduce the curvature of the neck region (decrease the dihedral angle), while that of bulk or grain boundary diffusion will be to restore the equilibrium value of the dihedral angle. This incremental or stepwise process will result in shrinkage and continue on an atomistic scale until all surface inflections are eliminated and a configuration approaching equilibrium conditions is attained.

Thus for models forming bridging necks, the equilibrium dihedral angle is approached in the initial stage of sintering during neck formation and the small incremental change in $\Delta\Phi$ is the thermodynamic driving force for densification. On the other hand, as discussed earlier, models which form no bridging neck are characterized by a dynamic, or experimental, dihedral angle which increases continuously from $\Phi = 0$ toward the equilibrium value, Φ_{eq}, during the entire sintering process as the interpenetration of the spherical particles proceeds. At any instance during sintering, the thermodynamic driving force is $\Phi_{eq}-\Phi_{dyn}$ and when

the equilibrium dihedral angle is attained, sintering ceases.

The general form of Eq. (35) will therefore be valid throughout the entire sequence of sintering of a powder compact with one, two or all three parameters contributing to $\Delta\Phi$. But it should be noted that $\Delta\Phi$ will generally change during each stage of sintering as the relative contributions of the parameters change. When a sintering compact is still in the open porosity stage, the value of $\Delta\Phi$, if determined by a corrosion effect due to a flowing ambient atmosphere above the surface of the compact, will remain relatively constant during sintering. When sintering has proceeded to the point where closed porosity forms, the internal dihedral angles will change toward Φ_{eq} either with or without additional sintering since a grain boundary intersecting an internal pore will no longer be in contact with the ambient atmosphere. Under isolated conditions the vapor phase within a pore will determine the value of Φ_{dyn} which will then become the determining factor in establishing the magnitude of the thermodynamic driving force for sintering.

On the other hand, if only the effect of geometric changes is considered in a system of spherical particles that maintains the lowest free energy configuration at each instant during sintering, Φ_{dyn} at the start of sintering is zero and increases as sintering proceeds. When Φ_{dyn} becomes equal to Φ_{eq}, sintering ceases. Therefore, if Φ_{eq} is greater than Φ_{crit} for a certain initial packing array (Fig. 4 in Section IIA), no thermodynamic barriers to the attainment of theoretical density exist. If Φ_{eq} is less than Φ_{crit}, an endpoint density as determined by the intersection of the value of Φ_{eq} with the appropriate curve of Fig. 4 will result.

C. Thermodynamics of Grain Growth

It has long been realized that if the pores stay at the grain boundaries during sintering, they have a much better chance of being annihilated than if they are trapped as isolated spherical pores at large diffusion distances from grain boundaries.[13-15] It has thus been argued that in order to achieve theoretical density, the grain boundaries must be prohibited from sweeping out past pores thus leaving them isolated. Therefore, in numerous sintering studies, additives are introduced to compacts for the stated purpose of pinning grain boundaries to pores. In some cases, the additive acts as a sparingly soluble second phase which segregates at grain boundaries; the analysis is then modified from that being discussed in this report.

1. Lenticular Pore at a Planar Grain Boundary

It is of interest to examine the thermodynamics of a planar grain boundary breaking away from a lenticular shaped pore. The geometry to be examined in detail is shown in Fig. 17 in which the isolated pore attains the low free energy spherical form as the grain boundary moves away. This process, however, contributes to an increase of the free energy of the system because solid/solid interfacial area is created. Therefore, the net free energy of the system will be a function of the relative interfacial areas and energies. The analysis proceeds as follows.

From Fig. 17, half the dihedral angle is given by

$$\cos \phi/2 = \frac{r^2-h^2}{r^2+h^2} \tag{36}$$

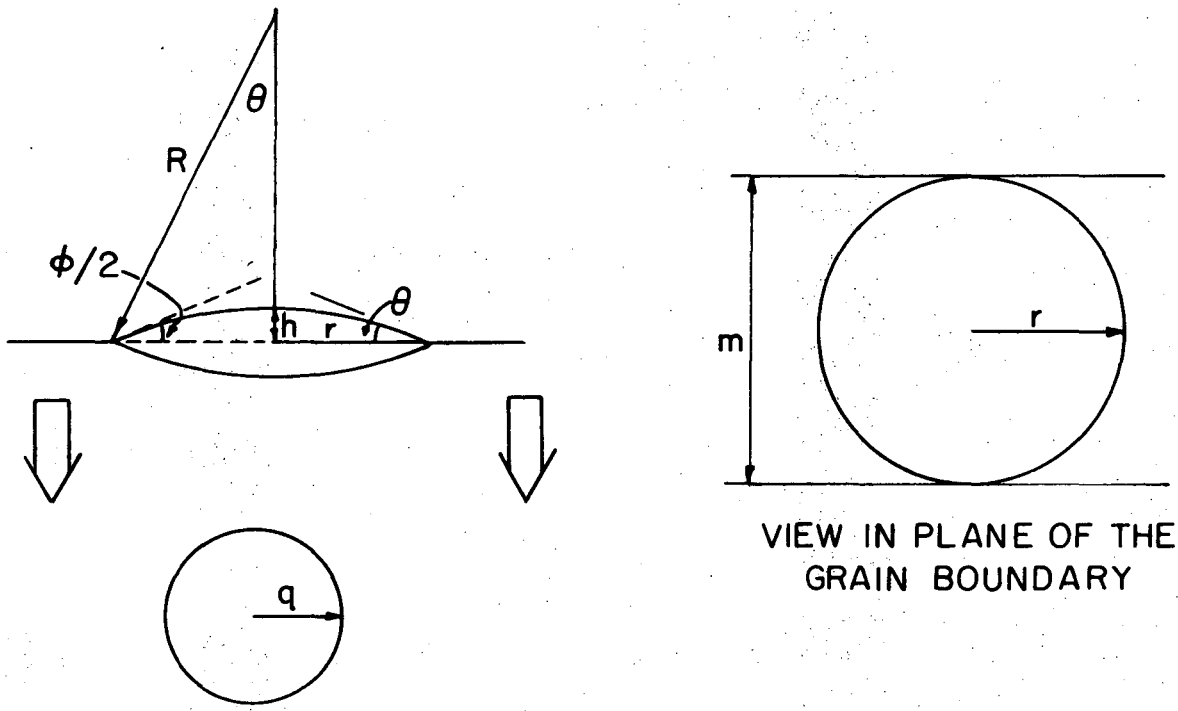

Figure 17. A planar grain boundary sweeping past a lenticular pore. $\phi/2 = \theta$ = solid/vapor-solid/solid dihedral angle of the enclosed pore. q = the radius of the spherical pore formed after the planar grain boundary has swept through the lenticular pore leaving it isolated.

where r is the radius of the lenticular pore. From (3) and by setting $\gamma_{ss}/2\gamma_{sv}$ equal to A, we get

$$A = \frac{r^2-h^2}{r^2+h^2} \tag{37}$$

Algebraic maniupulation leads to

$$h^2 = \frac{r^2(1-A)}{(1+A)} \tag{38}$$

$$h = \frac{r(1-A)^{1/2}}{(1+A)^{1/2}} \tag{39}$$

Referring to Fig. 17, the change in free energy of the system is

$$\Delta G_{syst} = G_{II} - G_I \tag{40}$$

where

$$G_{II} = A_{ss}^{II}\gamma_{ss} + A_{sv}^{II}\gamma_{sv}, \tag{41}$$

and

$$G_I = A_{ss}^{I}\gamma_{ss} + A_{sv}^{I}\gamma_{sv} \tag{42}$$

Therefore,

$$\Delta G_{syst} = \gamma_{ss}(A_{ss}^{II} - A_{ss}^{I}) + \gamma_{sv}(A_{sv}^{II} - A_{sv}^{I}) \tag{43}$$

$$\Delta G_{syst} = \gamma_{ss}\Delta A_{ss}\, A_{ss} + \gamma_{sv}\Delta A_{sv} \tag{44}$$

If we consider the overall area of the grain boundary to be fixed and circular, then

$$A_{ss}^{I} = \pi(\ell)^2 - \pi r^2 \tag{45}$$

and

$$A_{ss}^{II} = \pi(\ell)^2 \tag{46}$$

where ℓ is the radius of the planar grain boundary. Thus

$$\Delta A_{ss} = \pi(\ell)^2 - \pi(\ell)^2 + \pi r^2 \tag{47}$$

$$\Delta A_{ss} = \pi r^2 \tag{48}$$

The solid-vapor area of the lenticular pore is given by

$$A_{sv}^{I} = 2(2\pi Rh) \tag{49}$$

If we substitute

$$R = \frac{r^2 + h^2}{2h} \tag{50}$$

obtained from geometry (Fig. 17) into (49), then

$$A_{sv}^{I} = \frac{2(2\pi h)(r^2 + h^2)}{2h} \tag{51}$$

$$A_{sv}^{I} = \pi 2(r^2 + h^2) \tag{52}$$

When the grain boundary moves, the volume of the resulting pore remains constant. The volume of the lenticular pore is

$$V_{sv}^{I} = 2(\frac{\pi}{6} \; h(3r^2 + h^2)) \tag{53}$$

and the volume of the spherical pore is

$$V_{sv}^{II} = \frac{4\pi q^3}{3} \tag{54}$$

where q is the radius of the spherical pore. Equating (53) and (54) results in

$$q^2 = [\frac{h(3r^2 + h^2)}{4}]^{2/3} \tag{55}$$

Substituting this value for q^2 into

$$A_{sv}^{II} = 4\pi q^2 \tag{56}$$

gives the value of the resulting spherical pore in terms of r and h

$$A_{sv}^{II} = \frac{4\pi}{4^{2/3}} \left[h(3r^2 + h^2)\right]^{2/3} \tag{57}$$

$$A_{sv}^{II} = 4^{1/3}\ \pi(h(3r^2 + H^2))^{2/3} \tag{58}$$

Then, combining (52) and (58)

$$A_{sv} = 4^{1/3}\ \pi(h(3r^2 + h^2))^{2/3} - 2\pi(r^2 + h^2) \tag{59}$$

Substituting (48) and (59) into (44), we get

$$\Delta G_{syst} = \gamma_{ss}\pi r^2 + \gamma_{sv}\left\{4^{1/3}\ \pi(h(3r^2 + h^2))^{2/3} - 2\pi(r^2 + h^2)\right\} \tag{60}$$

$$\frac{\Delta G_{syst}}{\pi} = \gamma_{ss} r^2 + \gamma_{sv}\left\{4^{1/3}\ (h(3r^2 + h^2))^{2/3} - 2(r^2 + h^2)\right\} \tag{61}$$

Further substitution of (39) into (61) gives

$$\frac{\Delta G_{syst}}{\pi} = \gamma_{ss} r^2 + \gamma_{sv}\left\{4^{1/3}\left[\left(\frac{1-A}{1+A}\right)^{1/2}\ r\left(3r^2 + r^2\left(\frac{1-A}{1+A}\right)\right)\right]^{2/3}\right.$$

$$\left. -2\left(r^2 + r^2\left(\frac{1-A}{1+A}\right)\right)\right\} \tag{62}$$

$$\frac{\Delta G_{syst}}{\pi} = \gamma_{ss} r^2 + \gamma_{sv} r^2 \left\{ 4^{1/3} \left[\left(\frac{1-A}{1+A} \right)^{1/2} \left(\frac{4+2A}{1+A} \right) \right]^{2/3} - \frac{4}{1+A} \right\} \tag{63}$$

Then, substituting $2A\gamma_{sv}$ for γ_{ss} we get

$$\frac{\Delta G_{syst}}{\pi r^2} = 2A\gamma_{sv} + \gamma_{sv} \left\{ 4^{1/3} \left[\left(\frac{1-A}{1+A} \right)^{1/2} \left(\frac{4+2A}{1+A} \right) \right]^{2/3} - \frac{4}{1+A} \right\} \tag{64}$$

$$\frac{\Delta G_{syst}}{\pi r^2 \gamma_{sv}} = 2A + 4^{1/3} \left[\left(\frac{1-A}{1+A} \right)^{1/2} \left(\frac{4+2A}{1+A} \right) \right]^{2/3} - \frac{4}{1+A} \tag{65}$$

A plot of the net integral normalized free energy change vs cos $\phi/2$, which is equal to A in (65), is shown in Fig. 18. The graph also shows the integral free energy changes due to the solid/solid and solid/vapor area changes individually. Since solid/solid area is always created by movement of the grain boundary, this factor always makes a positive contribution to the free energy of the system. On the other hand, the solid/vapor area is always reduced and makes a negative contribution; the small contribution at small values of cos $\phi/2$ is a reflection of the small area change because the lenticular pores, with a large dihedral angle, are almost spherical. The net free energy change for the system, however, is always positive throughout the entire range of dihedral angles from 180° to 0° (cos $\phi/2$ = 0 to 1.0).

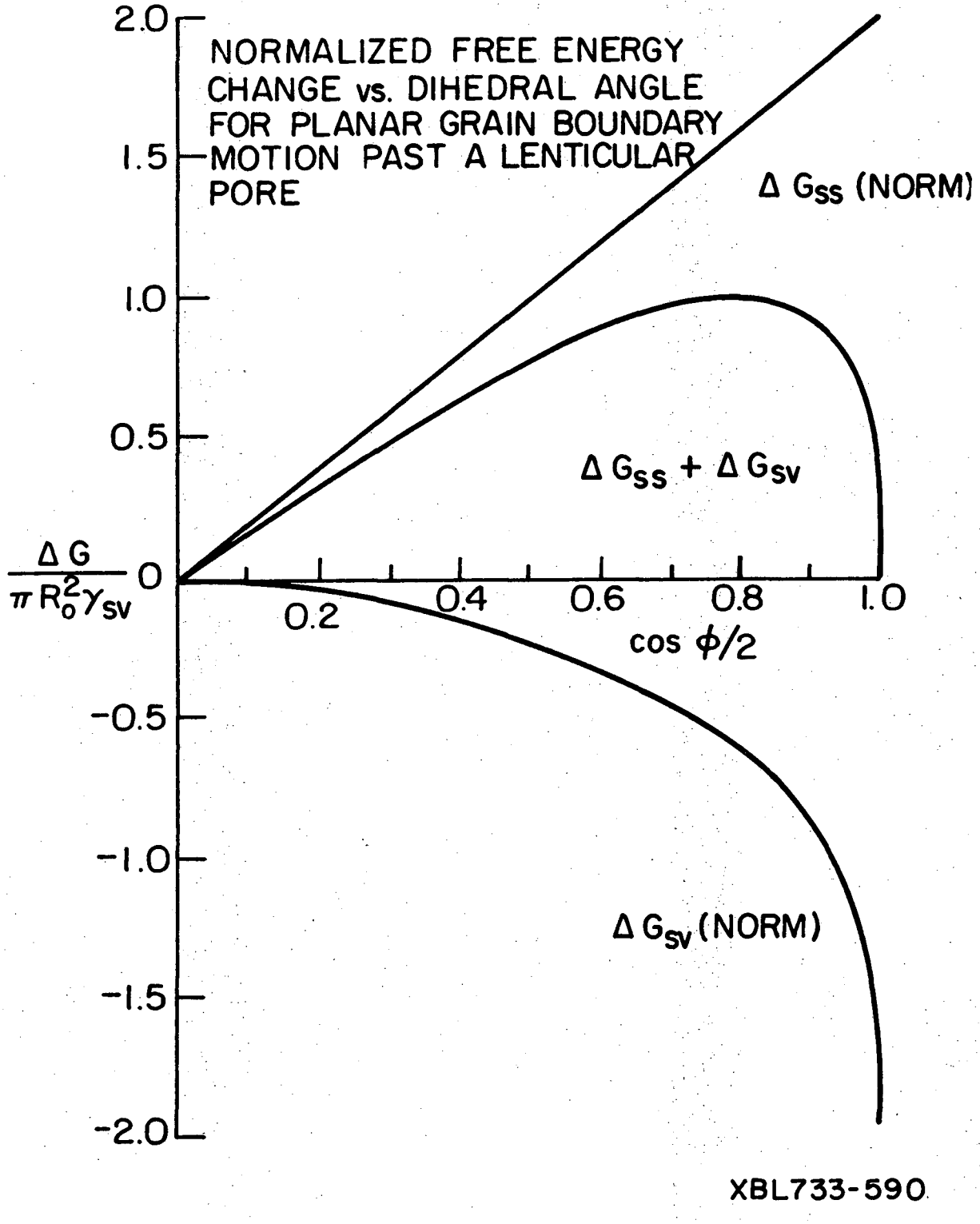
NORMALIZED FREE ENERGY CHANGE vs. DIHEDRAL ANGLE FOR PLANAR GRAIN BOUNDARY MOTION PAST A LENTICULAR PORE
2.0
1.5
1.0
0.5
0
-0.5
-1.0
-1.5
-2.0
ΔG / πR₀²γSV
0.2
0.4
0.6
0.8
1.0
cos φ/2
ΔGSS (NORM)
ΔGSS + ΔGSV
ΔGSV (NORM)
XBL733-590

Figure 18

An effort has not been made here to analyze cases of elongated pores on two or three grain junctions and pores at four grain junctions. Observations have been reported, however, that three grain junctions do not break away from pores.[18] Also, it can be deduced by inspection that the breaking away of the grain boundaries from the pore would be energetically even less favorable than the breaking away of a grain boundary from a lenticular pore because the increase of the solid/solid area relative to the decrease in the solid/vapor area would be much larger. From an energetic viewpoint it would be expected that the geometry would change progressively by grain boundary motions to the configuration treated here.

This thermodynamic analysis indicates that the presence of a lenticular pore with any dihedral angle on a planar grain boundary will always pin the grain boundary or the pore will move with the boundary. Thus, for grain boundary movement away from a pore to occur, there must be another negative contribution to the free energy of the system.

2. Lenticular Pore at a Curved Grain Boundary

The geometry to be examined in detail is shown in Fig. 19 which represents a circular sector of width m, arc length L, and angle in terms of Ψ which is the angle of curvature of the grain boundary as determined by two grain boundary triple points. Then, for a pore-free sector of boundary $L_f = \rho_f \Psi$, the area is $L_f m$ or $\rho_f \Psi m$ and the free energy is $G = \rho_f \Psi m \gamma_{ss}$. A differential change in ρ_f with a constant Ψ leads to

$$dG = \Psi m \gamma_{ss} d\rho_f \tag{66}$$

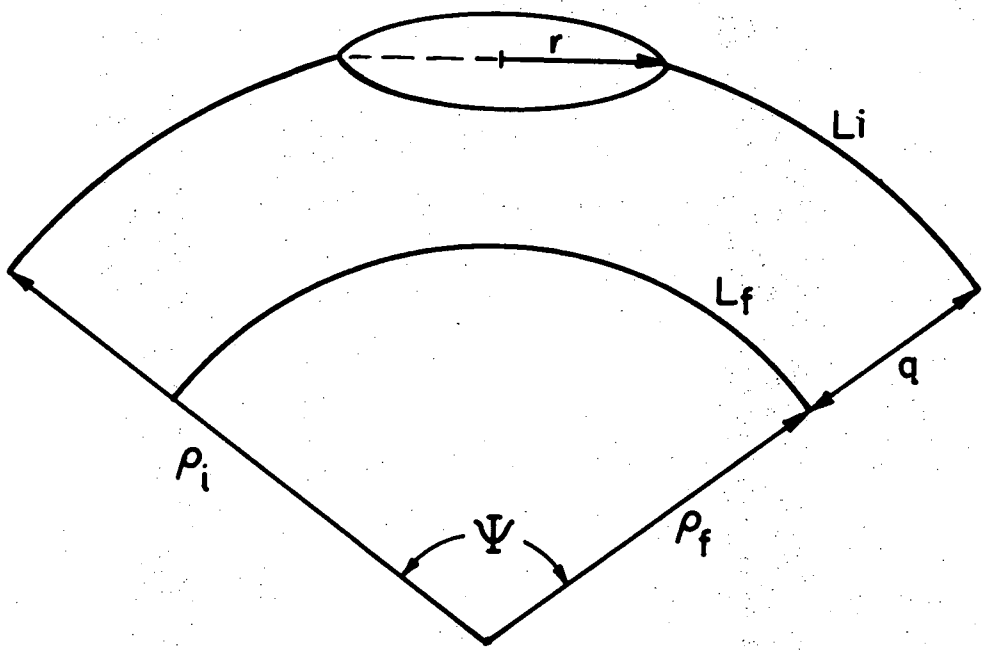

LENTICULAR PORE
AT A CURVED GRAIN BOUNDARY

XBL 733-5899

Figure 19. Ψ = the angle of curvature of the grain boundary as determined by the intersection of two grain boundary triple points in the plane of the diagram.

If $d\rho_f$ is positive, so is dG and vice versa. Therefore, a grain boundary will always have a tendency to move toward its center of curvature with a constant curvature of Ψ because the incremental free energy change is then negative. Likewise, a movement toward the center of curvature will tend to occur even with a constant chord length if the curvature is decreased in movement because the length of the boundary will then decrease.

The next step is to analyze the free energy changes when a boundary with a pore (L_i) moves to position L_f leaving the pore behind with the geometry of Fig. 19. The sum of the free energy changes due to the creation of the grain boundary and the change in the shape of the pore is positive for all dihedral angles as has been shown in the previous section. There is, however, an additional effect due to the reduction in grain boundary area as the boundary moves toward its center which is always negative. For grain growth or boundary movement to occur, the latter term must have a large enough negative value to make the net free energy change for the system negative. A detailed analysis for movement with constant curvature and within a given sector follows.

The initial area of the grain boundary, making m equal to 2r and neglecting the slight curvature of the boundary through the pore region, is

$$A_{ss}^{I} = L_i(2r) - \pi r^2 = \rho_i \Psi 2r - \pi r^2 \qquad (67)$$

and the final solid/solid interfacial area after movement, where q is equal to the radius of the resulting spherical pore with volume equal to

the original lenticular pore, is

$$A_{ss}^{II} = L_f(2r) = \rho_f \Psi 2r = (\rho_i - q)\Psi 2r \tag{68}$$

The change in area is

$$\Delta A_{ss} = 2r\Psi\rho_i - 2r\Psi q - \rho_i \Psi 2r + \pi r^2 \tag{69}$$

$$\Delta A_{ss} = \pi r^2 - 2r\Psi q \tag{70}$$

Substituting (39) into (55) and solving, we get

$$q = \frac{r}{4^{1/3}} \left\{ \left(\frac{1-A}{1+A} \right)^{1/2} \left(\frac{4+2A}{1-A} \right) \right\}^{1/3} \tag{71}$$

The substituting (71) into (70) results in

$$\Delta A_{ss} = \pi r^2 - 2\Psi r \left[\frac{r}{4^{1/3}} \left\{ \left(\frac{1-A}{1+A} \right)^{1/2} \left(\frac{4+2A}{1+A} \right) \right\} \right]^{1/3} \tag{72}$$

$$\Delta A_{ss} = r^2 \left[\pi - \frac{2\Psi}{4^{1/3}} \left\{ \left(\frac{1-A}{1+A} \right)^{1/2} \left(\frac{4+2A}{1+A} \right) \right\}^{1/3} \right] \tag{73}$$

The change in solid/vapor interfacial area obtained from the planar grain boundary by substituting (71) into (57) is

$$\Delta A_{sv} = \left[4^{1/3} \left\{ \left(\frac{1-A}{1+A} \right)^{1/2} \left(\frac{4+2A}{1+A} \right) \right\}^{2/3} - \frac{4}{1+A} \right] \pi r^2 \qquad (74)$$

The free energy change of the system, substituting $\gamma_{sv} 2A$ for γ_{ss}, then becomes

$$\Delta G_{syst} = \gamma_{sv} (2A \, \Delta A_{ss} + \Delta A_{sv}) \qquad (75)$$

On substituting (73) and (74) into (75) and solving, we obtain

$$\frac{\Delta G_{syst}}{\pi r^2 \gamma_{sv}} = 2A \left\{ 1 - \frac{2\Psi}{4^{1/3}\pi} \left[\left(\frac{1-A}{1+A} \right)^{1/2} \left(\frac{4+2A}{1+A} \right) \right]^{1/3} \right\}$$

$$+ 4^{1/3} \left[\left(\frac{1-A}{1+A} \right)^{1/2} \left(\frac{4+2A}{1+A} \right) \right]^{2/3} - \frac{4}{1+A} \qquad (76)$$

This equation gives the normalized free energy change as a function of angle of curvature (Ψ) for various dihedral angles (represented by A). Solutions for dihedral angles from 168.4° to 106° are plotted in Fig. 20 and for angles from 73.6° to 16.2° in Fig. 21. The integrated free energy curves are positive for low angles of curvature Ψ, and become negative as the angle of curvature increases due to the continuing reduction of the grain boundary length as the curvature becomes larger. Inspection of the graphs indicates that for dihedral angles (ϕ) above about 73° boundary movement can occur at boundary curvatures above about

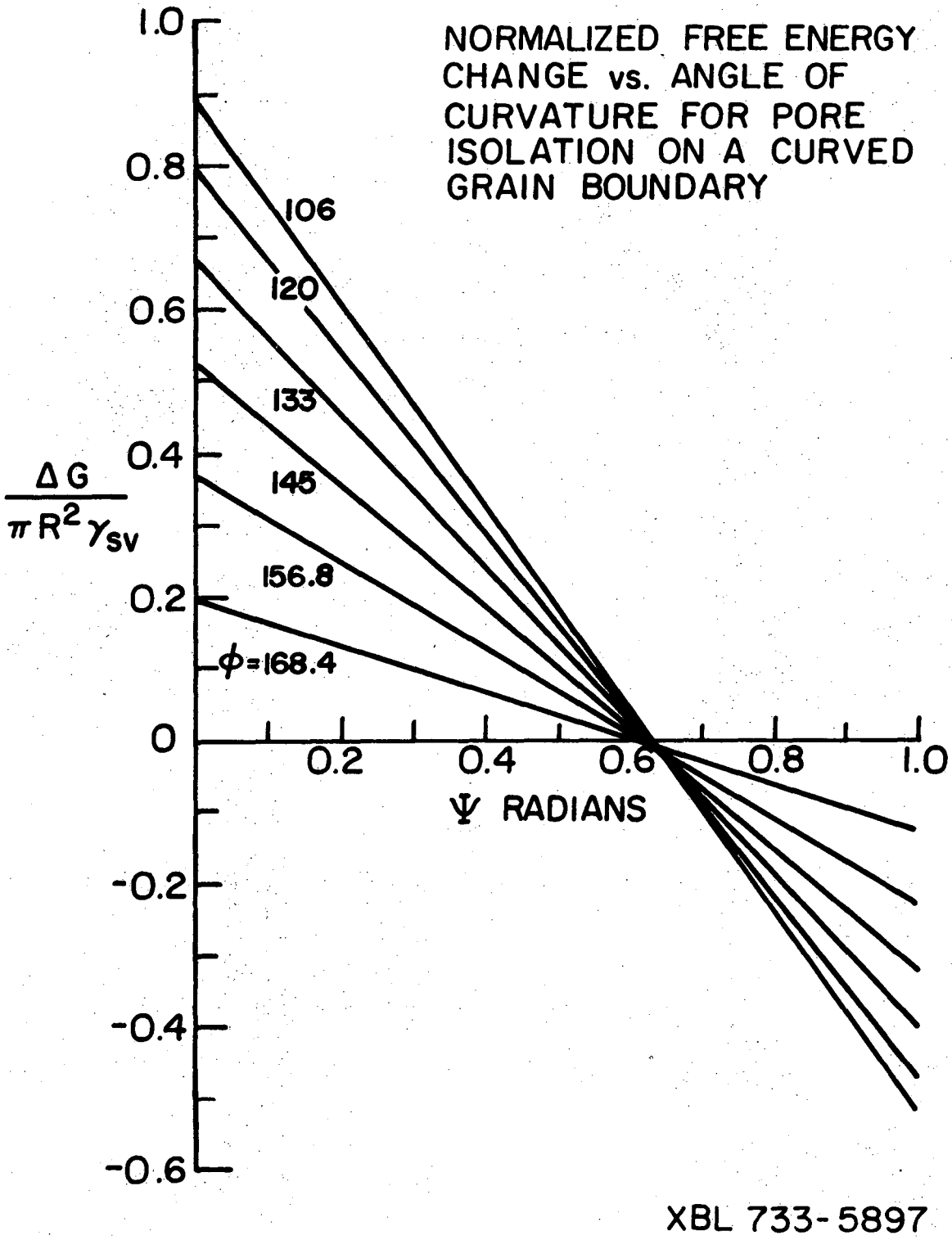
NORMALIZED FREE ENERGY CHANGE vs. ANGLE OF CURVATURE FOR PORE ISOLATION ON A CURVED GRAIN BOUNDARY
1.0
0.8
0.6
0.4
0.2
0
-0.2
-0.4
-0.6
ΔG / πR²γsv
106
120
133
145
156.8
φ=168.4
0.2
0.4
0.6
0.8
1.0
Ψ RADIANS
XBL 733-5897

Figure 20

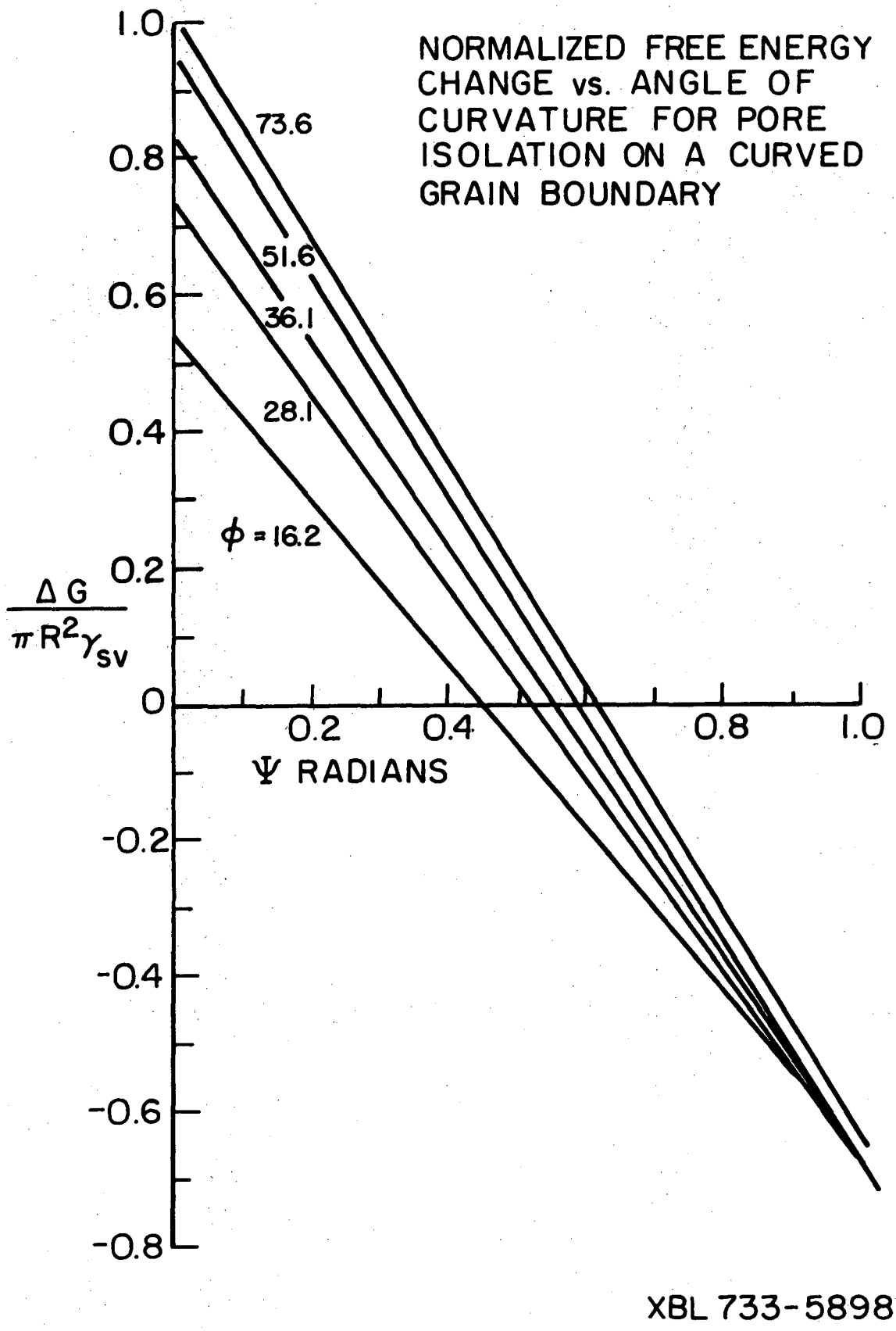
NORMALIZED FREE ENERGY CHANGE vs. ANGLE OF CURVATURE FOR PORE ISOLATION ON A CURVED GRAIN BOUNDARY
73.6
51.6
36.1
28.1
ϕ = 16.2
ΔG / πR²γsv
Ψ RADIANS
1.0
0.8
0.6
0.4
0.2
0
-0.2
-0.4
-0.6
-0.8
0.2
0.4
0.8
1.0
XBL 733-5898

Figure 21

0.62 radions or about 36°. With the decrease of dihedral angles below 73° boundary movement can occur at decreasing values of curvature; with Φ at 16°, grain growth can occur at curvatures above about 26°.

Another informative relationship is indicated in Fig. 22 whi h is a plot of Ψ versus half the dihedral angle $\phi/2$. The locus of points which fall below the curve yield positive values of the free energy for pore isolation, ΔG_{syst}. Whereas, points lying above the curve yield negative ΔG's. Inspection of the graph reveals that the critical angle of curvature is relatively independent of the dihedral angle for large values of $\phi/2$. While at $\phi/2$ less than about 36°, the value of Ψ critical decreases sharply as $\phi/2$ decreases. This result indicates that control of the curvature of the grain boundary is the critical factor in preventing pore isolation and that the introduction of additives to a system causing the γ_{ss}/γ_{sv} ratio to be reduced beyond the critical value has little effect on pinning grain boundaries.

3. Effect of a Mixture of Particle Sizes

A properly-oriented planar cross-section of a model microstructure of a crystalline material with uniform grain size and with grain boundary energy independent of orientation would show hexagonal grains with three grain junctions of 120° and straight line boundaries; the system would then be in metastable equilibrium since there would be no driving force for boundary movement. A variation in grain size would result in grain boundary curvatures because the three grain junctions will always attempt to maintain equilibrium angles of 120°. Grains with less than six sides would have their boundaries curve outward since the polygon angles with straight sides would be less than 120° while grains with more than six

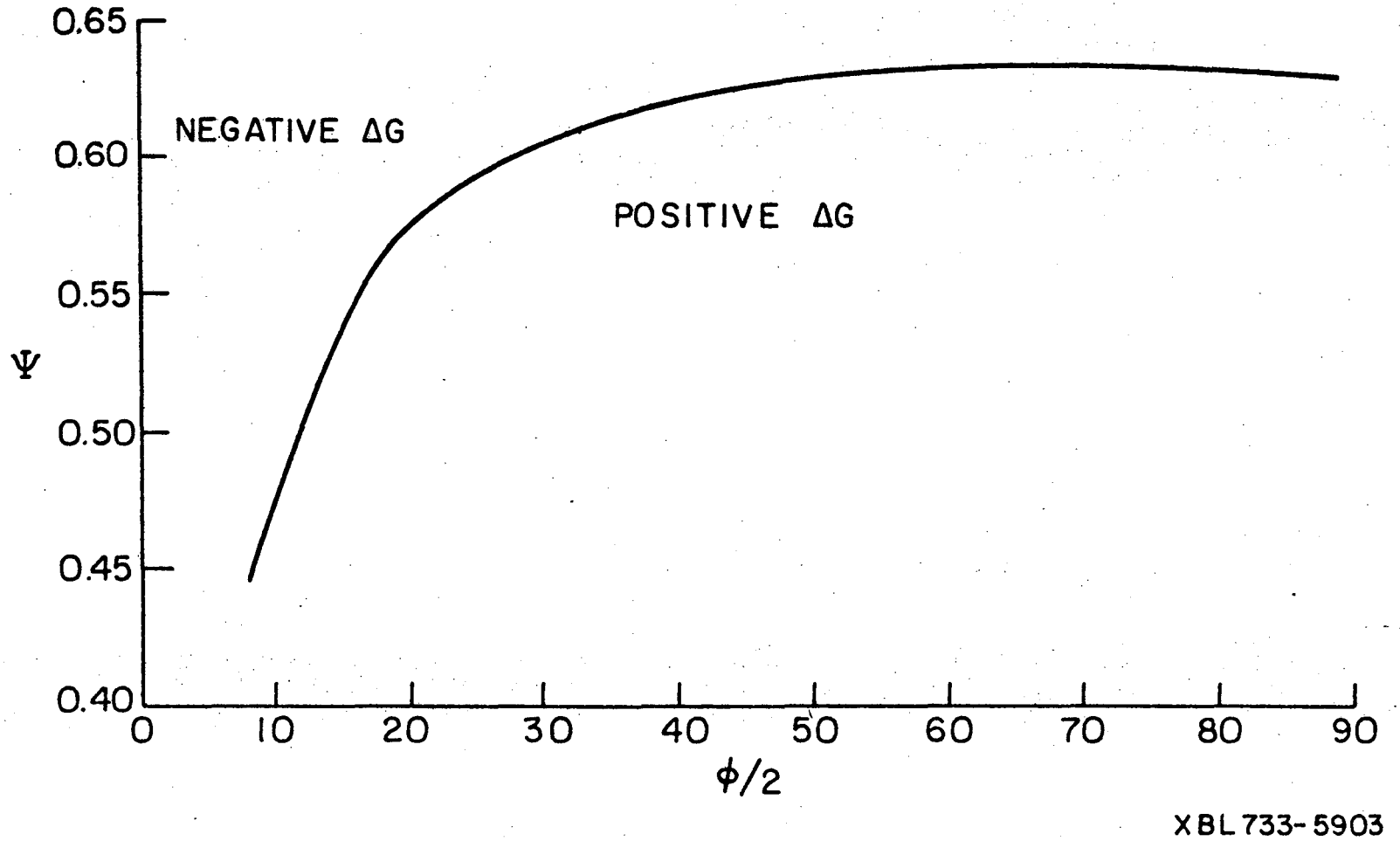

Fig. 22. Curvature, Ψ, vs half the dihedral angle, $\phi/2$. Regions where ΔG are negative indicate that the grain boundary will sweep past the pore leaving it isolated.

sides would have boundaries curving inward since the polygon angles would be greater than 120°. Thus, thermodynamically there would be an additional driving force for a grain with less than six sides to shrink and with more than six sides to grow since the grain boundaries would have a tendency to move toward their centers of curvature as described above.

With grains of two sizes the length and number of grain boundaries relative to the large grain will be dependent on the size of the small grain. The curvature between two adjacent triple points in all cases according to geometry would be spherical and the angle of curvature Ψ would be 60°; therefore, the boundaries would not be pinned by any pores that may be present on the boundaries. The greater the length of the grain boundary, however, particularly on an atomistic scale, the greater will be the probability that the center portion of the boundary will acquire a smaller angle of curvature because of the driving force to flatten out the boundary, i.e. the grain boundary would become elliptical or a flattened circle since the angles at the triple points would be maintained at 120°. If the curvature through the central portion decreases below about 36° the pore can then pin the grain boundary. It thus appears that from a thermodynamic viewpoint a starting powder with a single particle size or the smallest particle size range possible is desirable for sintering; the actual sizes of the particles become important only from a kinetic viewpoint.

III. EXPERIMENTAL STUDIES

A. Experimental Procedure

The ultimate purpose of all mathematical sintering models is to describe the sintering behavior of real powder compacts. The success or accuracy of a model is determined by the closeness with which it matches real systems. Most kinetic models for sintering predict densification rates, or some parameter of densification as a function of time, for a given set of initial conditions. Experimental verification of a model is then obtained by measurement of similar parameters for real compacts and comparison of the two sets of data. The extent to which a model deviates from actual sintering behavior can then be attributed to idealizations or approximations used in formulating the model. If the discrepancy between real and predicted sintering behavior is too great, the model must be modified. Therefore, experimental evidence provides an estimate of the confidence level of a model.

The thermodynamic model for solid phase sintering developed here predicts that when all conditions and packing densities are identical, the larger the equilibrium dihedral angle determined by relative values of γ_{ss} and γ_{sv}, the greater will be the endpoint density, and that if the equilibrium dihedral angle is greater than the critical angle for a given packing, the system should reach theoretical density from a thermodynamic viewpoint. Also, the model indicates that when the experimental or dynamic dihedral angle at any point in sintering is less than the equilibrium value, there exists a thermodynamic driving force for continued densification. This driving force is increased when the difference between the actual angle and the equilibrium angle is increased.

This effect can be seen from the slope of the P_0 versus γ_{ss}/γ_{sv} curve, Fig. 4 (Section IIA) or from Eq. (20).

A simple experimental verification of the model could consist of choosing several single phase isotropic materials having different equilibrium dihedral angles, cold pressing them to the same green density, and sintering them under identical conditions. If the model is correct, the materials forming the largest equilibrium dihedral angles should have the highest endpoint densities; on the other hand, if all the angles are larger than the critical angle, all the materials would reach theoretical density from a thermodynamic viewpoint but at different rates. The major problem in performing such a series of experiments is that the geometry of all the compacts must be very similar and therefore, aside from cold pressing the powders to a constant green density, they must also have similar particle shapes and the same size distributions. If the shapes of the particulates vary from materials to material, nearest neighbor contacts of particles will be different for each material. That is, a material which has particulates very similar in shape to spheres will yield a different packing distribution than a material which has irregular shaped particles. Therefore, a compact pressed from spherical material may approximate a simple cubic array while a compact pressed from irregular shaped material may form a combination of packings, e.g. diamond cubic and body-centered cubic. Although both such compacts would have the same green density, the differences in packing distributions between the two could cause attempted correlations between densities and dihedral angles for the two materials to lead to erroneous results, i.e. the compacts would be characterized by different curves in Fig. 4

(Section IIA), instead of one curve. Of still greater concern from a processing viewpoint is that a non-homogeneous distribution of several types of packings in a given compact could lead to a non-homogeneous distribution of entrapped closed pores.

Another approach is to fabricate compacts from one single phase material. Such compacts could then be sintered at the same temperature but in different atmospheres. If the gases in the atmosphere affect γ_{sv} and/or γ_{ss}, or create corrosive effects, the experimental dihedral angles will vary; these differences can then be correlated to the densities and/or rates of densification of the sintering powder compacts. The major advantage of this approach is that all the green compacts will have a similar structure. Even though there may be a wide density distribution in a compact, such a distribution would be expected to be the same in every compact. Thus, the only parameter which will vary, and can therefore cause differences in sintering, is the experimental or dynamic dihedral angle. For this reason, the latter approach was chosen for the experimental study.

1. Preparation of Powder Compacts

MgO was selected as the material for the experimentation. In order to obtain a uniform starting material, Mallinckrodt $MgCO_3$ was calcined at 1000°C to yield MgO. The powder was calcined in a heavy duty type furnace for 24 hours in air and furnace-cooled. The powder was then ground in an alumina mortar with pestle to break up the calcined cake. After grinding, the powder was dispersed in ethyl alcohol and immediately dried at 110°C.

Compacts were then cold pressed in a steel die using no binders to a green density of 45% of theoretical. Fifteen compacts were prepared for each sintering run.

2. Sintering and Density Measurements

A quench type furnace, Fig. 23A, was used for the sintering anneals with three different atmospheric conditions: static air, flowing air, and flowing water vapor. For the static air experiments, the specimens were arranged on a ceramic pedestal that was raised into the furnace which was maintained at a temperature of 1200°C. The furnace was then heated as quickly as possible to 1510°C, (30 minutes). The specimens were annealed for three different times: 100, 700, and 1440 minutes. After annealing, they were cooled to 1200°C and removed from the furnace. All sintering runs regardless of the atmosphere used during the experiment had the same heating and cooling cycles.

For the series of experiments with flowing air, compressed air was passed into the furnace by means of a tube running along the axis of the pedestal, Fig. 23B. This setup permitted the air to flow directly over the specimens. A similar setup was used for the flowing water vapor atmosphere. Distilled water was boiled in a sealed vessel and carried through heated glass tubing directly into the furnace. The flow rate for both flowing air and flowing water vapor experiments was approximately 2.0 cu. ft/hr.

After each sintering run the bulk density was determined for each specimen. The standard deviation and variance were calculated for the distribution of 15, and for a reduced distribution of 13 specimens after the specimens with the largest positive and negative deviation were

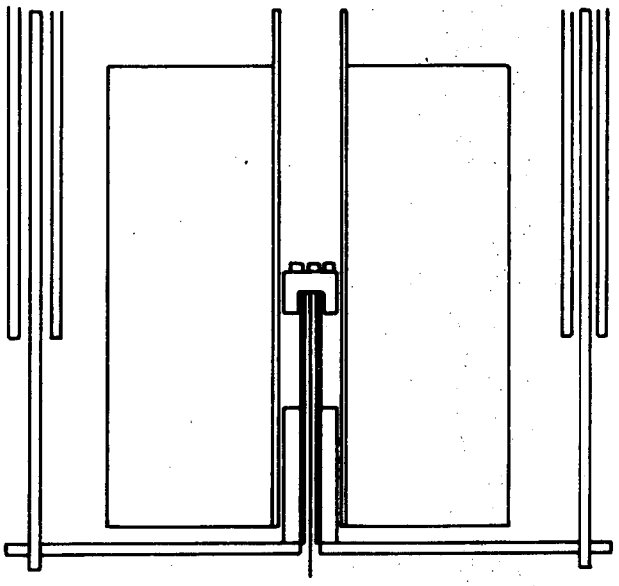

A

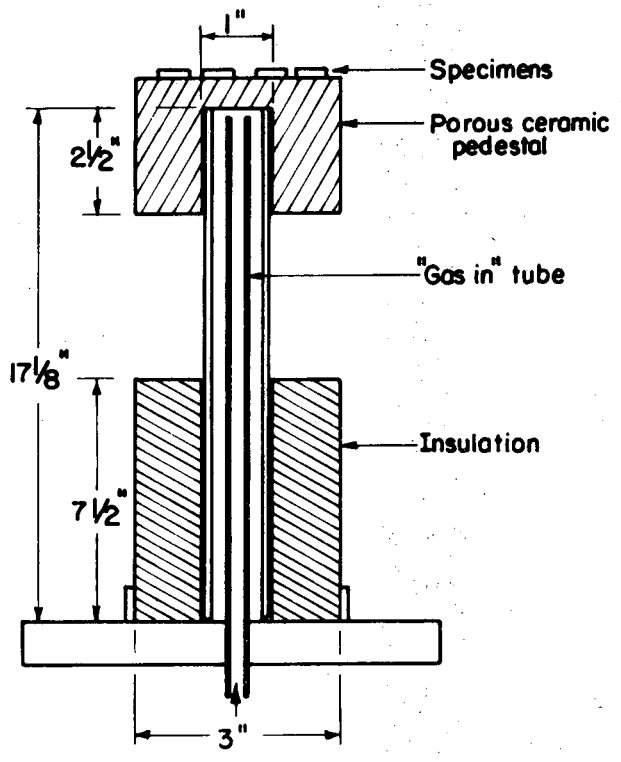

B

XBL749-7340

Figure 23. (A) Furnace used for the sintering studies.
(B) Pedestal arrangement for flowing gas into the furnace and supporting the sintered specimens.

eliminated. Fracture surfaces of selected specimens were also prepared for SEM examination.

3. Dihedral Angle Measurements

Direct measurements of the dihedral angles of sintered specimens could not be performed since the densities of the sintered compacts were low, less than 90% of theoretical, and the grain sizes were too small. Bicrystals of MgO were rejected for investigation since it was expected that the grain boundary of a bicrystal is more defect-free than that formed by sintering. In order to approximate sintering conditions as closely as possible, specimens for dihedral angle measurements were hot pressed from calcined $MgCO_3$ which was prepared in an identical manner as the powder used for sintering. The calcined powder was packed in a graphite die and hot pressed at 1200°C for 30 minutes in a vacuum of $5x10^{-4}$ torr to a density of 98.5% of theoretical. After hot pressing, the specimens were annealed at 1700°C for 24 hours (1440 minutes) in order to realize sufficient grain growth for dihedral angle measurements. The grain size after the anneal was approximately 100 microns.

The annealed polycrystalline material was cut into 0.5 cm cubes and one surface of each cube was polished on a succession of diamond wheels and cloths to a finish of 0.25 microns. A final polish with Linde B alumina was performed just prior to experimentation. A polished specimen was then annealed for 24 hours at 1510°C in each of the atmospheres used in the sintering study. Twenty-four hours was chosen as an annealing time since it allowed sufficient diffusion so that grain boundaries intersecting the polished surface were thermally grooved to a width and a depth to permit measurement of the dihedral angles. After annealing,

the specimens were prepared for SEM investigation; dihedral angle measurements were performed according to the method of Achutaramayya and Scott.[19] The technique consisted of orienting the surface of the specimen perpendicular to the beam of the SEM. A contamination line of carbon was deposited perpendicular to the grain boundary groove. The specimen was then tilted 47° around the axis of the contamination line and the profile of the groove was photographed.

The true dihedral angle, Φ, was calculated from the measured groove angles θ_1 and θ_2 according to Eqs. (77), (78), and (79).

$$\text{Tan } \alpha_1 = \sin(\text{tilt angle}) \tan \theta_1 \tag{77}$$

$$\tan \alpha_2 = \sin(\text{tilt angle}) \tan \theta_2 \tag{78}$$

$$\Phi = \alpha_1 + \alpha_2 \tag{79}$$

Since θ_1 and θ_2 are measured separately, the true dihedral angle is obtained even if the grain boundary is not perpendicular to the surface of the specimen.

B. Results and Discussion

1. Sintering

Density values of sintered specimens which were annealed at the test temperature of 1510°C for several different times and in different atmospheres are given in Table II and are plotted in Fig. 24 as density versus time. The fastest densification rate was observed in flowing water vapor; a rapid increase in density occurred during the first 50 minutes of sintering with little further increase in density with

Table II. Sintering data for MgO specimens annealed in static air, flowing air, and flowing water vapor at 1510°C

Time in Minutes	50	100	700	1440	2880
Static Air					
Density (15 specimens)	-	1.923	2.551	3.044	3.266
Std. Deviation	-	0.031	0.148	0.026	0.049
Density (13 specimens)	-	1.921	2.550	3.043	3.270
Std. Deviation	-	0.024	0.131	0.018	0.038
Flowing Air					
Density (15 specimens)	-	2.039	3.016	3.280	-
Std. Deviation	-	0.049	0.041	0.047	-
Density (13 specimens)	-	2.039	3.017	3.280	-
Std. Deviation	-	0.042	0.035	0.038	-
Flowing Water Vapor					
Density (15 specimens)	3.166	3.200	3.324	3.330	-
Std. Deviation	0.040	0.045	0.023	0.021	-
Density (13 specimens)	3.165	3.200	3.324	3.299	-
Std. Deviation	0.033	0.040	0.019	0.019	-

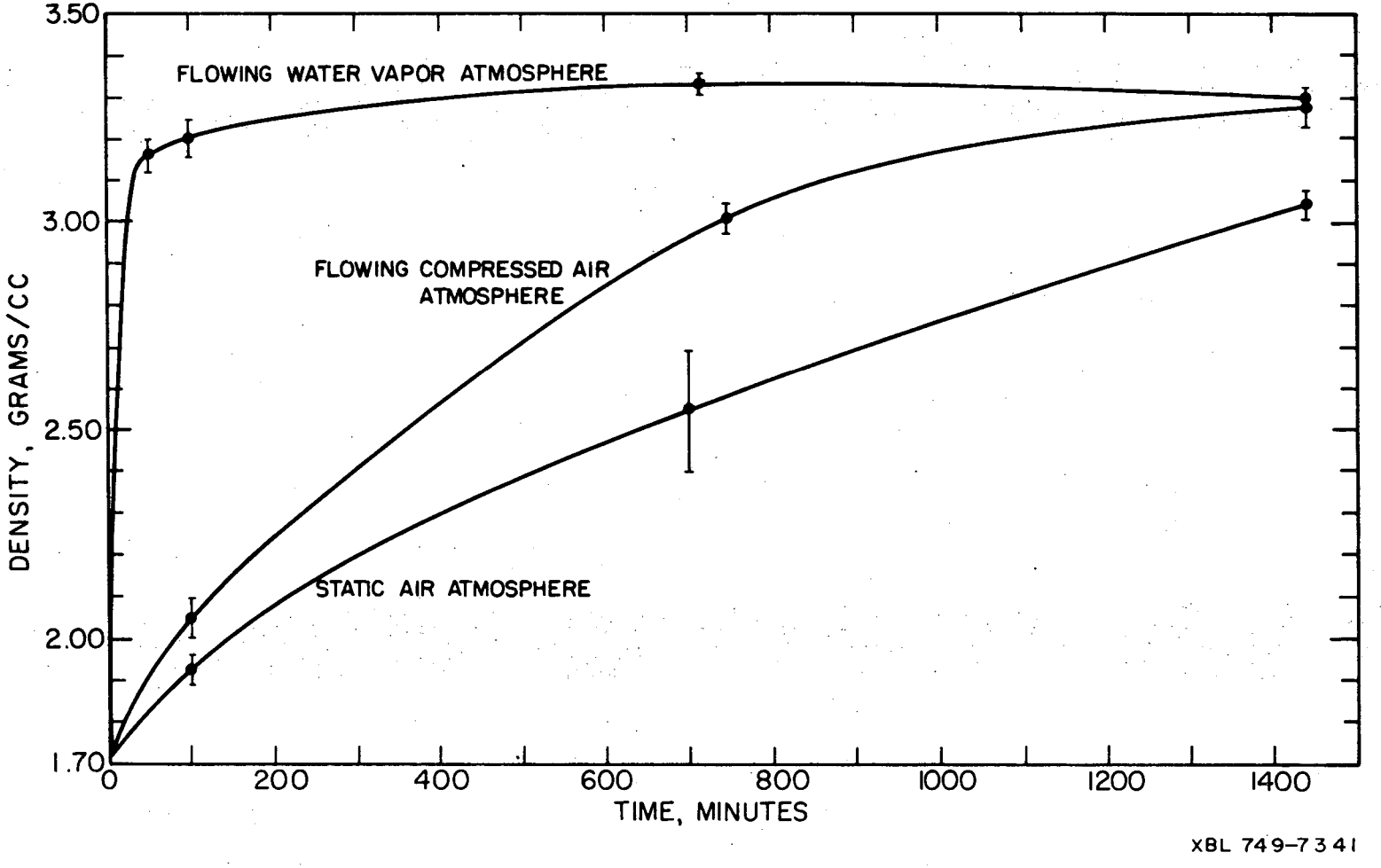

Figure 24. Density versus time for sintering of MgO under three different atmospheric conditions.

continued heating at temperature. Similar results have been observed by others[20-23] for sintering of MgO in water vapor.

Slower sintering rates were observed in flowing air and static air atmospheres but if the time at temperature was extended sufficiently, all sintered specimens approached the same endpoint density. The effect of flowing gases did not reduce the measured temperature in the furnace since the greatest densification rates were observed under flowing conditions. Specimens sintered in water vapor were at their maximum density (3.3 g/cc) at 700 minutes; in flowing air by about 1440 minutes, and in static air, at about 2880 minutes. This density corresponds to about 93% of theoretical; it was considered that non-homogenity was at least partially responsible for this endpoint density.

Figures 25, 26, and 27 are fracture surfaces of specimens sintered in flowing water vapor for 100, 700, and 1440 minutes, respectively. No significant grain growth occurred during the first 100 minutes of sintering although most of the densification took place in this interval. Approximately a five fold increase in grain size occurred between 100 and 1440 minutes.

Fracture surfaces of specimens sintered in static air and flowing air for 24 hours at 1510°C are shown in Figs. 28 and 29, respectively. Both have similar grain sizes which are about as large as the grain size of specimens sintered in flowing water vapor for 700 minutes, Fig. 26. It should be noted in comparing Figs. 25, 26, and 27 that as the grain size increases, the pore size also increases because the densities were essentially the same and the pores remained essentially on grain boundaries. Since the latter two compacts fractured transgranularly,

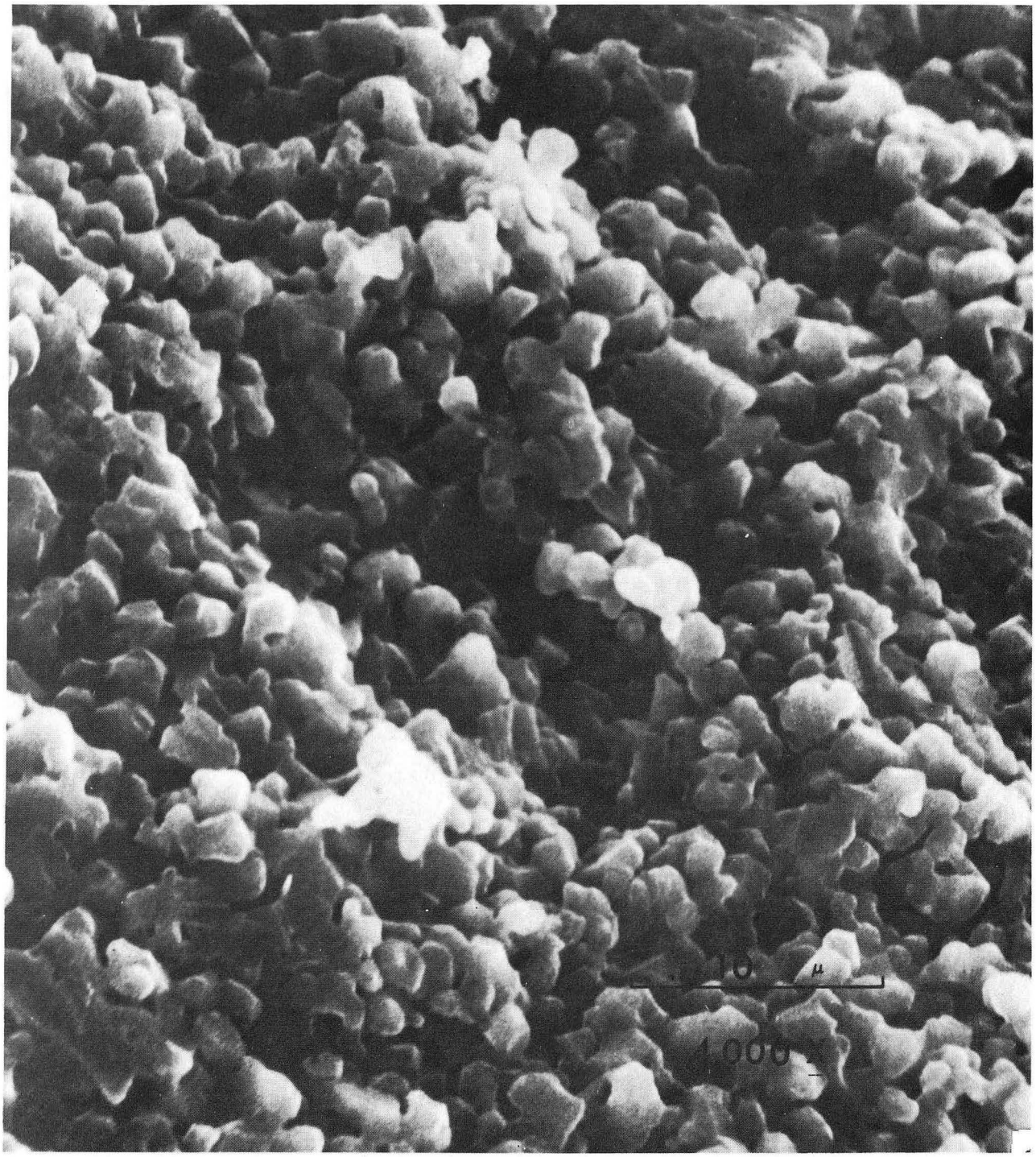

XBB 747-4566

Fig. 25. Fracture surface of MgO sintered at 1510°C for 100 min in flowing water vapor.

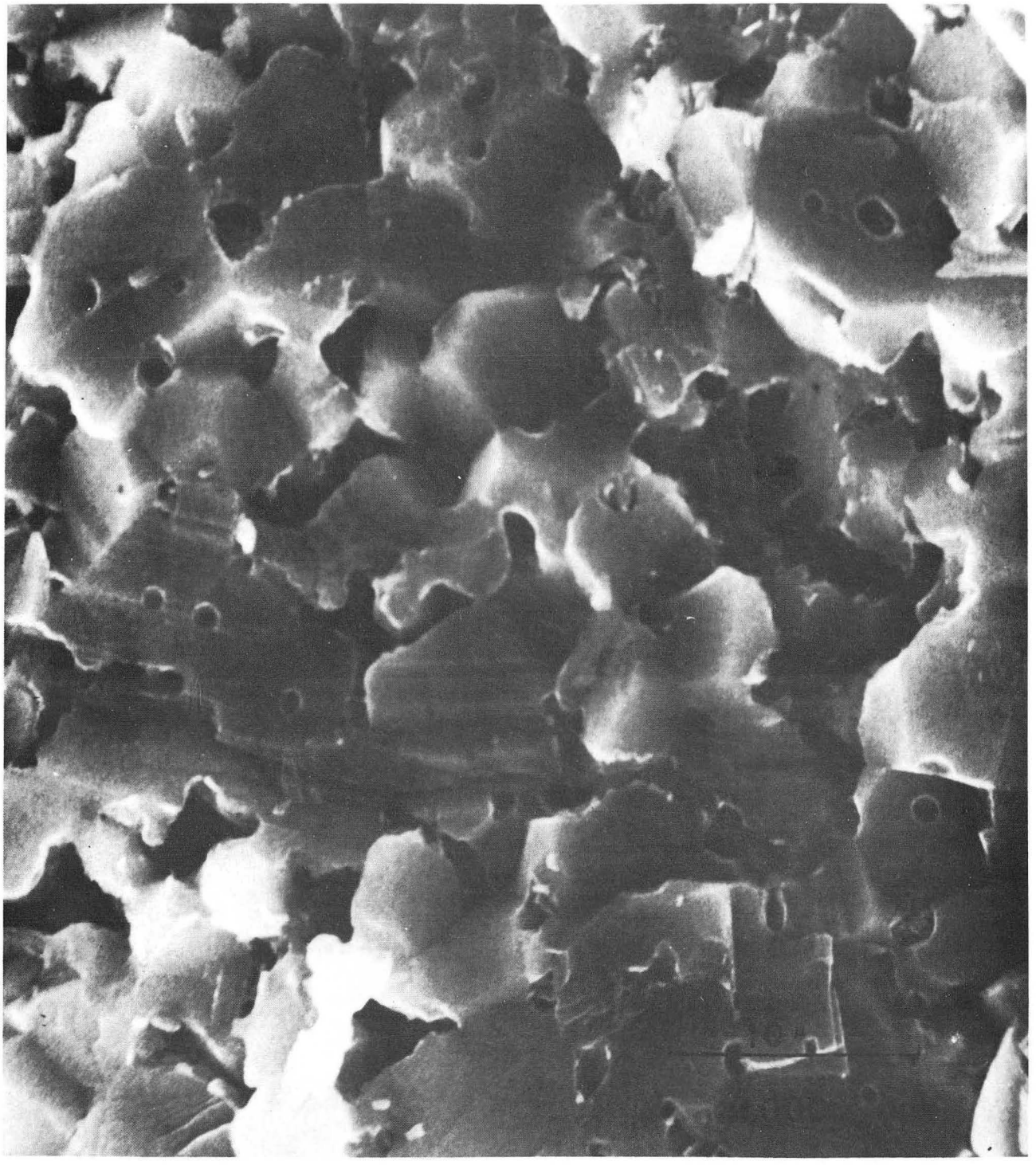

XBB 747-4567

Fig. 26. Fracture surface of MgO sintered at 1510°C for 700 min in flowing water vapor.

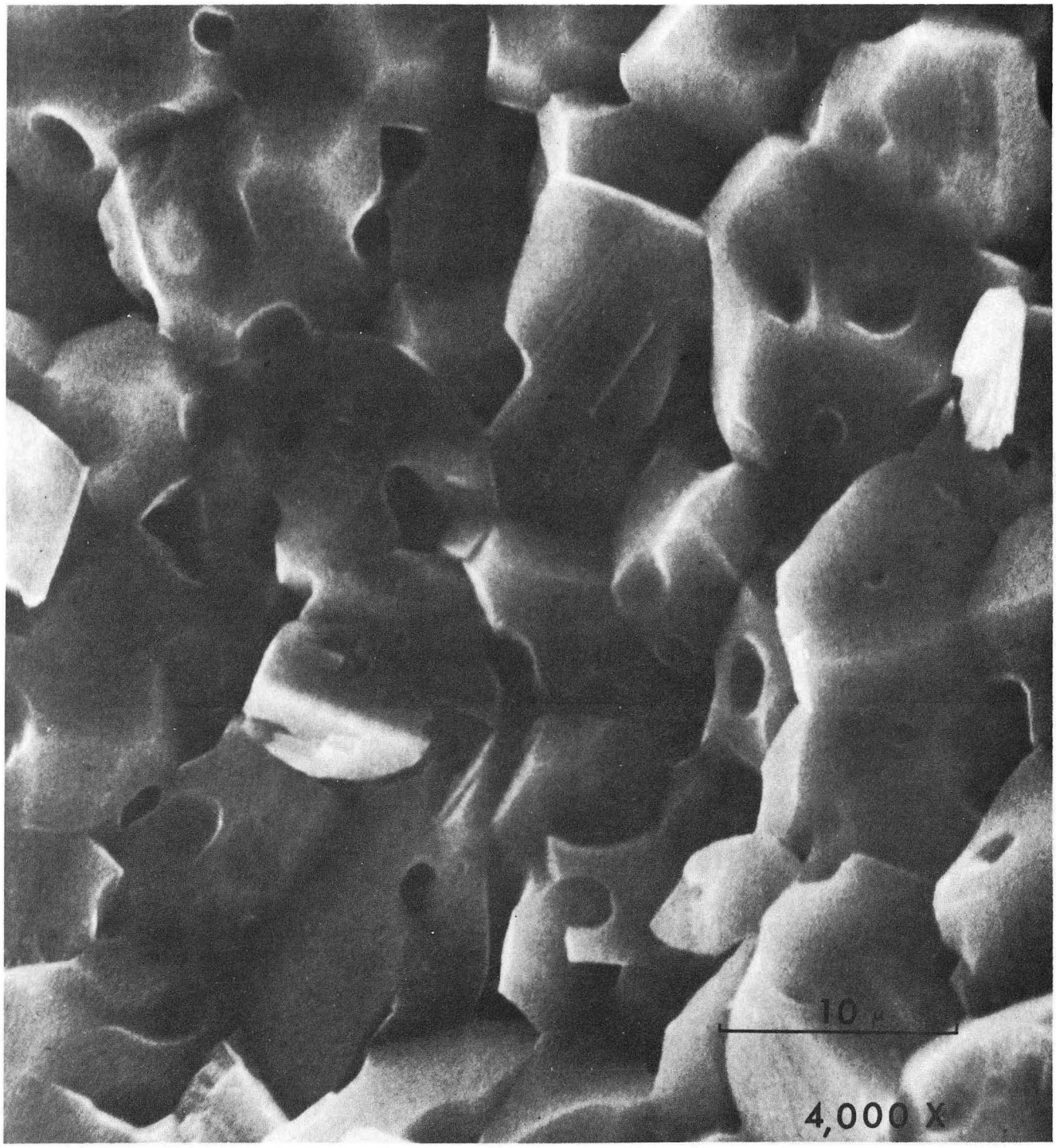

XBB 747-4564

Fig. 27. Fracture surface of MgO sintered at 1510°C for 1440 min in flowing water vapor.

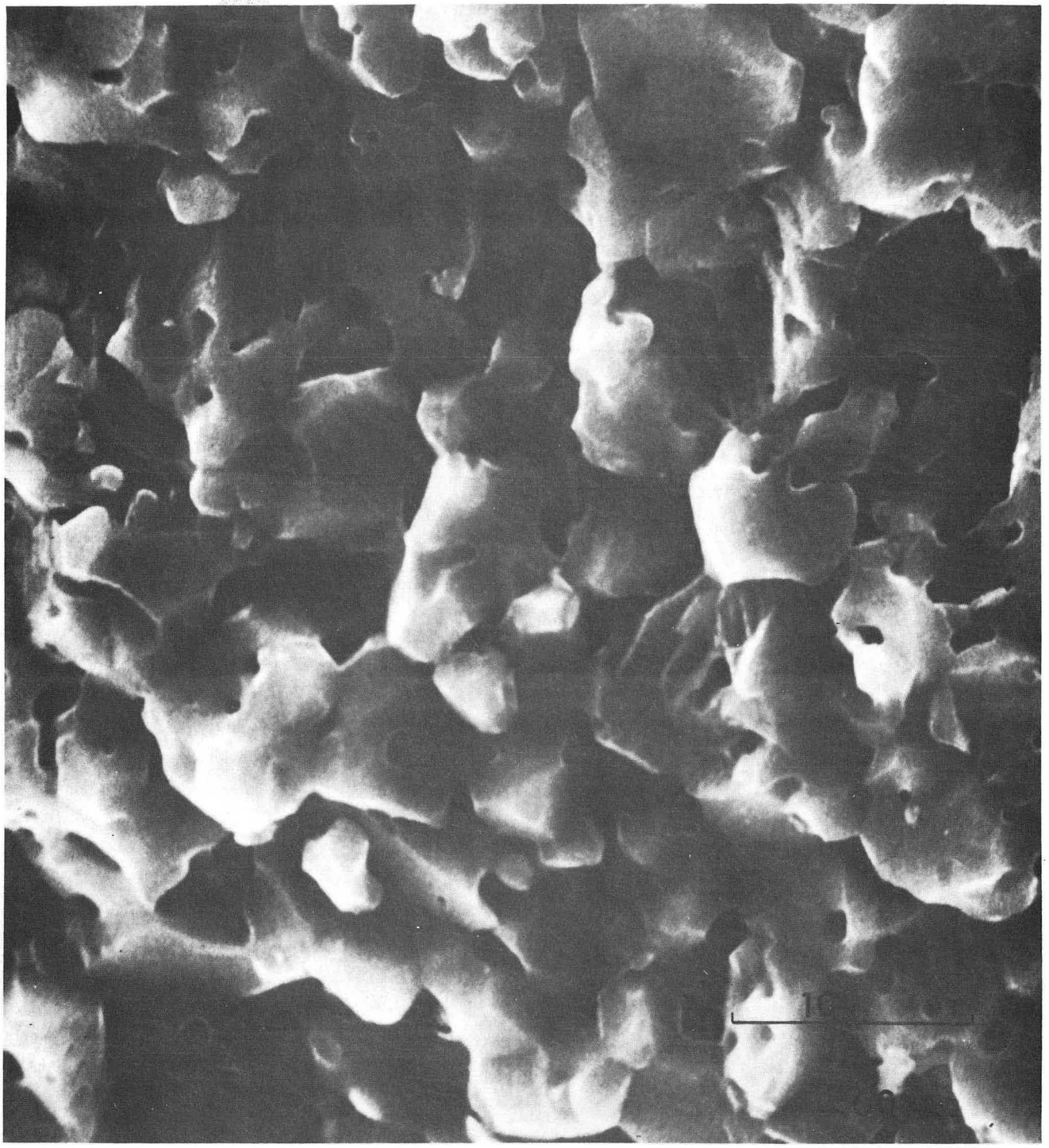

XBB 747-4565

Fig. 28. Fracture surface of MgO sintered at 1510°C for 1440 min in statis air.

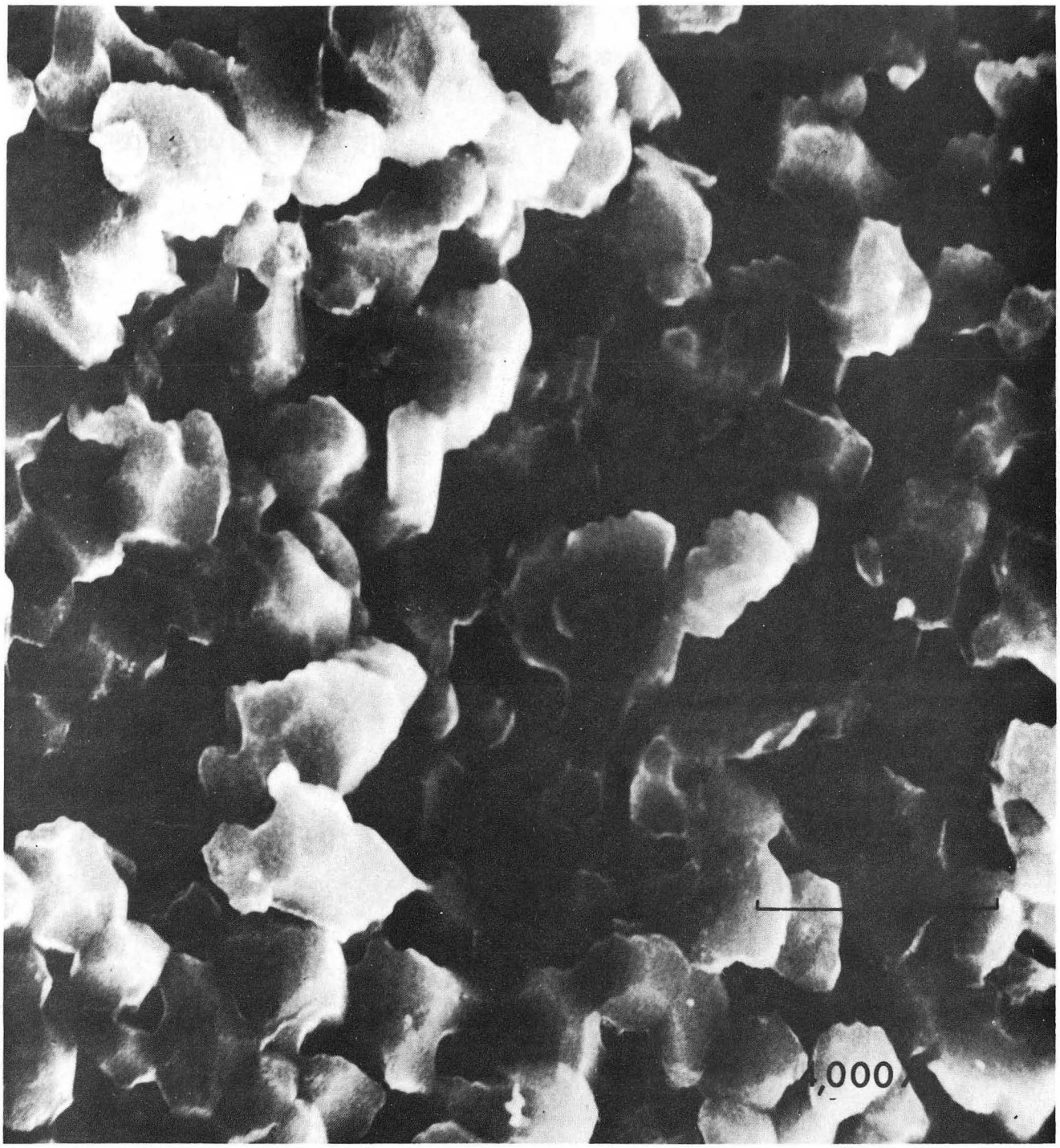

XBB 747-4563

Fig. 29. Fracture surface of MgO sintered at 1510°C for 1440 min in flowing compressed air.

pores are also visible on the cleavage planes which indicates that some of the pores are trapped within the grains and are not associated with grain boundaries; these pores may in some way be associated with non-homogeneity in the green compact. It is a well established experimental fact that as the volume fraction of inclusions or porosity decreases the mobility of grain boundaries increases.[13-15] Therefore, in comparing Figs. 26, 27, 28, and 29 it can be assumed that the larger grain size in Fig. 27 than in Figs. 28 and 29 is due to the faster initial densification rate of the compacts sintered in flowing water vapor as compared to flowing air or static air. This rapid densification during the first 50 minutes of sintering reduced the volume fraction of porosity which permitted a greater mobility of the grain boundaries and more rapid grain growth during the rest of the anneal.

2. Dihedral Angles

Table III gives the results for dihedral angle measurements of grain boundary grooves of hot pressed polycrystalline MgO in atmospheres of static air, flowing air, flowing water vapor, slowly flowing water vapor, and flowing water vapor followed by static air. Actual grain boundary grooves for each atmosphere are shown in Figs. 30-34, respectively, at a magnification of 20,000X. Static air atmospheres yielded the largest dihedral angle, 96°, while flowing water vapor resulted in the smallest value, 32°. Figure 35 shows a low magnification (2000X) of a surface of a hot pressed specimen of MgO which was annealed in static air. Figure 30 shows a high magnification (20000X) of a grain boundary groove of this specimen tilted relative to the axis of the contamination line (dark line) permitting measurement of the dihedral angle. Figure 31

Table III. Data for dihedral angle measurements of MgO annealed under five different atmospheric conditions

Experimental Conditions	Dihedral Angle	γ_{ss}/γ_{sv}	$\Delta\Phi$
Static Air	96°	1.33	0.0°
Flowing Air	56°	1.81	40°
Flowing Water Vapor	32°	1.92	64°
Slow Flowing Water Vapor	79°	1.53	16°
Flowing Water Vapor Followed by Static Air	96°	1.33	0.0°

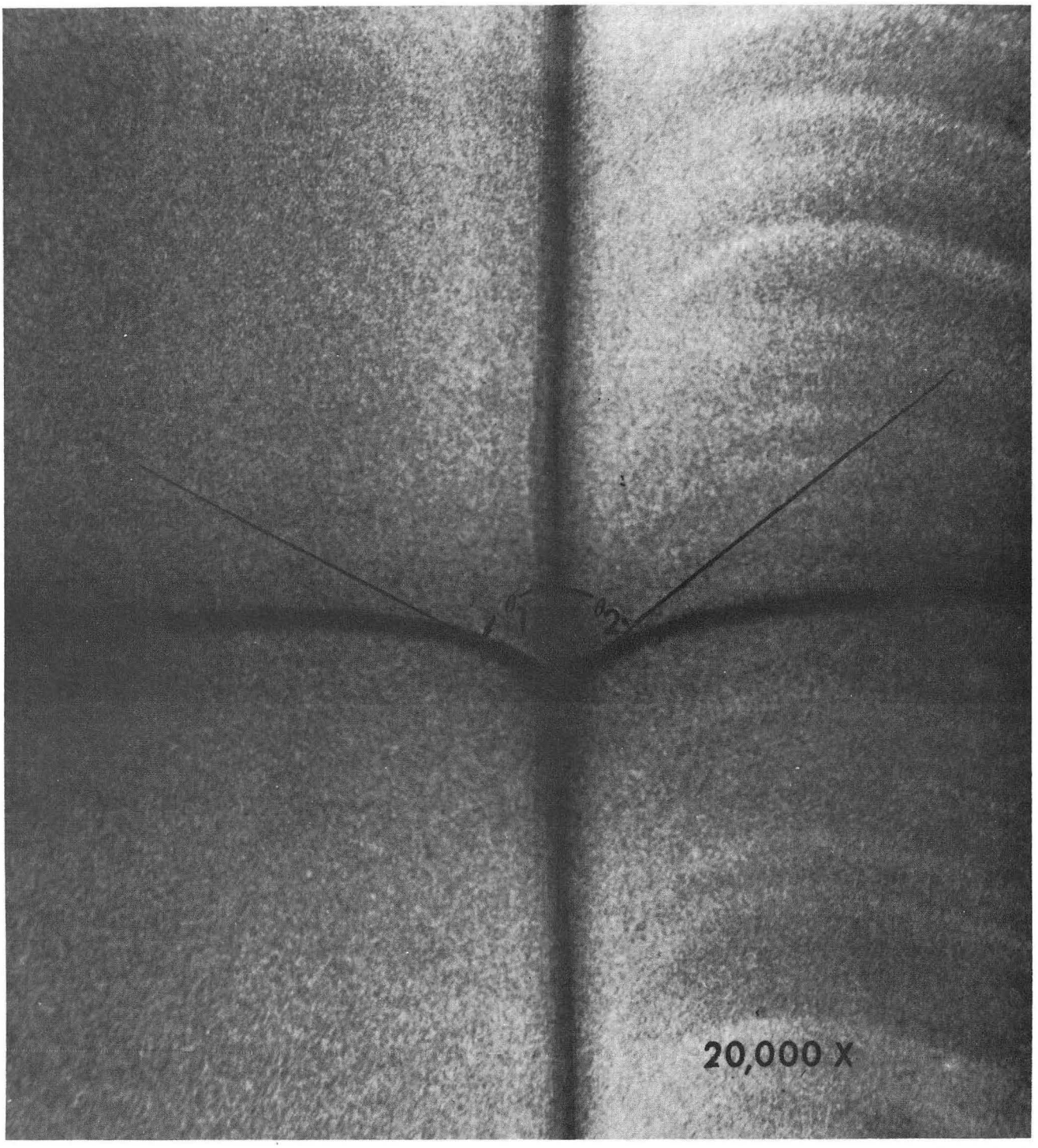

XBB 747-4558

Fig. 30. A grain boundary groove of an MgO specimen annealed at 1510 °C for 1440 min in static air. The grain boundary is tilted 47° relative to the axis of the electron beam of the SEM. The horizontal line is a contamination line of carbon which reveals the contour of the groove.

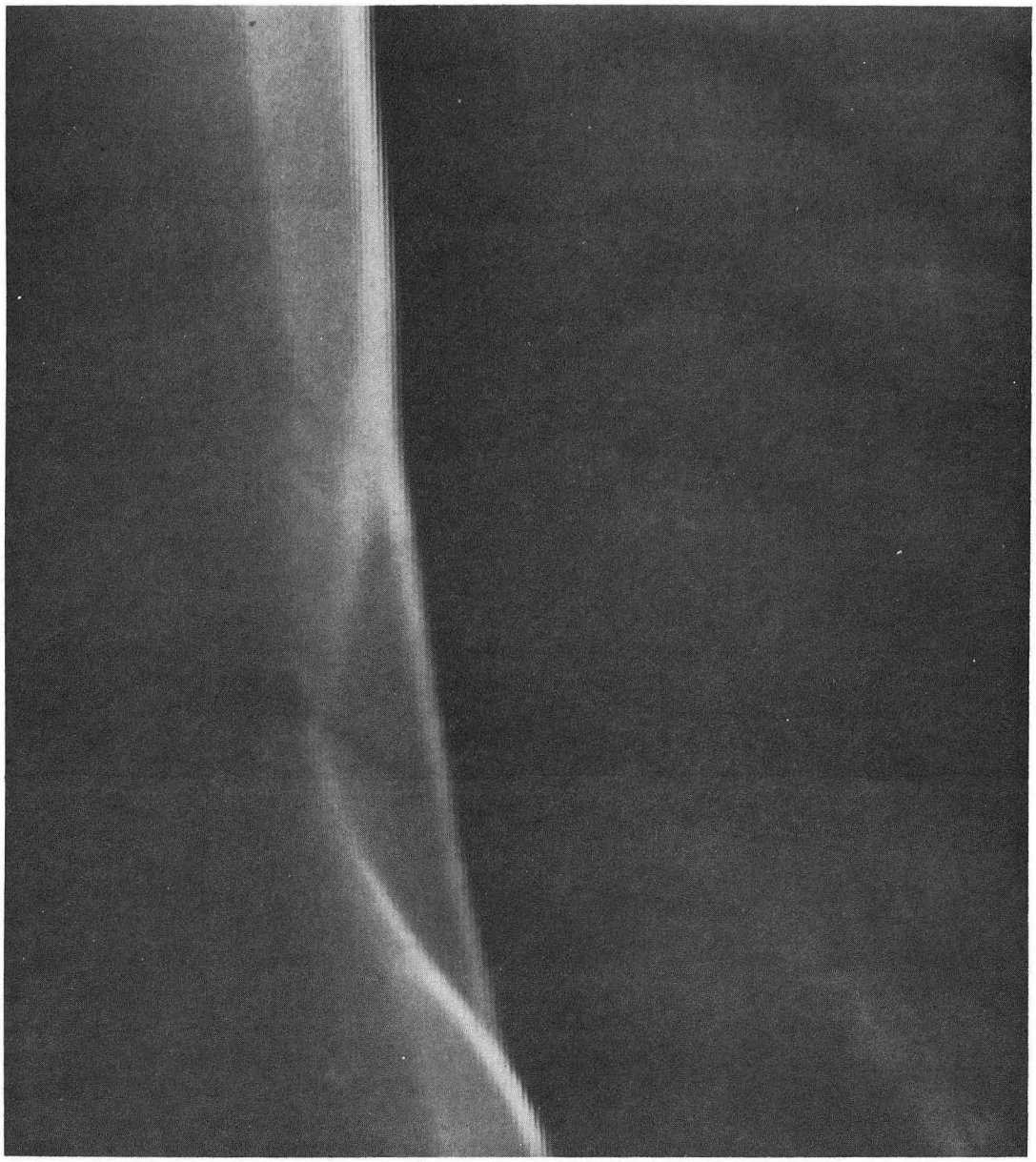

XBB 749-6236

Fig. 31. A grain boundary groove of an MgO specimen annealed at 1510°C for 1440 min in flowing compressed air. The grain boundary is tilted 47° relative to the axis of the electron beam of the SEM. The horizontal line is a contamination line of carbon which reveals the contour of the groove.

(20,000×)

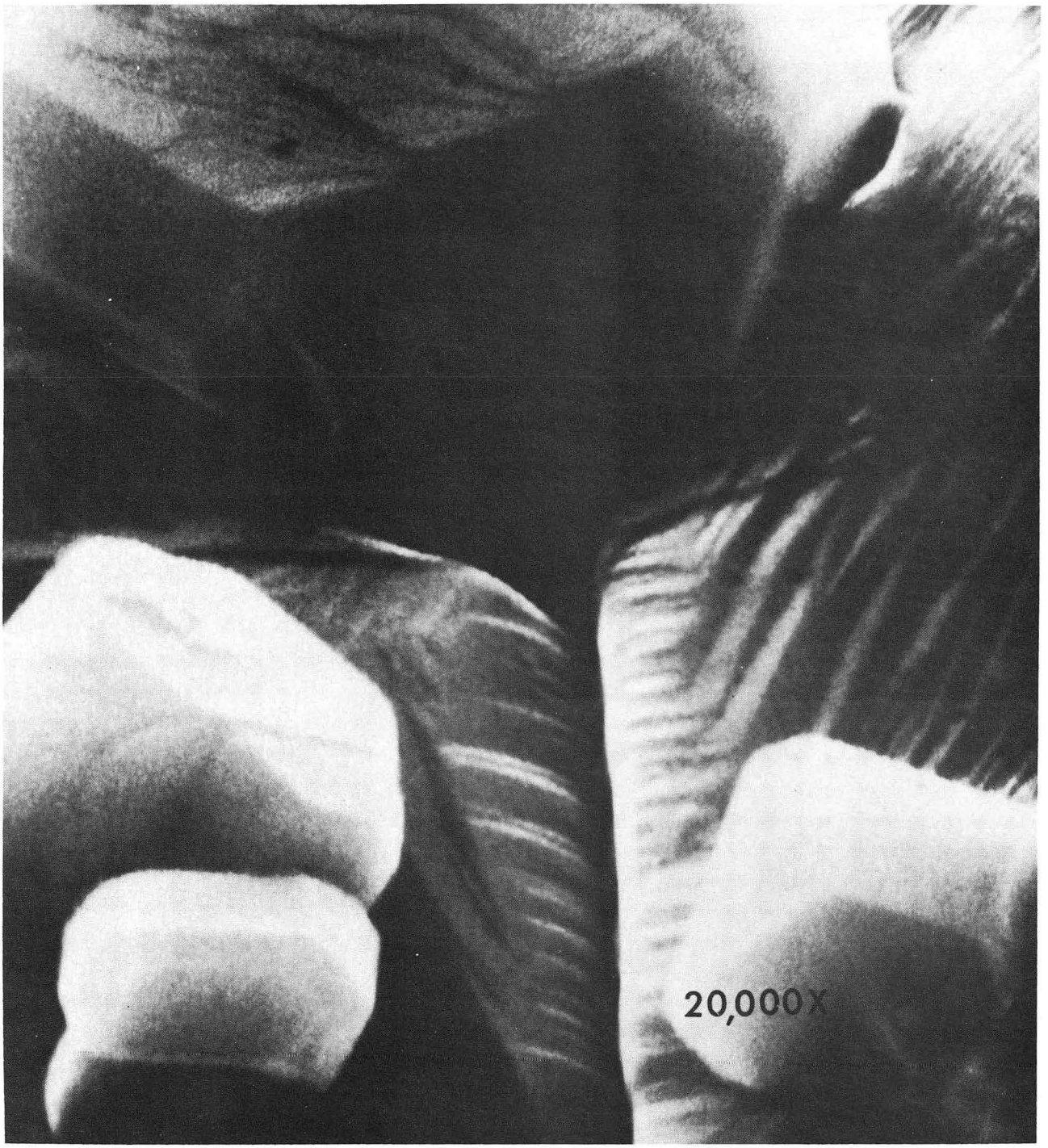

XBB 747-4559

Fig. 32. A grain boundary groove of an MgO specimen annealed at 1510°C for 1440 min in flowing water vapor. The grain boundary groove is tilted 47° relative to the axis of the electron beam of the SEM. The horizontal line is a contamination line of carbon which reveals the contour of the groove.

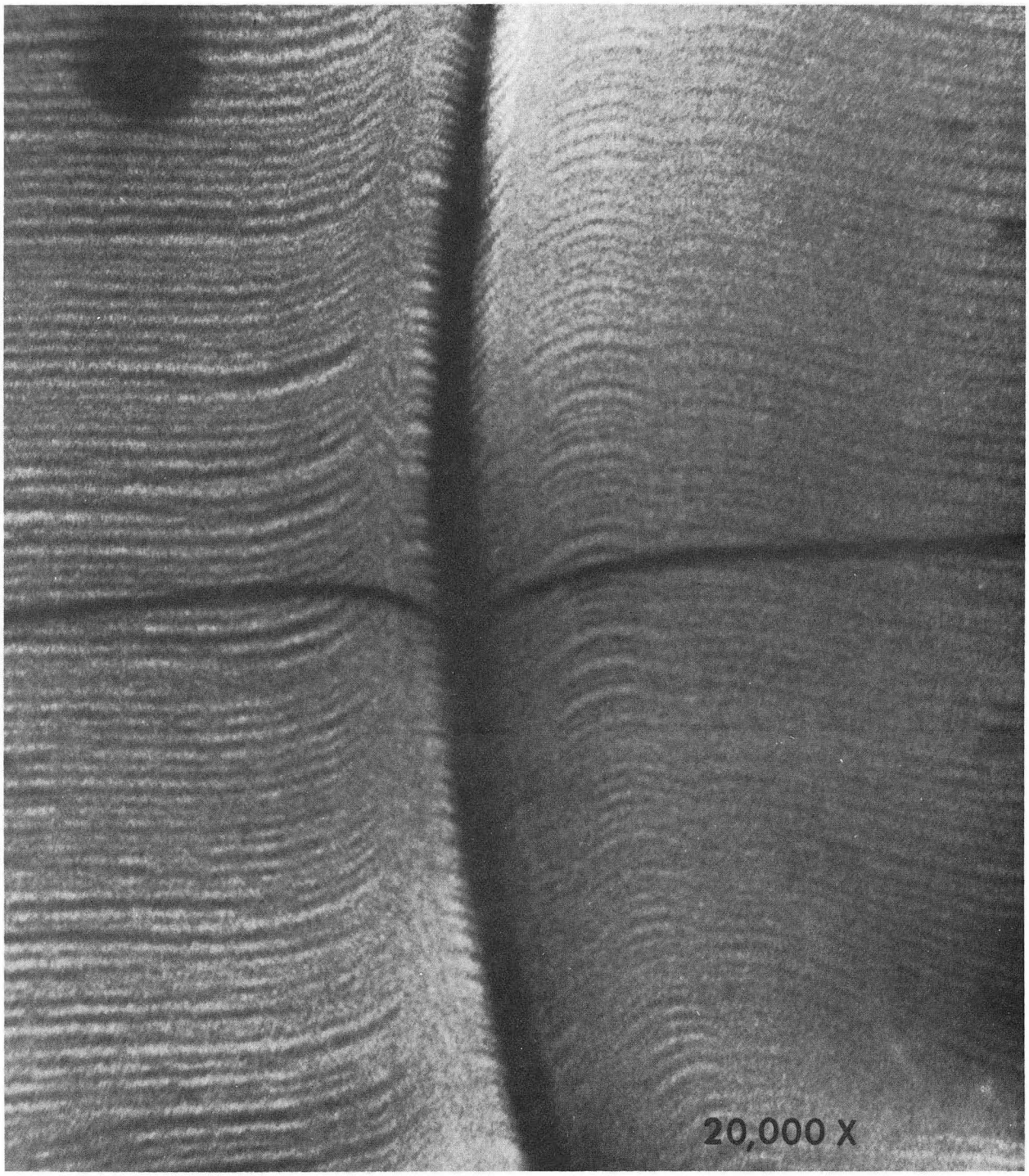

XBB 747-4557

Fig. 33. A grain boundary groove of an MgO specimen annealed at 1510°C for 1440 min in slowly flowing water vapor. The grain boundary is tilted 47° relative to the axis of the electron beam of the SEM. The horizontal line is a contamination line of carbon which reveals the contour of the groove.

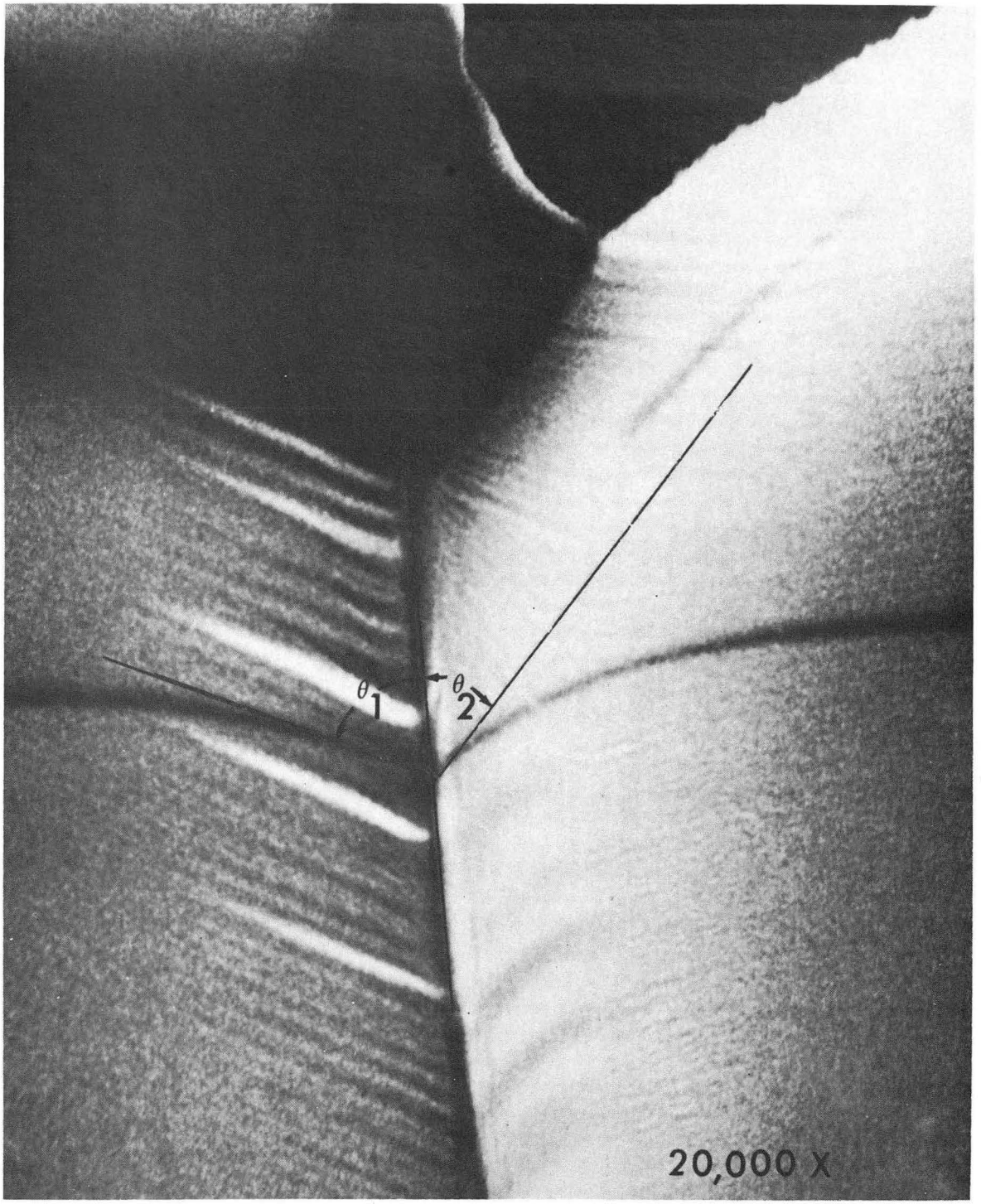

XBB 747-4556

Fig. 34. A grain boundary groove of an MgO specimen annealed at 1510°C for 700 min in flowing water vapor followed by an additional 700 min in static air. The grain boundary is tilted 47° relative to the axis of the electron beam of the SEM. The horizontal line is a comtamination line of carbon which reveals the contour of the groove.

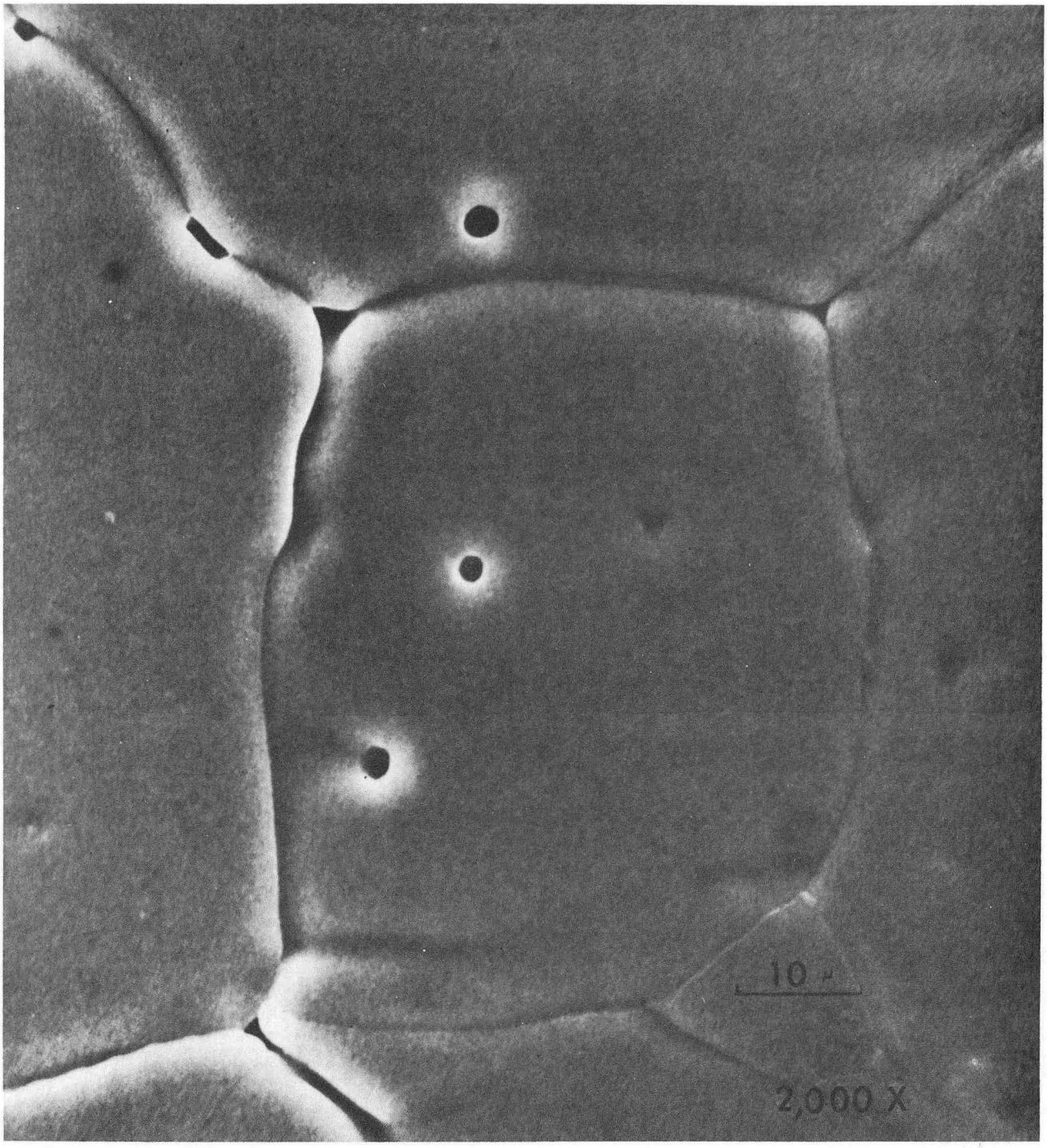

XBB 747-4568

Fig. 35. A low magnification of an MgO specimen annealed at 1510°C for 1440 min in static air. A high magnification of this specimen is shown in Fig. 30.

shows a grain boundary groove of a specimen which was annealed in flowing air. A low magnification of this surface looks similar to that of Fig. 35, but upon comparison of Figs. 30 and 31, one sees that the groove is deeper in the latter and therefore the dihedral angle is smaller (96° compared to 56°). Figure 36 shows the surface of a specimen annealed in flowing water vapor with angular precipitates on the surface which formed during the anneal. Figure 32 shows a grain boundary groove from this surface which is more irregular than grain boundary grooves of specimens sintered in other atmospheres, and has a much deeper groove angle than the other specimens (32°). Due to the precipitation on the surface of this specimen and the highly irregular grain boundaries, measurement of the dihedral angle was difficult and the value of 32° is reported with some uncertainty. However, on comparison of the three grain boundary grooves in Figs. 30, 31, and 32, it is evident that there is a definite and continuing decrease in the values of the dihedral angles.

The static air experiment in the absence of water vapor and flow would be expected to most closely approach equilibrium conditions, and exhibits the largest dihedral angle. The equilibrium dihedral angle for a system at the lowest energy state would be formed when a defect free planar grain boundary intersecting a surface, such as a bicrystal, is in equilibrium with its own vapor. Such a system is expected to have a larger dihedral angle than 96°.

The specimen sintered in flowing air, Fig. 31, which has a dihedral angle of 56° shows the effect of dynamic conditions on the dihedral angle which is 96° in static air. Since the groove root of a grain boundary

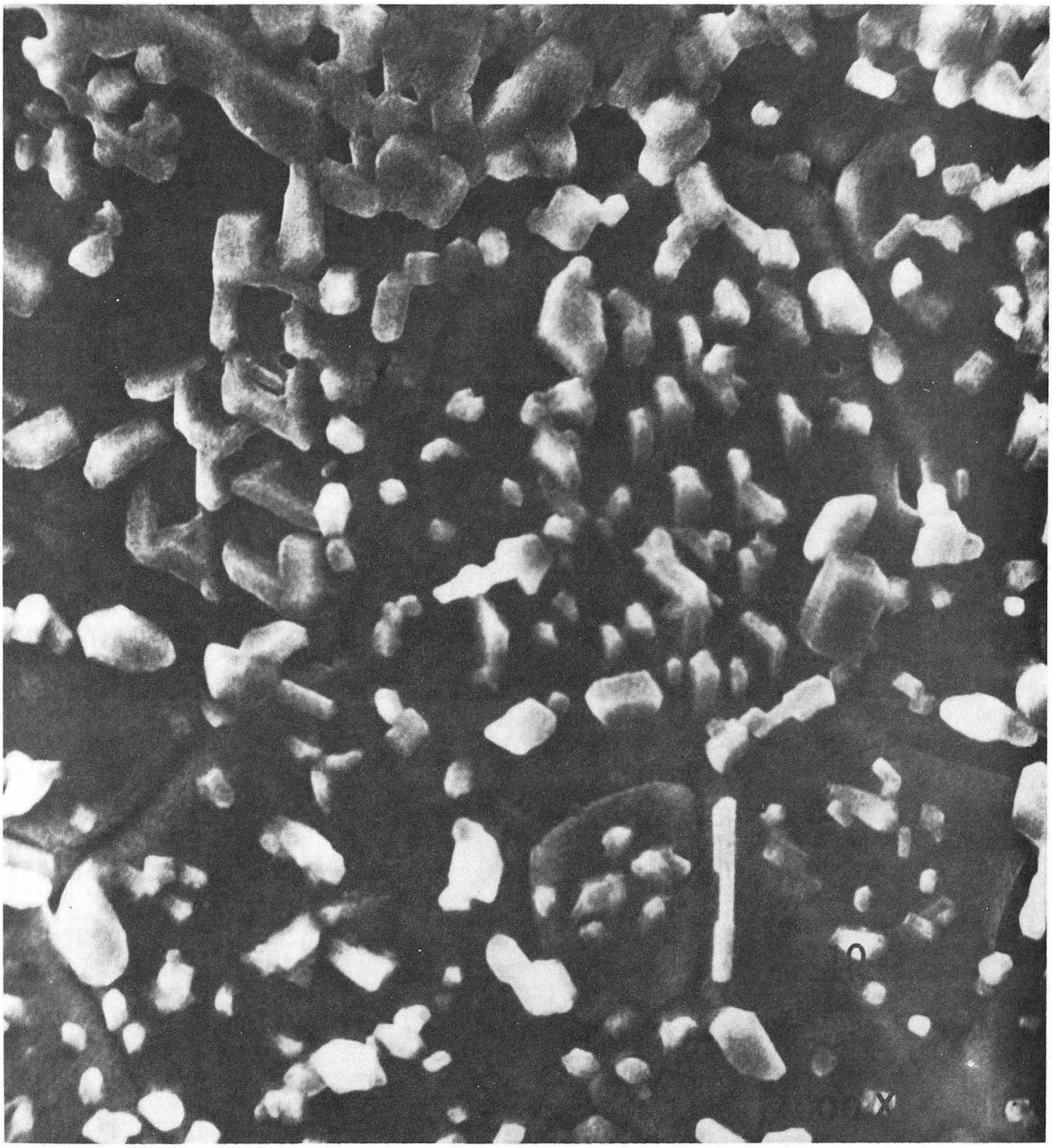

XBB 747-4562

Fig. 36. A low magnification of an MgO specimen annealed at 1510°C for 1440 min in flowing water vapor. A high magnification of this specimen is shown in Fig. 32.

intersecting a surface has a positive curvature and a stress concentration exists in the grain boundary at the root, there exists a higher vapor pressure above the groove root than above a planar surface. Under static conditions where the vapor phase is in equilibrium with the solid, an equilibrium dihedral angle is attained. However, under dynamic conditions, the vapor species above a specimen can be swept away, and in an attempt to restore the equilibrium vapor pressure for the system material will vaporize more from the higher energy curved surface at the groove root. If vaporization is rapid compared to other mass transport mechanisms which attempt to restore the equilibrium shape of the dihedral angle, a nonequilibrium or experimental dihedral angle which is smaller than the equilibrium angle will result. This decrease has been described previously as a "corrosion" effect. It is believed that this phenomenon occurs in flowing air and in flowing water vapor.

The measured dihedral angle for a specimen annealed in slowly flowing water vapor was 79° (Fig. 33). It is not known what effect water vapor may have on relative interfacial energies, but it has been reported that negligible water vapor exists on the surface of MgO at 1000°C.[24-26] In the presence of water vapor, however, a transient molecular adsorption or chemisorption of water vapor on MgO may occur with a reduction of γ_{sv}.[27] If the grain boundary energy is essentially unaffected, then the dihedral angle is reduced over that in static air as observed. A more likely explanation is that under flowing conditions a molecular layer of adsorbed hydroxide does not form, but a vapor complex of H_2O and MgO can form which has a higher vapor pressure than MgO gas.[22] This condition would then result in a corrosion effect and a smaller nonequilibrium

dihedral angle on the basis of a γ_{sv} that remains the same as that for the static air value, as described previously for flowing air. The larger angle was due to the slower flow rate of the atmosphere containing H_2O.

Figure 32 shows a groove formation for the flowing water vapor experiment, the grain boundary groove being deeper or more corroded with a dihedral angle of 32°. The "corrosion" effect is more severe in this case because of the higher flow rate. This behavior is indicated by the formation of MgO precipitates on the previously smooth surface, Fig. 36.

Another experiment was performed to determine the effect on the dihedral angle if nonequilibrium conditions were introduced and then essentially removed. Figure 34 shows the grain boundary groove of a specimen that was annealed for the first 700 minutes in flowing water vapor and then for an additional 700 minutes in static air. The measured dihedral angle for this specimen was 96° which is identical to the static air value. Therefore, the dihedral angle which is 32° under nonequilibrium conditions of flowing water vapor, increased towards its equilibrium value of 96° when static conditions were substituted. The presence of flowing gases with or without water vapor thus causes a smaller nonequilibrium or dynamic dihedral angle to form in comparison with static air conditions.

3. Correlation of Densification with Driving Forces for Sintering

The purpose of the experimental work was to correlate endpoint density and relative rates of densification with the thermodynamic driving force for sintering. At any instance during sintering, if the experimental or dynamic dihedral angle is less than the equilibrium value,

there is a thermodynamic driving force for continued mass transport and sintering. The further the experimental dihedral angle is from the equilibrium value, the more negative is the differential free energy in going from the nonequilibrium to the equilibrium configuration and the greater is the thermodynamic driving force for densification, $\Delta\Phi$. Thus, although the absolute values of the dihedral angles are not directly useful for correlation with compact densities, the differences between the dynamic values and the equilibrium values of the dihedral angles are a valid measure of the thermodynamic driving force for sintering. The value of Φ measured in static air was used as the equilibrium dihedral angle. Table II gives the differences, $\Delta\Phi$, between the dihedral angles in static air and other atmospheres. Figure 37 is a plot density versus these values of $\Delta\Phi$ at three different times. The larger is the value of $\Delta\Phi$, the greater is the density at any constant time. As the time and densities increase, the curves flatten out and the effect of the dynamic dihedral angle on density becomes reduced. It is felt that similar inhomogeneous density distributions in all of the green compacts were responsible for large voids and some enclosed pores in grains to form as sintering proceeded. Therefore, the final densities of about 3.3 g/cc of the sintered specimens were determined by such voids as well as by the relatively low equilibrium Φ measured in static air.

The results of this experimental work show that normal dynamic conditions modified by atmospheric conditions enhance densification rates by increasing the difference between the static and dynamic dihedral angles. The model for the thermodynamics of solid phase sintering predicts that the thermodynamic driving force for sintering is greatest the

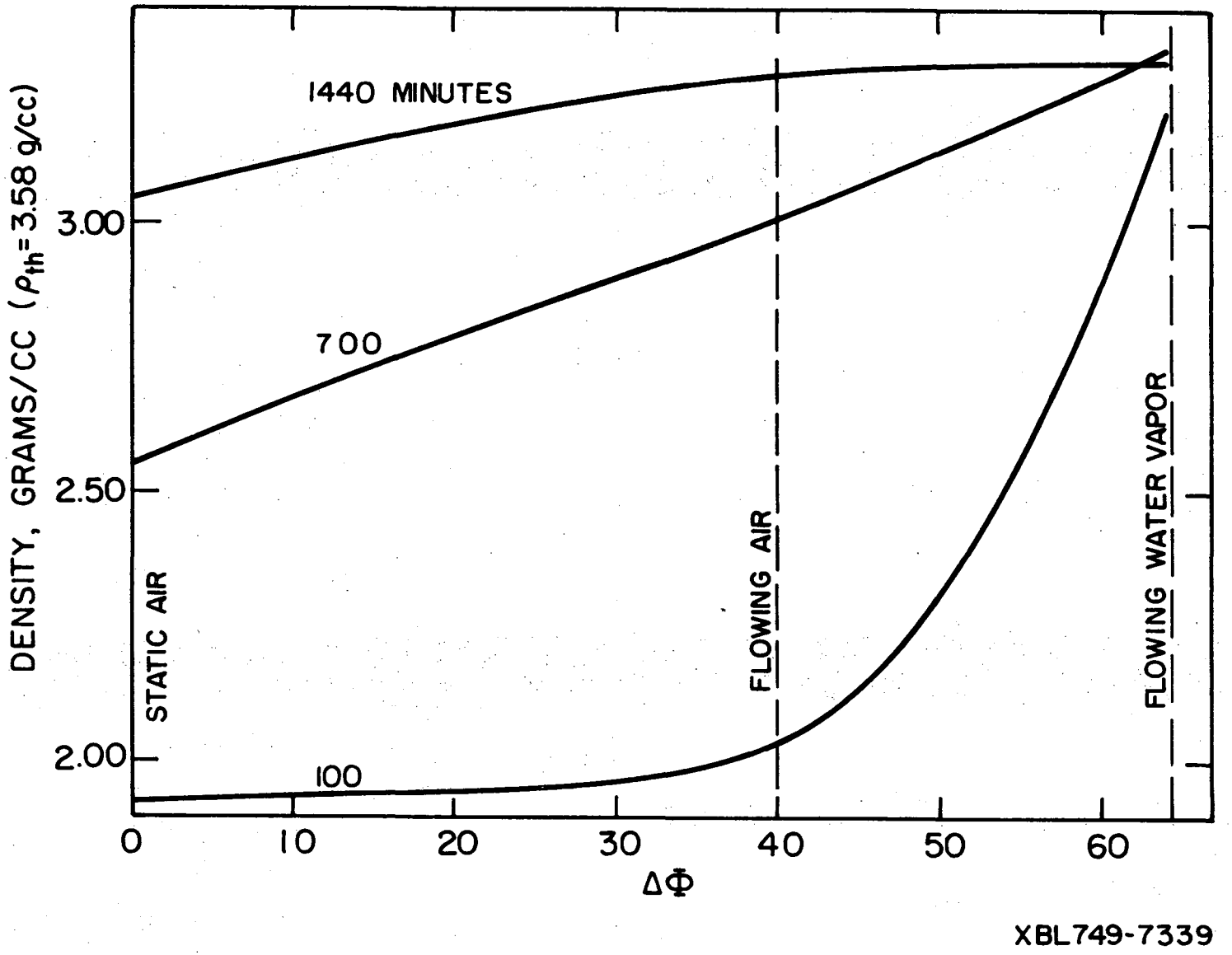

Figure 37. Density versus the difference between the static and the dynamic dihedral angle, $\Delta\Phi$, for sintering of MgO at 1510°C in three different atmospheres. $\Delta\Phi$ is the thermodynamic driving force for densification.

further the value of the dynamic dihedral angle is from the equilibrium value assuming that it is retained during the initial stage of sintering. It is felt that a large value of $\Delta\Phi$ was maintained during the first 100 minutes of sintering in flowing water vapor during which time most of the densification occurred. The results of the experimental work performed here indicate that the dependence of the value of $\Delta\Phi$ on atmospheric conditions can be quite large, (64° for flowing water vapor). The growth of grains and pores with essentially no increase in density during the sintering of compacts in H_2O vapor beyond 100 minutes of sintering suggests that Φ_{dyn} increased as closed porosity developed and the corrosion effect of a flowing ambient atmosphere was eliminated. Φ_{dyn} thus approached Φ_{eq} (probably due to neck formation in closed pores), and therefore, the thermodynamic driving force for densification was reduced.

For MgO compacts used in this study, the maximum measured value of Φ was 96°. Although the particle packing was inhomogeneous, the total or average green density approached that of simple cubic packing which has a value of Φ_{crit} of 90° when second nearest neighbors touch and of 109° for complete densification. Therefore, no thermodynamic barrier exists for densification to the point where second nearest neighbors touch, but there may be one for complete densification resulting in an endpoint density. The 93% theoretical density realized in this study could be partially due to this factor and to the inhomogeneity of the compacts.

The slow densification rate for the sintering experiments in static air suggests that "necks" formed at particle-particle contacts resulting

in equilibrium dihedral angles. The driving force then is due to a reduction of Φ occurring because of mass transport due to reverse curvatures in the surfaces of the particles attempting to reach a minimum energy configuration. Under these conditions, $\Delta\Phi$ remains small. In flowing air the corrosion effect tends to increase $\Delta\Phi$, above the value for static air, and thus, the sintering rates.

IV. SUMMARY AND CONCLUSIONS

A. Theoretical Considerations

The thermodynamic analysis of solid state sintering indicates that a decrease in the γ_{ss}/γ_{sv} ratio and an increase in the density of the unfired compact favor densification. When second nearest neighbor spheres form contacts, or a crystallographic face in the unit cell has densified, however, nonuniform redistribution of material must occur in order to achieve complete densification for DC, SC, and FCC models. BCC packing arrays sinter uniformly to theoretical density. The effect of nonuniform sintering is to reduce the critical value for γ_{ss}/γ_{sv}. In order to achieve complete densification, the critical ratio must be less than 1.625 for BCC packing of uniform spherical particles, 1.161 for SC and FCC, and 1.074 for DC: correspondingly, the dihedral angle has to be greater than 71.5°, 109°, and 115°, respectively. Therefore, any additives that would tend to reduce γ_{ss} relative to γ_{sv} would enhance sintering, or make sintering possible if the γ_{ss}/γ_{sv} ratio for a given material is above the critical value.

Additionally, the thermodynamic driving force for sintering, $\Delta\Phi$, is given by

$$\Delta\Phi = \Phi_{eq} - \Phi_{dyn} \tag{80}$$

where Φ_{eq} is the equilibrium dihedral angle and Φ_{dyn} is the experimental or dynamic dihedral angle. Φ_{dyn} is determined by three parameters: corrosion, chemical effects, and geometry; and is mathematically always less than or equal to Φ_{eq}.

During the initial stages of sintering, Φ_{dyn} can be affected by all three parameters but upon formation of closed porosity in a sintering specimen, the corrosion effect is generally eliminated and only chemical effects and geometry contribute to Φ_{dyn}. Therefore, Φ_{dyn} will increase and approach Φ_{eq} as pore closure occurs, thus reducing the magnitude of $\Delta\Phi$. Since $\Delta\Phi$ is a measure of the thermodynamic driving force for sintering, as $\Delta\Phi$ is reduced, so is the sintering rate.

A pore on a planar grain boundary effectively pins the boundary for all values of the γ_{ss}/γ_{sv} ratio and thus the dihedral angle. A curved grain boundary, however, can move away from a pore if the curvature is above the critical value. As the dihedral angle increases above about 73°, although the magnitude of the driving force decreases, movement in all cases will occur toward the center of curvature at curvatures above about 36°; as the dihedral angle decreases from 73° to about 16°, the critical curvature value decreases to about 26°. Grain boundaries with lesser curvature tend to be pinned by pores. Additives which reduce the γ_{ss}/γ_{sv} ratio beyond that necessary for dense sintering, therefore, have essentially no effect on the pinning of a grain boundary by a pore.

It thus is evident that the most critical factor in the pinning of grain boundaries by pores is the degree of curvature of the boundaries and not the magnitude of the dihedral angle. Factors that lead to curvature should be controlled. A uniform packing of spheres of a given size should densify to a microstructure with uniform grain size with planar grain boundaries. Compacts with a range of particle sizes, however, will tend to form curved grain boundaries. If this curvature is above about 36°, the boundaries will be able to move away from pores.

Narrow particle size ranges will tend to form relatively longer grain boundaries which will tend to flatten and thus develop smaller curvatures.

Another factor that has not been discussed or analyzed is the effect of anisotropy of interfacial energies. Irregular movement of grain boundaries and different angles at three grain junctions due to anisotropy could lead to boundary curvatures that would allow them to break away from pores. Additives in this case could be beneficial if their effect would be to reduce any existing anisotropy.

All of the discussions have been based on a uniform and homogeneous distribution of particles. Poor processing that would introduce varying packing densities or introduce agglomerates of higher or lower density than the matrix would result in a range of grain sizes in the early stages of sintering as well as introduce other factors that would interfere with realizing theoretical density in the entire compact. An additive in this case could have a beneficial effect if it played some role in reducing agglomeration or increasing uniformity of particle distribution during the preparation of the compacts.

B. Experimental Considerations

Sintering studies of MgO compacts annealed in three different atmospheres at 1510°C reveal that the fastest sintering rate occurs in flowing water vapor. The slowest sintering rate is observed in static air and an intermediate rate is observed in flowing air. All specimens yield approximately the same endpoint density of 93% of theoretical although they attain this density at different sintering rates.

Corresponding dihedral angle measurements indicate that the smallest value (32°) occurs in flowing water vapor; the largest value is observed in static air (96°); and an intermediate value (56°) is observed in flowing air. Taking the static air value as Φ_{eq}, $\Delta\Phi$ was calculated for each case. Results indicate that the larger is the magnitude of $\Delta\Phi$ the greater is the densification rate, a conclusion, which is in agreement with theoretical considerations. It is believed that in flowing water vapor atmospheres corrosive effects lead to a small dynamic dihedral angle ($\Delta\Phi = 64°$) with essentially no neck formation between particles. In static air, ($\Delta\Phi = 0$), no corrosive effects occur; a bridging neck probably forms between particles and the sintering rates are reduced.

It is not known whether the 93° of theoretical density which was attained is a true endpoint density or is due to inhomogeneities inherent in the cold pressed compacts. The thermodynamic model for simple cubic packing arrays predicts that sintering should proceed uniformly to the point where second nearest neighbors touch ($\Phi = 90°$). Since the static air value of Φ (96°) is greater than $\Phi_{critical}$ (90°), sintering should proceed up to this point. The critical value of Φ for complete densification is 109°. Therefore, if 96° is the true equilibrium dihedral angle for MgO at the temperature of experimentation, then the endpoint densities observed here are not due to inhomogeneities but rather are characteristic endpoints for simple cubic packing of MgO particles.

PART B: THERMODYNAMICS AND KINETICS OF LIQUID PHASE SINTERING

I. INTRODUCTION

Many of the sintering characteristics of a multiphase system are similar to those of a single phase system; however, formation of intermediate phases or solid solutions complicates kinetic and thermodynamic analyses. Generally, two phases have dissimilar melting points and show a eutectic reaction. If sintering of a multiphase compact occurs below the temperature at which a liquid phase appears, solid phase sintering mechanisms are operative. However, if the sintering temperature is raised above this point, sintering proceeds by liquid phase sintering mechanisms.[28-35] Intermediate cases can result at the sintering temperature such as: solid phases reacting to form a liquid, solid and liquid phases reacting to form an intermediate solid phase, and solid solution formation from solid and liquid phases.

Experimental investigation of liquid phase sintering has led to a general classification of sintering kinetics into three separate stages; viscous flow, rearrangement of solution-precipitation, and coalescence.[30,33] A sintering compact may undergo one, two, or all three stages depending on the physical and environmental parameters of the system. Each of these stages will be discussed below in terms of idealized models based on thermodynamic and kinetic considerations.

A. Rearrangement

The formation of a liquid at sintering temperature in a two or more phase powder compact, causes the creation of liquid-vapor interfaces. These interfaces, which are usually curved in shape, give rise to capillary forces within the powder compact. If the liquid wets the solid,

i.e., the contact angle is less than 90°, the resulting forces in turn in the initial stages of sintering can cause relative motion of solid particles and corresponding flow of liquid. The rearrangement continues until the compact attains a configuration corresponding to a minimum packing volume. The interfacial free energy decrease caused by this process has been equated to the energy of viscous flow by Frenkel.[28] For pure viscous flow, e.g., glass spheres,

$$\Delta L/L_0 \propto t^{(3/2)} \tag{1}$$

where $\Delta L/L_0$ is the densification parameter, and t is the time. When this equation is applied to liquid phase sintering of multiphase powder compacts, experimental results indicate that

$$\Delta L/L_0 \propto t^{(1+y)} \tag{2}$$

where (1+y) is greater than unity.[33]

The exponent (1+y) varies from compact to compact depending on the environmental and physical parameters of the system. Flow rates tend to increase as pore size decreases, while particle-particle interactions cause frictional effects which in turn reduce flow rates. The volume fraction of liquid phase, wetting angle, dihedral angle and particle shape determine the configuration of the solid and liquid in the compact, the capillary forces acting on the system, and in turn the exponent of time in Eq. (2).

If sufficient liquid is present, viscous flow alone can cause complete densification or zero porosity of a particulate system. With normal compact green densities, between 35 and 40% by volume of liquid phase, (volume of liquid divided by the volume of solid plus liquid), is required to attain theoretical density.[33] If less liquid is present, flow continues until a configuration of minimum liquid-vapor interfacial area and a corresponding minimum of free energy is achieved.

The dihedral angle formed between the solid and liquid phase is very important in determining the extent of viscous flow in powder compacts. The solid-solid interfacial energy and the solid-liquid interfacial energy are related through the dihedral angle equation[31]

$$\gamma_{ss}/\gamma_{s\ell} = 2 \cos \phi/2 \qquad (3)$$

where γ_{ss} is the solid-solid interfacial energy, $\gamma_{s\ell}$ is the solid-liquid interfacial energy, and ϕ is the dihedral angle measured in the liquid. Systems with zero dihedral angles have complete penetration of the solid by the liquid, and thus no solid-solid contacts.[31] On the other hand, in systems forming finite equilibrium dihedral angles, the liquid does not separate of flow between solid-solid contacts.

Therefore, viscous flow is enhanced by a zero dihedral angle, and retarded by a finite dihedral angle. Compacts that contain small amounts of liquid phase which form finite dihedral angles and whose phases have a small difference in melting points, can sinter sufficiently to form rigid solid skeletons before the liquid appears. Under such conditions the liquid will not cause any particle flow but rather will form bridges

around the contacts between particles.

As a result, two extreme cases are possible: one is viscous flow leading to complete densification (zero dihedral angle and large liquid volumes), and the other is the creation of a solid skeleton before the liquid forms resulting in no viscous flow at all (nonzero dihedral angle, similar melting points, and small volumes of liquid phase). The rearrangement or viscous flow stage thus does not necessarily lead to significant shrinkages.

B. Solution-Precipitation

When the rearrangement stage is completed and residual porosity remains, densification must proceed by another mechanism. Therefore, a different model is necessary. The earliest investigations proposed a mechanism based on solubility differences between small and large particles in liquids, called the heavy alloy theory.[37] This theory was based on the concept that particles of small radii were dissolving in the liquid and larger particles were growing at their expense. The basis for this argument is that a higher solubility exists over a surface with a small radius of curvature than over one with a large radius of curvature.[38-41] In order for the mechanism to be operative, the formulators of the heavy alloy theory stipulated that: (1) there must be an appreciable difference in melting point between the high and low melting phases, (2) the high melting phase should be soluble in the low melting phase, and (3) the low melting phase should be insoluble or only slightly soluble in the high melting phase. The theory makes no stipulations concerning the magnitude of dihedral angles or the volume fraction of liquid phase. However, it is apparent that for the mechanism to

be operative, sufficient liquid must be present to form a continuous liquid film in the compact in order to allow a diffusion path for material. Additionally, the dihedral angle must be equal to zero, since if the dihedral angle were finite, solid-solid contacts and a framework would form. These contacts would restrict the shape of the curvature of the solid-liquid interface. Small particles would lose material from their surfaces and large particles would gain material, but particle centers would not move together. Therefore, no densification could occur. This process is analogous to vaporization-condendsation and surface diffusion in solid-vapor systems. However, if the dihedral angle is zero, particles can completely dissolve and the redistribution of material may occur.

The heavy alloy theory was criticized by Kingery[33] on the basis that large volumes of liquid were necessary for the above mechanism to be feasible, yet experimental results indicated that densification was often achieved with extremely small amounts of liquid phase. He proposed an alternate mechanism based on the fact that if the partial molar volume of a solid dissolving in a liquid is positive, then the solubility of that component is increased by pressure. He argued that compressive stresses were created between particles by capillary forces arising from liquid bridges connecting the particles. Therefore, a higher solubility of the solid would exist in the region between the particles where capillary forces cause compressive stresses than at surfaces away from the stressed region. Thus, material would dissolve between the particles, diffuse through the liquid under a concentration gradient, and precipitate at surfaces of lower solubility. Particle centers would

move together and densification would occur.

In order for this mechanism to be operative, there must be some solubility of the solid in the liquid, and a film of liquid between the particles, i.e., a zero dihedral angle. No stipulation was made by Kingery concerning the volume of liquid necessary, although it is evident that the mechanism may proceed at low or high liquid contents providng that some porosity is present. Kingery derived a kinetic relationship for spherical particles

$$\Delta L/L_0 = KR^{(-4/3)}\ t^{(1/3)} \qquad (4)$$

where $\Delta L/L_0$ is the densification parameter, K is a constant for the particular system, R is the initial particle radius, and t is the time.

No directly comparable kinetic equations are available for models based on the heavy alloy theory, although Greenwood[29] did investigate the growth of coarse particles and the dissolution of fine particles in solvent liquids. He derived the following equation for the growth of large particles,

$$a_f^3 - a_i^3 = \frac{6DM\,\gamma_{s\ell}\,t}{NkTR^2} \qquad (5)$$

where a_f is the final particle size, a_i is the original particle size, D is the diffusivity in the liquid, M is the molecular weight, $\gamma_{s\ell}$ is the solid-liquid interfacial energy, Nk is the gas constant, R is the radius of curvature of the particle, and t is the time.

Neglecting the initial particle size, the growth rate is proportional to the 1/3rd power of time. The above equation is not specifically valid for liquid phase sintering since it assumes that the particles are widely dispersed in the liquid, under which conditions no porosity could exist. The time dependency, however, is identical to that derived by Kingery.[33]

C. Coalescence

Kingery recognized that a liquid film is now always present between solid particles, i.e., a finite solid-liquid dihedral angle forms. He argued that orientation effects can cause certain grains to form solid-solid contacts.[33] Therefore, these grains could not sinter by solution-precipitation. In a sintering compact such grains would sinter by solid state diffusion mechanisms, obeying solid phase sintering kinetics.[32,42-47] He called this stage of liquid phase sintering coalescence and implied that it would follow the solution-precipitation stage, i.e., that in a sintering compact, the dihedral angle would increase from zero to a finite value with time.

Consider a solid-liquid-vapor system which forms a nonzero dihedral angle which is independent of time. The liquid exists as bridges between the solid particles, and the vapor phase is above the liquid phase. A situation analogous to vaporization-condensation occurs except that material transport is through the liquid phase instead of through the vapor. Material is deposited in the neck region forming a curved interface as in solid phase sintering. Sintering then proceeds by vacancy diffusion mechanisms in the solid phase as discussed in Part A. However, the presence of a liquid phase provides additional interfaces, i.e., the

liquid-vapor and solid-liquid interfaces. For solid-vapor systems, the curvature of the solid-vapor interface creates tensile stresses in the neck region as was shown by Nabarro.[3] The presence of solid-liquid and liquid-vapor interfaces also creates tensile stresses in the neck, due to capillary pressure. These stresses enhance the vacancy concentration in the neck region relative to the vacancy concentration created by a solid-vapor interface only. As will be shown later, the vacancy concentration gradient is greater than in the solid-vapor case, and therefore results in somewhat different sintering kinetics.

As discussed earlier for the sintering of solid-vapor systems, knowledge of thermodynamic as well as kinetic factors are of fundamental importance in understanding the entire sintering process. Therefore, in the next section, a thermodynamic analysis of sintering of a solid-liquid-vapor system will be presented based on an idealized geometric model. This section will be followed by a section on kinetics in which solutions to kinetic equations will be formulated for solid-liquid systems based on models which are different from those now appearing in the literature.

II. THERMODYNAMICS OF DENSIFICATION IN THE PRESENCE OF A LIQUID PHASE

As discussed in Part A, the basic driving force for sintering a powder compact is the reduction in free energy for the system resulting from the decrease in interfacial area. As long as the differential free energy δG is negative, densification is thermodynamically favored. If δG becomes zero or positive, densification ceases and endpoint densities result. It is of interest to determine the critical interfacial energy ratios which yield endpoint densities for ideal systems undergoing sintering in the presence of a liquid phase. The driving force for the initial stage of liquid phase sintering, rearrangement, is the reduction in liquid-vapor interfacial area. δG is therefore negative until a steady state configuration is reached. No further decrease in the free energy or increase in density of the compact can then result without mass transfer of the solid phase. The following arguments assume that rearrangement has taken place and a steady state configuration has been attained.

The model assumes 8 uniform sized crystalline spherical particles with an isotropic surface energy in a simple cubic array with a wetting liquid that forms toroidal bridges between the spheres. It is further assumed that the solid is soluble in the liquid and the liquid is insoluble in the solid. The volume of a unit cell formed by such a configuration is $8R_0^3$ where R_0 is the initial radius of the particles. Each cell contains an equivalent of one spherical particle occupying a volume of $4.16R_0^3$. The remaining volume in such a cell is $3.84R_0^3$ or 48% of the total, which can be occupied by liquid and/or vapor. If less than 16% of the initial volume of the cell (i.e., 16% of $8R_0^3$) is occupied by

liquid, residual solid-vapor area remains with the shape of the liquid-vapor interface being toroidal. In compacts containing between 16 and 27.6% liquid, the spheres are completely coated (i.e., no solid-vapor area remains) and the shape of the liquid-vapor interface changes from toroidal to spherical. Above 27.6% liquid, spherical porosity begins to form at the center of the cell. Sintering for zero dihedral angles, proceeds by solution-precipitation with material being removed from spherical caps at particle contacts and deposited at particle surfaces away from the contact points in an identical manner as for the model for solid phase sintering (Part A). Particle centers then move together with shrinkage of the cell and reduction of the pore space, as shown in Fig. 1. For nonzero dihedral angles, sintering proceeds by solid state diffusion mechanisms discussed in Part A, with the removal and deposition of cap material and shrinkage being identical to the zero dihedral angle case.

A. Zero Dihedral Angle

1. Acute Contact Angle

When the rearrangement stage is completed for the model system with less than 16 vol% of liquid, the compact is characterized by solid-vapor, solid-liquid, and liquid-vapor interfaces. As sintering proceeds due to the reduction in interfacial energy, the differential of free energy, δG, at constant T, P, and n_i, may be expressed as

$$\delta G = \delta A_{sv}\, \gamma_{sv} + \delta A_{s\ell}\, \gamma_{s\ell} + \delta A_{\ell v}\, \gamma_{\ell v} \qquad (6)$$

where γ_s' and $\delta A_s'$ are respectively the interfacial energy and differential

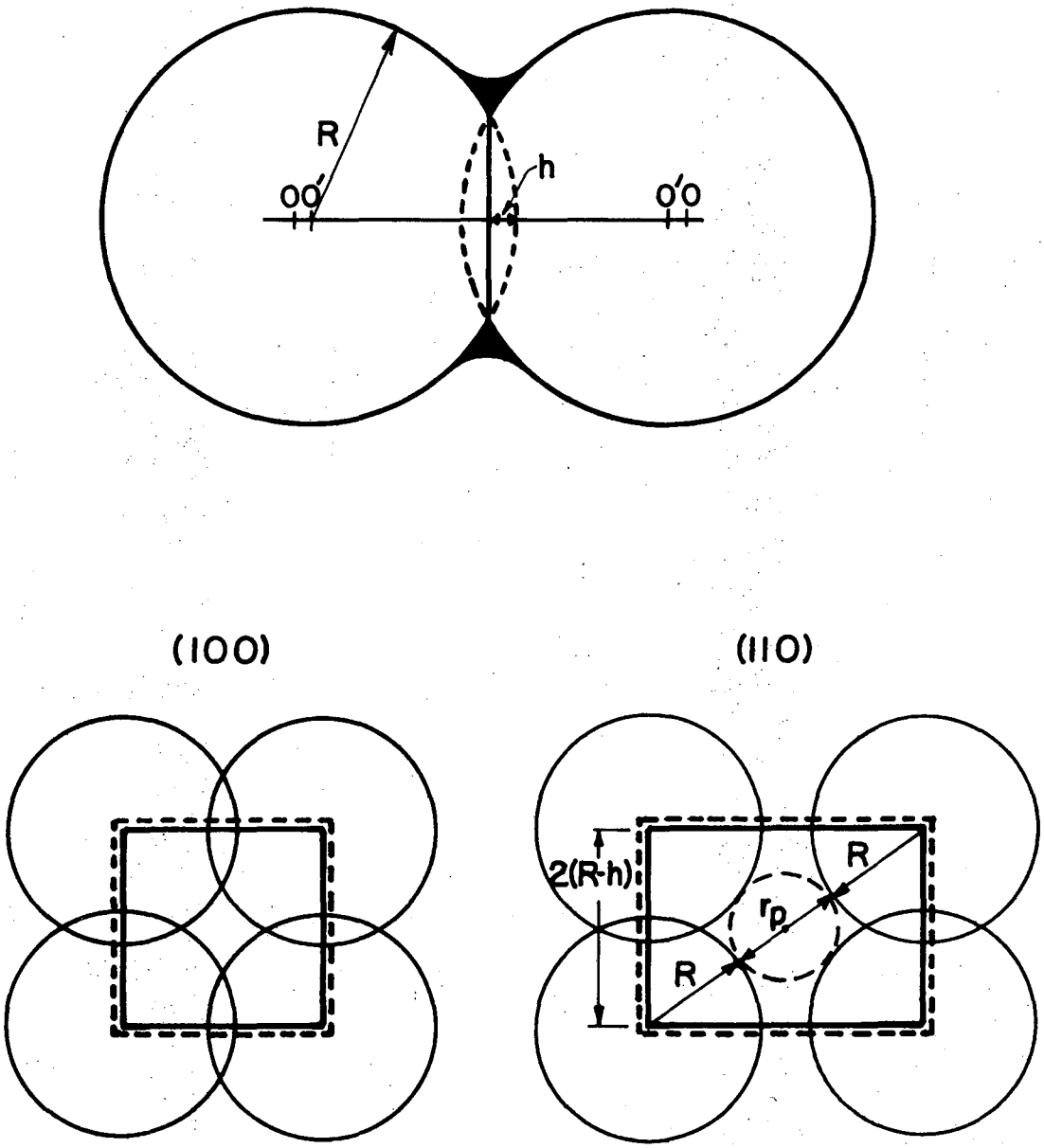

Figure 1. (Top) Two sphere model for liquid phase sintering with wetting liquid bridge between the spheres.
(Bottom) Densification model for simple cubic packing of spheres which forms after the rearrangement stage is completed.

areas. From Young's equation,

$$\gamma_{sv} = \gamma_{s\ell} + \gamma_{\ell v} \cos \theta \tag{7}$$

where θ is the contact angle. Substituting (7) into (6)

$$\delta G = (\delta A_{sv} + \delta A_{s\ell})\ \gamma_{s\ell} + (\delta A_{\ell v} + \delta A_{sv} \cos \theta)\ \gamma_{\ell v} \tag{8}$$

As the compact sinters, $\delta A_{s\ell}$ increases while δA_{sv} decreases. The former term provides a positive contribution to the free energy of the system while the latter provides a negative contribution. $\delta A_{\ell v}$ increases as long as the liquid forms a contact angle with the solid surface. However, when the solid surface is completely covered with liquid, i.e., δA_{sv} becomes zero, $\delta A_{\ell v}$ begins to decrease. The liquid becomes continuous in the (100) plane of the simple cubic cell before the solid-vapor interface is eliminated completely in the (110) plane. Thus, in the (100) plane, the liquid provides a negative contribution to the free energy of the system while in the (110) plane it provides a positive term. This implies that although $\delta A_{\ell v}$ is positive until all the solid-vapor interfacial area is destroyed, it increases in magnitude at a decreasing rate as the compact sinters.

When the compact has sintered to the point where the liquid completely coats the solid surface,

$$\delta G = \delta A_{s\ell}\ \gamma_{s\ell} + \delta A_{\ell v}\ \gamma_{\ell v} \tag{9}$$

On further densification $\delta A_{s\ell}$ remains positive but $\delta A_{\ell v}$ becomes negative and becomes the driving force for sintering until endpoint density or theoretical density is attained.

2. Zero Contact Angle

The model is identical to case A-1 except that Young's equation may now be written as

$$\gamma_{sv} = \gamma_{s\ell} + \gamma_{\ell v} \tag{10}$$

substituting (10) into (6)

$$\delta G = (\delta A_{sv} + \delta A_{s\ell})\ \gamma_{s\ell} + (\delta A_{sv} + \delta A_{\ell v})\ \gamma_{\ell v} \tag{11}$$

Again $\delta A_{s\ell}$ and $\delta A_{\ell v}$ provide positive contributions to the free energy while that of δA_{sv} is negative. Since $\cos \theta < 1$ in Eq. (8), comparison of Eqs. (9) and (11) indicates that δG is more negative for compacts having zero contact angles than those having nonzero contact angles. Sintering continues until the solid-vapor interface is eliminated. At this point,

$$\delta G = \delta A_{s\ell}\ \gamma_{s\ell} + \delta A_{\ell v}\ \gamma_{\ell v} \tag{12}$$

which is identical to Eq. (9). The contact angle no longer affects the free energy of the system. Therefore, when the solid-vapor area is eliminated, the free energy of the compact becomes independent of the contact angle.

B. Nonzero Dihedral Angle

1. Acute Contact Angle

This model assumes that the solid and liquid form a nonzero dihedral angle, which implies that material transport is through the solid phase instead of through the liquid phase since the liquid does not penetrate between the solid-solid contacts. As discussed in thermodynamics of solid phase sintering in Part A, this model assumes that necks do not form between the particles but rather that material is distributed uniformly over the entire surface of the spheres. Although such a model does not comply with most kinetic observations during sintering,[42-44] it does represent the lowest free energy configuration for the system, as discussed earlier.

In the initial stage of densification, the differential free energy for the system may be written as

$$\delta G = \delta A_{ss}\ \gamma_{ss} + \delta A_{s\ell}\ \gamma_{s\ell} + \delta A_{\ell v}\ \gamma_{\ell v} + \delta A_{sv}\ \gamma_{sv} \qquad (13)$$

Using Eq. (7)

$$\delta G = \delta A_{ss}\ \gamma_{ss} + (\delta A_{sv} + \delta A_{s\ell})\ \gamma_{s\ell} + (\delta A_{\ell v} + \delta A_{sv} \cos\theta)\ \gamma_{\ell v} \qquad (14)$$

The dihedral angles relates γ_{ss} to $\gamma_{s\ell}$.

$$\gamma_{ss} = 2\gamma_{s\ell} \cos\theta/2 \qquad (15)$$

Substituting (15) into (14)

$$\delta G = (2\cos\ \theta/2\ \delta A_{ss} + \delta A_{sv} + \delta A_{s\ell})\gamma_{s\ell} + (\delta A_{\ell v} + \delta A_{sv}\ \cos\ \theta)\ \gamma_{\ell v} \quad (16)$$

As in cases A1 and A2, $\delta A_{s\ell}$ and $\delta A_{\ell v}$ provide positive contributions to δG, while that of δA_{sv} is negative. In this case, however, there is an additional positive contribution to the free energy of the system from δA_{ss}, which results from the formation of solid-solid interfaces. When the compact has sintered to the point where the solid-vapor interfacial area is eliminated, δG may be written as

$$\delta G = \delta A_{ss}\ \gamma_{ss} + \delta A_{s\ell}\ \gamma_{s\ell} + \delta A_{\ell v}\ \gamma_{\ell v} \quad (17)$$

Using Eq. (15)

$$\delta G = (2\ \cos\ \theta/2\ \delta A_{ss} + \delta A_{s\ell})\ \gamma_{s\ell} + \delta A_{\ell v}\ \gamma_{\ell v} \quad (18)$$

Here the contributions of $\delta A_{s\ell}$ and $\delta A_{\ell v}$ become negative while the contribution of δA_{ss} remains positive. Sintering continues until spherical pores form. At this point, $\delta A_{\ell v}$ becomes the differential area for a spherical pore. In comparing Eqs. (9) and (8), it should be noted that in the zero dihedral angle case, $\delta A_{s\ell}$ contributes positively to the free energy of the system while $\delta A_{\ell v}$ contributes negatively. For nonzero dihedral angles, $\delta A_{s\ell}$ and $\delta A_{\ell v}$ are both negative while δA_{ss} is positive.

This fact arises since a zero dihedral angle causes the liquid to penetrate between the particle contacts. Therefore, $\delta A_{s\ell}$ describes the

differential area of the sphere minus caps, plus the area of the contact region, all of which increase as sintering proceeds. While for nonzero dihedral angles, solid-solid contacts form, and $\delta A_{s\ell}$ is the differential area of the sphere minus caps, which decreases during sintering.

2. Zero Contact Angle

Proceeding in a similar manner as above, δG may be represented as

$$\delta G = \delta A_{ss}\ \gamma_{ss} + \delta A_{s\ell}\ \gamma_{s\ell} + \delta A_{\ell v}\ \gamma_{\ell v} + \delta A_{sv}\ \gamma_{sv} \tag{19}$$

Using Eq. (10)

$$\delta G = \gamma_{ss}\ \delta A_{ss} + (\delta A_{sv} + \delta A_{s\ell})\ \gamma_{s\ell} + (\delta A_{sv} + \delta A_{\ell v})\ \gamma_{\ell v} \tag{20}$$

and with Eq. (15)

$$\delta G = (2\delta A_{ss}\ \cos\ \theta/2 + \delta A_{sv} + \delta A_{s\ell})\ \gamma_{s\ell} + (\delta A_{\ell v} + \delta A_{sv})\ \gamma_{\ell v} \tag{21}$$

When sufficient sintering has occurred, the solid-vapor interfacial area is eliminated and

$$\delta G = \gamma_{ss}\ \delta A_{ss} + \gamma_{s\ell}\ \delta A_{s\ell} + \gamma_{\ell v}\ \delta A_{\ell v} \tag{22}$$

or

$$\delta G = (2\ \cos\ \theta/2\ \delta A_{ss} + \delta A_{s\ell})\ \gamma_{s\ell} + \gamma_{\ell v}\ \delta A_{\ell v} \tag{23}$$

As in the zero dihedral angle cases, (A-1 and A-2), the contact angle no longer affects the system, and Eq. (23) is identical to Eq. (18).

C. Critical Ratios of Interfacial Energies for Theoretical Density

Although the above equations are useful in understanding the contributions of interfacial areas to the free energy for liquid phase sintering systems, it is extremely important to be able to obtain quantitative values of γ_{ss}, $\gamma_{s\ell}$, and $\gamma_{\ell v}$ at which the above equations yield $\delta G = 0$, because sintering then ceases since any further interpenetration of spheres would cause δG to become positive. Theoretically, one could obtain critical values of γ_{sv}, $\gamma_{s\ell}$, γ_{ss}, and $\gamma_{\ell v}$ for each corresponding equation that would correspond to no further shrinkage. However, the surfaces are extremely difficult to describe in many of these cases. In lieu of taking such an approach, one should note that a spherical pore forms in the center of the unit cell after a specified degree of densification. The geometry of such a configuration, although still somewhat complicated, is much simpler to describe than the geometry for the earlier stages of sintering. Additionally, this configuration corresponds to the final step in the densification process. Therefore, critical ratios of interfacial tensions will be obtained starting from the point at which a spherical pore forms in the unit cell and continuing until the pore is eliminated and theoretical density is attained.

1. Critical Interfacial Energy Ratios for a Zero Dihedral Angle

The model is identical to cases A-1 and A-2, and is described by Eqs. (9) and (12). The original volume of the simple cubic cell is $8R_0^3$ and consists of 8 spherical crystalline particles at the corners of a

unit cell. A wetting liquid phase forms toroidal shaped bridges between the particles, and pore space fills the remainder of the cell. As sintering proceeds, material is removed from contacts between particles, diffuses through the liquid, and is deposited on surfaces away from the contact points. The volume of the cell shrinks and the liquid is squeezed into the void space with the porosity being decreased. Figure 1a shows caps of height h removed from two spherical contacts and figure 1b reveals the manner in which the cell shrinks.

The volume of the cell at any degree of densification is

$$V_{cell} = 8(R-h)^3 \tag{24}$$

Let P = h/R, and substitute into (24)

$$V_{cell} = 8R^3(1-P)^3 \tag{25}$$

For simple cubic packing,

$$R^3 = 4R_0^3/(4-18P^2 + 6P^3) \tag{26}$$

thus

$$V_{cell} = 32R_0^3(1-P)^3/(4-18P^2 + 6P^3) \tag{27}$$

The volume of the spherical particle remains constant and is given by

$$V_{sphere} = \frac{4\pi R_0^3}{3} \tag{28}$$

The volume of liquid phase in the cell is designated V_{liq}. Therefore, the volume of porosity at any degree of densification is

$$V_{porosity} = V_{cell} - V_{sphere} - V_{liq} \tag{29}$$

Substituting (27) and (28) into (29)

$$V_{porosity} = \frac{32R_0^3(1-P)^3}{(4-18P^2+6P^3)} - \frac{4\pi R_0^3}{3} - V_{liq} \tag{30}$$

When sufficient sintering has occurred, a spherical pore forms in the center of the unit cell. Its volume is

$$V_{pore} = \frac{4\pi r_p^3}{3} \tag{31}$$

r_p being the radius of the pore. Substituting (31) into (30),

$$\frac{4\pi r_p^3}{3} = \frac{32R_0^3(1-P)^3}{(4-18P^2+6P^3)} - \frac{4\pi R_0^3}{3} - V_{liq} \tag{32}$$

Solving for r_p

$$\frac{r_p}{R_0^3} = \left\{ \frac{24(1-P)^3}{(4-18P^2+6P^3)\pi} - \left(1 + \frac{3V_{liq}}{4\pi}\right) \right\}^{1/3} \tag{33}$$

This equation is only true above the particular value of P at which a spherical pore forms. The method of obtaining the value at which the equation becomes valid will be discussed later.

The area of the pore is

$$A_{pore} = 4\pi r_p^2 \tag{34}$$

or substituting (33) into (34)

$$\frac{A_{pore}}{R_0^2} = 4\pi \left\{ \frac{24(1-P)^3}{\pi(4-18P^2+6P^3)} - \left(1 + \frac{3V_{liq}}{4\pi} \right) \right\}^{2/3} \tag{35}$$

The solid-liquid interfacial area is given by the area of the effective spherical particle minus the area of the caps removed plus the area created between the spheres. The area of the spherical particle at any value of P is

$$A_{s\ell} = 4\pi R^2 \tag{36}$$

The area of the caps is

$$A_{caps} = 6\pi(2Rh) \tag{37}$$

and the area created between the particles is

$$A_{interface} = 6\pi h(2R-h) \tag{38}$$

Combining

$$A_{s\ell} = 4R^2\pi - 6\pi(2Rh) + 6\pi h(2R-h) \tag{39}$$

Rearranging and substituting $P = h/R$, and R_0 for R

$$\frac{A_{s\ell}}{R_0^2} = 2\pi(4)^{2/3}\ (2-3P^2) \Big/ (4-18P^2 + 6P^3)^{2/3} \tag{40}$$

Recalling Eq. (24) of Part A, the change in free energy from a degree of densification P_A to a degree of densification P_B is

$$\Delta G = \gamma_{s\ell}\ (A_{s\ell}(P_B) - A_{s\ell}(P_A)) + \gamma_{\ell v}\ (A_{\ell v}(P_B) - A_{\ell v}(P_A)) \tag{41}$$

At equilibrium, $\Delta G = 0$, and therefore, from Eq. (25) of Part A

$$\frac{\gamma_{s\ell}}{\gamma_{\ell v}} = -\frac{(A_{\ell v}(P_B) - A_{\ell v}(P_A))}{A_{s\ell}(P_B) - A_{s\ell}(P_B))} \tag{42}$$

Substituting (35) and (40) into (42)

$$\frac{\gamma_{s\ell}}{\gamma_{\ell v}} = -4\pi\left[\left\{\frac{24(1-P_B)^3}{\pi(4-18P_B^2+6P_B^3)} - \frac{(1+3V_{liq})}{4\pi}\right\}^{2/3} - \left\{\frac{24(1-P_A)^3}{\pi(4-18P_A^2+6P_A^3)} - \frac{(1+3V_{liq})}{4\pi}\right\}^{2/3}\right] \Big/ 2\pi(4)^{2/3}\left[\frac{(2-3P_B^2)}{(4-18R_B^2+6P_B^3)^{2/3}} - \frac{(2-3P_A^2)}{(4-18P_A^2+6P_A^3)^{2/3}}\right] \tag{43}$$

Equation (43) yields critical values of $\gamma_{s\ell}/\gamma_{\ell v}$ at any degree of densification after spherical porosity has formed. If the critical ratio is smaller than the actual ratio for a real compact, the model predicts that densities less than theoretical will result as will be discussed later.

2. Critical Ratios of Interfacial Energies for Nonzero Dihedral Angles

The model is identical to cases B-1 and B-2, and is described by Eqs. (18) and (23)

$$\delta G = (2 \cos \Phi/2 \ \delta A_{ss} + \delta A_{s\ell}) \ \gamma_{s\ell} + \delta A_{\ell v} \ \gamma_{\ell v} \tag{44}$$

The solid-solid interfacial area is the area of the grain boundary created between the sintering spheres.

$$A_{ss} = 6\pi(2Rh-h^2)/2 \tag{45}$$

Substituting P and R_0 into (5)

$$\frac{A_{ss}}{R_0^2} = \frac{3\pi(4)^{2/3}(2P-P^2)}{(4-18P^2+6P^3)^{2/3}} \tag{46}$$

The solid-liquid interfacial area is given by

$$A_{s\ell} = \pi(4R^2 - 12Rh) \tag{47}$$

and on substitution,

$$\frac{A_{s\ell}}{R_0^2} = \frac{4\pi(4)^{2/3}(1-3P)}{(4-18P^2+6P^3)^{2/3}} \tag{48}$$

The liquid-vapor interfacial area is identical to Eq. (35), and at equilibrium, $\Delta G = 0$, and Eq. (42) becomes

$$\frac{\gamma_{s\ell}}{\gamma_{\ell v}} = \frac{-[A_{\ell v}(P_B) - A_{\ell v}(P_A)]}{2\cos(\Phi/2)[A_{ss}(P_B) - A_{ss}(P_A)] + [A_{s\ell}(P_B) - A_{s\ell}(P_A)]} \tag{49}$$

Substituting Eqs. (46), (48) and (35) into (49)

See next page for Eq. (50).

$$\frac{\gamma_{s\ell}}{\gamma_{\ell v}} = -\frac{4\pi}{2\cos(\Phi/2)}\left[\left\{\frac{24(1-P_B)^3}{\pi(4-18P_B^2+6P_B^3)} - \frac{(+3V_{liq})}{4\pi}\right\}^{2/3} - \left\{\frac{24(1-P_A)^3}{\pi(4-18P_A^2+6P_A^3)} - \frac{(1+3V_{liq})}{4\pi}\right\}^{2/3}\right]$$
$$\left[\frac{3\pi(4)^{2/3}(2P_B-P_B^2)}{(4-18P_B^2+6P_B^3)^{2/3}} - \frac{3\pi(4)^{2/3}(2P_A-P_A^2)}{(4-18P_A^2+6P_A^3)^{2/3}}\right] + (4)^{5/3}\pi\left[\frac{(1-3P_B)}{(4-18P_B^2+6P_B^3)^{2/3}} - \frac{(1-3P_A)}{(4-18P_A^2+6P_A^3)^{2/3}}\right]$$

(50)

Equation (50) yields critical ratios for $\gamma_{s\ell}/\gamma_{\ell v}$ at any degree of densification.

Equations (43) and (50) are only valid above the particular value of P at which a spherical pore forms in the cell. Equation (35) was derived assuming the void space was spherical in shape. If Eq. (35) is used at void volumes which do not correspond to spherical porosity, the calculated value of r_p is too large. Therefore, Eq. (35) is not valid until sufficient densification has occurred to form a spherical pore. The amount of densification necessary for such a configuration depends on the volume of liquid phase present. A method for calculating the value of P at which Eq. (35) becomes valid is given below.

Figure 1 shows the (100) and (110) planes of the simple cubic unit cell for a sintering compact. An imaginary pore is inscribed in the center of the cell. The original radius of such a pore is

$$r_{p_0} = R_0 \ (\sqrt{3} - 1) \tag{51}$$

At any degree of densification,

$$r_p = \sqrt{3} \ (R-h) - R \tag{52}$$

Substituting P and R_0,

$$\frac{r_p}{R_0} = \frac{(\sqrt{3} \ (1-P) - 1)(4)^{1/3}}{(4-18P^2 + 6P^3)^{1/3}} \tag{53}$$

The volume of such a pore is

$$V_{pore} = \frac{4\pi r_p^3}{3} \tag{54}$$

Since Eq. (29) gives the volume of the porosity at any particular liquid content and at any particular value of P, when

$$V_{porosity} = V_{pore} \tag{55}$$

sufficient densification has occurred to form a spherical pore within the liquid. The value of P at which this relationship becomes valid, called P_s, is the minimum value of P for which Eq. (35) becomes valid. Using an electronic computer, values of P_s were obtained for various liquid contents. The results are given in Fig. 2. Equations (43) and (50) were also solved in a similar manner at several liquid volumes and several dihedral angles from P_s to the value of P at which theoretical density occurred, P_{th}.

The results of these equations yielded critical values of $\gamma_{s\ell}/\gamma_{\ell v}$ for the particular sets of conditions. $\gamma_{s\ell}/\gamma_{\ell v}$ ratios were then plotted versus P_0, (h_0/R_0), which is a measure of linear shrinkage, to give critical ratios of interfacial energies as a function of densification.

Results for Eq. (43), the zero dihedral angle case, are shown in Fig. 3 for volumes of liquid phase from 2.33% to 10.6%. Each of these curves has a different value of P_s and P_{th} corresponding to the particular volume of liquid phase in the unit cell. Between P_s and P_{th}, the curves decrease, go through a minimum, and then asymptotically approach P_{th}.

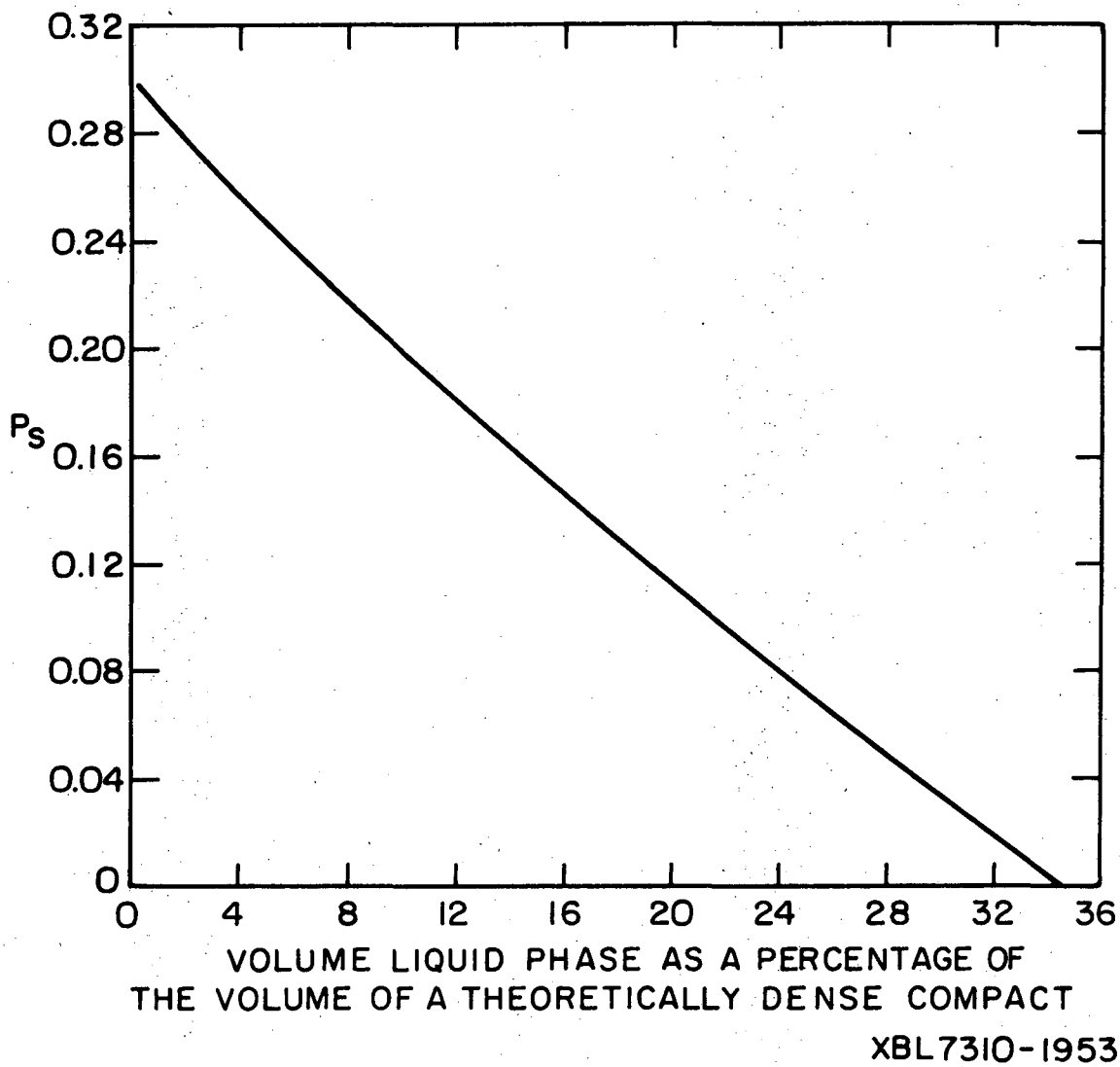

Figure 2. P or h/R, at which a spherical pore forms in the simple cubic array versus the volume percentage of liquid phase in a theoretically dense compact. For a given volume of liquid phase, this plot determines the value of P above which Eq. (50) becomes valid.

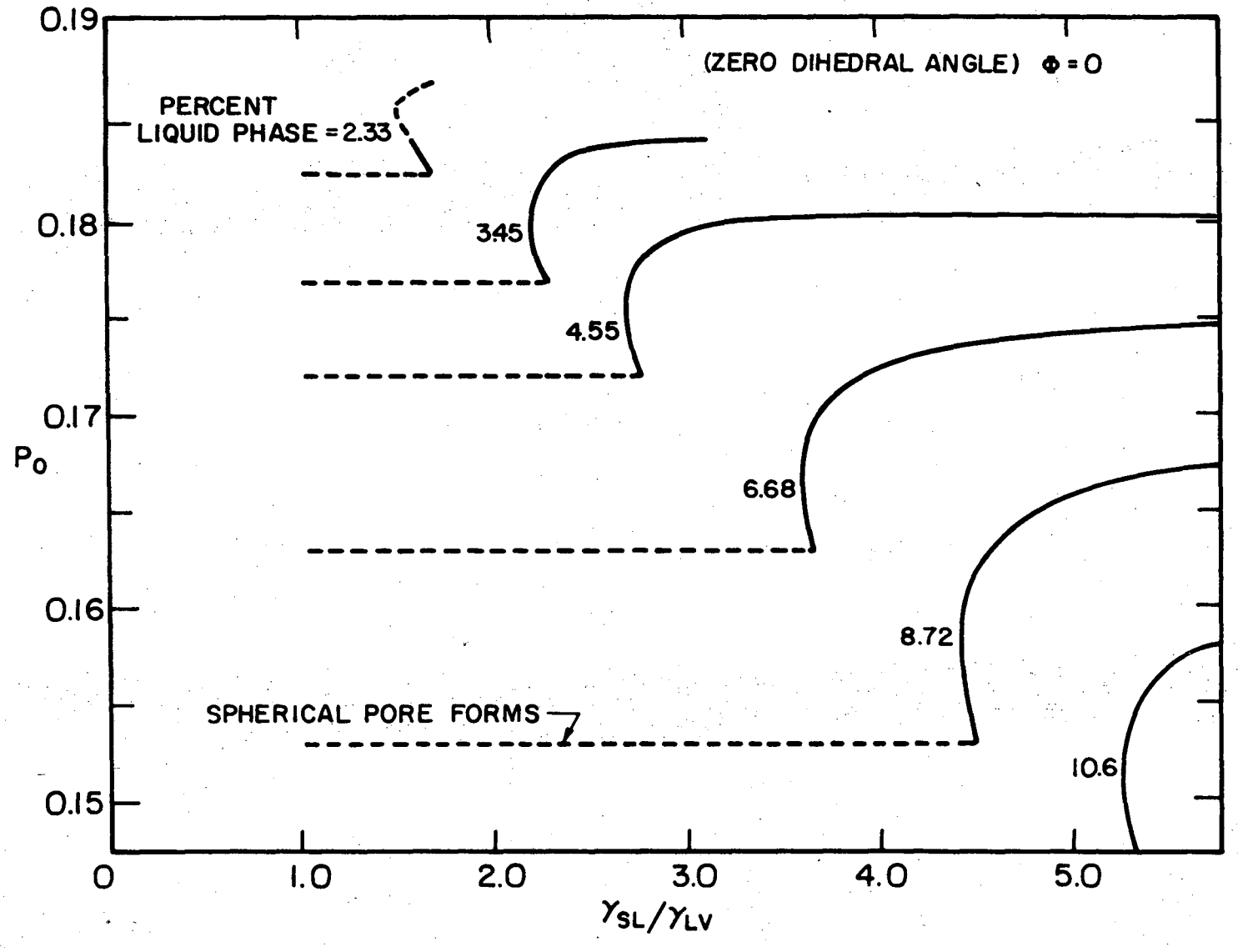

XBL 749-7284

Figure 3. Critical ratios of $\gamma_{s\ell}/\gamma_{\ell v}$ as a function of density for liquid phase sintering systems forming a zero solid/liquid dihedral angle.

The critical ratio of $\gamma_{s\ell}/\gamma_{\ell v}$, as far as attaining theoretical density is concerned, is the minimum value of $\gamma_{s\ell}/\gamma_{\ell v}$ for any particular curve. Thus for 3.45% liquid phase (Fig. 3), spherical porosity forms as $P_0 = P_s = 0.177$; at $P_0 = 0.180$, the minimum value of $\gamma_{s\ell}/\gamma_{\ell v} = 2.205$ occurs; and at $P_0 = P_{th} = 0.184$, the unit cell has completely densified. The model therefore predicts that in order to completely densify an array of simple cubic packing of spherical particles, containing 3.45% liquid phase and forming a zero solid-solid solid-liquid dihedral angle, the ratio of $\gamma_{s\ell}/\gamma_{\ell v}$ must be less than 2.205. If the ratio is greater, end-point densities less than theoretical will result.

For compacts containing 2.33% liquid phase, somewhat different results occur. Spherical porosity forms at $P_0 = P_s = 0.182$; at $P_0 = 0.1842$, the (100) face of the unit cell is completely densified. At this point, the model breaks down as did the model for simple cubic packing of spheres in the solid phase sintering model, and $\gamma_{s\ell}/\gamma_{\ell v} = 1.590$; but since the unit cell has not yet densified completely, sintering must proceed by some other mechanism than that described by the present model. The dashed line in Fig. 5 indicates the value $\gamma_{s\ell}/\gamma_{\ell v}$ would have if the present model is carried past the point where the (100) face has completely densified. The minimum value of $\gamma_{s\ell}/\gamma_{\ell v}$ occurs at $P_0 = 0.186$ and theoretical density occurs at $P_0 = P_{th} = 0.1875$. Although the value of $\gamma_{s\ell}/\gamma_{\ell v} = 1.543$ at $P_0 = 0.186$ is not correct, the shape of the curve indicates that the critical ratio of $\gamma_{s\ell}/\gamma_{\ell v}$ for 2.33% liquid phase must be somewhat less than the value of 1.590 which is predicted at the maximum value of P_0 for which the model is still valid.

Figure 3 also indicates that for a system forming a zero dihedral angle, the critical ratio of $\gamma_{s\ell}/\gamma_{\ell v}$ increases as the volume fraction of liquid phase increases. For wetting systems, $\gamma_{s\ell}$ has a value between γ_{sv} and $\gamma_{\ell v}$, and therefore, $\gamma_{s\ell}/\gamma_{\ell v}$ is greater than unity. Since this ratio for a real system must be less than the minimum predicted by the model, as the volume fraction of liquid phase decreases, the critical ratio will approach unity. The reason for this fact is that as the liquid volume decreases, $\delta A_{s\ell}$ becomes large relative to $\delta A_{\ell v}$ and therefore, $\gamma_{\ell v}$ must be large relative to $\gamma_{s\ell}$ in order for δG to remain negative. Only in the final increments of densification does $\delta A_{\ell v}$ become large relative to $\delta A_{s\ell}$ since the pore shrinks very rapidly near theoretical density. Therefore, the barriers to complete densification are greatest for small liquid volumes and least for large liquid volumes.

Figures 4-7 are plots of $\gamma_{s\ell}/\gamma_{\ell v}$ versus P_0, (Eq. (50) the nonzero dihedral case), at different volume fractions of liquid phase and several dihedral angles. In each figure, as for the zero dihedral angle case, the greater the volume of liquid phase, the larger is the value of $\gamma_{s\ell}/\gamma_{\ell v}$ critical. Additionally, by comparing Figs. 8-10 which are plots of $\gamma_{s\ell}/\gamma_{\ell v}$ versus P_0 at constant liquid contents and several different dihedral angles, it is evident that as the dihedral angle increases, the critical ratio also increases, and therefore, the thermodynamic barriers are reduced.

The reason for this trend is that in systems forming nonzero dihedral angles, as described by Eqs. (18) and (23), the solid-solid interfacial area provides a positive contribution to the free energy of the system while the solid-liquid and liquid-vapor interfaces provide negative

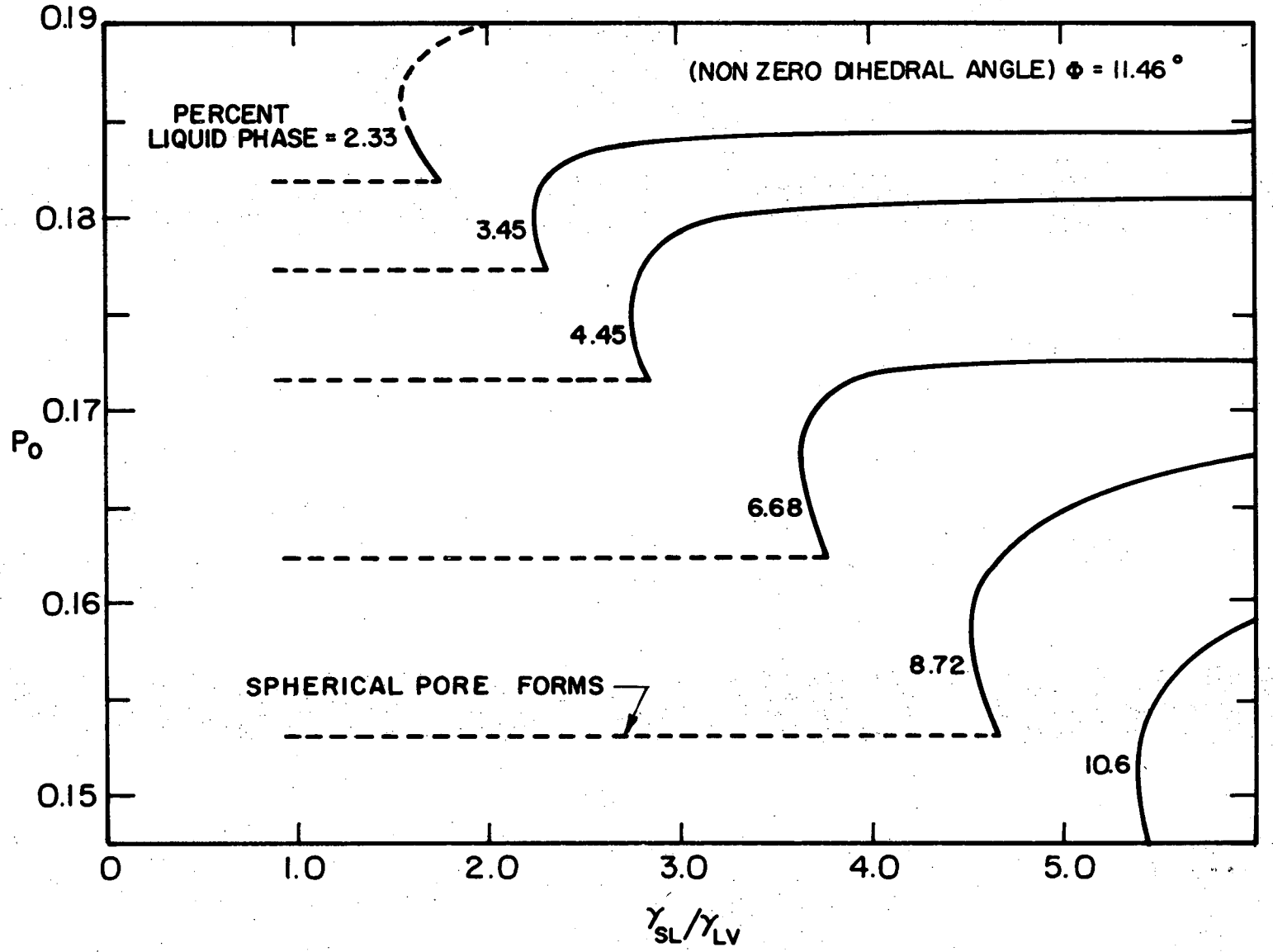

Figure 4. Critical ratios of $\gamma_{s\ell}/\gamma_{\ell v}$ as a function of density for liquid phase sintering systems forming a solid/liquid dihedral angle equal to 11.46°.

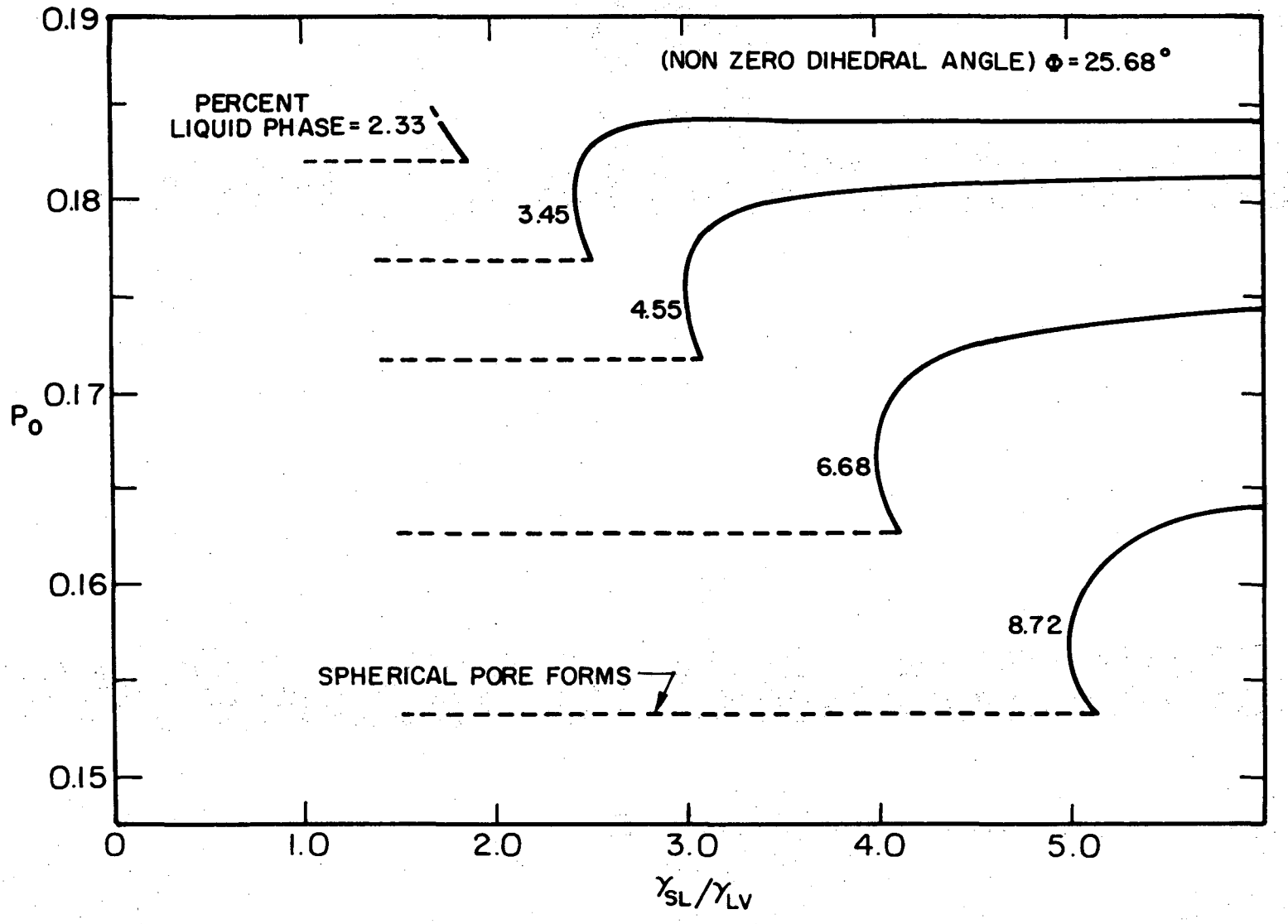

XBL 749-7286

Figure 5. Critical ratios of $\gamma_{s\ell}/\gamma_{\ell v}$ as a function of density for liquid phase sintering systems forming a solid/liquid dihedral angle equal to 25.68°.

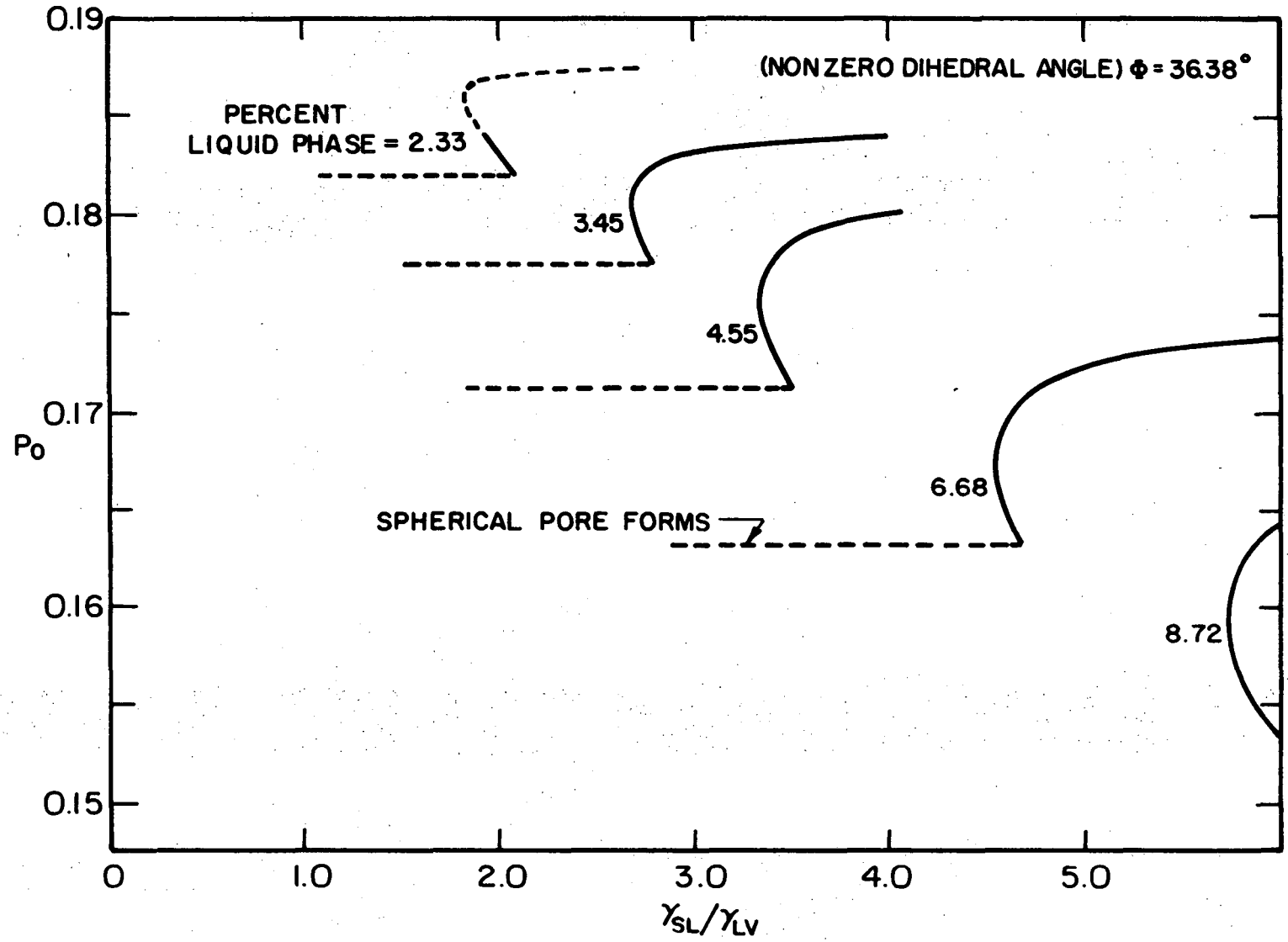

Figure 6. Critical ratios of $\gamma_{s\ell}/\gamma_{\ell v}$ as a function of density for liquid phase sintering systems forming a solid/liquid dihedral angle equal to 36.38°.

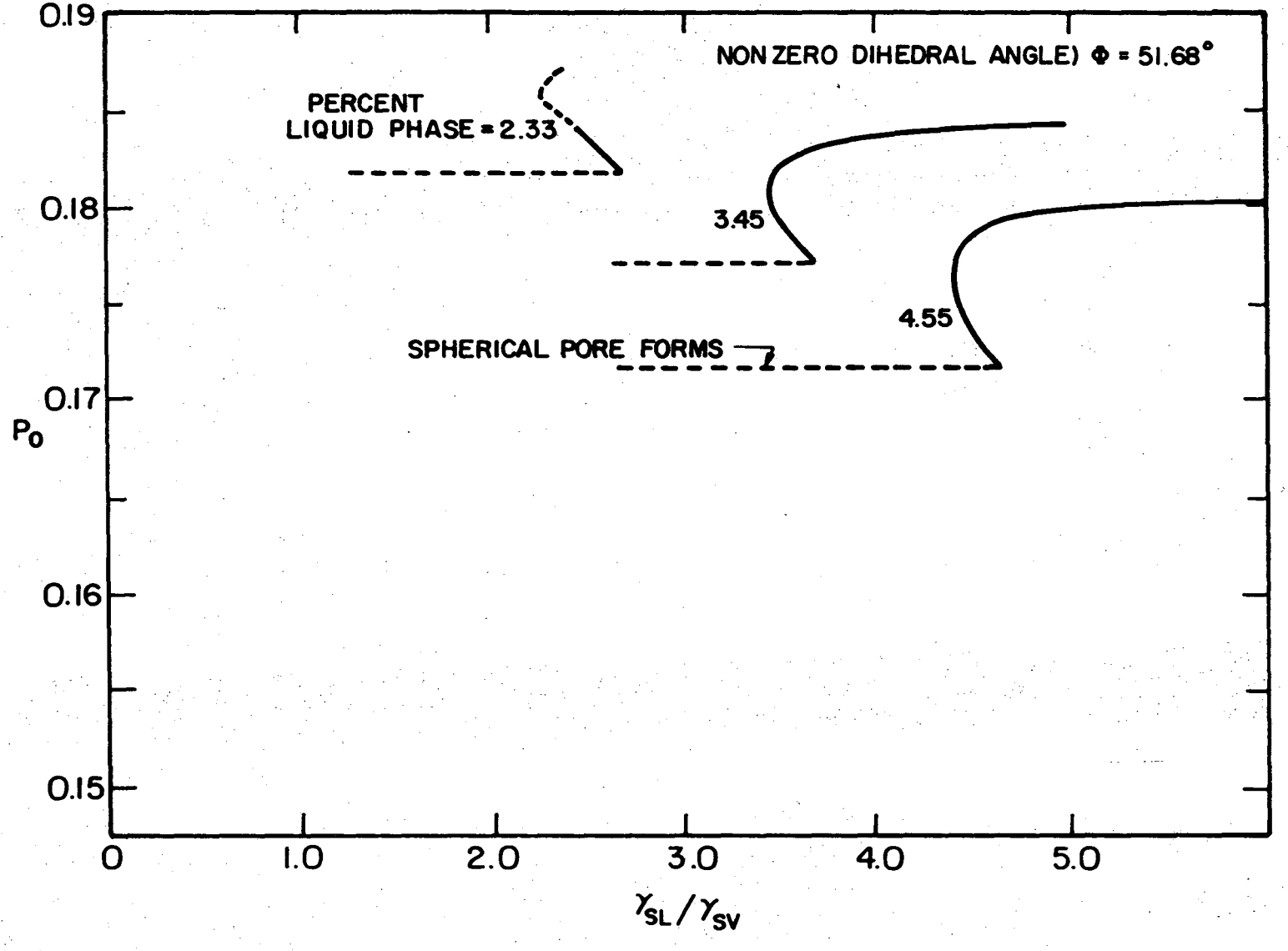

XBL749-7288

Figure 7. Critical ratios of $\gamma_{s\ell}/\gamma_{\ell v}$ as a function of density for liquid phase sintering systems forming a solid/liquid dihedral angle equal to 51.68°.

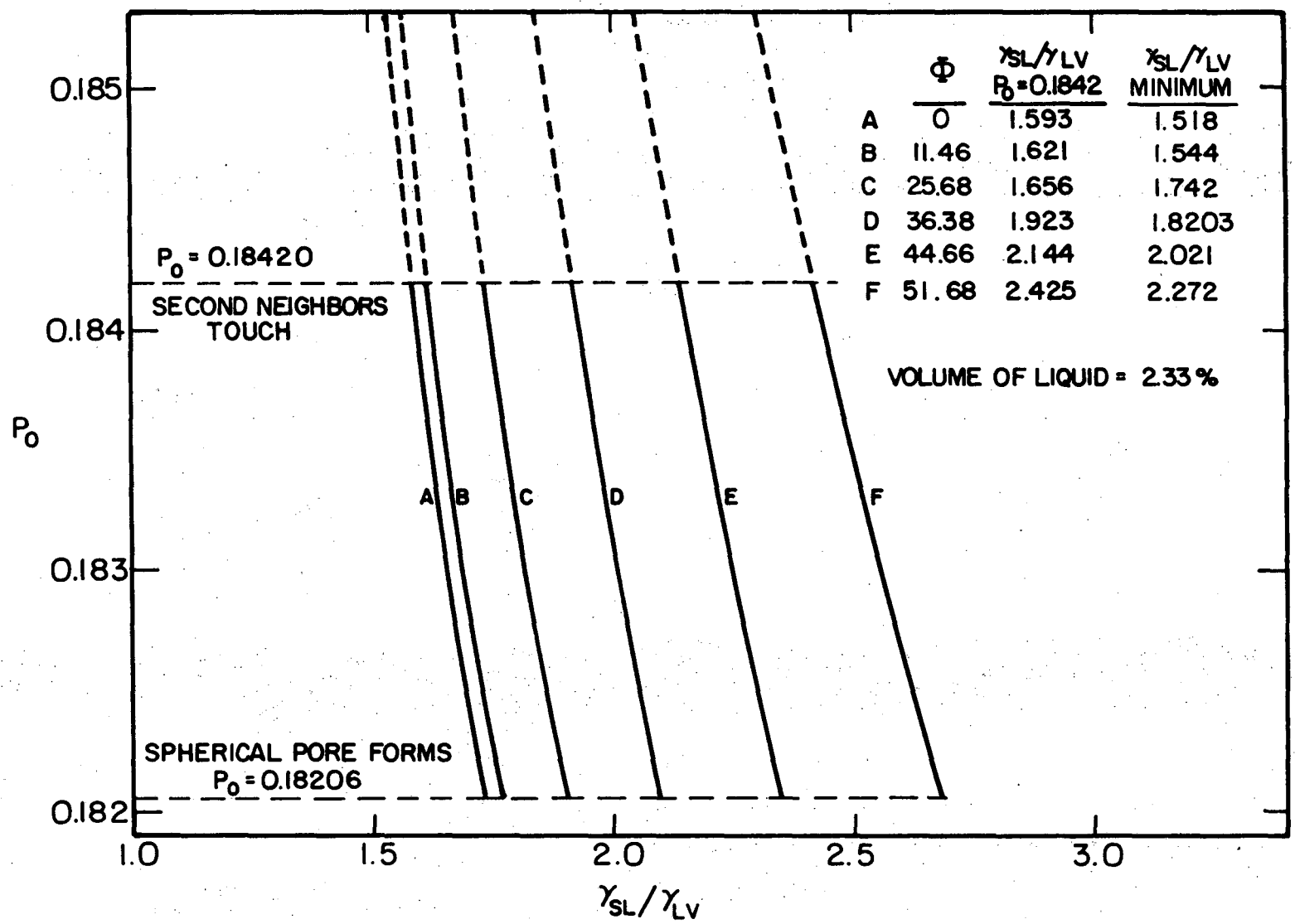

XBL749-7289

Figure 8. Critical ratios of $\gamma_{s\ell}/\gamma_{\ell v}$ as a function of density for liquid phase sintering systems containing 2.33% liquid phase.

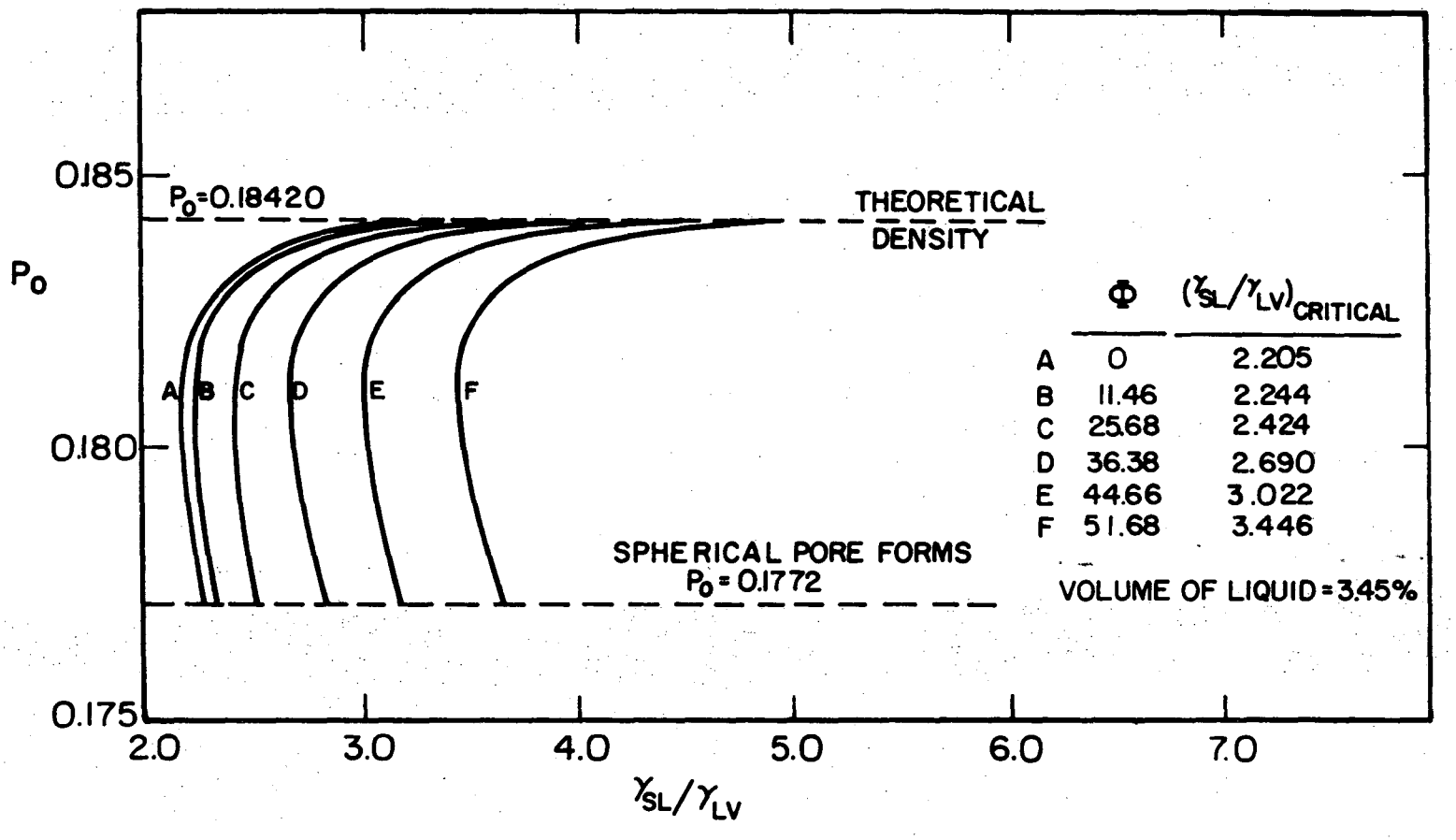

XBL 749-7291

Figure 9. Critical ratios of $\gamma_{s\ell}/\gamma_{\ell v}$ as a function of density for liquid phase sintering systems containing 3.45% liquid phase.

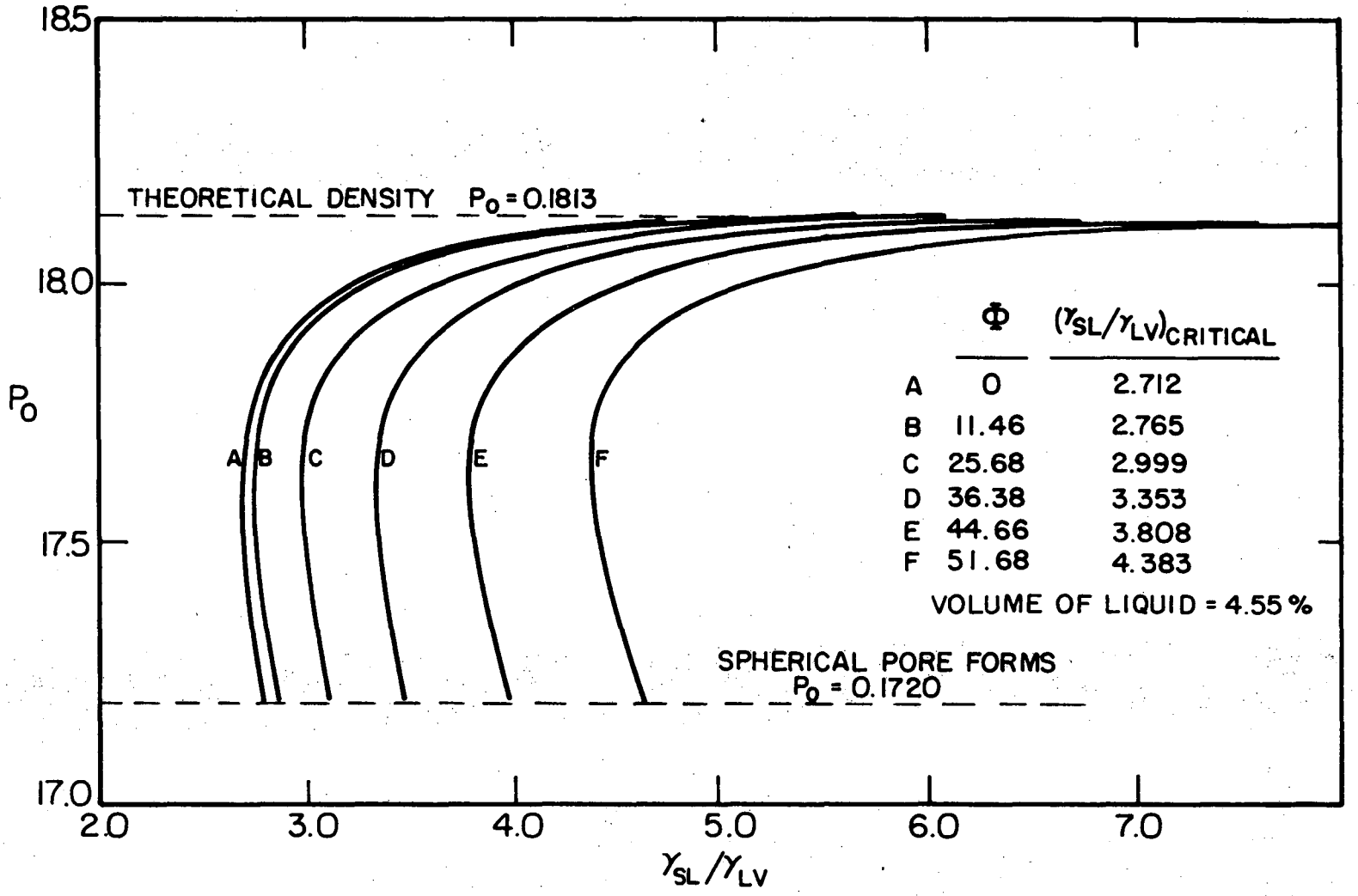

XBL 749-7290

Figure 10. Critical ratios of $\gamma_{s\ell}/\gamma_{\ell v}$ as a function of theoretical density for liquid phase sintering systems containing 4.55% liquid phase.

contributions to the free energy. Since the dihedral angle relates solid-solid and solid-liquid interfacial energies and the smaller the dihedral angle, the larger is γ_{ss} relative to $\gamma_{s\ell}$, systems forming small dihedral angles will have a proportionately larger positive contribution from $\gamma_{ss}\ \delta A_{ss}$ than systems forming large dihedral angles. For wetting systems, ($\gamma_{s\ell}/\gamma_{\ell v}$ greater than unity), in order to overcome the large positive contribution to the free energy of the system of $\gamma_{ss}\ \delta A_{ss}$, the ratio of $\gamma_{s\ell}/\gamma_{\ell v(critical)}$ must decrease as the dihedral angle decreases so that $\gamma_{\ell v}\ \delta A_{\ell v}$ can provide a larger fraction of the negative contribution to the free energy of the system.

One point of comparison is necessary between the analyses for solid phase sintering, (Part A), and liquid phase sintering. The model for solid phase sintering required that densification continued for any system until the interpenetration of spheres was sufficient to form the equilibrium dihedral angle at the solid-solid/solid-vapor triple point. When this configuration was attained, the compact had reached its minimum free energy configuration relative to the geometry of the surfaces, and therefore, sintering ceased.

Applying the same criterion to liquid phase sintering and neglecting the contribution to the free energy of the system of the liquid-vapor interfacial area, would yield the prediction that systems forming an equilibrium zero dihedral angle would have no interpenetration of spheres, and thus no densification. While in systems forming equilibrium non-zero dihedral angles, interpenetration and therefore densification would increase as the equilibrium dihedral angle increased. Such a thermodynamic analysis was presented by Stephenson and White[16] although these

authors did realize that the liquid-vapor interface must be considered in the analysis in order to be consistent with theory and with experimental evidence.

When the contribution of the liquid-vapor interface is considered in the analysis as in the present model, interpenetration of spheres occurs past the equilibrium dihedral angle for all systems. The free energy of the solid-solid interface plus the solid-liquid interface passes through a minimum at an interpenetration corresponding to the equilibrium dihedral angle and begins to increase. However, the liquid-vapor interface provides a negative contribution to δG during further interpenetration which counterbalances this positive contribution and continues to maintain a negative free energy for the entire system. For the most unfavorable case, $\Phi_{eq} = 0$, the contribution of $\gamma_{\ell v}\ \delta A_{\ell v}$ is great enough to cause sufficient interpenetration of the spheres to attain theoretical density for the model.

It should be noted for the zero dihedral angle case, that the liquid phase sintering model assumes that a film of liquid exists between the spheres although the macro-shape of the solid-liquid triple point defines a finite dihedral angle much larger than zero. The micro-shape of the triple point, however, would indicate a zero dihedral angle.

For all these models, once the porosity and thus the liquid-vapor interface is eliminated, the solid-solid and solid-liquid interfaces may be in a nonequilibrium state, since the macro-dihedral angle is greater than Φ_{eq}. Thus a driving force exists for the motion of internal surfaces to attain a lower free energy configuration, i.e., the equilibrium dihedral angle. This driving force is largest for an equilibrium zero

dihedral angle and decreases as the dihedral angle increases. Since the motion of internal surfaces is associated with grain growth, the model then predicts that when porosity in a certain region of a compact is eliminated, the driving force for grain growth increases with decreasing dihedral angles. This postulate is consistent with experimental results for real systems which show a similar relationship between the magnitude of the dihedral angle and the degree of grain growth.[16]

D. Discussion

The analysis for the thermodynamics of liquid phase sintering indicates that the critical ratios of $\gamma_{s\ell}/\gamma_{\ell v}$ for the attainment of theoretically dense compacts are dependent on two parameters: the volume fraction of liquid phase, and the magnitude of the solid-liquid dihedral angle. For a constant value of the dihedral angle, as the volume fraction of liquid phase increases, the critical ratio of $\gamma_{s\ell}/\gamma_{\ell v}$ also increases as shown in Figs. 3-7. Therefore, as the volume fraction of liquid increases, the thermodynamic barriers to the attainment of a theoretically dense compact decrease.

The effect of increasing values of the dihedral angle, at constant volume fractions of liquid phase, on the critical ratio of $\gamma_{s\ell}/\gamma_{\ell v}$ is shown in Figs. 8-10. As the solid-liquid dihedral angle increases, so does the critical ratio, and therefore, the thermodynamic barriers to the attainment of a theoretically dense compact are reduced.

The most unfavorable case for the attainment of theoretical density involves a system which forms a zero solid-liquid dihedral angle and has a small volume fraction of liquid phase. In order to obtain more favorable thermodynamic conditions for the sintering of such a system, two

approaches are possible. One method involves the use of additives which reduce the value of γ_{ss} relative to $\gamma_{s\ell}$ and $\gamma_{\ell v}$. By decreasing γ_{ss}, the equilibrium solid-liquid dihedral angle increases. As the dihedral angle increases, the critical ratio of $\gamma_{s\ell}/\gamma_{\ell v}$ must also increase. As an example, assume that for a sintering system the ratio of $\gamma_{s\ell}/\gamma_{\ell v}$ is 2.230, and that the equilibrium dihedral angle is zero. This value of the dihedral angle corresponds to curve A of Fig. 9. The critical ratio of $\gamma_{s\ell}/\gamma_{\ell v}$ for this curve is 2.205 which indicates that an endpoint density less than theoretical will result. However, if the introduction of an additive causes the equilibrium dihedral angle to increase from 0° to 11.46°, curve B will govern the sintering of the compact instead of curve A. The critical ratio of $\gamma_{s\ell}/\gamma_{\ell v}$ therefore increases from 2.205 to 2.244 and the model predicts that theoretical density will be attained since no thermodynamic barriers exist.

For systems where it is undesirable to introduce impurities, theoretical density can still be attained by increasing the volume fraction of liquid phase. For systems forming a zero solid-liquid dihedral angle and having a ratio of $\gamma_{s\ell}/\gamma_{\ell v}$ of 2.230, Fig. 3 indicates that if less than 3.45% liquid phase is present in a sintering compact, endpoint densities less than theoretical will result. However, if the volume fraction of liquid phase is increased to 4.55%, no barriers to the attainment of theoretical density will arise.

Therefore, by increasing the volume fraction of liquid phase in a sintering compact and/or increasing the magnitude of the solid-liquid dihedral angle, most solid-liquid-vapor systems can in principle be sintered to theoretical density.

III. KINETICS OF LIQUID PHASE SINTERING

A. Introduction

Liquid phase sintering kinetics are governed by the magnitudes of capillary forces which arise in sintering compacts due to the formation of toroidal shaped liquid bridges connecting solid particles. The geometry of the solid particles, the volume fraction of liquid phase, and the relative values of the interfacial energies determine the magnitudes of these capillary forces.

In order to accurately describe sintering kinetics, models must be formulated based on each of these parameters. As yet, little work has been performed in this area. Therefore, models are presented here for solution-precipitation mechanisms and bulk diffusion mechanisms of liquid phase sintering systems. Cases treated here for solution-precipitation mechanisms include: (1) small volumes of liquid, (2) large volumes of liquid, and (3) dissimilar sized particles. For bulk diffusion mechanisms the small volume fraction of liquid case is treated for different values of the solid-liquid dihedral angle.

Prior to the development of these models, a short discussion of capillary phenomena is presented.

B. Capillary Forces

When a curved interface is formed between a liquid and a vapor, there exists a pressure difference across that interface. In order to determine the pressure difference, two principal radii of curvature describing the curved interface must be known. Consider the surface in Fig. 11, which has area A = xy and is extended outward by a small increment, dz. The area of the extended surface is

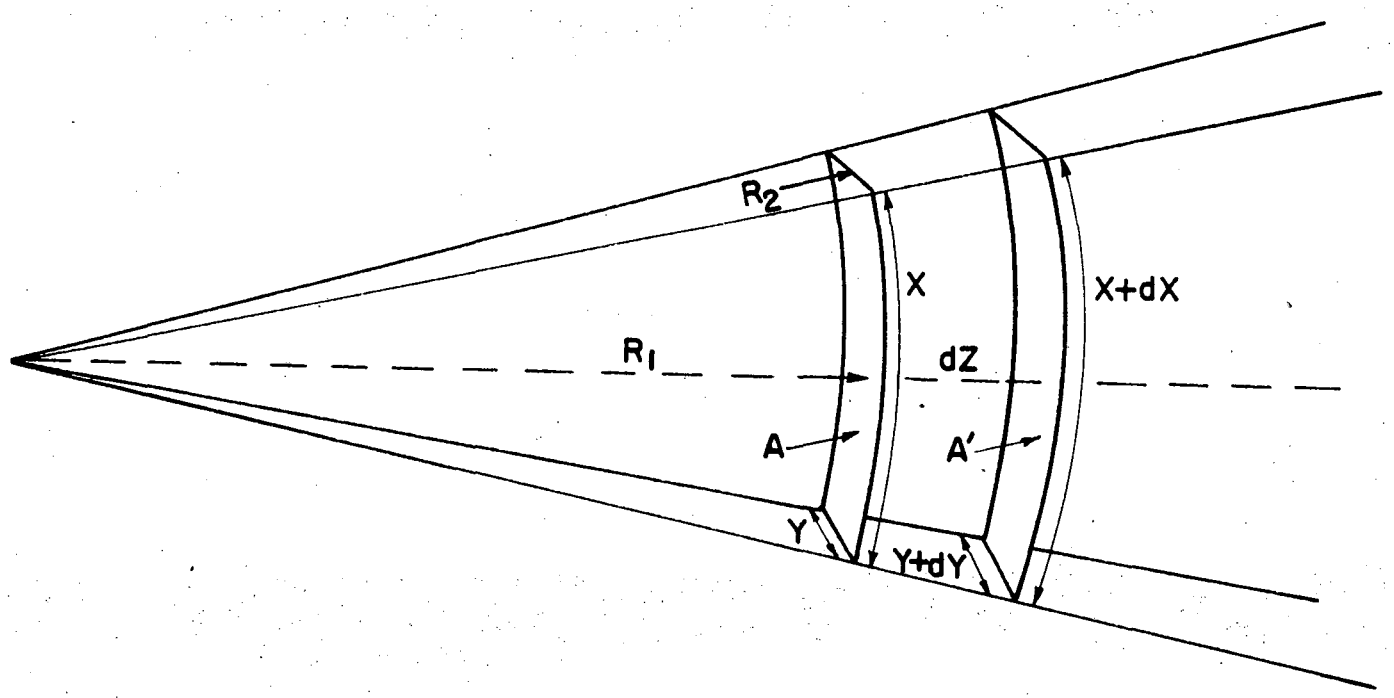

Figure 11. Schematic diagram showing the work required to stretch a curved interface. The curvature of the interface introduces a pressure difference on either side of the interface.

$$A' = (x + dx)\ (y + dy) \tag{56}$$

or

$$A' = xdy + ydx + xy + dxdy \tag{57}$$

The work done in forming the new surface area $(A' - A)$ is $\gamma(xdy + ydx)$ where γ is the interfacial tension. The work done in extending the surface from A to A' is $\Delta p xydz$ where Δp is the pressure difference across the interface. Using the relationship for similar triangles,

$$\frac{x + dx}{R_1 + dz} = \frac{x}{R_1} \quad \text{yielding } dx = \frac{xdz}{R_1} \tag{58}$$

and

$$\frac{y + dy}{R_2 + dz} = \frac{y}{R_2} \quad \text{yielding} \quad dy = \frac{ydz}{R_2} \tag{59}$$

Equating the two work terms,

$$\gamma(xdy + ydx) = \Delta p xydz \tag{60}$$

and

$$\gamma\left(\frac{dy}{ydz} + \frac{dx}{xdz}\right) = \Delta p \tag{61}$$

Substituting Eqs. (58) and (59) into (61)

$$\gamma\left(\frac{1}{R_1} + \frac{1}{R_2}\right) = \Delta p \tag{62}$$

This equation was first derived by Young.[48] The derivation given here is due to Adamson,[49] and indicates that the pressure difference across a curved interface is a function of γ the interfacial tension, and the two principal radii of curvature, R_1 and R_2.

Now consider two isotropic spheres which are brought together with a torodial liquid bridge forming a zero contact angle between them, Fig. 12. Let the plane of the figure be described by the x-axis along 0-0 and the y-axis perpendicular to 0-0. An analogous pressure difference exists across the liquid-vapor interface. In this case, the pressure in the liquid is less than in the vapor. Therefore, a net compressive force results at the particle-particle contacts. This force was shown by Heady and Cahn[50] et al.[51,52] to be equal to

$$F = 2\pi y\, \gamma_{\ell v} \cos\theta + \pi y^2 \Delta p \qquad (63)$$

where

$$\Delta p = (p_{vap} - p_{liq})$$

Many previous authors neglected the first term in discussing such force relationships, arguing that since both components of the force are due to $\gamma_{\ell v}$, only the latter term is necessary. However, Heady and Cahn[50] showed that Eq. (63) is the integral form of Eq. (62) with F being a constant of integration, and that only differentation of Eq. (63) will yield Eq. (62).

Using the relationship

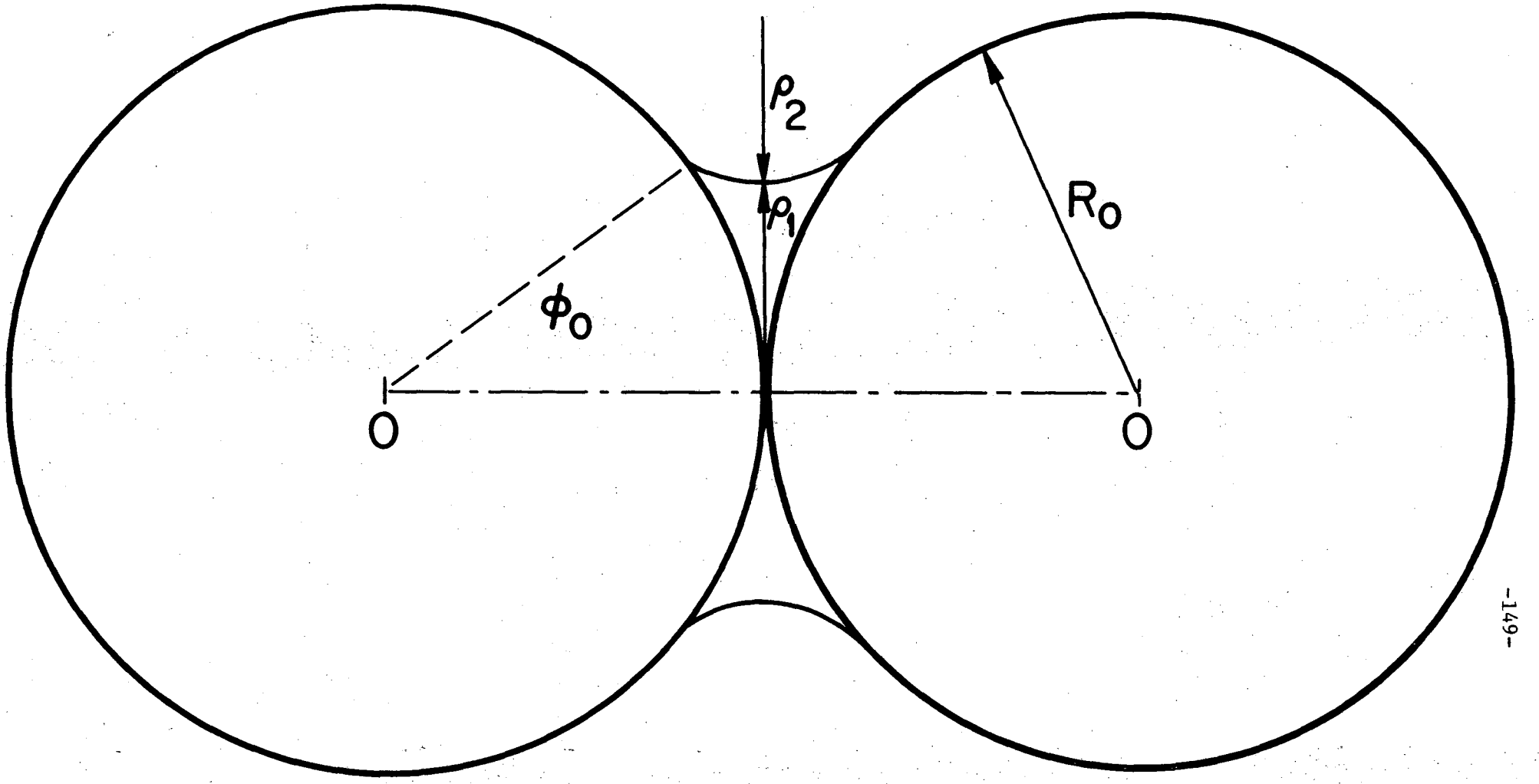

Figure 12. Two sphere model for liquid phase sintering with a wetting liquid forming a bridge between the spheres.

R_o Initial radii of the particles

ρ_1 & ρ_2 Principal radii of curvature of the liquid-vapor interface

XBL7210-4140

$$\cos\ \theta = \frac{1}{\left[1+\left(\frac{dy}{dx}\right)^2\right]^{1/2}} \tag{64}$$

and substituting into Eq. (62)

$$F = \frac{2\pi y\ \gamma_{\ell v}}{\left[1+\left(\frac{dy}{dx}\right)^2\right]^{1/2}} + \pi y^2\ \Delta p \tag{65}$$

since $y = f(x)$

$$\frac{dF}{dx} = 2\pi\ \gamma_{\ell v}\left\{\frac{\left[1+\left(\frac{dy}{dx}\right)^2\right]^{1/2}\ \frac{dy}{dx} - y\left[1+\left(\frac{dy}{dx}\right)^2\right]^{-1/2}\ \left(\frac{dy}{dx}\right)\left(\frac{d^2y}{dx^2}\right)}{\left[1+\left(\frac{dy}{dx}\right)^2\right]}\right\} + 2\pi y\Delta p\ \frac{dy}{dx} \tag{66}$$

Setting $dF/dx = 0$

$$\gamma_{\ell v}\left\{\frac{\frac{dy}{dx}}{\left[1+\left(\frac{dy}{dx}\right)^2\right]^{1/2}} - y\ \frac{\left(\frac{dy}{dx}\right)\left(\frac{d^2y}{dx_2}\right)}{\left[1+\left(\frac{dy}{dx}\right)^2\right]^{3/2}}\right\} = -\ y\Delta p\ \frac{dy}{dx} \tag{67}$$

The radius of curvature in the xy plane is

$$\frac{1}{R_2} = \frac{d^2y}{dx^2} \Big/ \left(1 + \left(\frac{dy}{dx}\right)^2\right)^{3/2} \tag{68}$$

and the radius of curvature perpendicular to $1/R_2$ is

$$\frac{1}{R_1} = \frac{-\quad 1}{y\left[1+\left(\frac{dy}{dx}\right)^2\right]^{1/2}} \tag{69}$$

The minus sign occurs in Eq. (69) since R_1 and R_2 are of opposite curvatures.

Substituting Eqs. (68) and (69) into (67) yields

$$\gamma_{\ell v}\left[-\frac{1}{R_1} - \frac{1}{R_2}\right] = -\Delta p \quad \text{or} \quad \gamma_{\ell v}\left[\frac{1}{R_1} + \frac{1}{R_2}\right] = \Delta p \tag{70}$$

which is identical to Eq. (62). The above derivation is due to Heady and Cahn.[50]

Eremenko[35] has derived a general equation for the force between two identical spheres as a function of radii of curvature, contact angle θ, and the degree of coverage of the spheres by the liquid, Φ_0. Although the shape of the liquid-vapor interface, called the Noidoid of Plateau,[51] is not circular using the approximation of a circular arc introduces only slight errors into the analysis and circuvents much mathematical difficulty. Thus the force is given by[50]

$$F = \gamma_{\ell v}\left[\pi R_0^2 \sin \Phi_0 \left(\frac{1}{\rho_2} - \frac{1}{\rho_1}\right) + 2\pi R_0 \sin^2 \Phi_0\right] \tag{71}$$

where

$$\rho_1 = R_0 \sin \Phi_0 - (R_0 (1-\cos \Phi_0))\left(1 - \frac{\sin (\Phi_0 + \theta)}{\cos (\Phi_0 + \theta)}\right) \tag{72}$$

and

$$\rho_2 = \frac{R_0(1 - \cos \Phi_0)}{\cos (\Phi_0 + \theta)} \tag{73}$$

Increasing amounts of liquid cause the forces between the particles to decrease as do increasing values of the contact angle[35] at values of $\theta > 90°$, the particles begin to repel since tensile forces result.

For the case where the particles in a compact are completely coated with liquid, spherical pores tend to develop in the liquid as discussed in the previous section. In such configurations, there is no solid-liquid-vapor triple point and the force is given by

$$F = \pi R^2 \Delta p \tag{74}$$

The formation of spherical pores containing vapor can lead to entrapment of gases and thus back pressures can build up in the pores. If one assumes that the pressure difference between the pore and the liquid is proportional to the volume of the pore at any time, divided by the original pore volume,

$$R^3/R_0^3 \tag{75}$$

then the pressure difference may be approximated as

$$\Delta p = \frac{2\gamma}{R} \quad (R^3/R_o^3) \tag{76}$$

and therefore Eq. (74) would become

$$F = \pi R^2 \left(\frac{2\delta_{\ell v}}{R}\right)\left(\frac{R_3}{3}\right)_{R_0} \tag{77}$$

As the pore radius shrinks, the pressure difference approaches zero.

C. Kinetics of Liquid Phase Sintering: Solution-Precipitation

1. Small Volumes of Liquid; Similar Sized Particles

Upon completion of the rearrangement stage of liquid phase sintering, the liquid content, the solid-liquid-vapor contact angle, and the liquid-vapor interfacial energy control the shape of the porosity in the sintering compact.[16] The shape of the porosity in turn determines the capillary forces acting on the system. Figure 12 shows a two sphere model having a liquid bridge between the spheres. The curvature of the liquid-vapor interface causes a lower pressure in the liquid than in the pore, and a corresponding increased pressure in the region between the spheres.[50,33,35] The pressure difference between the liquid and the region between the spheres may be expressed as

$$\Delta p = \gamma_{\ell v} \left(\frac{1}{\rho_2} - \frac{1}{\rho_1}\right) + \frac{2\gamma_{\ell v}}{R_0} \tag{78}$$

where ρ_1 and ρ_2 are the principal radii of curvature and R_0 is the radius of the particle. The first term in this equation is the Laplace pressure difference due to the curvature of the liquid-vapor interface and the second term is due to the surface tension force around the perimeter of the liquid-vapor interface.

If sufficient liquid is present to form a spherical pore directly after rearrangement, the pressure difference is given by

$$\Delta p = \gamma_{\ell v} \left(\frac{1}{r_p} + \frac{1}{r_p}\right) = \frac{2\gamma_{\ell v}}{r_p} \tag{79}$$

where r_p is the radius of the spherical pore. The fugacity of a component in a liquid increases with increasing pressure if the partial molar volume of that component is positive,[53] and the relationship between the fugacity and the pressure is then given by

$$\int_{p_r}^{p} \frac{\bar{v}_2 \, dp}{NkT} = \int_{f(p_r)}^{f(p)} d\ell nf \tag{80}$$

where $\bar{v}_2$ is the partial molar volume of the solute, called component 2; p_r is the pressure in the liquid; p is the pressure between the spheres which is caused by stresses created by the curvature of the liquid-vapor interface; and f is the fugacity of the solute (component 2). If Amagat's law is assumed to hold,[53] the partial molar volume of component i in the liquid, $\bar{v}_i$ is equal to the molar volume, v_i^o, that is

$$V = \sum_i x_i \bar{v}_i = \sum_i x_i v_i^o \tag{81}$$

since

$$\bar{v}_i = \left(\frac{\partial V}{\partial n_i}\right)_{T,P,n_j} = v_i^o \tag{82}$$

v_i^o the molar volume, which is constant at a particular temperature and pressure can then be substituted into Eq. (80) and can be removed from the integral. Thus Eq. (80) may be integrated directly to yield

$$\ell n \left(\frac{f_{(p)}}{f_{(p_r)}} \right) = \frac{v_2^o \, \Delta p}{NkT} \tag{83}$$

Using the ideal solution approximation,

$$\ell n \left(\frac{x_{(p)}}{x_{(p_r)}} \right) = \frac{v_2^o \, \Delta p}{NkT} \tag{84}$$

where x is the mole fraction of component 2. Equation (84) is similar in form to the equation used by Kingery[33] in his derivation of a densification versus time equation for the solution-precipitation stage of liquid phase sintering for systems forming zero dihedral angles. In his derivation, the pressure difference, $(p-p_r)$, corresponded to that determined by Eq. (80). That is, spherical shaped porosity which occurs after the rearrangement stage in compacts having large volume fractions of liquid phase. Additionally, he did not differentiate between the geometry of Fig. 12, toroidal shaped porosity (small volume fraction of liquid case), and spherical shaped porosity.

If one defines a stage in sintering as an interval during which the pore shape remains constant, as well as an interval during which the sintering mechanism remains constant, there are clearly two stages of solution-precipitation in compacts having small volume fractions of liquid phase and therefore, two models are necessary to describe the sintering kinetics.

The first stage is characterized by toroidal shaped porosity, as shown in Fig. 12, and the second stage is characterized by the formation of spherical porosity. Compacts containing small volume fractions of liquid phase are subjected to both stages during densification. If sufficient liquid is present to form spherical porosity directly after the rearrangement stage, the first stage (toroidal shaped porosity), does not occur and the kinetics correspond to Kingery's solution which will be designated the second stage or the final stage of solution-precipitation. Since the first stage has not previously been treated, kinetic solutions will be presented here for several sintering geometries using numerical integration techniques which allow more precise geometric descriptions of the sintering models than the method of analytical integration used by Kingery.

Consider a model system consisting of two identically sized spherical particles with a small toroidal shaped liquid bridge between the spheres, Fig. 12. Mechanistically it is assumed that: (1) the rearrangement stage has been completed; (2) only solution-precipitation occurs; (3) the volume of the liquid remains constant; (4) the dihedral angle and contact angle are both equal to zero; (5) the solid is soluble in the liquid but the liquid is insoluble in the solid; (6) material from the region between the spheres is deposited uniformly on the free surfaces of the spheres; and (7) the solid-liquid and liquid-vapor interfacial energies are isotropic.

Referring to Fig. 12, R_0 is the initial radius of the particles, Φ_0 is the angle formed by the intersection of the R_0 vector at the solid-

liquid-vapor triple point and the line 0-0', Φ_0 is determined by the volume of liquid and by R_0. ρ_1^0 and ρ_2^0 are the initial radii of curvature which determine the magnitude of the compressive stresses acting between the two particles.

As sintering proceeds, the particle centers move together along the line 0-0' due to solution of material in the region between the spheres. This material then diffuses through the liquid and is reprecipitated uniformly on the surfaces away from the solution region. Therefore, as sintering proceeds, R_0 increases to R; Φ_0 increases to Φ; and ρ_1^0 and ρ_2^0 increase to ρ_1 and ρ_2, Fig. 13, and a spherical cap of material of height h and radius u is removed from each sphere at the "contact" region and is assumed to be uniformly distributed on the surface of the spheres.

The force between the particles is given by Eq. (71)

$$F = \gamma_{\ell v} \left\{ \pi R^2 \sin^2(\Phi) \left[\frac{1}{\rho_2} - \frac{1}{\rho_1} \right] + 2\pi R \sin^2(\Phi) \right\} \tag{85}$$

In order to convert Eq. (85) to a pressure, it must be divided by an area term. The area chosen will be the projection of the radius of the particles at the solid-liquid-vapor interface onto a plane normal to the line 0-0'. This area increases as the interpenetration of the spherical particles increases, and is given by

$$A = \pi R^2 \sin^2(\Phi) \tag{86}$$

dividing Eq. (85) by Eq. (86),

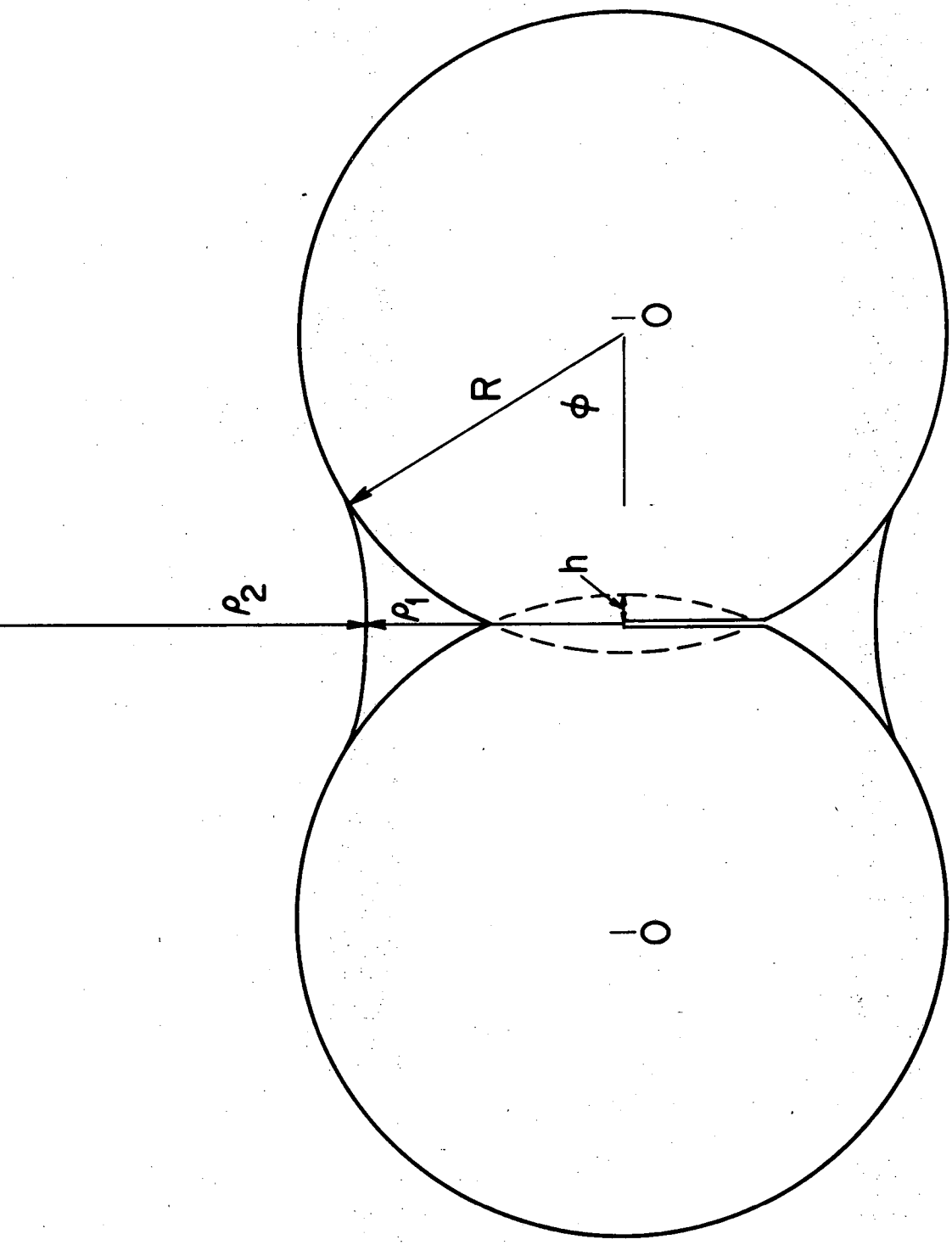

Compressive stresses cause a higher solubility of the solid in the liquid in the "contact" region. A spherical cap of height h is removed from the particles.

XBL 7210-4139

Figure 13. Two sphere model for liquid phase sintering showing the removal of cap material in the "contact" region between the spheres.

$$\frac{F}{A} = \gamma_{\ell v}\left\{\frac{1}{\rho_2} - \frac{1}{\rho_1} + \frac{2}{R}\right\} \tag{87}$$

It is necessary to relate the pressure at the contact region to the pressure exerted by the liquid, and one can reasonably assume that the pressure in the contact or neck region will be inversely proportional to the ratio of the area of the contact region divided by the area of the projection of the particle radius.[34]

$$\frac{F}{A} \alpha \frac{\pi R^2}{\pi u^2} \tag{88}$$

substituting Eq. (88) into (87)

$$\frac{F}{A} = \frac{R^2}{u^2}\gamma_{\ell v}\left\{\frac{1}{\rho_2} - \frac{1}{\rho_1} + \frac{2}{R}\right\} \tag{89}$$

The remainder of the kinetic analysis will be similar to that employed by Kingery for the kinetics of solution-precipitation. The diffusion flux of material from the contact region may be approximated by the radial heat flow from a cylindrical solid that is electrically heated,

$$\frac{J}{A} = 4\pi D\Delta C \tag{90}$$

where J is the diffusion flux, A is a characteristic area, D is the

diffusivity of the solid in the liquid, and ΔC is the difference between the concentration of the solid in the liquid in the contact region and the concentration of the solid in the liquid in regions away from the contact region. If ℓ is the radial diffusion length in the liquid and $\delta = A/\ell$ then

$$J\delta = \frac{dv}{dt} = 4\pi D\Delta C\delta \tag{91}$$

where dv is the differential of volume and dt is the differential of time. Rewritting Eq. (84)

$$x_p - x_{p_r} = x_{p_r}\left\{\exp\left(\frac{\Delta p v_2^o}{NkT}\right) - 1\right\} \tag{92}$$

and substituting Eq. (92) into Eq. (91)

$$\frac{dv}{dt} = 4\pi D\delta x_{p_r}\left\{\exp\left(\frac{\Delta p v_2^o}{NkT}\right) - 1\right\} \tag{93}$$

Since the expansion of an exponential function is given by

$$e^w = \Sigma \frac{w^m}{m!} = \left(1 + \frac{w}{1!} + \frac{w^2}{2!} + \frac{w^3}{3!}\right) \tag{94}$$

by using the first two terms of the expansion of Eq. (94), and substituting the right side of Eq. (93) for w,

$$\frac{dv}{dt} = \frac{4\pi\delta\ Dx_{p_r}\ \Delta p v_2^o}{NkT} \tag{95}$$

Then substituting Eq. (89) into (95)

$$\frac{dv}{dt} = \frac{4\pi\delta Dx\, p_r\, \gamma_{\ell v}}{NkT} \left(\frac{R^2}{u^2}\right) \left\{\frac{1}{\rho_2} - \frac{1}{\rho_1} + \frac{2}{R}\right\} \tag{96}$$

The volume of material removed from the spherical caps between the spheres is

$$V_{cap} = n\pi Rh^2 - \frac{n\pi h^3}{3} \tag{97}$$

where n is the nearest neighbor coordination number of spheres around each particle. The dummy variable P = h/R is then inserted into Eq. (97)

$$V = n\pi R^3 \left(P^2 - \frac{P^3}{3}\right) \tag{98}$$

From a volume balance R is related to R_0,

$$R^3 = \frac{4R_0^3}{(4-3nP^2 + nP^3)} \tag{99}$$

Substituting Eq. (99) into (98) yields

$$\frac{V}{\pi R_0^3} \quad \frac{4n\left(P^2 - \frac{P^3}{3}\right)}{(4-3nP^2 + nP^3)} \tag{100}$$

On differentiating Eq. (100)

$$d\left(\frac{V}{\pi R_0^3}\right) = \frac{16nP(2-P)}{(4-3nP^2 + nP^3)^2}\ dP \tag{101}$$

The differential with respect to time is

$$\frac{dv}{dt} = \frac{16\pi nR_0^3 P(2-P)}{(4-3nP^2 + nP^3)^2}\ \frac{dP}{dt} \tag{102}$$

The radii of curvature in Eq. (96) can be written in terms of the variables, R, h, and Φ, as follows

$$\rho_2 = \frac{R(1 - \cos\ \Phi) - h}{\cos\ \Phi} \tag{103}$$

and

$$\rho_1 = (r-h)\ \tan\ \Phi - (R-h)\ \sec\ \Phi + R \tag{104}$$

R, h, and Φ cannot be related directly but may be related by use of the following approximation which is very accurate for small volume fractions of liquid phase.

$$\cos\ \Phi = \frac{R-2h}{R} \tag{105}$$

Therefore,

$$\rho_2 = \frac{Rh}{R-2h} \tag{106}$$

$$\rho_1 = \frac{2(R-h)\sqrt{Rh - h^2} - Rh}{R-2h} \tag{107}$$

Combining Eqs. (89), (106) and (107),

$$\frac{F}{A} = \frac{\gamma_{\ell v} R^2}{u^2} \left\{ \frac{(R-2h)}{Rh} + \frac{2}{R} - \frac{(R-2h)}{2(R-h)\sqrt{Rh-h^2} - Rh} \right\} \tag{108}$$

rearranging

$$\frac{F}{A} = \frac{2\gamma_{\ell v} R^2}{u^2} \frac{[(R-h)\sqrt{Rh-h^2} - h]}{h\{2(R-h)\sqrt{Rh-h^2} - Rh\}} \tag{109}$$

substituting

$$u^2 = 2Rh-h^2 \text{ and } h = PR \tag{110}$$

into Eq. (109)

$$\frac{F}{A} = \frac{2\gamma_{\ell v} \{(1-P)\sqrt{(1-P)P} - P\}}{RP^2(2-P)\{2(1-P)\sqrt{(1-P)P} - P\}} \tag{111}$$

combining Eqs. (73) and (111)

$$\frac{dV}{dt} = \frac{8\pi\delta DX_{(p_r)} V_2^o \gamma_{\ell v} \{(1-P)\sqrt{(1-P)P} - P\}}{NkTRP^2(2-P)\{2(1-P)\sqrt{(1-P)P} - P\}} \tag{112}$$

Substituting R_0 for R, Eq. (99)

$$\frac{dv}{dt} = \frac{8\pi\delta DX_{(p_r)} V_2^o \quad _v \{(4-3nP^2 + nP^3)^{1/3}}{NkTR_0(4)^{1/3}} \quad X$$

$$X \frac{[(1-P)\sqrt{(1-P)P} - P]\}}{\{P^2(2-P)[2(1-P)\sqrt{(1-P)P} - P]\}} \tag{113}$$

Equating Eqs. (113) and (102)

$$\frac{16n\pi P(2-P)R_0^3}{(4-3nP^2 + nP^3)^2} \frac{dP}{dt} = \frac{8\pi\delta DX_{(p_r)} V_2^o \gamma_{\ell v}}{NkTR_0(4)^{1/3}} \dot{X}$$

$$X \frac{\{(4-3nP^2 + nP^3)^{1/3} [(1-P)\sqrt{(1-P)P} - P]\}}{\{P^2(2-P)[2(1-P)\sqrt{(1-P)P} - P]\}} \tag{114}$$

rearranging

$$\frac{\delta DX_{p_r} V_2^o \gamma_{\ell v} dt}{2nKTR_0^4(4)^{1/3}} = \frac{P^3(2-P)^2}{(4-3nP^2 + nP^3)^{7/3}} \quad X$$

$$X \frac{[2(1-P)\sqrt{(1-P)P} - P]}{[(1-P)\sqrt{(1-P)P} - P]} \quad dP \tag{115}$$

Equating (115) is the differential equation for the kinetics of the initial stage of solution-precipitation. Now let

$$M_1 = \frac{\delta DX_{(p_r)}\ V_2^o\ \gamma_{\ell v}}{2nKTR_0^4\ (4)^{1/3}} \tag{116}$$

and

$$f(P) = \frac{P^3(2-P)[2(1-P)\sqrt{(1-P)P} - P]}{(4-3nP^2 + nP^3)^{7/3}[(1-P)\sqrt{(1-P)P} - P]} \tag{117}$$

Then

$$\int_o^t M_1 dt = \int_o^P f(P)\,dP \tag{118}$$

M_1 is a constant for a particular sintering system and can be removed from the integral. Therefore,

$$M_1 \int_o^t dt = M_1 t \tag{119}$$

On the other hand,

$$\int_o^P f(P)\,dP$$

cannot be integrated analytically, but it may be integrated using numerical techniques. The area under the f(P) versus P curve gives the integral of Eq. (118) up to any value of P. Dividing the integral area term by M_1 yields a value of time, t, corresponding to a particular value of P. Therefore, evaluating Eq. (118) up to a certain value of P, and dividing by M_1 yields the corresponding value of t. Using an electronic

computer, the areas under the f(P) versus P curves were obtained. These areas were then divided by an appropriate value of M_1 to yield values of time. Since the change in volume of a compact is related to h, and its initial volume is related to R_0, h/R_0 may then be plotted versus t to give shrinkage as a function of time. The slope of the curve that is generated gives the exponent of time. From such curves, h/R_0 may be replotted versus R_0 at constant times to give the exponent of particle size. Therefore, one obtains a proportionality of the form

$$h/R_0 \propto (R_0^z)(t^y) \tag{120}$$

This proportionality is independent of the value of M_1 and therefore, the values of y and z are constants for the initial stage of solution-precipitation. They are valid as long as the parameters of the model are not violated. By choosing a particular sintering system, a value of M_1 can be calculated from estimated values of the diffusivity, $\delta = A/\ell$, liquid-vapor interfacial energy, particle size, solubility, and temperature. Figure 14 gives the results of densification versus time for a hypothetical solid-liquid system from P = 0.00 to P = 0.25, (h/R_0 = 0.276), assuming initial particle sizes of 5 microns. The slope of the curves obtained from a log linear least squares analysis yields a value of y = 0.24297. If the least squares analysis is performed from P = 0.00 to P = 0.17, the value of y is 0.24482 indicating that the log (h/R_0) versus log(t) curves are not quite linear. Therefore, the results of the least squares analysis will depend on the upper value of P that is chosen.

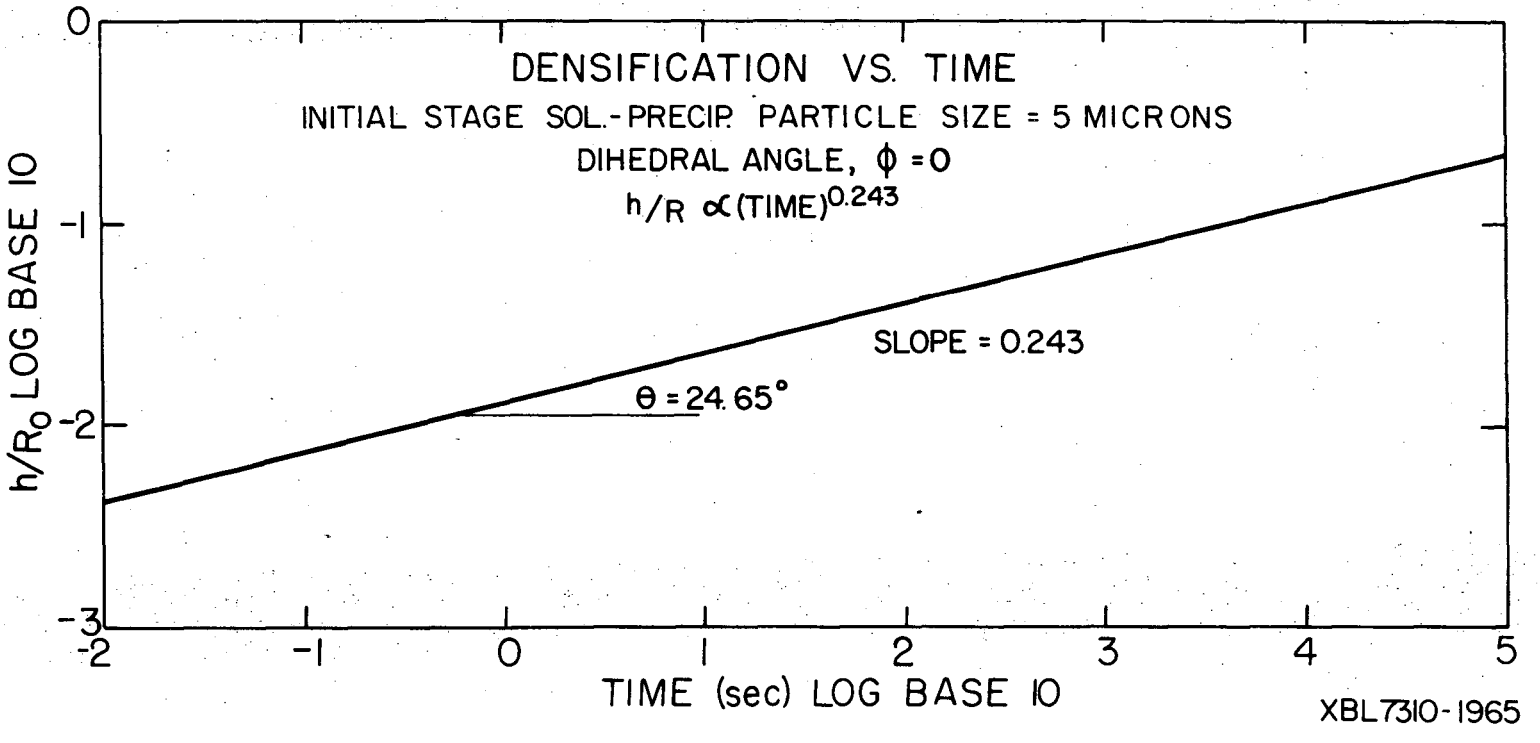

Figure 14. Densification versus time for the initial stage of solution-precipitation. The slope of the curve yields the exponent of time, y.

Figure 15 is a plot of h/R_0 versus the initial particle size of the spheres, R_0, (for P = 0.25). The slope of this curve, determined by using a similar least squares analysis, is z = -0.97186. Substituting these results into Eq. (120)

$$h/R_0 = (R_0^{-0.97186}) \ (t^{0.24297}) \tag{121}$$

Similar results can be obtained for other coordinations of particles. When the upper limit of P is 0.17, the values of y range from 0.24522 to 0.244156 for nearest neighbor particle coordinations from 2 to 12. Corresponding values of z range from -0.98088 for two-fold coordination to -0.97670 for twelve-fold coordination. These results indicate that the values of y and z are relatively independent of the nearest neighbor coordination of spheres.

The initial stage of solution-precipitation is completed upon formation of spherical porosity. At this point, the radii of curvature of the liquid-vapor interface both have the same sign, i.e., the radius of the pore. Since the pressure difference between the pore and the liquid is the described by Eq. (79) instead of Eq. (78), different kinetic conditions apply upon completion of the initial stage of solution-precipitation.

2. Large Volumes of Liquids

As discussed in Section III-C-1, for liquid phase sintering compacts, the initial stage of solution-precipitation is terminated in systems containing less than 27.6% liquid phase (27.6% of the original volume of the simple cubic cell, or 34.3% of the volume of a theoretically dense

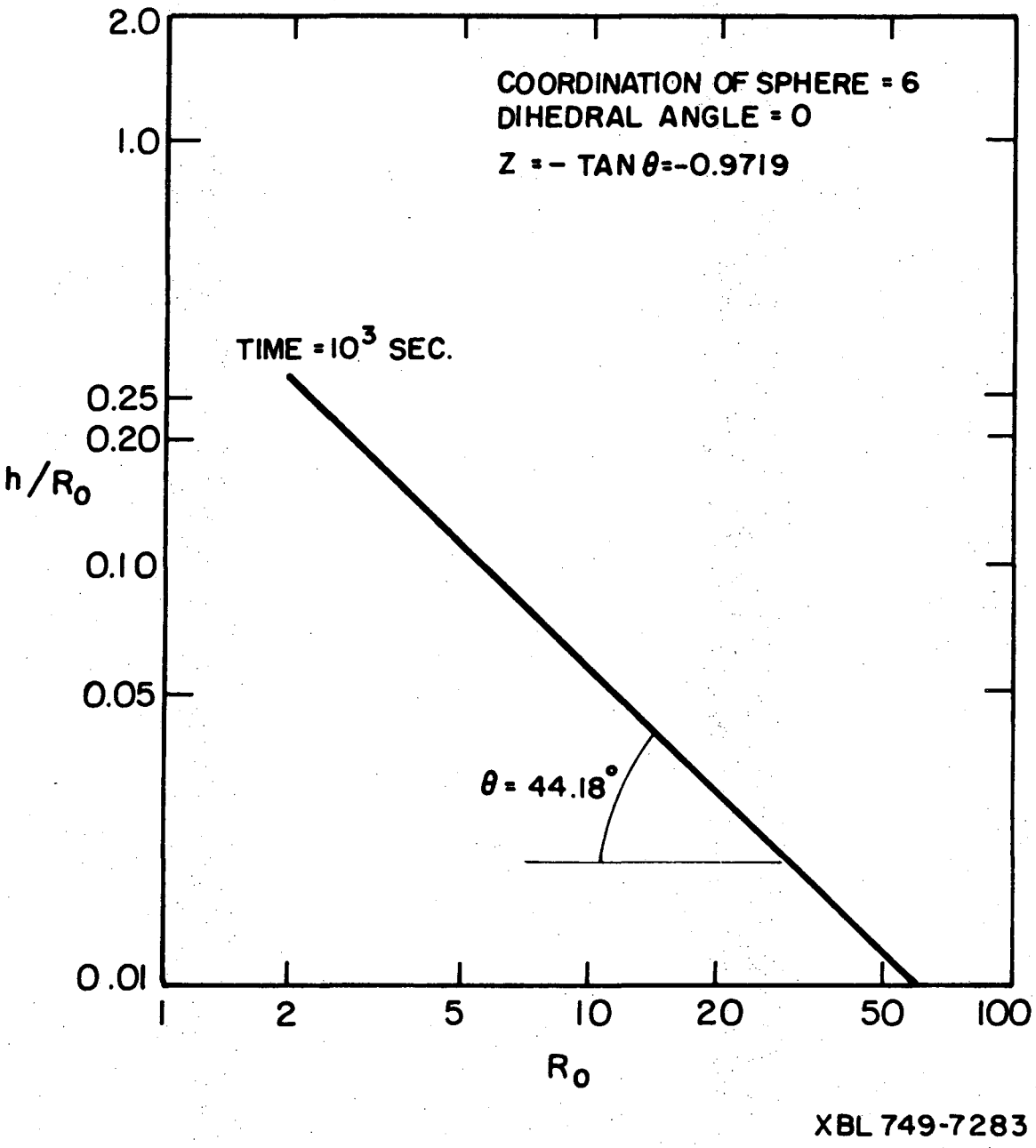

Figure 15. Densification versus initial particle size. The slope of the curve yields the exponent of particle size, z.

compact), upon formation of spherical porosity. At this point, both principal radii of curvature of the liquid-vapor interface have the same sign and magnitude, i.e., the radius of the pore, r_p. The kinetic equation derived in Section III-C-1 corresponds to the initial stage of solution-precipitation and breaks down at this point. The equations derived below are valid for the final stage or for compacts having more than 27.6% liquid phase. The geometry of these systems is characterized by spherical pores and it is assumed that sintering has proceeded through the initial stage, or that the compact contains sufficient liquid to form spherical porosity directly upon completion of the rearrangement stage. Since the initial stage of solution-precipitation is characterized by open porosity, there is no effect of the ambient atmosphere above the compact on sintering kinetics. However, since the final stage is characterized by a closed pore phase, two cases must be considered: the first neglecting the effect of atmosphere and the second, taking into account the effect of the buildup of a back pressure in the pores.

As was shown in Section III-C-1, the coordination of uniform sized spherical particles has only a slight effect on sintering kinetics. Therefore, without loss of generality, it is possible to treat the simplest geometric model and to expect that similar sintering kinetics would apply to more complex geometric assemblages.

The model described here is identical to the thermodynamic model of Section II, (for a zero dihedral angle), and assumes that the rearrangement stage is completed and has resulted in an array of eight uniform sized, isotropic, spherical particles in a simple cubic array. The volume of a unit cell formed by such a configuration is $8R_0^3$, where R_0 is

the initial radius of the particles. Each cell contains the volume of one spherical particle occupying a volume of $4.16R_0^3$. The remaining void space in the cell is $3.84R_0^3$ which can contain liquid and pore phases. If less than 16.3% of the original cell volume is liquid phase, insufficient liquid is present to completely coat the spheres.[51] Between 16.3% and 27.6%, the spheres are completely coated but the shape of the liquid-vapor interface is toroidal. At liquid volumes larger than 27.6%, spherical porosity forms at the center of the simple cubic cell.

For any volume fraction of pore phase, as sintering proceeds, material is removed from spherical caps at particle-particle contacts, and is deposited at particle surfaces away from the contact region in a mechanistically identical manner as described for the initial stage of solution-precipitation. Particle centers thus move together, shrinking the volume of the cell and squeezing liquid into the remaining void space, causing densification.

Compacts containing less than 27.6% liquid phase follow the sintering kinetics characterized by the initial stage of solution-precipitation (Section III-C-1) until spherical porosity forms. Upon formation of spherical pores, the sintering kinetics change and the value of P at which the model breaks down is then determined by the volume fraction of liquid phase in the compact.

Proceeding with the analysis, all conditions of Section III-C-1 apply except that the shape of the porosity is spherical. The volume of the sintering cell (Fig. 1 of Section II), at any degree of densification is

$$V_{cell} = 8(R-h)^3 \tag{122}$$

Substituting h = PR into Eq. (122)

$$V_{cell} = 8R^3(1-P)^3 \tag{123}$$

For simple cubic packing, R and R_0 are related by

$$F^3 \frac{4R_0^3}{(4-18P^2 + 6P^3)} \tag{124}$$

Substituting Eq. (124) into Eq. (123)

$$V_{cell} = \frac{32R_0^3(1-P)^3}{(4-18P^2 + 6P^3)} \tag{125}$$

The volume of the spherical particle remains constant, and is given by

$$V_{sphere} = \frac{4\pi R_0^3}{3} \tag{126}$$

The volume of liquid in the cell is called $V_{liq}R_0^3$, and therefore, the volume of the porosity at any degree of densification is

$$V_{pore} = V_{cell} - V_{sphere} - V_{liq}\,R_0^3 \tag{127}$$

Substituting Eqs. (125) and (126) into (127)

$$V_{pore} = \frac{32R_0^3(1-P)^3}{(4-18P^2 + 6P^3)} - \frac{4\pi R_0^3}{3} - V_{liq} R_0^3 \tag{128}$$

When sufficient sintering has occurred, a spherical pore forms in the center of the simple cubic cell. Its volume is given by

$$V_{pore} = \frac{4\pi r_p^3}{3} \tag{129}$$

Substituting Eq. (129) into (128)

$$\frac{4\pi r_p^3}{3} = \frac{32R_0^3 (1-P)^3}{(4-18P^2 + 6P^3)} - \frac{4\pi R_0^3}{3} - V_{liq} R_0^3 \tag{130}$$

and rearranging,

$$\frac{r_p}{R_0} = \left\{ \frac{96(1-P)^3 - (4\pi + 3V_{liq})(4-18P^2 + 6P^3)}{4\pi(4-18P^2 + 6P^3)} \right\}^{1/3} \tag{131}$$

The pressure difference between the pore and the liquid is given by Eq. (79) of Section III-C, Part B.

$$\Delta p = \frac{2\gamma_{\ell v}}{r_p} \tag{132}$$

Substituting Eq. (131) into Eq. (132)

$$\Delta p = \frac{2\,\gamma_{\ell v}}{R_0}\left\{\frac{4\pi(4-18P^2+6P^3)}{96(1-P)^3-(4\pi+3V_{liq})(4-18P^2+6P^3)}\right\}^{(1/3)} \tag{133}$$

assuming that

$$\Delta p \propto \frac{R^2}{\mu^2} = \frac{1}{P(2-P)} \tag{134}$$

and substituting Eq. (134) into Eq. (133)

$$\Delta p = \frac{2\,\gamma_{\ell v}}{R_0 P(2-P)}\left\{\frac{4\pi(4-18P^2+6P^3)}{96(1-P)^3-(4\pi+3V_{liq})(4-18P^2+6P^3)}\right\}^{1/3} \tag{135}$$

Substituting Eq. (134) into Eq. (95) of Section III-C, Part B,

$$\frac{dV}{dt} = \frac{8\pi D\delta\,\gamma_{\ell v}\,X_{(p_r)}\,V_2^0}{NkT\,R_0 P(2-P)}\;X$$

$$X\left\{\frac{4\pi(4-18P^2+6P^3)}{96(1-P)^3-(4\pi+3V_{liq})(4-18P^2+6P^3)}\right\}^{1/3} \tag{136}$$

For a nearest neighbor particle coordination of n = 6, Eq. (102) of Section III-C becomes

$$\frac{dV}{dt} = \frac{96\pi R_0^3\,P(2-P)}{(4-18P^2+6P^3)}\,\frac{dP}{dt} \tag{137}$$

Equating Eqs. (136) and (137)

$$\frac{\delta D\, \gamma_{\ell v}\, X_{(p_r)} V_2^0 dt}{12NKT\, R_0^4} = \left\{ \frac{P^2(2-P)^2}{(4-18P^2+6P^3)^{7/3}} \right\} \quad X$$

$$X \left\{ \frac{4\pi}{96(1-P)^3 - (4\pi + 3V_{liq})(4-18P^2+6P^3)} \right\}^{[-1/3]} dP \qquad (138)$$

Equation (138) is the differential equation for the kinetics of densification for the final stage of solution-precipitation, or for compacts containing large liquid volumes, neglecting the effect of back pressure in the pores. If sintering occurs under conditions where the gas phase affects kinetics, the back pressure in the pores must be considered, and it is reasonable to assume that the pressure difference between the pore and the liquid, Δp is proportional to the cube of the radius of the pore at any particular value of P divided by the cube of the radius of the pore when spherical porosity first forms, r_{p_0}.

$$\Delta p \propto \frac{r_p^3}{r_{p_0}^3} \qquad (139)$$

Using this relationship, a similar equation to Eq. (138) can be derived,

FINAL STAGE OF SOLUTION-PRECIPITATION

$$\frac{\delta D x^L V_0 \gamma_{LV}}{12 N k T R_0^4}\, dt = \frac{P^2(2-P)}{(4-18P^2+6P^3)^{7/3}} \left\{ \frac{4\pi}{96(1-P)^3-(4\pi+3V_{LIQ})(4-18P^2+6P^3)} \right\}^{-1/3} dP$$

NO BACK PRESSURE

$$\frac{\delta D x^L V_0 \gamma_{LV}}{12 N k T R_0^4}\, dt = \frac{P^2(2-P)\, r_{P_0}^3}{(4-18P^2+6P^3)^{4/3}} \left\{ \frac{4\pi}{96(1-P)^3-(4\pi+3V_{LIQ})(4-18P^2+6P^3)} \right\}^{+2/3} dP$$

BACK PRESSURE INCLUDED

XBL7310-1956

$$\frac{D\delta X_{(P_r)}\ \gamma_{\ell v}\ V_2^0\ dt}{12NKT\ R_0^4} = \left\{ \frac{P^2(2-P)^2\ r_{P_0}^3}{(4-18P^2+6P^3)^{4/3}} \right\} \quad X$$

$$X \left\{ \frac{96(1-P)^3 - (4\pi - 3V_{liq})(4-18P^2+6P^3)}{4\pi} \right\}^{-(2/3)} \qquad (140)$$

This equation is the differential equation for the kinetics of the final stage of solution-precipitation with the effect of back pressure included.

For sintering systems containing more than 27.6% liquid, (34.3% of the volume of a theoretically dense compact), Eqs. (138) and (140) are valid at any value of P. In systems containing less than this volume of liquid, Eqs. (138) and (140) are only applicable at values of P greater than the particular value of P at which spherical porosity forms in the cell. Equation (131) was derived assuming that the void volume was in the shape of a sphere. If Eq. (131) is used at void volumes which do not correspond to spherical porosity, the calculated value of r_p is too large. Therefore, Eq. (131) is not valid until sufficient densification has occurred to form spherical porosity at the center of the sintering simple cubic cell. The amount of densification necessary for such a configuration depends on the volume of liquid phase present in the compact. The method for calculating the value of P at which Eq. (131) becomes valid was presented in Section II of Part B. This value, called p_s, corresponds to the completion of the initial stage of solution-precipitation and the start of the final stage, and is shown as a

function of the volume fraction of liquid phase in Fig. 2 of Section II, Part B.

Using an analysis similar to that used in Section III-C, of Part B, numerical integration of Eq. (138) and (140) yields the areas under the f(P) versus P curves. From these curves, $\log(h/R_0)$ vs log(time plots) are obtained yielding, from their slopes, the exponent of time, y. Corresponding plots of $\log(h/R_0)$ vs log (R_0) at constant time, yield the exponent of particle size, z.

Figure 16 is a fourth order fit of $\log(h/R_0)$ vs log(time) for a liquid content of 34.3% assuming no back pressure effects in the pores and Fig. 17 is a similar plot for 34.3% liquid assuming a back pressure in the pores. For this volume fraction of liquid, the initial stage does not occur and sintering proceeds directly from the rearrangement stage to the final stage of solution-precipitation. The exponent of time, y, in Figs. 16 and 17, which was obtained using a linear least squares analysis, is given in Table I.

Table I

Final Stage of Solution-Precipitation	
Volume of liquid as percent of a theoretically dense compact	Exponent of time, y
4.4%	0.540
20.0%	0.465
34.3% (no back pressure)	0.362
34.3% (with back pressure)	0.282

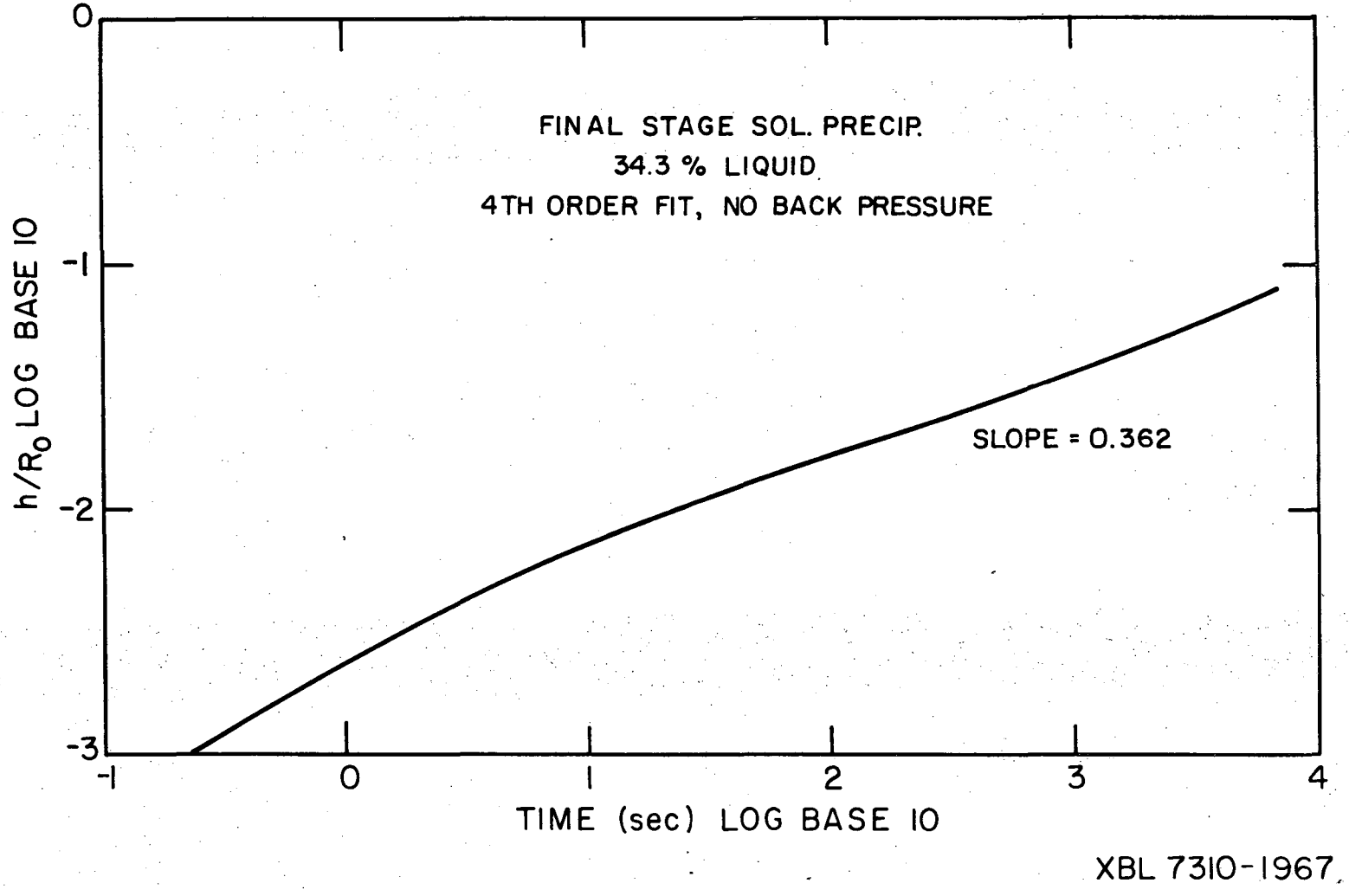

Figure 16. Densification versus time for the final stage of solution-precipitation with no back pressure in the pores.

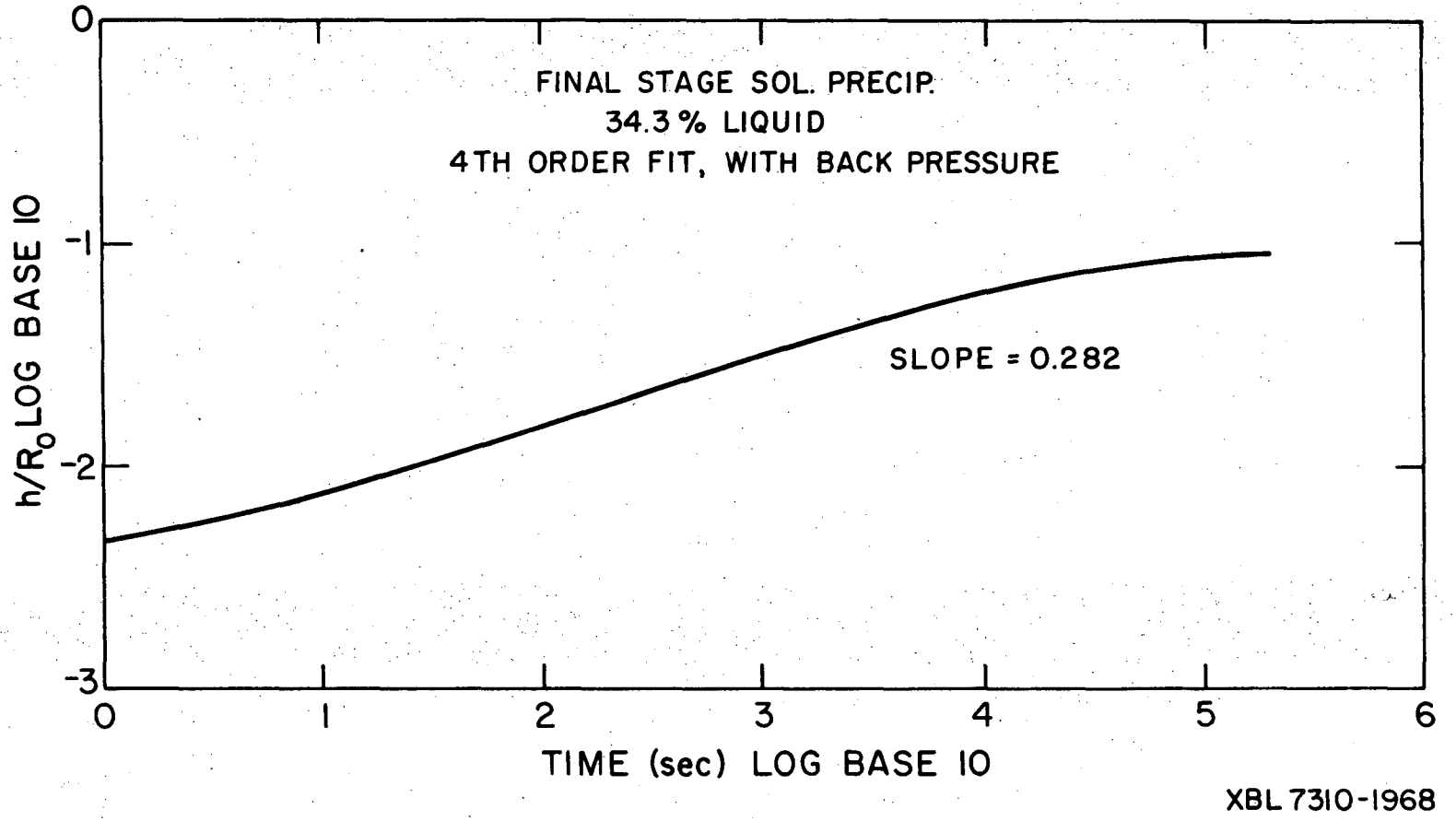

Figure 17. Densification versus time for the final stage of solution-precipitation with a buildup of a back pressure in the pores as sintering proceeds.

The value of y is 0.36 when the back pressure is neglected, Fig. 16, and is 0.28 when the back pressure is included, Fig. 17. Therefore, the effect of back pressure in the pores is to retard the sintering kinetics. Additionally, the densification versus time curve in Fig. 17 approaches theoretical density for the model asymptotically, thus theoretical density is never attained. Also included in Table I are the values of the exponent, y, for the final stage of solution-precipitation for compacts containing 4.4% liquid and 20% liquid. In such systems, after rearrangement, the kinetics are characterized by the initial stage of solution-precipitation until spherical porosity forms. The exponent of time for the final stage in compacts containing 4.4% liquid phase then becomes equal to 0.54 and for compacts containing 20% liquid phase it becomes 0.465. By comparing the volume fraction of liquid phase with the magnitude of the exponent, y, for the final stage of solution-precipitation one sees that as the volume fraction of liquid decreases, the value of y increases. The reason for this increase in the magnitude of the exponent y, is that the spherical pore shrinks at a nonuniform increasing rate as the radius of the pore decreases. In systems containing small volume fractions of liquid phase, spherical porosity does not form until the cubic cell is practically densified. Therefore, the radius of the spherical pore that forms is small and shrinks rapidly as P increases. The corresponding pressure difference between the pore and the liquid thus becomes large and the kinetics are enhanced.

Since the final stage of solution-precipitation occurs in conjunction with the initial stage for compacts with less than 34.3% liquid, log linear combinations have been made for liquid contents corresponding

to 4.4% and 20% liquid phase, Figs. 18 and 19. The resulting combinations were then refitted to a log linear least squares fit, yielding from the slopes of the curves, y = 0.25 for 4.4% liquid and y = 0.305 for 20% liquid. Therefore, as the volume fraction of liquid phase increases, the exponent of time increases for the combination of the initial and final stages of solution-precipitation and the value of y approaches 0.36 which corresponds to the formation of spherical porosity directly after the rearrangement stage.

3. Particles of Dissimilar Sizes

In a two component system if a semi-infinite planar solid, (called component 2), is in contact with a liquid, (called component 1), interdiffusion will occur in both phases until[53]

$$f_1^S = f_1^L \quad \text{and} \quad f_2^S = f_2^L \tag{141}$$

where f is the fugacity and S and L refer to the solid and liquid phases respectively. If the liquid is insoluble in the solid, but the solid is soluble in the liquid and use is made of the ideal solution approximation, it can be shown that[53]

$$\ell n(X_2^L) = \frac{-\Delta h^f(T_t)}{NKT}\left(1 - \frac{T}{T_t}\right) + \frac{(T_t - T)}{T}\Delta Cp - \Delta Cp\ \ell n\left(\frac{T_t}{T}\right) \tag{142}$$

where X_2^L is the mole fraction of the solid (component 2) in the liquid

T_t is the triple point temperature

$\Delta h^f_{(T_t)}$ is the heat of formation at the triple point

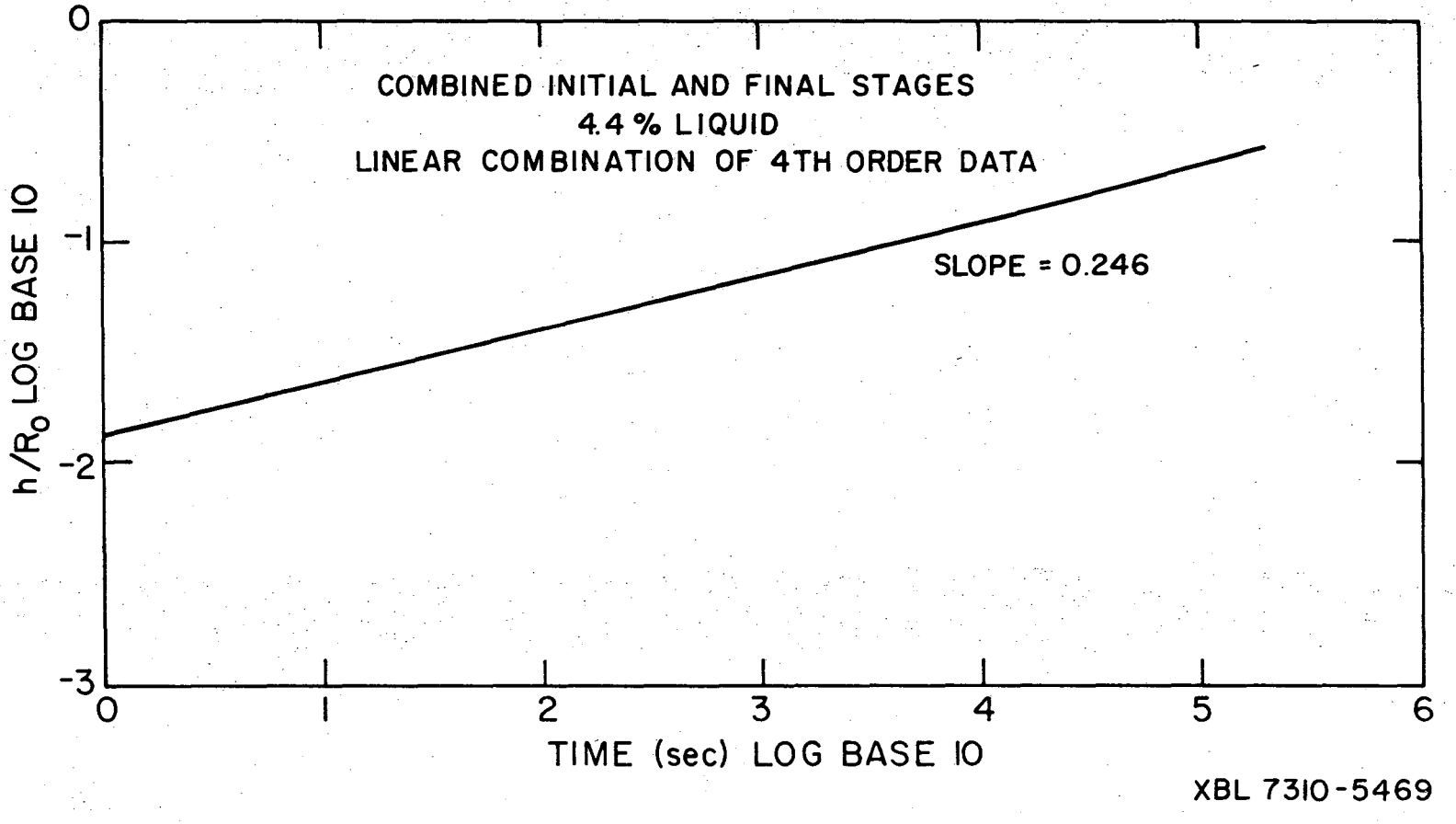

Figure 18. Densification versus time for a combination of the initial stage and final stage of solution-precipitation for a compact containing 4.4% liquid phase.

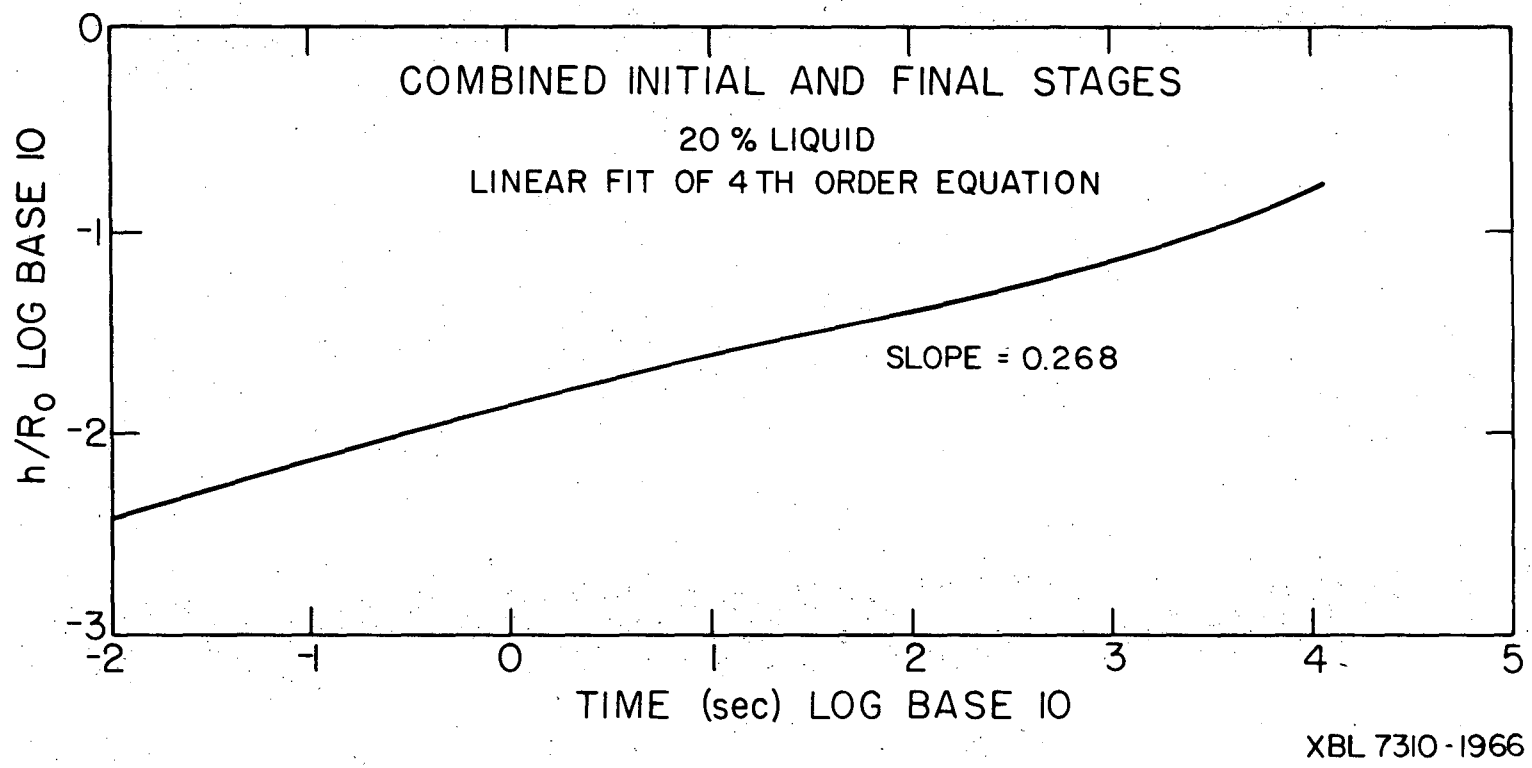

Figure 19. Densification versus time for a combination of the initial stage and the final stage of solution-precipitation for a compact containing 20% liquid phase.

ΔC_p is the difference in heat capacity between the liquid and the solid.

If a solid surface is not planar but rather convex, as is the case for spherical particles, the solubility of the solid (component 2) in the liquid is greater than above, a planar interface as shown by the Kelvin equation[38-41]

$$\ell n \left(\frac{X^L_{2(R)}}{X^L_{2(\infty)}} \right) = \frac{V^0_2}{NKT} \left\{ \frac{1}{r_1} + \frac{1}{r_2} \right\} \tag{143}$$

where $X^L_{2(R)}$ is the mole fraction of component 2 over a convex surface

V^0_2 is the molar volume of component 2

r_1 and r_2 are the principal radii of curvature of the solid surface

$X^L_{2(\infty)}$ is the solubility above a planar surface.

Consider the geometry of Fig. 20, all the conditions of Section III-C apply except that the two spherical particles are of dissimilar size. The solubility of the solid in the liquid above the smaller particle is $X^L_{2(R_s)}$ where R_s is the radius of the small particle, and the solubility above the larger particle is $X^L_{2(R_L)}$ where R_L is the radius of the larger particle.

If the dissolution step of component 2 is not rate determining but rather diffusion of component 2 in the liquid is rate controlling, the concentration of the solid in the liquid in Fig. 20 will approach $X^L_{2(R_s)}$. Therefore, component 2 will tend to dissolve at the surface of the smaller particle and to precipitate at the surface of the larger particle. In a sintering compact, this type of solution-precipitation does not lead to densification since the particle centers do not move

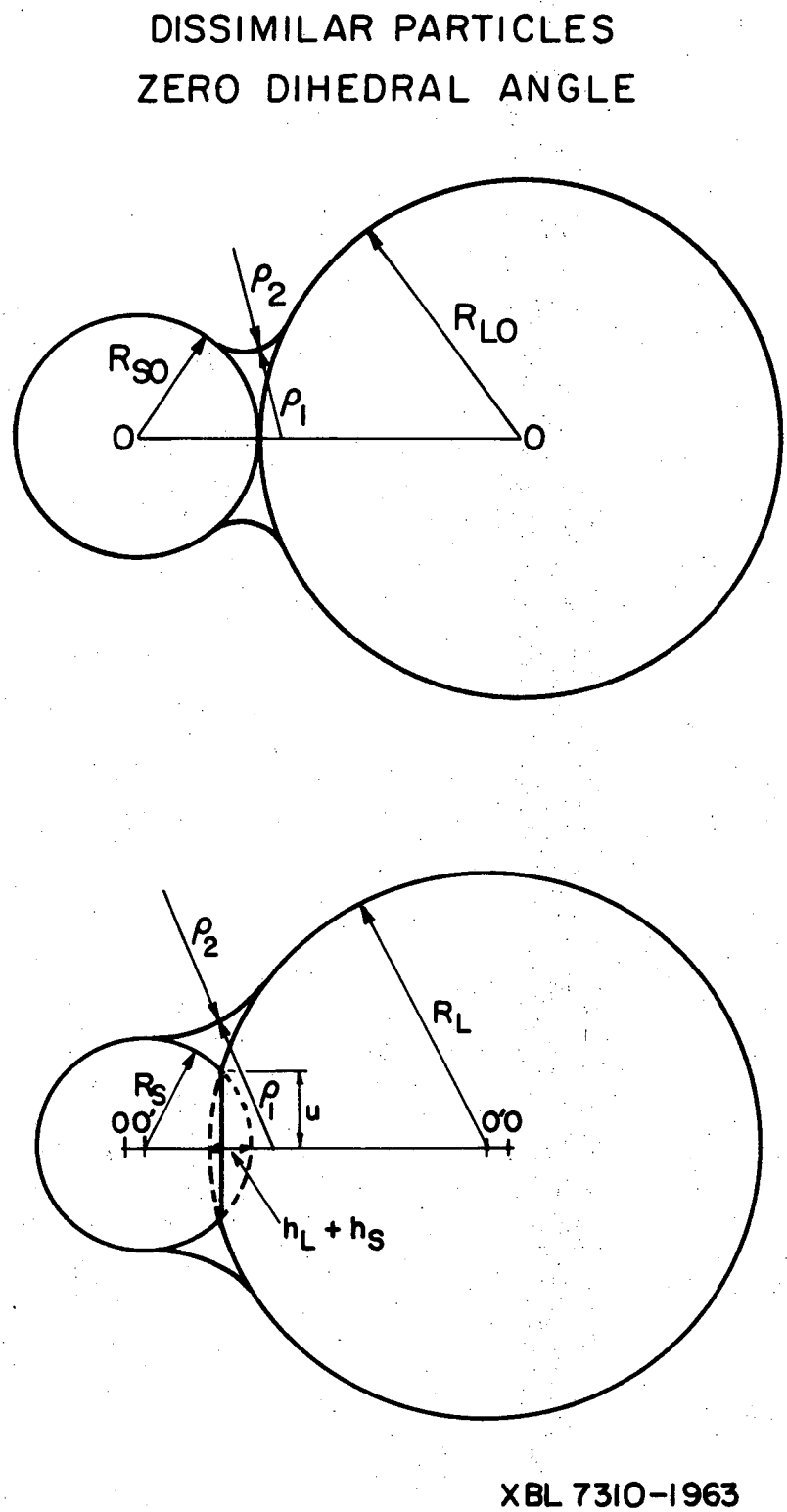

Figure 20. Two sphere model for liquid phase sintering by solution-precipitation for dissimilar sized spherical particles, (top). Configuration when particles just touch.
(bottom) Configuration after some degree of densification.

together even though there is a redistribution of material from the smaller particle to the larger particle. However, densification can occur by the same solution-precipitation mechanism discussed in Section III-C-1 due to the pressure difference created by the curvature of the liquid-vapor interface, assuming that the solid-liquid dihedral angle is zero. Equation (84) of Section III-C-1 relates the solubility of the solid in the liquid in the "contact" region between the spheres to the solubility in the liquid at the free surfaces,

$$\ell n \left(\frac{X^L_{2(P)}}{X^L_{2(P_r)}} \right) = \frac{V^0_2 \, \Delta P}{NKT} \tag{144}$$

For particles of similar size $X^L_{P(r)}$ the solubility of the solid in the liquid, (equal to $X^L_{2(R)}$), is the same near the surface of each spherical particle. Precipitation of material diffusing from the "contact" region occurs equally on the surfaces of both particles. However, in compacts containing different size particles $X^L_{P(r)}$ is determined by the solubility of the smaller particle which has a higher solubility. Material dissolving in the contact region and diffusing toward the free surfaces of the particles thus can deposit on the larger or the smaller particle but since the solubility is less above the surface of the larger particle than above the surface of the smaller particle, there will be a preferential precipitation of material on the larger particle. In real systems it is not known what fraction of material diffusing from the contact region will deposit on either surface but it will definitely depend on the particle size difference since the concentration gradient between the contact region and the region above the surface

of the larger particle will increase as the particle size difference increases.

Therefore to simplify the analysis somewhat, it is assumed here that all the material removed from the contact region between the spheres will precipitate on the surface of the larger particle. Therefore, all the material removed from the spherical caps between the particles is assumed to deposit on the surface of the larger particle.

Proceeding with the analysis, the same conditions will apply as for the model in Section III-C-1 except that the particles have different radii. The radius of the larger particle increases during solution-precipitation, while the radius of the smaller particle stays constant although the volume of the smaller particle decreases due to the loss of cap material from the "contact" region.

After some degree of densification, the particle geometry is similar to that of Fig. 20b. A contact region of radius u forms between the particles, (actually there is a thin film of liquid between the particles as dictated by the criterion of a zero dihedral angle). A cap of material of height h_s is removed from the small sphere and one of height h_L is removed from the large sphere. Let $P_s = h_s/R_{so}$ and $P_L = h_L/R_L$. Since all material removed from the caps is assumed to be deposited on the large particle, the radius of the large particle increases from R_{LO} to R_L but the radius of the small particle remains constant at R_{so}.

The volume of the large and small caps are respectively

$$V_{\text{large cap}} = \frac{n_L \pi P_L^2 R_L^3 (3-P_L)}{3} \qquad (145)$$

where n_L is the coordination of the smaller particles around the larger particle.

$$V_{\text{small cap}} = \frac{n_s \pi P_s^2 R_{so}^3 (3-P_s)}{3} \tag{146}$$

and n_s is the coordination of large particles around the small particle.

Balancing the volumes, the effective volume of the large sphere is

$$\frac{4\pi R_L^3}{3} = \underbrace{\frac{n_L \pi P_L^2 R_L^3 (3-P_L)}{3}}_{\text{cap of large particle}} + \underbrace{\frac{n_s \pi P_s^2 R_{so}^3 (3-P_s)}{3}}_{\text{cap of small particle}} + \underbrace{\frac{4 R_{LO}^3}{3}}_{\text{original volume of large particle}} \tag{147}$$

rearranging,

$$R_L^3 \left[1 - \frac{n_L P_L^2 (3-P_L)}{4} \right] = R_{LO}^3 + \frac{n_s P_s^2 R_{so}^3 (3-P_s)}{4} \tag{148}$$

The area of the contact region is given by

$$\pi u^2 = R_{so}^2 P_s (2-P_s) = R_L^2 P_L (2-P_L) \tag{149}$$

solving for R_L^3

$$R_L^3 = \left[\frac{(2-P_s)}{(2-P_L)} \frac{P_s}{P_L} \right]^{3/2} R_{so}^3 \tag{150}$$

Substituting for R_L^3 in Eq. (148) and rearranging

$$\left[\frac{(2-P_s)\ P_s}{(2-P_L)\ P_L}\right]^{3/2}\left\{1 - \frac{n_L P_L^2(3-P_L)}{4}\right\} - \frac{n_s P_s^2(3-P_s)}{4} = \frac{R_{LO}^3}{R_{so}^3} = W \qquad (151)$$

Using an electronic computer, values of P_L corresponding to incremental changes in P_s of 0.01 were obtained for several different ratios of $R_{LO}^3/R_{so}^3 = W$. These P_L and P_s values were then fitted to a third order polynomial equation using a least squares analysis. Equations of the form $P_L = f(P_s) = A + B(P_s) + C(P_s) + D(P_s)$ were obtained for a two sphere model ($n_L = n_s = 1$). Results are given in Table II.

Table II. Third order fit of P_L as a function of P_s

ratio	$P_L = f(P_s)$
2:1	$P_L = 0.000125 + 0.2635(P_s) - 0.2062(P_s)^2 + 0.22297(P_s)^3$
5:1	$P_L = 0.000474 + 0.040414(P_s) - 0.022398(P_s)^2 + 0.00169(P_s)^3$
20:1	$P_L = 0.001$

Substituting $f(P_s)$ into Eq. (148),

$$\frac{R_L}{R_{LO}} = \left\{\frac{4W + n_s P_s^2(3-P_s)}{W[4-n_L\ f(P_s)^2(3-f(P_s))]}\right\}^{1/3} \qquad (152)$$

The concentration of component 2 in the liquid, X_2^L is determined by $X_{2(R_{so})}^L$, the concentration above the surface of the small particle, and

the concentration difference between the surface of the larger sphere and the liquid is

$$\ell n\left(\frac{X^L_{2(R_{so})}}{X^L_{2(R_L)}}\right) = \frac{2V^0_2\,\gamma_{\ell v}}{NkT}\quad\left[\frac{1}{R_{so}} - \frac{1}{R_L}\right] \tag{153}$$

Using Eqs. (144) and (153), the concentration difference between the contact region and the large sphere is given by

$$\ell n\left(\frac{X^L_{2(P)}}{X^L_{2(Pr)}}\right) = \frac{2\,\gamma_{\ell v}\,V^0_2}{NkT}\quad\left[\frac{1}{R_{so}} - \frac{1}{R_L}\right]\quad + \frac{\Delta p V^0_2}{NkT} \tag{154}$$

The pressure difference, Δp, is described by the two principal radii of curvature of the liquid-vapor interface. As can be seen from Fig. 20b, these radii cannot be uniquely determined. Therefore, as an additional approximation, the pressure difference corresponding to two similar sized particles will be used, (this approximation actually underestimates the pressure difference between the liquid and the pore). From Eq. (111) of Section III-C-1

$$\Delta p = \frac{2\,\gamma_{\ell v}\,[1-P_L)\,\sqrt{(1-P_L)P_L} - P_L]}{R_L(2-P_L)P_L^2\,[2(1-P_L)\sqrt{(1-P_L)P_L} - P_L]} \tag{155}$$

Substituting Eq. (155) into Eq. (154)

$$\ell n\left(\frac{X_{2(P)}^{L}}{X_{2(Pr)}^{L}}\right) = \frac{2V_2^0\,\gamma_{\ell v}}{NkT}\left\{\frac{W^{1/3}}{R_{LO}} - \frac{1}{R_{LO}}\left[\frac{4W + n_s P_s^2(3-P_s)}{W[4-n_L P_L^2(3-P_L)]}\right]^{-1/3}\right\}$$

$$+ \frac{2V_2^0\,\gamma_{\ell v}}{NkT\,R_L}\left\{\frac{(1-P_L)\sqrt{(1-P_L)P_L} - P_L}{P_L^2(2-P_L)[2(1-P_L)\sqrt{(1-P_L)P_L} - P_L]}\right\} \qquad (156)$$

now substituting R_{LO} for R_L

$$\ell n\left(\frac{X_{2(P)}^{L}}{X_{2(Pr)}^{L}}\right) = \frac{2V_2^0\,\gamma_{\ell v}}{NkT}\left\{\frac{W^{1/3}}{R_{LO}}\left[\frac{4W + n_s P_s^2(3-P_s)}{W[4-n_L P_L^2(3-P_L)]}\right]^{-1/3}\frac{1}{R_{LO}} +\right.$$

(157)

$$\left. + \frac{1}{R_{LO}}\left[\frac{4W + n_s P_s^2(3-P_s)}{W[4-n_L P_L^2(3-P_L)]}\right]^{-1/3}\left[\frac{(1-P_L)\sqrt{(1-P_L)P_L} - P_L}{P_L^2(2-P_L)[2(1-P_L)\sqrt{(1-P_L)P_L} - P_L]}\right]\right\}$$

Using Eqs. (90) through (95) of Section III-C (Part B)

$$\frac{dV}{dt} = \frac{8\pi\delta D V_2^0\,\gamma_{\ell v}\,X_{2(RL)}^{L}}{NkT\,R_{LO}}\left\{W^{1/3} + \left[\frac{4W + n_s P_s^2\,(3-P_s)}{W[4-n_L P_L^2(3-P_L)]}\right]^{-1/3}\right.$$

$$\left. X\left[\frac{(1-P_2)\sqrt{(1-P_L)P_L} - P_L}{P_L^2(2-P_L)[2(1-P_L)\sqrt{(1-P_L)P_L} - P_L]} - 1\right]\right] \qquad (158)$$

The volume of material removed from the spheres is

$$V_{total} = V_{small\ cap} + V_{large\ cap} \tag{159}$$

Using Eqs. (145) and (146)

$$V_{total} = \frac{n_s \pi R_{so}^3 (3-P_s) P_s^2}{3} + \frac{n_L \pi R_L^3 P_L^2 (3-P_L)}{3} \tag{160}$$

substituting $\frac{R_{LO}^3}{W} = R_{so}^3$ and Eq. (152) for R_L^3

$$V_{total} = \frac{n_s \pi R_{LO}^3 P_s^2 (3-P_s)}{W \quad 3} + \frac{\pi n_L R_{LO}^3 P_L^2 (3-P_L)}{3} \quad X$$

$$X \left[\frac{4W + n_s P_s^2 (3-P_s)}{W[4-n_L P_L^2 (3-P_L)]} \right] \tag{161}$$

on differentiating Eq. (161)

$$dV_{TOTAL} = \pi R_{LO}^3 \left\{ \frac{n_S}{W} (2P_S - P_S^2) + n_L (2P_L - P_L^2)\, dP_L \left[\frac{4W + n_S P_S^2 (3 - P_S)}{W\left[4 - n_L P_L^2 (3-P_L)\right]} \right] \right.$$

$$\left. + n_L \left(P_L^2 - \frac{P_L^3}{3}\right) \left[\frac{W\left[4 - n_L P_L^2 (3-P_L)\right](6n_S P_S - 3n_S P_S^2) - (4W + n_S P_S^2 (3-P_S))\left[W(-6n_L P_L + 3n_L P_L^2)\, dP_L\right]}{W^2\left[4 - n_L P_L^2 (3-P_L)\right]^2} \right] \right\} dP_S$$

XBL7412-7684

$$dV_{total} = \pi R_{LO}^3 \left\{ \frac{n_s}{W} (2P_s - P_s^2) + \right.$$

$$+ \left\{ n_L \left[\frac{4W + n_s P_s^2 (3-P_s)}{W[4-n_L P_L^2 (3-P_L)]} \right] (2P_L - P_L^2) \right\} dP_L$$

$$+ n_L \left\{ \left(P_L^2 - \frac{P_L^3}{3} \right) \frac{W[4-n_L P_L^2 (3-P_L)][6n_s P_s - 3n_s P_s^2]}{W^2[4-n_L P_L^2 (3-P_L)]^2} - \right.$$

$$\left. \left. - \frac{[4W + n_s P_s^2 (3-P_s)][-6Wn_L P_L + 3Wn_L P_L^2]}{W^2[4-n_L P_L^2 (3-P_L)]^2} \right\} dP_s \right\} \qquad (162)$$

After differentiating both sides of Eq. (162) with respect to time, it may be equated to Eq. (158) and upon substitution of $f(P_s)$ for P_L,

$$\left(\frac{8 D \delta V_2^0 x_{2(RL)}^L \gamma_{LV}}{NkT R_{LO}^4}\right) dt = \left\{ \frac{n_S}{W} (2P_S - P_S^2) + n_L \left[\frac{4W + n_S P_S^2 (3 - P_S)}{W\left[4 - n_L f(P_S)^2 (3 - f(P_S))\right]} \right] (2f(P_S) - f(P_S)^2)\, df(P_S) \right.$$

$$+ n_L \left[f(P_S) - \frac{f(P_S)^3}{3} \right] \left(\frac{W\left[4 - n_L f(P_S)^2 (3 - f(P_S))\right](6 n_S P_S - 3 n_S P_S^2) - \left[4W + n_S P_S^2 (3 - P_S)\right]}{W^2 \left[4 - n_L f(P_S)^2 (3 - f(P_S))\right]^2} \right.$$

$$\left. \left. \times \frac{(3 W n_L f(P_S)\, df(P_S)\, (f(P_S) - 2))}{1} \right) \right\} dP_S \Bigg/ \left\{ W^{1/3} + \left[\frac{4W - n_S P_S^2 (3 - P_S)}{W\left[4 - n_L f(P_S)(3 - f(P_S))\right]} \right]^{-1/3} \right.$$

$$\left. \times \left[\frac{(1 - f(P_S)) \sqrt{(1 - f(P_S)) f(P_S)} - f(P_S)}{f(P_S)^2 (2 - f(P_S)) \left[2(1 - f(P_S)) \sqrt{(1 - f(P_S)) f(P_S)} - f(P_S)\right]} \right] - 1 \right\}$$

XBL 7310-1960

(163)

Equation (163) is the differential equation for the kinetics of the initial stage of solution-precipitation for particles of dissimilar size. The right side of this equation cannot be solved analytically; however, the integral areas may be found using numerical techniques similar to those used in Section III-C. The shrinkage may be expressed as h/R_0, and for the case of dissimilar sized particles,

$$h/R_0 = (h_s + h_L)/(R_{so} + R_{LO}) = P_0 \tag{164}$$

Plots of log P_0 versus log time are shown in Fig. 21 for initial particle size ratios of 2:1, 5:1, and 20:1 assuming a nearest neighbor coordination of 1, (two sphere model). The locus of points of these curves is not linear on a log-log scale. However, by fitting the curves to a linear least squares plot, the exponents of time, y, were obtained, as were the exponents of particle size, z. Results for the three particle size ratios are given in Table III, which indicate that the exponent of time increases as the particle size ratio increases. Sintering kinetics are therefore enhanced with large particle size differences. The reason for this enhancement is that the larger the particle size difference, the larger is the solubility difference between the contact region and the surface of the larger sphere. Therefore, the magnitude of the diffusion flux of solid diffusing in the liquid becomes greater which in turn increases the corresponding densification rate.

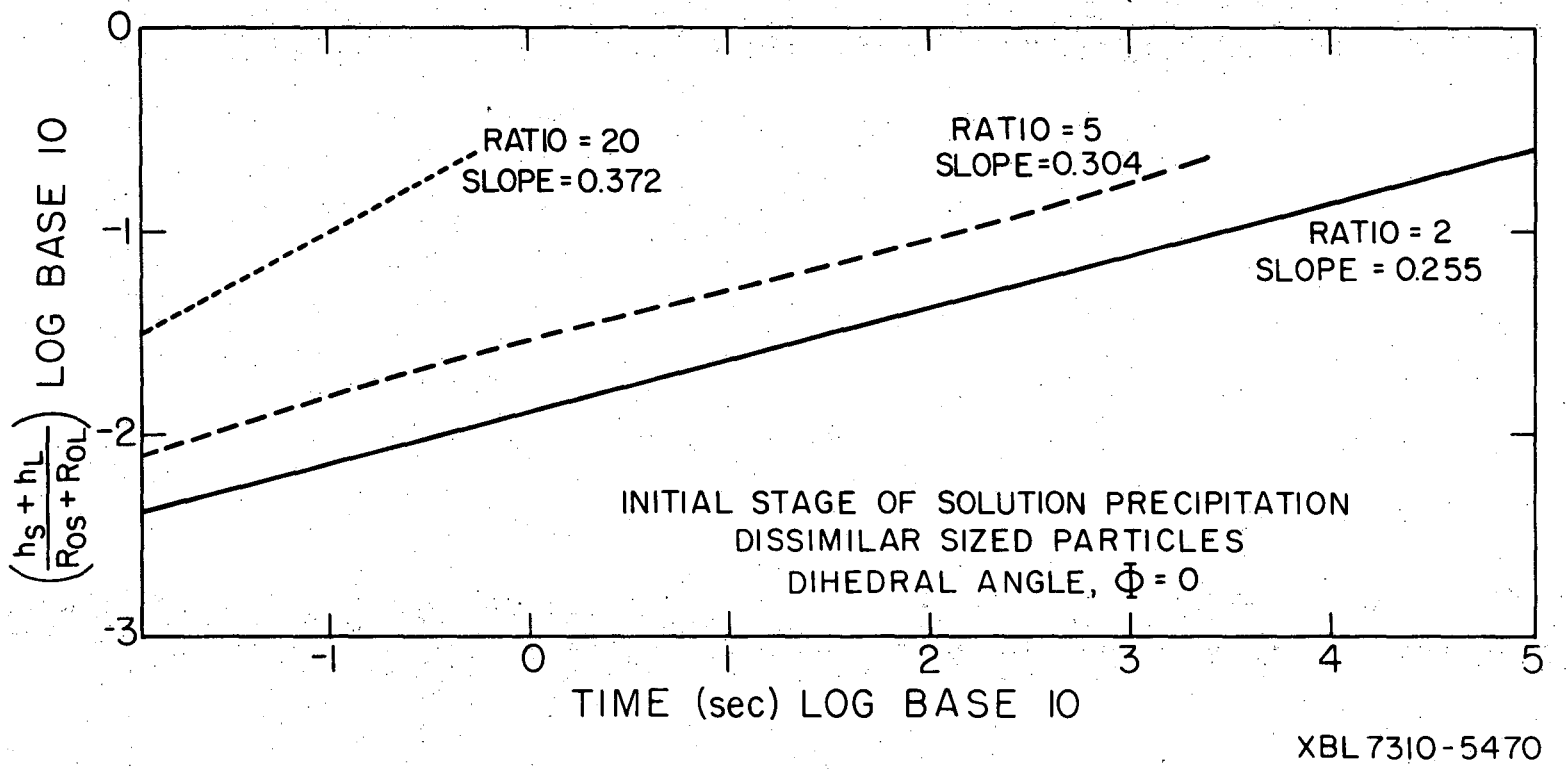

Figure 21. Densification versus time for the initial stage of solution-precipitation for dissimilar sized particles.

Table III. Exponents of time, y, and particle size, z, for sintering by solution-precipitation of dissimilar sized particles

Initial particle size ratio	Exponent of time, y	Exponent of particle size, z
2:1	0.255	-1.019
5:1	0.304	-1.215
20:1	0.372	-1.488

D. Bulk Diffusion: Nonzero Solid-Liquid Dihedral Angle

In a solid-liquid system which does not form an equilibrium dihedral angle of zero degrees, solid-solid contacts are thermodynamically favored. When solid-liquid interfaces are formed, solution-precipitation (Section III-C) can cause surface rearrangement but does not lead to densification. Sintering kinetics are therefore characterized by solid phase diffusion mechanisms, either volume or grain boundary.

Consider a two sphere model (Fig. 2b, Part A: Section II-A) for solid phase sintering. After some degree of densification, solid-solid contacts have formed between the spheres along with a small circular shaped neck region connecting the spheres. Nabarro[3] has shown that the pressure exerted on a solid surface affects the concentration of vacancies in the regions adjacent to that surface. For surfaces exposed to a compressive stress, the vacancy concentration is less than the thermal equilibrium vacancy concentration under a surface free of normal stresses, while surfaces in tension have a greater vacancy concentration. For a two sphere model forming a neck, the region under the convex

surface is in compression and has a deficiency of vacancies, while the region under the concave surface is in tension and has an excess concentration of vacancies. Neglecting the effect of the tensile stresses created by the dihedral angle at the grain boundary, it is assumed that the grain boundary region is stress free. Diffusion of vacancies thus occurs from the neck region to the grain boundary with a corresponding counter flux of atoms toward the neck which leads to interpenetration of the spheres and to densification.

Now consider the case where a small amount of wetting liquid is present between the spheres and solid-solid contacts have formed between the spheres, (nonzero solid-liquid dihedral angle). The pressure difference between the pore, i.e., vapor, and the liquid is

$$p_{pore} - p_{liq} = \gamma_{\ell v} \left[\frac{1}{\rho_2} - \frac{1}{\rho_1}\right] \tag{165}$$

where ρ_1 and ρ_2 are the radii of curvature of the liquid-vapor interface. Equation (165) indicates that the pressure is less in the liquid than in the vapor. Additionally, the pressure difference between the liquid and the region just under the solid surface is

$$p_{liq} - p_{solid} = \gamma_{s\ell} \left[\frac{1}{\rho_3} - \frac{1}{W}\right] \tag{166}$$

where ρ_3 is the radius of the neck, which is assumed to be circular, and w is half the length of the grain boundary. The pressure difference between the pore and the region just under the surface of the solid is

obtained by combining Eqs. (165) and (166)

$$p_{pore} - p_{solid} = \gamma_{\ell v} \left[\frac{1}{\rho_2} - \frac{1}{\rho_1}\right] + \gamma_{s\ell} \left[\frac{1}{\rho_3} - \frac{1}{w}\right] \tag{167}$$

The curvatures of the two interfaces cause an effective tensile stress on the solid surface and the vacancy concentration under such a surface is given by Nabarro[3] as

$$N_v = N_c(\infty) \exp\left(\frac{pa^3}{kT}\right) \tag{168}$$

where $N_v(\infty)$ is the equilibrium thermal vacancy concentration at the temperature, T, corresponding to no external normal stress at the surface. p is the pressure at the surface and a^3 is the atomic volume.

If the vacancy concentration at the grain boundary is assumed to be $N_v(\infty)$, there is a concentration difference of vacancies between the neck and the solid-solid contact region.

$$\Delta C = N_v - N_v(\infty) \tag{169}$$

Substituting Eq. (168) into (169)

$$\Delta C = N_v(\infty) \exp\left(\frac{pa^3}{KT}\right) - 1 \tag{170}$$

Following an analysis similar to that of Coble,[6,42] the diffusion flux of vacancies per unit length is given by

$$J(\frac{A}{\ell}) = \Delta C \; D_{vac} \; 4\pi \tag{171}$$

where $(\frac{A}{\ell})$ is a characteristic area divided by a length and D_{vac} is the vacancy diffusion coefficient, which is related to the volume self diffusion coefficient by

$$D_{vac} = D_{vol}/N_v(\infty) \; a^3 \tag{172}$$

Substituting Eqs. (170) and (172) into (171)

$$J(\frac{A}{\ell}) = \frac{D_{vol} \; [\exp(\frac{pa^3}{KT}) - 1]}{a^3} \tag{173}$$

Using ρ_3 as the length of the vacancy source, the volume of material diffused per second is

$$\frac{dV}{dt} = (\frac{A}{\ell}) \; J\rho_3 \; a^3 \tag{174}$$

or

$$\frac{dV}{dt} = 4\pi \; D_{vol} \; \rho_3[\exp(\frac{pa^3}{KT}) - 1] \tag{175}$$

The first two terms of the expansion of e^f are

$$\exp(f) = 1 + f/1! \tag{176}$$

Therefore,

$$\frac{dV}{dt} = \frac{4\pi D_{vol} \rho_3 a^3 p}{KT} \tag{177}$$

Substituting Eq. (167) for p,

$$\frac{dV}{dt} = \frac{4\pi D_{vol} p_3 a^3}{KT} \left[\gamma_{\ell v}\left(\frac{1}{\rho_2} - \frac{1}{\rho_1}\right) + \gamma_{s\ell}\left(\frac{1}{\rho_3} - \frac{1}{w}\right)\right] \tag{178}$$

From Section III-C Eqs. (106) and (107)

$$\rho_1 = \frac{2(R_0-h)\sqrt{R_0 h - h^2} - Rh}{R_0 - 2h} \tag{179}$$

and

$$\rho_2 = \frac{R_0 h}{R_0 - 2h} \tag{180}$$

where R_0 is the radius of the particle, (which remains constant during interpenetration of the spheres), and h is the height of the cap material removed from between the spheres. Following the same convention as in Sections III-C to E, let

$$P = h/R_0 \quad \text{or} \quad h = PR_0 \tag{181}$$

Substituting Eq. (181) into (179) and (180)

$$\rho_1 = R_0 \frac{[2(1-P)\sqrt{(1-P)P} - P]}{1-2P} \tag{182}$$

and

$$\rho_2 = \frac{R_0 P}{1-2P} \tag{183}$$

Substituting Eqs. (182) and (183) into Eq. (178),

$$\frac{dV}{dt} = \frac{4\pi D_{vol} \rho_3 a^3}{KT} \left\{ \frac{\gamma_{s\ell}}{R_0} \left(\frac{1}{\rho_3} - \frac{1}{w}\right) + \right.$$

$$\left. \frac{\gamma_{\ell v}}{R_0} \left(\frac{(1-2P)[2(1-P)\sqrt{(1-P)P} - 2P]}{P[2(1-P)\sqrt{(1-P)P} - P]} \right) \right\} \tag{184}$$

ρ_3 is given by Coble as approximately equal to h. Thus, $\rho_3 = PR_0$. Also, $4R_0\rho_3 = w^2$ or $w = 2R_0\sqrt{P}$. Substituting these equations into Eq. (184),

$$\frac{dV}{dt} = \frac{4\pi D_{vol} \rho_3 a^3}{R_0 KT} \left\{ \gamma_{s\ell} \left[\frac{2\sqrt{P} - P}{2P\sqrt{P}} \right] \right. \tag{185}$$

$$\left. + \gamma_{\ell v} \left[\frac{(1-2P)[2(1-P)\sqrt{(1-P)P} - 2P}{P[2(1-P)\sqrt{(1-P)P} - P]} \right] \right\} \tag{186}$$

Now letting $A = \gamma_{s\ell}/\gamma_{\ell v}$

$$\frac{dV}{dt} = \frac{4\pi\, D_{vol}\, \rho_3 a^3\, \gamma_{\ell v}}{R_0 KT} \left\{ A \left[\frac{2\sqrt{P} - P}{2P\sqrt{P}} \right] \right.$$

$$\left. + \left[\frac{(1-2P)[2(1-P)\sqrt{(1-P)P} - 2P]}{P[2(1-P)\sqrt{(1-P)P} - P]} \right] \right\} \qquad (187)$$

The volume flux of material removed from the region between the spheres and deposited in the neck is approximately given by[6,42]

$$\frac{dV}{dt} = 4\pi R^2 h \frac{dh}{dt} \quad \text{or} \quad \frac{dV}{dt} = 4\pi R_0^2 P \frac{dP}{dt} \qquad (188)$$

Equating (187) and (188)

$$\left\{ \frac{D_{vol}\, a^3\, \gamma_{\ell v}}{KT\, R_0^3} \right\} dt = \left\{ \frac{A[2\sqrt{P} - P}{2P\sqrt{P}} \right.$$

$$\left. + \left[\frac{(1-2P)[2(1-P)\sqrt{(1-P)P} - 2P]}{P[2(1-P)\sqrt{(1-P)P} - P]} \right] \right\}^{-1} \qquad (189)$$

Equation (189) is the kinetic differential equation for the initial stage of liquid phase sintering for systems forming nonzero dihedral angles, derived from Coble's model for solid phase sintering.

Following techniques similar to Sections III-C to E, log (P_0) versus log(time) plots yield the exponent of time, y, and log (P_0) versus log(R_0) plots yield the exponent of particle size, z. These results are

given in Table IV for several ratios of and are shown in Fig. 22.

Johnson[47] has used graphical techniques to more accurately describe the geometry of the neck region between the two spheres. His results for the area of the neck, the radius of the neck and the radius of curvature of the solid neck surface are

$$A_{neck} = 7\pi R_0^2 P^{3/2} \tag{190}$$

$$w = (5\pi/9) R_0 P^{0.46} \tag{191}$$

$$\rho_3 = (7\pi/8) R_0 P^{6/5} \tag{192}$$

Using the same flux equation as that used by Coble, and employing Fick's first law, Johnson obtained

$$\frac{dV}{dt} = \frac{126\ D_{vol}\ \Delta C}{5\ N_v(\infty)}\ [R_0 P^{1.04}] \tag{193}$$

Applying these equations to liquid phase sintering, the concentration difference of vacancies between the neck and the grain boundary is

$$\Delta C = \frac{a^3 N_v(\infty)}{KT} \left\{ \frac{\gamma_{\ell v}}{R_0} \frac{(1-2P)[2(1-P)\ \sqrt{(1-P)P} - 2P]}{P[2(1-P)\ \sqrt{(1-P)P} - P]} \right. \tag{194}$$

$$\left. + \frac{\gamma_{s\ell}}{R_0}\ [\frac{1}{\rho_3} - \frac{1}{w}] \right\}$$

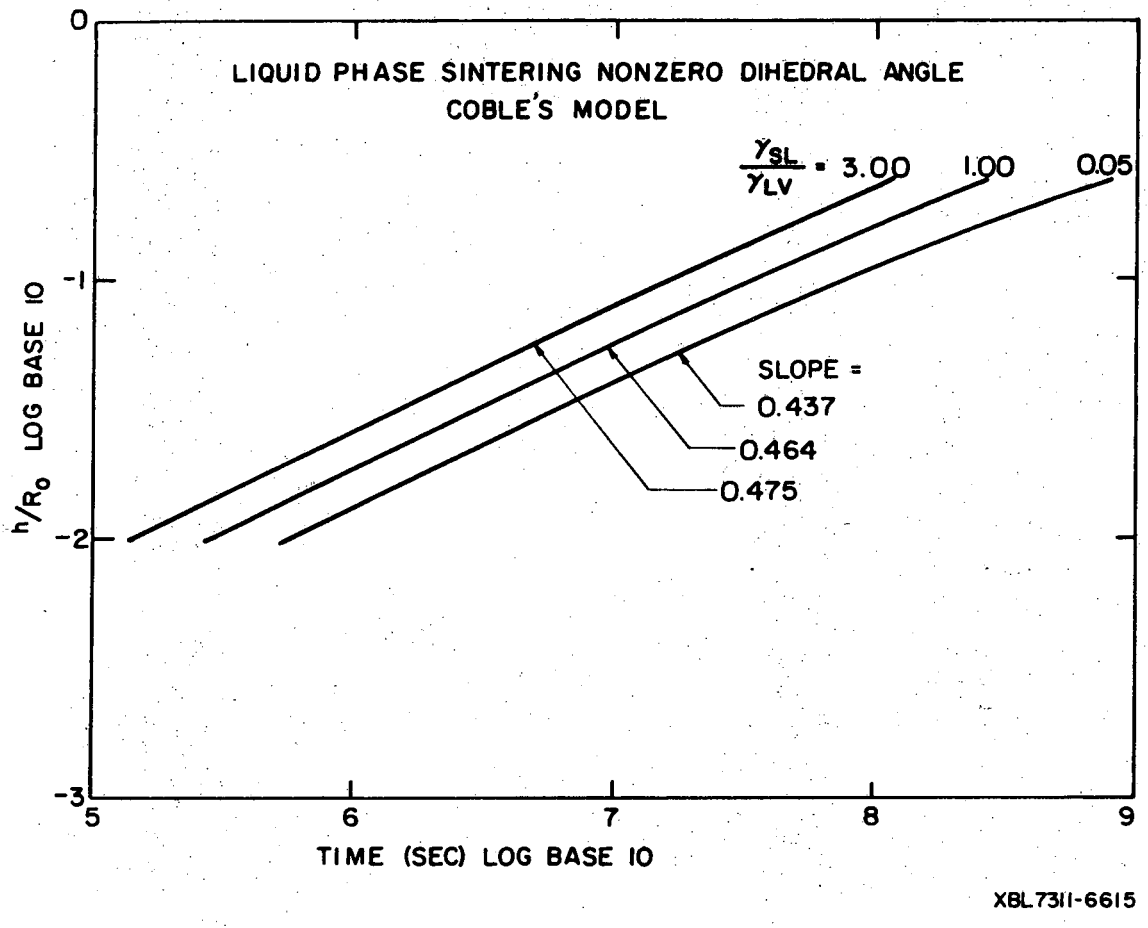

Figure 22. Densification versus time for liquid phase sintering systems forming nonzero equilibrium solid/liquid dihedral angles using Coble's geometry.

Table IV. Exponents of time using Coble's geometry

Ratio of A	y Exponent of time	z Exponent of particle size
1.00	0.464	-1.390
1.50	0.468	-1.405
2.00	0.471	-1.414
2.50	0.473	-1.420
3.00	0.475	-1.425

Substituting Eq. (191) and (192) and (194)

$$\Delta C = \frac{a^3 \gamma_{\ell v} N_v(\infty)}{KTR_0} \left\{ \frac{(1-2P)[2(1-P)\sqrt{(1-P)P} - 2P]}{P[2(1-P)\sqrt{(1-P)P} - P]} \right.$$

$$\left. + \frac{A}{\pi} \left[\frac{8(P)^{-6/5}}{7} - \frac{9(P)^{-0.46}}{5} \right] \right\} \qquad (195)$$

Substituting Eq. (195) into (193)

$$\frac{dV}{dt} = \frac{126\, D_{vol}\, a^3\, \gamma_{\ell v}\, R_0 P^{1.04}}{5KT} \left\{ \frac{A}{\pi} \left[\frac{8(P)^{-6/5}}{7} - \frac{9(P)^{-0.46}}{5} \right] \right.$$

$$\left. + \left[\frac{(1-2P)[2(1-P)\sqrt{(1-P)P} - 2P]}{P[2(1-P)\sqrt{(1-P)P} - P]} \right] \right\} \qquad (196)$$

LIQUID PHASE SINTERING, NON-ZERO DIHEDRAL ANGLE

$$\left\{\frac{126\, D_V a^3 \gamma_{LV}}{5\pi kT R_0^3}\right\} dt = P^{-1.04}(2P-P^2)\left\{\left[\frac{(1-2P)\left[2(1-P)\sqrt{(1-P)P}-2P\right]}{P\left[2(1-P)\sqrt{(1-P)P}-P\right]}\right]+\frac{A}{\pi}\left[\frac{8}{7}P^{-6/5}-\frac{9}{5}P^{-0.46}\right]\right\}^{-1} dP$$

D_V = VOLUME DIFFUSION COEFFICIENT

a^3 = ATOMIC VOLUME

$P = h/R$

$A = \gamma_{SL}/\gamma_{LV}$

XBL7310-1957

The volume of material removed from the caps between the spheres and deposited in the neck region was approximated by Johnson as

$$V_{cap} = \pi R_0^3 P^2 \tag{197}$$

the exact volume is

$$V_{cap} = \pi R_0^3 (P^2 - P^3/3) \tag{198}$$

Using Eq. (198) and differentiating with respect to time,

$$\frac{dV_{cap}}{dt} = \pi R_0^3 (2P - P^2) \frac{dP}{dt} \tag{199}$$

Equating (196) and (199)

$$\left\{ \frac{126\ D_{vol}\ a^3\ \gamma_{\ell v}}{5\pi K T R_0^3} \right\} dt = P^{-1.04} (2P - P)^2 \left\{ \frac{A}{\pi} \left[\frac{8(P)^{-6/5}}{7} - \frac{9(P)^{-0.46}}{5} \right] \right.$$

$$\left. + \left[\frac{(1-2P)[2(1-P)\sqrt{(1-P)P} - 2P]}{P[2(1-P)\sqrt{(1-P)P} - P]} \right] \right\}^{(-1)} dP \tag{200}$$

Kinetic results for densification versus time are shown in Fig. 23 and in Table V for Eq. (200). The differences between Johnson's and Coble's solutions, when applied to liquid phase sintering, result from the differences in the relationships used to describe the geometry of the

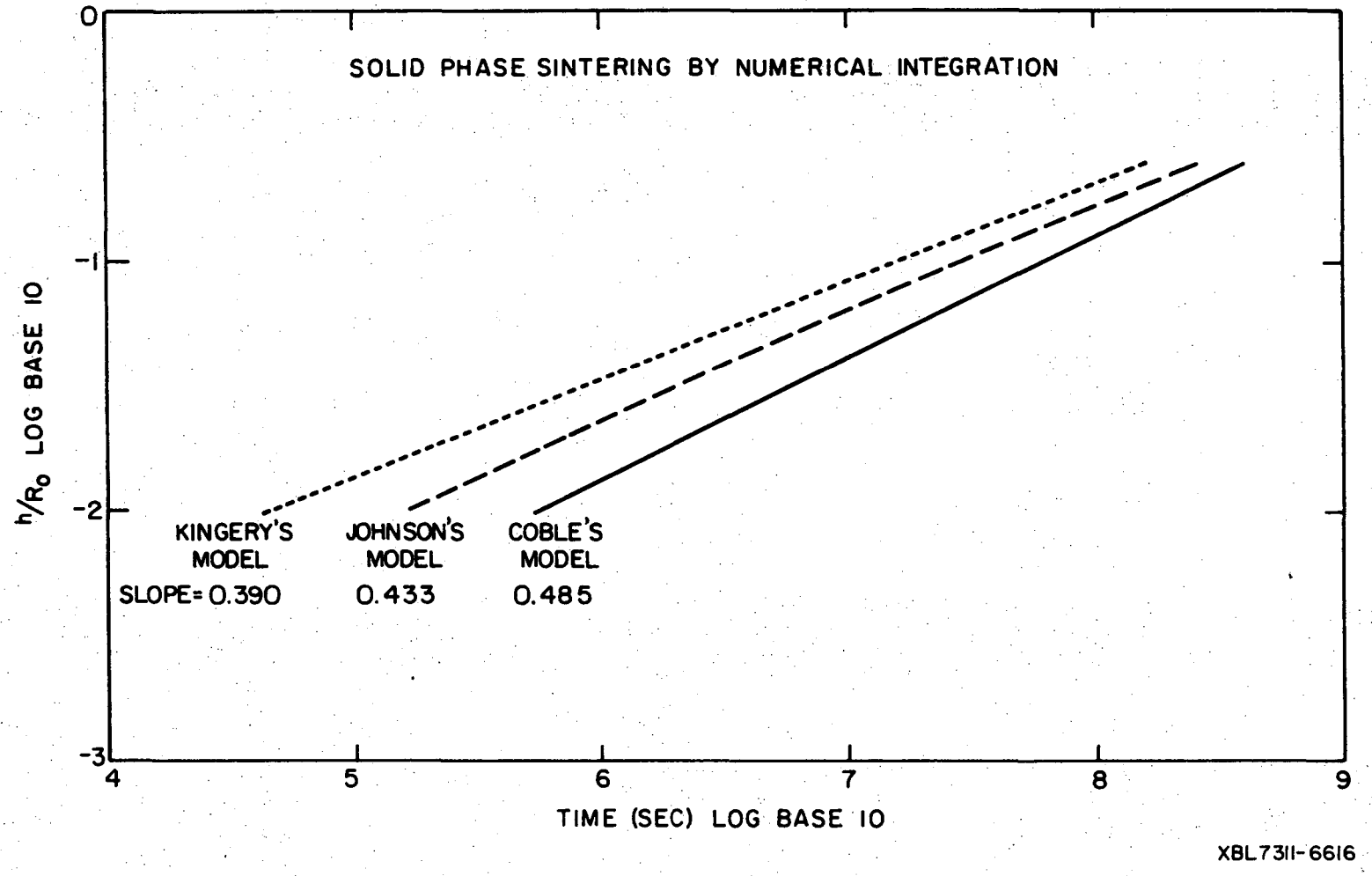

Figure 23. Densification versus time for solid phase sintering for Kingery's, Johnson's and Coble's models using numerical integration techniques.

Table V. Exponents of time using Johnson's geometry

Ratio of A	y Exponent of time	z Exponent of particle size
0.01	0.437	*
3.00	0.448	*

* not determined

neck region and the volumes of material removed from between the spheres.

Figure 24 is a comparison of kinetic curves for solid phase sintering, (solid-vapor), of uniform sized spherical particles based on numerical integration of differential kinetic equations which were derived analytically and in a more approximate form by Kingery,[4] Coble[6,42] and Johnson.[47]

Table VI shows the exponents of time for each model obtained by numerical integration techniques and by analytical integration. The differences in the exponents of time are due only to the fact that two radii of curvature were used for the numerically integrated kinetics, whereas only one radius of curvature is used in the analytical method. Since the two radii of curvature describing the neck region are of opposite sign, the capillary pressure is less for the numerical method. Comparison of the numerical results for solid phase sintering and liquid phase sintering for each model indicates that the sintering kinetics are enhanced by the presence of the liquid phase. The increased vacancy concentration gradient resulting from the presence of a liquid-vapor interface causes sintering rates to be greater for liquid phase sintering

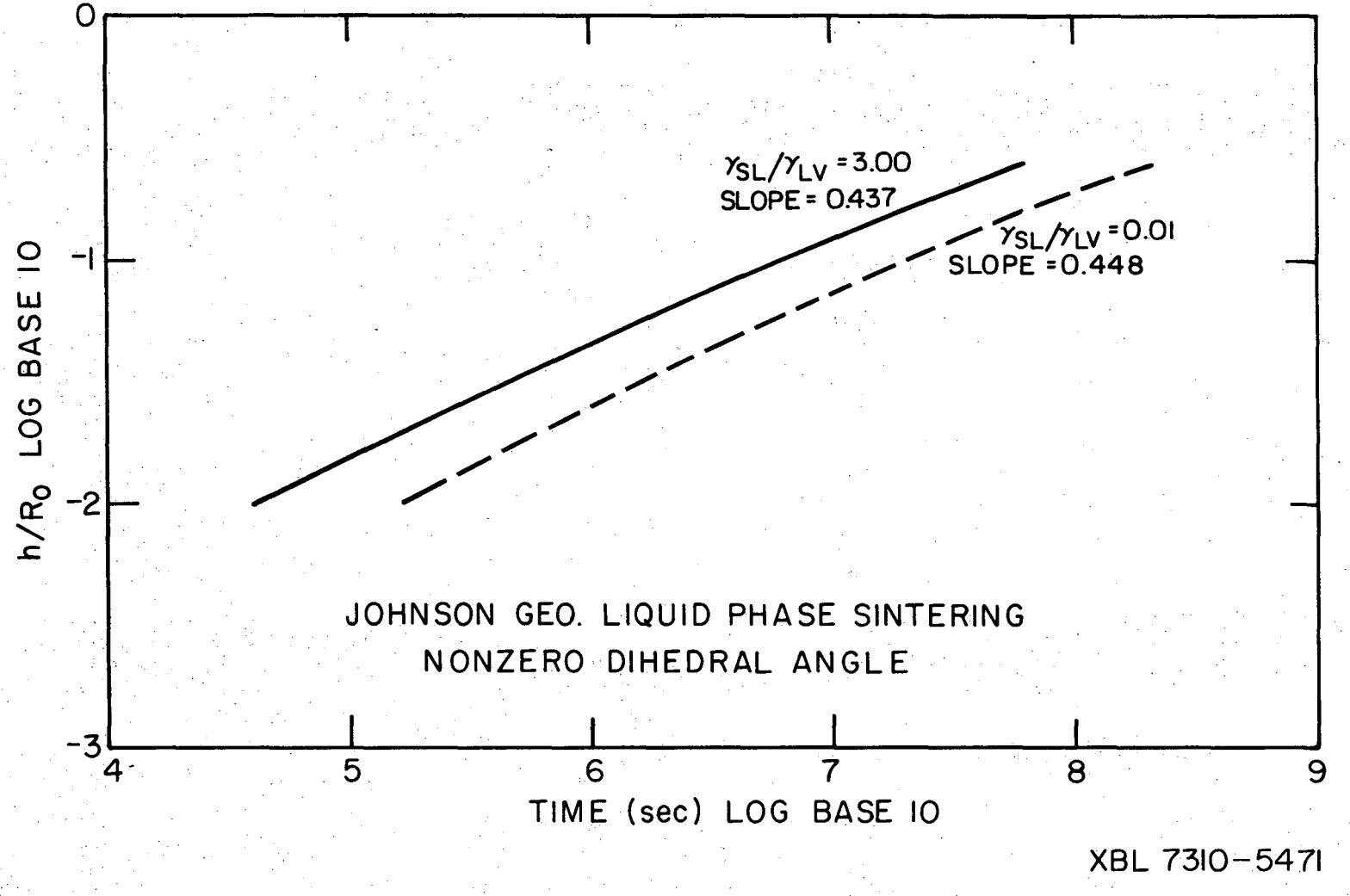

Figure 24. Densification versus time for liquid phase sintering systems forming nonzero equilibrium solid/liquid dihedral angles using Johnson's geometry.

Table VI. Exponents of time for solid-phase sintering

Kingery's model	Johnson's model	Coble's model	
0.390	0.427	0.485	numerical method
0.400	0.460	0.500	analytical method

systems than for solid phase sintering systems, as shown in Fig. 25 for a solid-liquid-vapor contact angle of 75°.

E. Discussion

The solutions of the kinetic equations derived in Sections III-C and III-D indicate that the time dependency, y, and the particle size dependency, z, of densification, $\Delta L/L_0$, for idealized models of spherical particles are governed by the magnitude of the dihedral angle, i.e. zero or nonzero, the volume of liquid phase, and the particle size distribution. Table VII gives a summary of the values of y and z for different stages and conditions of liquid phase sintering of these models.

Referring to the Table VII, and assuming first the case of a zero dihedral angle and uniform particle size throughout the sintering compact, one sees that the exponent of time, y, is smaller for the initial stage of solution-precipitation than for the final stage. Thus, the compact sinters more slowly during the initial stage than during the final stage. The reason for the slower kinetics is mainly due to the capillary forces acting on the system. During the initial stage, the radii of curvature of the liquid-vapor interface are of opposite sign

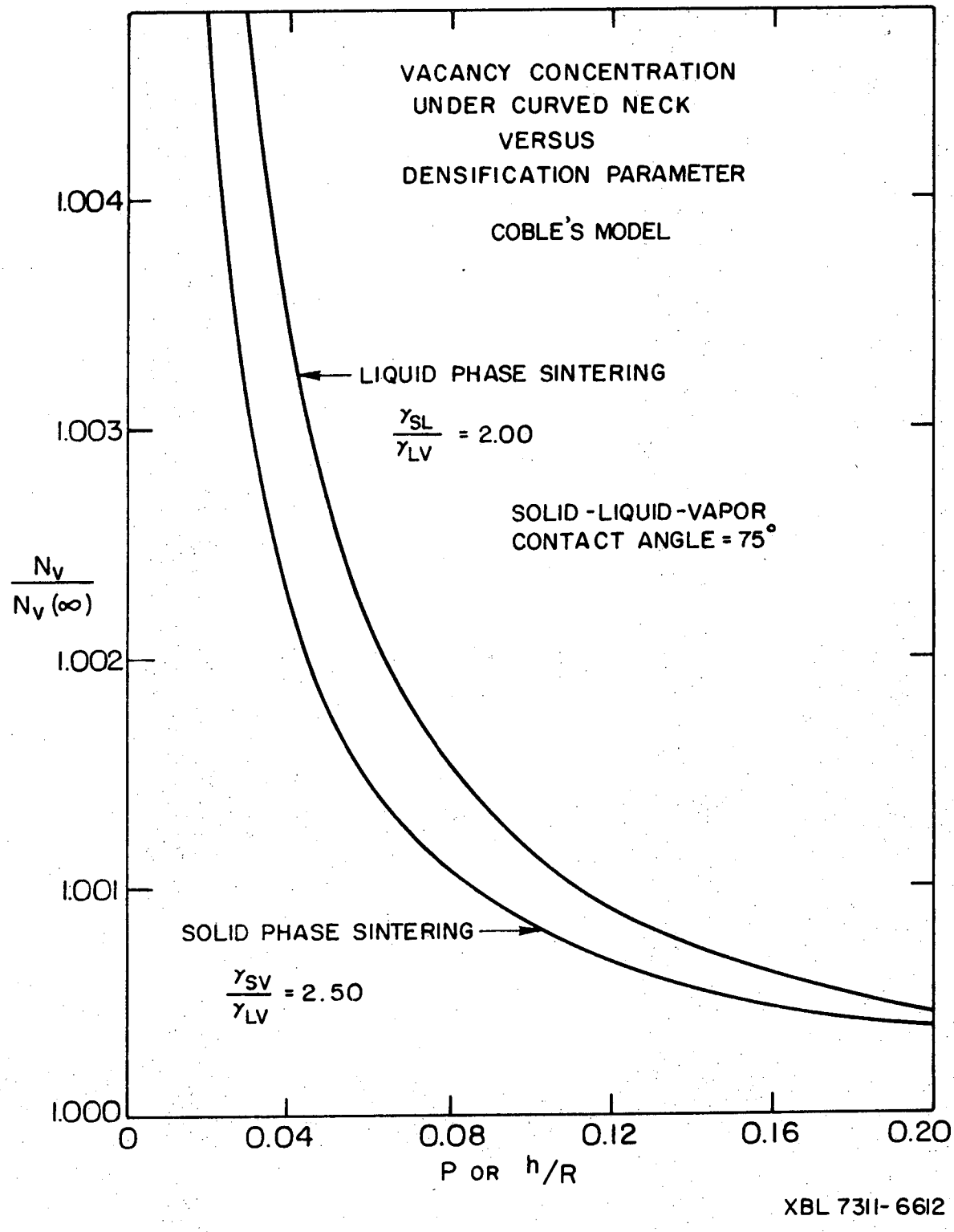

Figure 25. Comparison of the vacancy concentrations under concave necks for solid phase sintering and for liquid phase sintering systems forming nonzero equilibrium solid/liquid dihedral angles.

Table VII. Table of exponents

$\frac{h}{R_0} \alpha t^y R_0^z$	y	z
Zero Dihedral Angle		
Initial stage	0.243	-0.977
Combination of initial and final stage		
4.4% liquid	0.246	*
20% liquid	0.268	*
Final stage large liquid volume 34.3%		
No back pressure	0.362	-1.45
With back pressure	0.282	-1.13
Dissimilar particles		
Ratio 2:1	0.255	-1.019
5:1	0.304	-1.215
20:1	0.372	-1.488
Nonzero Dihedral Angle		
Johnson's model $\gamma_{s\ell}/\gamma_{\ell v} = 0.01$	0.437	*
$\gamma_{s\ell}/\gamma_{\ell v} = 3.00$	0.448	*
Coble's model $\gamma_{s\ell}/\gamma_{\ell v} = 1.00$	0.464	-1.390
$\gamma_{s\ell}/\gamma_{\ell v} = 3.00$	0.475	-1.425

*Not determined

while during the final stage, the capillary forces have the same sign. Since the magnitude of the capillary force affects the pressure in the region between the particles, and therefore, the solubility of the component of the solid phase in the liquid phase, it is evident that the sintering rate is enhanced by large capillary forces.

The second comparison to be discussed is the time dependency of the densification parameter on different particle size ratios. As seen in Table VII, the greater the particle size difference, the larger is the exponent of time, y, and therefore, the sintering rate.

The physical reason for this increase is that when a small and a large particle are in contact, the smaller particle determines the solubility of the solid in the liquid between the two particles and in the liquid in regions away from the "contact" area. Since all material is assumed to condense on the larger sphere, the solubility difference used in kinetic equations must be the difference between the solubility in the "contact" region and the solubility above the surface of the larger particle. This difference increases as the particle size difference increases. Thus, the sintering kinetics are enhanced by a large particle size difference.

In real compacts, where a particle size distribution is always present, inhomogeneties due to agglomeration or poor mixing will lead to variations in sintering rates within the compact. Regions containing particles of widely differing size will sinter faster than regions containing homogeneous sized particles. Since the model shows that all material condenses on the larger particles, smaller particles are eventually consumed. Thus, a wide particle size distribution in a green

compact results in regions in the compact containing grains which are much larger than the average grain size for the homogeneous regions.

The third case to be discussed is that of a nonzero dihedral angle. As was shown in Section III-D, sintering proceeds by a solid phase vacancy mechanism, but the presence of a wetting liquid enhances the vacancy concentration gradient between the neck region and the solid-solid contact region. The effect is not large, however, and the exponents of time are very similar to those for solid-vapor sintering systems, although densification kinetics are always more rapid with a liquid phase present.

It should be noted that in comparing zero and nonzero dihedral angle cases, sintering kinetics are more rapid for the former than for the latter, even though the exponents of time are larger for solid phase sintering. The reason is that the diffusion coefficients, which appear in each densification equation are orders of magnitude smaller for the nonzero dihedral angle case, (bulk or grain boundary diffusion), than for the zero dihecral angle case, (diffusion through the liquid phase). This fact can be seen by comparison of the log densification versus log time curves for the initial stage of solution-precipitation (Fig. 14, Section III-C), with the curves for sintering with a nonzero dihedral angle (Fig. 22, Section III-D).

The dependency of densification on particle size is derived from the log densification versus log time curve by choosing a particular sintering time, t, and then obtaining h/R_0 for different initial particle sizes from the curves. It is seen from Table VII, that the absolute value of the exponent of particle size, z, increases as the

exponent of time, y, increases. This is to be expected since z was obtained from y, and therefore, is functionally similar to y.

Although there has been much experimental work in the measurement of liquid phase sintering kinetics, most investigations have not considered the possibility of an initial and a final stage of solution-precipitation nor has the effect of the magnitude of the dihedral been considered for comparison of experimentally measured densification versus time curves with curves predicted from idealized models. Experimental verification of a particular sintering model thus requires that the parameters of the sintering compact closely approach those of the model.

In any system where there is a solubility of the solid in the liquid, the composition of the liquid changes until it is saturated with the solid phase. This process is generally rapid especially when the compact has substantial solid-liquid interfacial area. This change in composition of the liquid causes the magnitude of $\gamma_{s\ell}$ to change until saturation is approached, and $\gamma_{s\ell}$ attains a static value.

In systems where there is mutual solubility, interfacial reactions can occur which give a dynamic dihedral angle of zero degrees.[55] This dihedral angle may then change to some finite value as the phases equilibrate. Thus, situations can arise where formation of a liquid leads to particle rearrangement and interdiffusion of components of each phase. These reactions at the solid-liquid interfaces can cause a dynamic zero dihedral angle, ($\gamma_{s\ell}$ decreases relative to γ_{ss} due to interfacial reactions at the solid-liquid interface), leading to penetration of the solid by the liquid and subsequent solution-precipitation mechanisms. Upon equilibration of the bulk liquid and bulk solid, finite

dihedral angles can form, or the zero dihedral angle can be maintained throughout the entire densification process. If the former occurs, liquid is squeezed from between grains, and solid-solid contacts begin to form. The sintering mechanisms then change from solution-precipitation to bulk or grain boundary diffusion.

The most well known kinetic data for liquid phase sintering was obtained by Kingery and Narasimhan[34] using the Fe-Cu system. Their results appeared to be in good agreement with Kingery's kinetic model for solution-precipitation. Unfortunately, the system chosen did not simulate the parameters of his model very closely. Smith[31] has reported that the equilibrium dihedral angle between solid Fe and liquid Cu at 1100 degrees centigrade is 20°. Although Kingery and Narasimhan did not report a value for the dihedral angle in their system, the equilibrium dihedral angle was undoubtedly finite at the temperatures used in their sintering experiments. Since solution-precipitation requires a zero dihedral angle to achieve densification of a compact, this mechanism could only be operative in the Fe-Cu system under the conditions of a dynamic zero dihedral angle which would result from interfacial reactions between the two phases. The mutual solubility of both components can lead to such reactions. However, upon equilibration of the phases, the equilibrium dihedral angle must form and solid-solid contacts will appear. Kingery referred to the formation of solid-solid contacts as the coalescence stage of sintering but he did not discuss coalescence with respect to a changing dihedral angle.

For the Fe-Cu system, log densification versus log time plots should reveal three or four linear regions (at least approximately linear

regions), corresponding to rearrangement, the initial and/or the final stage of solution-precipitation (depending on the volume of liquid in the compact), and solid phase sintering. In their Fig. 3,[34] only the compact containing 22% liquid Cu and 9.4 micron Fe powder showed three separate regions. Additionally, none of their compacts contained less than 11.3% liquid (Cu) which indicates that the initial stage of solution-precipitation would be of short duration. Spherical porosity would therefore form soon after the rearrangement stage and the final stage would become operative. It should be noted that the derivation for the kinetics of liquid phase sintering for systems having large volume fractions of liquid phase, yields an exponent of time of 0.362 while Kingery's derivation yields a value of 0.333. Therefore, the kinetic data obtained by Kingery and Narasimhan seems to correspond to the kinetics corresponding to the case of large volume fractions of liquid phase. The Fe-Cu system is not appropriate for verifying the kinetics of liquid phase sintering for systems containing small volume fractions of liquid phase. Recent work by Froschauer[56] in this laboratory with the Fe-Cu system using hot stage scanning electron microscopy, has shown that compacts containing small volume fractions of Cu exhibit little or no rearrangement. Since the melting point of Cu (1083) and Fe (1535) are similar, appreciable sintering of Fe-Fe particles can occur before liquid Cu forms. In compacts containing small volume fractions of liquid phase, equilibration of the solid and liquid phases can occur rapidly, forming a finite dihedral angle between the solid and the liquid. Thus, the liquid Cu will merely wet the solid Fe skeleton but will not penetrate between the grains. The failure of Kingery and Narasimhan to

observe the initial stage of solution-precipitation therefore becomes understandable.

Eremenko[35] has reported time exponents for cermet systems between 1.45 and 2.3 for the rearrangement stage and values of 0.11 to 0.40 for the succeeding stage, (solution-precipitation and/or solid phase sintering). No attempts were made in these experiments to form compacts having parameters approaching those of idealized models nor were dihedral angles reported. However, the range of values of the exponents of time are similar to those shown in Table VII indicating that, after rearrangement, several different sintering mechanisms are operative.

It is hoped that experimental verification of the models presented here can be performed in future work using real compacts which closely simulate the parameters of the models.

ACKNOWLEDGMENTS

I would like to express my sincere thanks to Professor Joseph A. Pask for his guidance and counciling during the course of this research project, and to Professor Thomas Hays for his assistance with the SEM.

Additionally, I would like to thank the members and staff of the Inorganic Materials Research Division of the Lawrence Berkeley Laboratory. Specifically, thanks are extended to Kelly Radmilovic for typing the manuscript; to George Georgakopoulos for his assistance with the SEM; to Walt Toutolmin, Jack Wodei, and to Don Whittaker for their assistance with mechanical and electrical problems; and to Victor Draper for his assistance in formulating some of the computer programs used in this report and for his assistance in polishing specimens.

Finally, I would like to thank Dr. Milton R. Pickus and Professor James W. Evans for reading the manuscript.

This work was supported by the U. S. Energy Research and Development Administration.

REFERENCES

1. Kuczynski, G. C., Self-Diffusion in Sintering of Metallic Particles, Metals Transactions of AIME, Feb. 1949, pp. 169-77.

2. Nichols, F. A., Theory of Sintering of Wires by Surface Diffusion, Acta Met., 16, 103-13 (1968).

3. Nabarro, F. R. N., Deformation of Crystals by the Motion of Single Ions, Report of a Conference on the Strength of Solids, Phys. Soc. London, 1948, pp. 75-90.

4. Kingery, W. D. and Berg, M., Study of the Initial Stages of Sintering Solids by Viscous Flow, Evaporation-Condensation, and Self-Diffusion, J. Appl. Phys. 26 1205-12 (1955).

5. Johnson, D. L. and Cutler, I. B., Diffusion Sintering: I, Initial Stage Sintering Models and Their Application to Shrinkage of Powder Compacts, J. Amer, Ceram. Soc., 46 (11) 541-5, 1963.

6. Coble, R. L., Sintering Crystalline Solids. I. Intermediate and Final State Diffusion Models, J. Appl. Phys., 32 (5) 1961.

7. Iversen, V. A., Phenomenological Analysis of the Densification Kinetics of Metal Powders During Sintering IV. An Approximate Method of Evaluating the Parameters of an Arbitrary Beginning of Isothermal Densification, Soviet Powder Metallurgy and Metal Ceramics, Consultants Bureau, 1970, pp. 552-6.

8. Iversen, V. A., Phenomenological Analysis of the Densification Kinetics of Metal Powders During Sintering III. Dependence of the Pore Volume Reduction on Temperature at Constant Isothermal Sintering Time. ibid.

9. Kislyi, P. S. and Kuzenkova, M. A., Role of Surface Energy in the Initial Sintering Period, Soviet Pwdr. Met. and Met. Cer. 1969, No. 9 (81).

10. Iversen, V. A., Kinetics of Metal Powders During Sintering a Reduction of Pore Volume During Isothermal Sintering, Soviet Pwdr. Met. and Met. Ceramics, 1970.

11. Easterling, K. E. and Tholen, A. R., Computer Simulated Models of the Sintering of Metal Powders, Zeitschrift fur Mettalkunde, 1970.

12. Vdovic, J. Eine neue Sintergleichung und ihre Experimentelle Uberprufung, Planseeberichte fur Pulvermatallurgie, Bd. 19, 1971.

13. Alexander, B. H. and Balluffi, R. W., The Mechanism of Sintering of Copper, Acta Metallurgica, 5, Nov. 1957, pp. 666-77.

14. Burke, J. E., Role of Grain Boundaries in Sinteing, J. Am. Ceram. Soc. 40 (3) 1957.

15. Seigle, L., Kinetics of High Temperature Processes, "Role of Grain Boundaries in Sintering," Tech. Press M.I.T., and J. Wiley, London, 1959, ed. Kingery, pp. 172-8.

16. Stephenson, I. M. and White, J., Factors Controlling Microstructure and Grain Growth in Two-Phase (One Solid + One Liquid) and Three-Phase (Two Solid + One Liquid) Systems, Trans. British Ceram. Soc. 1967.

17. Coble, R. L., Effects of Particle-Size Distribution in Initial-Stage Sintering, J. Am. Ceram. Soc. 56 (9) 461-6 (1973).

18. Kingery, W. D. and Francois, B., Grain Growth in Porous Compacts, J. Am. Ceram. Soc., 48 (10) 546-7 (1965).

19. Achutaramayya, G. and Scott, W. D., Measurement of Dihedral Angles by Scanning Electron Microscopy, J. Am. Ceram. Soc., 56 (4) 230-1 (1973).

20. Eastman, P. F. and Cutler, I. B., Effect of Water Vapor on Initial Sintering of Magnesia, J. Am. Ceram. Soc. 49 (10) 526-30 (1966).

21. Anderson, P. J. and Morgan, P. L., Effect of Water Vapour on Sintering of MgO, Trans. Faraday Soc., 60 (5) 930-7 (1964).

22. White, J., Refractories Research II. Calcination and Sintering of Magnesia, J. Australian Ceram. Soc., 9 (2) 60-3 (1973).

23. Jonker, G. H. and Noorlander, W., Science of Ceramics, "Grain Size of Sintering Barium Titanate," ed. Stewart, Vol. 1, 1962, pp. 255-64.

24. Razouk, R. E. and Mikhail, R. Sh., The Sorption of Water Vapor on Magnesium Oxide, J. Phys. Chem., 59 (7) 636-40 (1955).

25. Anderson, P. J., Horlock, R. F., and Oliver, J. F., Interaction of Water with the Magnesium Oxide Surface, Trans. Faraday Soc., 61 (12) 2754-62 (1965).

26. Bessonov, A. F. and Ust'yantsev, V. M., Effect of the State of the Surface Layers of Particles on the Sintering of Magnesite Powders, Soviet Pwdr. Met. and Met. Cer. No. 5, 1965, pp. 365-7.

27. Anderson, P. J. and Morgan, P. L., Effect of Water Vapour on Sintering of MgO, Trans. Faraday Soc., 60 (5) 930-7 (1964).

28. Frenkel, J., Viscous Flow of Crystalline Bodies Under the Action of Surface Tension, J. Physics, 9 (5) 385-98 (1945).

29. Greenwood, G. W., The Growth of Dispersed Precipitates in Solutions, Acta Met., 4 243-48 (1956).

30. Lenel, F. V., Sintering in the Presence of a Liquid Phase, Trans. AIME,1948 pp. 878-905, No. 176 (Inst. of Metals Division).

31. Smith, C. S., Grains, Phases and Interfaces: An Interpretation of Microstructure, Trans AIME, 175 15-51 (1948).

32. Gessinger, G. H., Fischmeister, H. F., and Lukas, H. L., A Model for Second-Stage Liquid-Phase Sintering with a Partially Wetting Liquid, Acta Met., 21 715-24 (1973).

33. Kingery, W. D., Densification During Sintering in the Presence of a Liquid Phase. I. Theory, J. Appl. Phys. 30 (10) 301-6 (1959).

34. Kingery, W. D. and Narasimhan, M. D., Densification During Sintering in the Presence of a Liquid Phase. II. Experimental Ibid. 307-10.

35. Eremenko, V. N., Naidich, Yu. v., and Lavrinenko, I. A., Liquid-Phase Sintering, Institute of Materials Science, Academy of Sciences of Ukrainian SSR, Translated by Consurtants Bureau, New York-London, 1970.

36. Cahn, J. W. and Heady, R. B., Analysis of Capillary Forces in Liquid-Phase Sintering of Jagged Particles, J. Am. Ceram. Soc., 53 (7) 1970.

37. Price, H. S., Smithells, C. J., and Williams, S. V., Sintered Alloys. Part I. Copper-Nickel-Tungsten Alloys Sintered with a Liquid Phase Present. J. Inst. of Metals (1939) No. 62, pp. 239.

38. Thomson, Sir William, On the Equilibrium of Vapour at a Curved Surface of Liquid, Phil. Mag. S. 4, 42 (282) 448-52 (1871).

39. Sambles, J. R., Skinner, L. B. and Lisgarten, N. D., An Electron Microscope Study of Evaporating Small Particles: the Kelvin Equation for Liquid Lead and the Mean Surface Energy of Solid Silver,

Proc. Roy. Soc. Lond. A. 318, 507-22 (1970).

40. Sambles, J. R., An Electron Microscope Study of Evaporating Gold Particles: The Kelvin Equation for Liquid Gold and the Lowering of the Melting Point of Solid Gold Particles, Proc. R. Soc. Lond. A 324, 339-51 (1971).

41. Skinner, L. M. and Sambles, J. R., The Kelvin Equation--A Review, Aerosol Science, 1972, Vol. 3, pp. 199-210.

42. Coble, R. L., Initial Sintering of Alumina and Hematite, J. Am. Ceram. Soc., 41 (2) 55-62.

43. Coble, R. L., Sintering Alumina: Effect of Atmospheres, J. Am. Ceram. Soc., 45 (3)123-7 (1962).

44. Kuczynski, G. C., Abernethy, L., and Allan, J., Sintering Mechanisms of Aluminum Oxide, Argonne National Lab. Report.

45. Fletcher, G., James, M. R. and Moon, J. R., The Nickel Activated Sintering of Tungsten, Scripta Met. 5, 105-8 (1971).

46. Gessinger, G. H. and Fischmeister, H. F., A Modified Model for the Sintering of Tungsten with Nickel Additions, J. of the Less-Common Metals, 27 (2) 129-41 (1972).

47. Johnson, D. L., The Kinetics of the Sintering of Alumina, Ph.D. Thesis, Univ. of Utah, 1962, Published by University Microfilms, Inc., Ann Arbor, Michigan.

48. Young, T., Phil. Trans. Royal Society, London, 95, 65 (1805).

49. Adamson, A. W., Physical Chemistry of Surfaces, 2nd Edition 1967, John Wiley & Sons, Inc., New York.

50. Heady, R. B., and Cahn, J. W., An Analysis of the Capillary Forces in Liquid-Phase Sintering of Spherical Particles, Metallurgical Transactions, Vol. 1, Jan. 1970, pp. 185-89.

51. Fisher, R. A., On the Capillary Forces in an Ideal Soil; Correction of Formulae Given by W. B. Haines, J. of Agric. Sci. Vol. 16, 1926, pp. 493-505.

52. Melrose, J. C., Model Calculations for Capillary Condensation, J. A. I. Ch. E., Vol. 12, (5), 986-90 (1966).

53. Lewis, G. N. and Randall, M. (Revised by Pitzer, K. S., and Brewer, L.), Thermodynamics, 2nd Edition, 1961, McGraw-Hill Book Co., New York.

54. Coble, R. L., Diffusion Sintering in the Solid State, ibid. Same as 37.

55. Aksay, I. A., Hoge, C. E., and Pask, J. A., Wetting Under Chemical Equilibrium and Nonequilibrium Conditions, J. Phys. Chem., 78 (12) 1178-83 (1974).

56. Private communication.

APPENDIX

Calculations of the vacancy concentrations at a solid-vapor and solid-solid interface for two spherical particles, Fig. 13, are made as follows:

Assume that the spherical particles have radii of 10 microns, and that the concentration of vacancies at a stress-free planar solid-vapor interface is

$$N_{sv} = \exp(-10) \tag{1}$$

$$N_{sv} = 4.539993 \times 10^{-5} \tag{2}$$

The vacancy concentration at a solid-solid interface is then given by

$$N_{ss} = N_{sv}/\text{vac} \tag{3}$$

The value of vac is dependent on two parameters: the radius of the particle and the value of the equilibrium dihedral angle. For a 10 micron particle, vac = 1.000062 and corresponds to an equilibrium dihedral angle of 68.4°. Other values of vac would correspond to different equilibrium dihedral angles. Therefore,

$$N_{ss} = 4.539712 \times 10^{-5} \tag{4}$$

As the interpenetration of the spheres proceeds, the dihedral angle increases from zero toward the equilibrium value and the radii of the

spheres increases. The pressure change between the planar and the convex (spherical) surface is given by

$$\Delta p = 2\ \gamma_{sv}/R \tag{5}$$

where γ_{sv} is the solid-vapor interfacial energy (assumed to be 1000 ergs/cm^2) and R is the increasing radius of the sphere. From Eq. (6) of Part A for 2 spheres the radius at any value of P is related to the original radius, R_0 by

$$R = R_0\ (4)^{1/3}/(4-3P^2 + P^3)^{1/3} \tag{6}$$

and

$$\Delta p_{sv} = 2\ \gamma_{sv}\ (4-3P^2 + P^3)^{1/3}/(4)^{1/3}R_0 \tag{7}$$

At the solid-solid interface there is a tensile stress which is created by the horizontal component of the solid-vapor interfacial energy. This stress increases from zero as the spheres interpenetrate and the pressure difference between the stress free and the stressed case is

$$\Delta p_{ss} = \gamma_{sv}\ \sin(\Phi/2)/R \tag{8}$$

$$\sin(\Phi/2) = (2P-P^2)^{1/2} \tag{9}$$

Substituting Eqs. (9) and (6) into Eq. (8)

$$\Delta p_{ss} = \gamma_{sv} (2P-P^2)^{1/2}(4-3P^2 + P^3)^{1/3}/(4)^{1/3}R_0 \qquad (10)$$

Therefore, at any value of P

$$N_{ss}(R) = N_{ss} \exp (\Delta p_{ss} a^3/kT) \qquad (11)$$

and

$$N_{sv}(R) = N_{sv} \exp (-\Delta p_{sv} a^3/kT) \qquad (12)$$

where a^3 is the atomic volume which is equal to 3.375×10^{-24}; k is the Boltzmann constant; and T is the temperature which is 1000 degrees kelvin. Using Eqs. (11) and (12) the vacancy concentrations were calculated at each interface for Figs. 12, 13, and 14.

TECHNICAL INFORMATION DIVISION
LAWRENCE BERKELEY LABORATORY
UNIVERSITY OF CALIFORNIA
BERKELEY, CALIFORNIA 94720